



Multi-Scale Simulation of Electroceramics

By:

Robyn Elizabeth Ward

A thesis submitted in partial fulfilment of the requirements for the degree of
Doctor of Philosophy

The University of Sheffield
Faculty of Engineering
Department of Materials Science and Engineering

July 2018

Abstract

This thesis used a range of simulation techniques to investigate the various effects rare-earth element doping has on barium titanate with a focus on their ability to increase the lifetime of such ceramics.

Finite element simulation was used to look for a relationship between user generated regional input permittivities, conductivities and microstructures based on experimental core-shell microstructures formed in rare-earth element doped barium titanate and the simulated bulk output properties. No simple analytical relationship was found. Input properties for more local regions are needed for accurate simulations. These cannot easily be obtained from experiment.

Experimental spectra (XRD and TEM) of perovskites were simulated from molecular dynamics simulations. The simulated spectra include dynamical information. The spectra along with the in-house analytical PALAMEDES code were used to interpret tilt features in the simulated systems. The code gives quantitative values for tilt and volumes for A and B sites in the system and identifies tilt phase.

Static simulations of doped barium titanate demonstrate the affinity of rare-earth dopants to form specific compensation schemes. The simulation results agree with experiment. Lifetime improvements due to rare-earth dopants have been theorised to be due to oxygen vacancy trapping. Further simulations show that all mid-size trivalent rare-earth elements can strongly trap oxygen vacancies. The differences seen in lifetime improvements between rare-earths is due to their distribution and compensation schemes they adopt.

Advanced sampling techniques were used to look at self-diffusion and rare-earth diffusion in barium titanate. The applicability of Mean Squared Displacement, Steered MD, Umbrella sampling and Metadynamics to solid-state systems is discussed. The self-diffusion results agreed with available experimental values. Dysprosium was found to be the most mobile rare-earth of those investigated in barium titanate lattice suggesting that a combination of its mobility and preference to dope in a self-compensatory manner is the reason for its superior lifetime improvements.

Acknowledgements

The last 9 years at the University of Sheffield for both my undergraduate and postgraduate studies have been crucial to my development both as a person and as a researcher.

My first thanks go to Professor John H. Harding for his supervision, support, and alternative reading and to Dr Colin L. Freeman for constant feedback, support and stepping up to be my second supervisor as my project changed direction. This PhD would not have been possible without them. I would also like to thank Professor Derek C. Sinclair, Professor Ian M. Reaney and Dr Julian S. Dean for expert guidance in their specialist areas.

A special thanks to Dr Christopher M. Handley, and to Dr Nicola A. Morley for their friendship and support both academic and otherwise. Many thanks to current and former residents of H7 for help, advice (taken or not), food, drink and coffee.

Thank you to my friends from the SU, SingSoc, Sheffield and the department, for your support, brunch, beer and making me believe that I could get this finished.

Finally, thanks go to my family, especially my parents for helping me get this far.

Without their understanding and encouragement completing this thesis would not have been possible.

Table of contents

ABSTRACT	2
ACKNOWLEDGEMENTS	3
TABLE OF CONTENTS	4
1 INTRODUCTION	6
1.1 AIMS	6
1.2 INTRODUCTION TO PEROVSKITES	6
1.3 MULTILAYER CERAMIC CAPACITORS	7
1.4 BARIUM TITANATE	10
1.5 MOTIVATIONS	13
1.6 THESIS OUTLINE	14
1.7 REFERENCES	15
2 FINITE ELEMENT MODELLING OF ELECTROCERAMICS	18
2.1 INTRODUCTION	18
2.2 IMPEDANCE SPECTROSCOPY	19
2.3 FINITE ELEMENT MODELLING	24
2.4 FEM WORKFLOW	26
2.5 BILAYER SIMULATION	27
2.6 CORE-SHELL MICROSTRUCTURE SIMULATION	30
2.7 CONCLUSIONS	35
2.8 REFERENCES	35
3 ATOMISTIC SIMULATION METHODS	39
3.1 INTRODUCTION	39
3.2 INTRODUCTION TO FORCEFIELDS	39
3.3 ENERGY OPTIMISATIONS	45
3.4 DEFECT CALCULATIONS	54
3.5 TRANSITION STATE THEORY AND SADDLE POINT SEARCHING	57
3.6 MONTE CARLO SIMULATION	62
3.7 MOLECULAR DYNAMICS	63
3.8 SOFTWARE USED	67
3.9 REFERENCES	67
4 SIMULATION OF DYNAMIC TILT IN PEROVSKITES	71
4.1 INTRODUCTION	71
4.2 TILTED PEROVSKITES	71
4.3 INTRODUCTION TO TEM AND XRD	74
4.4 DEFINITIONS OF TILT IN PEROVSKITES	83
4.5 GEOMETRICAL TILT ANALYSIS	87
4.8 RESULTS – METHYL-AMMONIUM LEAD IODIDE	99
4.9 CONCLUSIONS	100
4.10 REFERENCES	101
5 RARE EARTH DOPING OF BARIUM TITANATE	104

5.1	INTRODUCTION	104
5.2	FORCEFIELD DETAILS	105
5.3	RARE EARTH DOPING SCHEMES	107
5.4	DEFECT ENERGIES IN BARIUM TITANATE	108
5.5	DEFECT POPULATIONS IN BARIUM TITANATE	114
5.6	OXYGEN SELF-DIFFUSION IN BARIUM TITANATE	116
5.7	OXYGEN VACANCIES AROUND RARE EARTH DOPANTS	118
5.8	OXYGEN DIFFUSION AROUND RARE EARTH DOPANTS	120
5.9	CONCLUSIONS	124
5.10	REFERENCES	124
6	ENHANCED SAMPLING TECHNIQUES IN MOLECULAR DYNAMICS	129
6.1	INTRODUCTION	129
6.2	WHY DO WE NEED ENHANCED SAMPLING TECHNIQUES?	129
6.3	METADYNAMICS	131
6.4	UMBRELLA SAMPLING	138
6.5	STEERED MD	143
6.6	SOFTWARE USED	144
6.7	REFERENCES	144
7	DIFFUSION IN BARIUM TITANATE	148
7.1	INTRODUCTION	148
7.2	MOLECULAR DYNAMICS AND MSD	148
7.3	METADYNAMICS DETAILS	150
7.4	STEERED MD	156
7.5	UMBRELLA SAMPLING CALCULATION DETAILS	158
7.6	SELF-DIFFUSION IN CUBIC BARIUM TITANATE	158
7.7	RARE EARTH DIFFUSION IN BARIUM TITANATE	165
7.8	CONCLUSIONS	177
7.9	REFERENCES	178
8	CONCLUSIONS AND FUTURE WORK	182
	APPENDIX 1	187

1 Introduction

1.1 Aims

This introduction gives a general background to the materials investigated in this work and their applications. Firstly, the structure and properties of perovskites as a class of materials will be discussed. The electroceramic capacitors will be introduced and some of the research that has been done on barium titanate over the past 70+ years will be surveyed. Finally, aims of the thesis will be outlined, giving the reader an idea of what to expect in each chapter. As this thesis contains widely varied simulation techniques, each chapter will have its own introduction and background as required.

1.2 Introduction to Perovskites

Perovskites are a class of minerals with the general formula ABX_3 that are both found in nature, and manufactured for their industrial use (Haertling, 1999). They are among the most abundant minerals found on earth. Due to the flexibility of the crystal structure, there are many possible perovskite systems, solid solutions and possible dopants. This allows for great variation in the properties and polymorphs exhibited by these materials and allows them to be optimised for many different industrial applications.

1.2.1 Crystal Structure

The prototype perovskite structure is pseudo cubic close packed with the A-site cation and the X-site ions forming a close packed structure and B-site cations located on the octahedral interstitial sites (Glaister and Kay, 2002)(Fig 1.1).

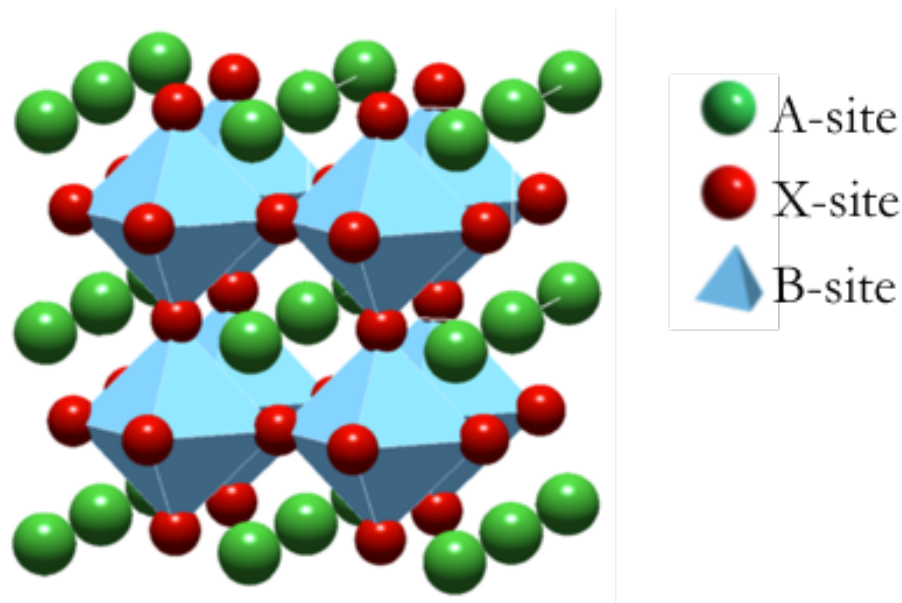


Figure 1.1: Prototype perovskite structure with A and X sites shown as green and red balls respectively. B-sites shown by blue polyhedra. The B-sites in perovskites form octahedra.

Examples of perovskite systems include calcium titanate (CaTiO_3) (Yashima and Ali, 2009), barium titanate (BaTiO_3), methyl-ammonium lead iodide ($\text{CH}_3\text{NH}_3\text{PbI}_3$) (Handley and Freeman, 2017) and strontium titanate (SrTiO_3) (Smith, 2012).

1.2.2 Applications

Perovskite based electroceramics can exhibit pyro, piezo and ferroelectric properties and are used for many applications (Haertling, 1999). They are prevalent throughout many industries and are used in areas including sensors, capacitors, energy storage devices and energy conversion devices (Alam, Zuga and Pecht, 2012).

One of the most important and widely used electro ceramics is, barium titanate (BT) which is used in capacitors. With a recent emphasis on reducing the use of devices that contain lead, BT is being used again for its piezoelectric properties (Kishi, Mizuno and Chazono, 2003)

1.3 Multilayer ceramic capacitors

Trillions of multilayer ceramic capacitor (MLCC) units, made using electroceramics such as barium titanate, are sold per year (Kishi, Mizuno and Chazono, 2003). They are

used in most electronic circuits and chip sets for computing, aviation, communication and many other industries. MLCCs consist of layers of dielectric electroceramic, with metal electrodes between each layer and each end capped with a connecting terminal (Moulson and Herbert, 2003) (Fig 1.2).

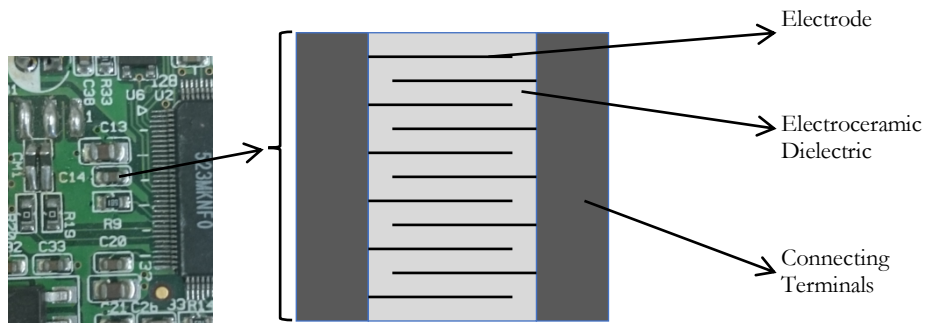


Figure 1.2: Schematic of an MLCC showing the main components, connection terminals, dielectric electroceramic and electrodes. A photograph of an example MLCC on an integrated circuit board is also shown.

The capacitance of a parallel-plate capacitor C is given in Equation 1.1 where A is the area of the capacitor plate, d the separation of the plates of the capacitor layer and ϵ_0 and ϵ_r are the permittivity of free space and the permittivity of the capacitor material between the plates.

$$C = \epsilon_0 \epsilon_r A / d \quad (1.1)$$

To optimise a capacitor without increasing the volume it occupies, either an increasingly small d or an increasingly large ϵ_r is desirable. To maximise the capacitance in an MLCC micrometer thin layers of electroceramic are used to minimize d and electroceramics are chosen to maximise ϵ_r . Multiple layers are used to maximize the total charge able to be stored by a capacitor.

Electroceramic capacitors are categorised into class I, or class II depending on their charge holding stability (Moulson and Herbert, 2003). Class I capacitors exhibit high stability and low losses. Class II capacitors exhibit lower stability and higher losses but are useful due to their greater volumetric efficiency. Within their respective classes, capacitors are classified based on their operating temperature range and the percentage variance in capacitance from room temperature in that range. The percentage variance

is known as the temperature coefficient of capacitance (TCC). One of the current industry standards for a Class II BT MLCC is X7R. rating. The letters and numbers in **X7R** refer to the temperature range (**X**) -55°C – (**7**) 125°C with variance (**R**) - ±15% TCC (Fig 1.3). Room temperature is taken as 25°C.

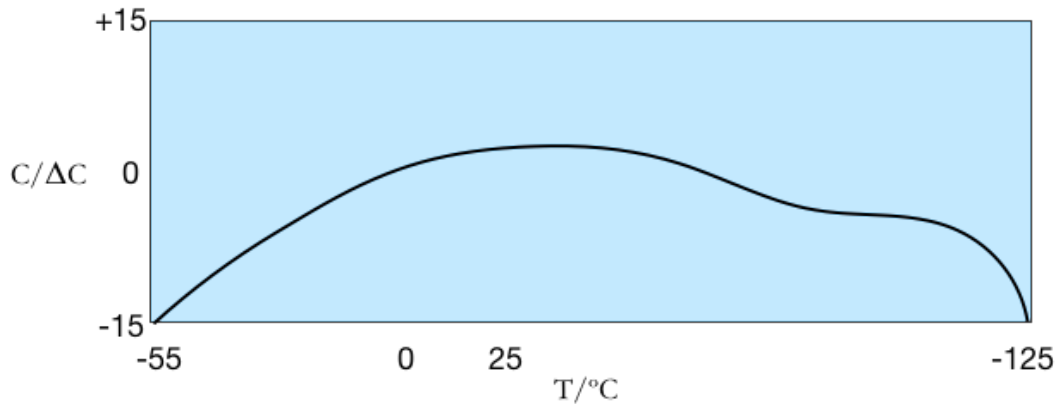


Figure 1.3: Typical TCC curve for Class II X7R Ceramic Capacitor exhibiting ±15% temperature coefficient of capacitance over the temperature range -50°C - 150°C. adapted from Moulson, A. and Herbert, J. (2003)

To optimise the TCC and therefore the stability of a class II BT MLCC, it is necessary to optimise the permittivity of the material over the device operating temperature range. Pure BT exhibits large permittivity changes with temperature, due to the phase transformations that it undergoes. Pure BT exhibits large permittivity changes with temperature, due to the phase transformations that it undergoes (Moulson and Herbert, 2003). Arguably the most important transformation for capacitor applications is from a tetragonal to a cubic crystal structure which occurs at the Curie temperature $\sim 130^\circ\text{C}$ (T_c). Above T_c the cubic structure prevents the titanium ions from forming dipoles and destroys the ferroelectric properties of the material, becoming paraelectric (Megaw, 1945). Approaching T_c the permittivity increases rapidly before dropping off sharply on the transformation to cubic where it subsequently obeys the Curie-Weiss law (Equation 1.2). This phase change drastically affects the TCC and therefore the stability of pure BT as a capacitor material above T_c .

$$\epsilon_r = \frac{A}{T - \theta_c} \quad (1.2)$$

where A is a constant for the specific material, T the temperature in Kelvin and θ_C is a temperature very close to but not the Curie temperature itself. Doping with elements such as lead or certain rare earth (RE) ions can increase the T_C leading to an improved TCC (Moulson and Herbert, 2003). Dopants can also influence the transition temperature of the lower temperature phase changes and can therefore influence the lower temperature end of TCC as well (Kishi, Mizuno and Chazono, 2003). Other materials with the perovskite structure such as NaNbO_3 have also been added to BT to optimise its TCC (Sarkar and Sharma, 1989). Some dopants, including rare earth elements, that are used in BT based MLCCs can fluctuate in cost wildly (Alam, Zuga and Pecht, 2012).

1.4 Barium Titanate

1.4.1 Background

First investigated in the 1940s (Haertling, 1999) barium titanate (BT) is one of the earliest high permittivity dielectric electro ceramics discovered, exhibiting permittivities of $\epsilon_r=2000-10000$ making it ideal for capacitor applications. Barium titanate has a wide range of polymorphs, or phases and due to this was also the first electro ceramic used in piezoelectric applications (Moulson and Herbert, 2003). Each phase change results in dimensional changes to the unit cell, these dimensional changes can be observed in the bulk ceramic. BT can be doped to make it into either an n-type or a p-type semiconductor at high temperatures with n-type BT also exhibiting conduction at room temperature (Moulson and Herbert, 2003). Such versatility in such a wide number of applications is the reason BT ceramics have been researched extensively in the last seven decades.

1.4.2 Properties and Phase Transformations

Barium titanate is a crystalline ceramic material with the ABX_3 perovskite structure §1.2, in which the barium sits on the A-site, titanium on the B-site and oxygen on the X-site. Pure barium titanate, is cubic above its Curie temperature T_C (approximately 130°C) (Megaw, 1945). It also exhibits further phase transitions at around 1430°C to the hexagonal structure (Rase and Roy, 1955). Below T_C the structure is tetragonal (von

Hippel *et al.*, 1946). Further low temperature phase transformations occur at $\sim 0^\circ\text{C}$ to the orthorhombic polymorph (Kay and Vousden, 1949) and at $\sim -90^\circ\text{C}$ to the rhombohedral polymorph (Rhodes, 1949). Barium titanate exhibits its highest permittivities when in the tetragonal polymorph.

In the tetragonal phase BT exhibits ferroelectric behaviour due to a dipole moment that is created along the c-axis with the elongation of the unit cell. The titanium ions can occupy one of two lower energy sites within the elongated BX_3 octahedra with a relatively small energy barrier between the two (Fig 1.4). The titanium offset creates a spontaneous dipole within the crystal and the movement of the ion between these two possible sites in the octahedra within the tetragonal phase gives rise to BT's ferroelectric properties (Moulson and Herbert, 2003). The size of the titanium ion dipole increases with increasing disorder through the tetragonal polymorph to the orthorhombic and then the rhombohedral polymorphs respectively.

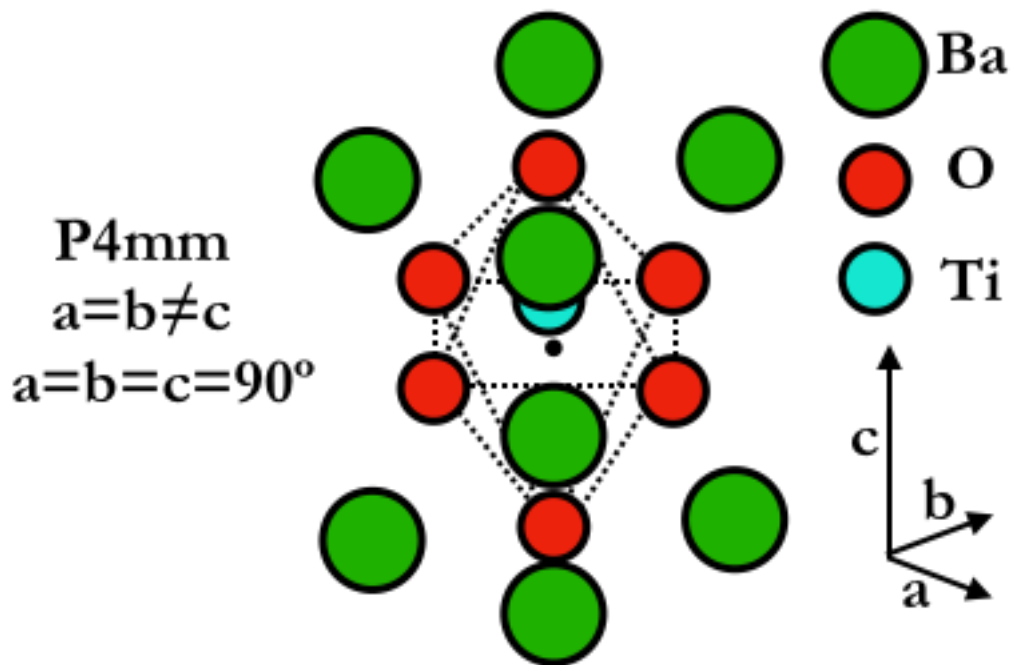


Figure 1.4: Schematic showing the titanium dipole observed in tetragonal barium titanate, shown by the off-centre blue titanium ion in the orthorhombic unit cell.

The relative permittivity of pure BT has been shown to increase with decreasing grain size down to $1\mu\text{m}$ (Kinoshita and Yamaji, 1976) which is due to lower internal strain the smaller the grain allowing for greater tetragonality within the particles and therefore higher permittivity. However, studies on nano size BT powders have shown that

reducing the initial particle size to below 40nm reduces the tetragonality of the initial powder and that this is due to increased strain due to the much larger surface area to volume ratio of the smaller powders which encourages a more cubic structure to lower the overall energy of the grains (Yashima *et al.*, 2005).

1.4.3 Dopants

As the grain size of the final polycrystalline material has a large effect on the resultant permittivity it is important to optimise this property during manufacturing. Additions of dopants such as La^{3+} , Gd^{3+} that have a higher charge than that of the A-site Ba^{2+} they substitute were shown by Buscaglia, V. *et al.* (Buscaglia *et al.*, 2006) to have a grain minimizing effect, thus increasing permittivity. This effect is also observed when substituting B-site Ti^{4+} with higher valency ions. These A-site and B-site substitutions can also have a marked difference on the T_c of the overall ceramic, raising or lowering T_c , which contributes to the stability of the material over a given temperature range. In the bulk material, unlike single crystals, grain boundaries can negatively contribute to the overall permittivity (Buscaglia *et al.*, 2006) so it is important to balance these competing contributions when optimizing grain size. As well as metallic ions, glasses are also sometimes added to BT to more closely control and lower sintering temperatures by facilitating liquid phase sintering.

The addition of dopants and other modifiers to perfect the properties of a BT ceramic for a specific purpose can also have other effects. For example, doping BT with rare-earth elements such as yttrium, gadolinium and dysprosium can create duplex or “Core-Shell” microstructures (Fig 1.5). These are structures in which a grain of pure BT is surrounded by a doped shell created by the limited diffusivity of the rare-earth dopants added to the ceramic (Jeon *et al.*, 2014).

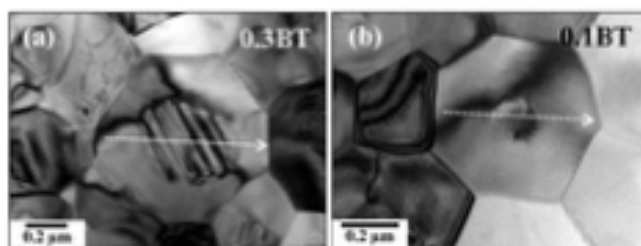


Figure 1.5: SEM images of duplex or “core-shell” structures in Y-Mg Doped BT reproduced from Jeon *et al.* (2014). The numbers shown are the average grain size in micrometres in the respective images.

The ‘core-shell’ structures consist of a conductive, ferroelectric core and a more resistive dopant containing shell. They are an example of how the heterogeneity in typical BT ceramics and thus the distribution of dopants and resultant properties of specific regions within the material can vary and may contribute towards the resultant properties of the bulk (Jeon *et al.*, 2014). The formation mechanism of these “core-shell” microstructures is much debated with Wang *et al.* (2014) suggesting that it is a solid-state diffusion process whereas Jeon, C. *et al.* (2012) suggest that in their Mg-Y doped BT the formation mechanism is that of liquid state sintering due to the uniform core sizes they observe. It may be the case that a combination of both solid-state diffusion and liquid sintering processes form these structures and that it depends on the individual recipe, and processing conditions as to which mechanism is dominant. To establish the compositional gradients and therefore an indication of the variability of the properties across these structures, techniques such as energy dispersive spectroscopy are necessary. Although compositional measurements are possible, direct electrical measurements of a specific point in a sample is not realistic.

The addition of rare-earth elements especially dysprosium is attributed with increasing the lifetime, or cycles to failure, for a given device. The mechanism behind this lifetime improvement is not fully understood, but is believed to be due to the ability of rare-earth elements to trap intrinsic oxygen vacancies (Waser, Baiatu and Härdtl, 1989). This lifetime improvement may also be related to the formation of the ‘core-shell’ microstructures (Jeon *et al.*, 2014). All rare-earth elements are trivalent ions however, when doping in barium titanate certain rare-earth elements outperform others in lifetime improvements. This difference in performance is not yet explained.

1.5 Motivations

The cost of the materials used in BT based MLCCs especially rare-earth elements as well as the difficulty in recycling low percentage dopants incentivise the search for alternatives and efficiencies (Alam, Zuga and Pecht, 2012). If this is to be successful, it is useful to understand the underlying processes by which these dopants work and their effect on material properties, to maximize their effectiveness without increasing the cost. Materials modelling is a cost-effective approach for facilitating the exploration of these processes; as the cost of lab time and consumables (other than computer time) is not a consideration. Simulation techniques also have the potential to observe behaviour

at scales not easily accessible via physical experiment. Using finite element modelling (FEM) simulation, the effect on the microstructures created by rare-earth dopants on the overall properties of a device can be examined. Atomistic simulation can be used to look at the energetics of doping, and the dynamic motion of the crystal. Diffusion of dopant species can also be looked at using atomistic simulations. The combination of the kinetic and thermodynamic information about different dopants in barium titanate should be invaluable for building up a picture of how and why dopants perform as they do.

1.6 Thesis Outline

This thesis uses many different simulation techniques to investigate rare earth element doping of BT and its effects on microstructure and properties.

In §2 the microstructures created by rare-earth element doping are probed using finite element simulation. The strengths and weaknesses of finite element simulation of impedance spectroscopy are discussed.

Atomistic simulation methods are discussed in §3. The fundamental concepts of atomistic simulations both static and dynamic as well their advantages and limitations are introduced.

§4 uses atomistic simulation to look at the structural implications of tilting in perovskites, barium titanate and calcium titanate included. TEM and XRD spectra are simulated from molecular dynamics simulations. Tilting in perovskites is explored using geometrical analysis.

Static simulations of rare earth doping of barium titanate are found in §5. The thermodynamics of doping with rare earths and their impact on O diffusion is investigated. Cation diffusion using static calculations are also attempted.

§6 explains advanced sampling techniques and free energy methods that can be used to investigate diffusion in crystals. The techniques include metadynamics, steered MD and umbrella sampling.

Free energy methods are used to investigate diffusion in barium titanate in §7. Standard MD is evaluated as a method for looking at diffusion. Metadynamics, steered MD, and umbrella sampling are all used to investigate oxygen diffusion in BT. Rare earth diffusion and cation self-diffusion are evaluated using metadynamics. Issues with

implementing the free energy methods are discussed as well as their suitability for use in solid-state simulations.

§8 contains the overall conclusions of this work and suggests future work that could be carried out based on it.

1.7 References

Alam, M. A., Zuga, L. and Pecht, M. G. (2012) 'Economics of rare earth elements in ceramic capacitors', *Ceramics International*. Elsevier, 38(8), pp. 6091–6098. doi: 10.1016/J.CERAMINT.2012.05.068.

Buscaglia, V., Buscaglia, M. T., Viviani, M., Mitoseriu, L., Nanni, P., Trefiletti, V., Piaggio, P., Gregora, I., Ostapchuk, T., Pokorný, J. and Petzelt, J. (2006) 'Grain size and grain boundary-related effects on the properties of nanocrystalline barium titanate ceramics', *Journal of the European Ceramic Society*, 26(14), pp. 2889–2898. doi: 10.1016/j.jeurceramsoc.2006.02.005.

Glaister, R. M. and Kay, H. F. (2002) 'An Investigation of the Cubic-Hexagonal Transition in Barium Titanate', *Proceedings of the Physical Society*, 76(5), pp. 763–771. doi: 10.1088/0370-1328/76/5/317.

Haertling, G. H. (1999) 'Ferroelectric ceramics: History and technology', *Journal of the American Ceramic Society*, 82(4), pp. 797–818. doi: 10.1111/j.1151-2916.1999.tb01840.x.

Handley, C. M. and Freeman, C. L. (2017) 'A new potential for methylammonium lead iodide', *Physical Chemistry Chemical Physics*, 19(3), pp. 2313–2321. doi: 10.1039/C6CP05829A.

von Hippel, A., Breckenridge, R. G., Chesley, F. G. and Tisza, L. (1946) 'High dielectric constant ceramics', *Industrial & Engineering Chemistry*. American Chemical Society, 38(11), pp. 1097–1109. doi: 10.1021/ie50443a009.

Jeon, S.-C., Lee, C.-S. and Kang, S.-J. L. (2012) 'The Mechanism of Core/Shell Structure Formation During Sintering of BaTiO₃-Based Ceramics', *Journal of the*

American Ceramic Society, 95(Core/Shell in BaTiO₃), pp. 2435–2438. doi: 10.1111/j.1551-2916.2012.05111.x.

Jeon, S.-C., Yoon, B.-K., Kim, K.-H. and Kang, S.-J. L. (2014) 'Effects of core/shell volumetric ratio on the dielectric-temperature behavior of BaTiO₃', *Journal of Advanced Ceramics*, 3(1), pp. 76–82. doi: 10.1007/s40145-014-0096-y.

Kay, H. F. and Vousden, P. (1949) 'XCV. Symmetry changes in barium titanate at low temperatures and their relation to its ferroelectric properties', *The London, Edinburgh, and Dublin Philosophical Magazine and Journal of Science*. Taylor & Francis, 40(309), pp. 1019–1040. doi: 10.1080/14786444908561371.

Kinoshita, K. and Yamaji, A. (1976) *Grain-Size Effects on Dielectric Properties in Barium-Titanate Ceramics*, *Journal of Applied Physics*. doi: 10.1063/1.322330.

Kishi, H., Mizuno, Y. and Chazono, H. (2003) 'Base-Metal Electrode-Multilayer Ceramic Capacitors: Past, Present and Future Perspectives', *Japanese Journal of Applied Physics*, 42(Part 1, No. 1), pp. 1–15. doi: 10.1143/JJAP.42.1.

Megaw, H. D. (1945) 'Crystal structure of barium titanate', *Nature*. MACMILLAN MAGAZINES LTD PORTERS SOUTH, 4 CRINAN ST, LONDON N1 9XW, ENGLAND, 155(3938), pp. 484–485.

Moulson, A. and Herbert, J. (2003) *Electroceramics - Materials, Properties and Applications*. 2nd edn. New York, NY: John Wiley and Sons.

Rase, D. E. and Roy, R. (1955) 'Phase Equilibria in the System BaO–TiO₂', *Journal of the American Ceramic Society*. Wiley/Blackwell (10.1111), 38(3), pp. 102–113. doi: 10.1111/j.1151-2916.1955.tb14585.x.

Rhodes, R. G. (1949) 'Structure of BaTiO₃ at low temperatures', *Acta Crystallographica*, 2(6), pp. 417–419. doi: 10.1107/S0365110X49001077.

Sarkar, S. K. and Sharma, M. L. (1989) 'Dielectric strength and dielectric constant of

BaTiO₃-NaNbO₃ composites at room temperature', *Journal of Materials Science Letters*, 8(12), pp. 1365–1367. doi: 10.1007/BF00720188.

Smith, a. G. H. (2012) 'Structural and defect properties of strontium titanate'.

Wang, M.-J., Yang, H., Zhang, Q.-L., Lin, Z.-S., Zhang, Z.-S., Yu, D. and Hu, L. (2014) 'Microstructure and dielectric properties of BaTiO₃ ceramic doped with yttrium, magnesium, gallium and silicon for AC capacitor application', *Materials Research Bulletin*. Elsevier Ltd, 60, pp. 485–491. doi: 10.1016/j.materresbull.2014.09.023.

Waser, R., Baiatu, T. and Härdtl, K. H. (1989) 'Degradation of dielectric ceramics', *Materials Science and Engineering: A*. Elsevier, 109, pp. 171–182. doi: 10.1016/0921-5093(89)90583-2.

Yashima, M. and Ali, R. (2009) 'Structural phase transition and octahedral tilting in the calcium titanate perovskite CaTiO₃', *Solid State Ionics*. Elsevier B.V., 180(2–3), pp. 120–126. doi: 10.1016/j.ssi.2008.11.019.

Yashima, M., Hoshina, T., Ishimura, D., Kobayashi, S., Nakamura, W., Tsurumi, T. and Wada, S. (2005) 'Size effect on the crystal structure of barium titanate nanoparticles', *Journal of Applied Physics*, 98(1). doi: 10.1063/1.1935132.

2 Finite Element Modelling of Electroceramics

2.1 Introduction

As discussed in §1 barium titanate (BT) has been optimised for use in multi-layer ceramic capacitors (MLCCs) using additives such as rare-earth (RE) elements and transition metals. These additives can create a ‘core-shell’ microstructure (Figure 2.1) during processing which can give the MLCC longer lifetimes (Waser, Baiatu and Hårdtl, 1989) and a more stable temperature coefficient of capacitance (TCC) (Jeon *et al.*, 2014).

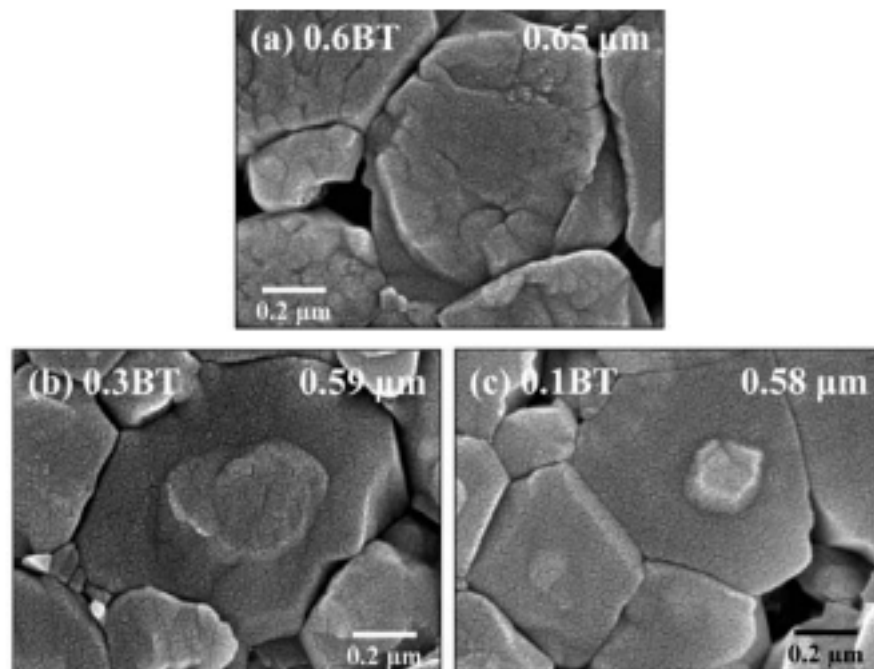


Figure 2.1: Barium titanate SEMs with a ‘core-shell’ microstructure reproduced from Jeon *et al.* (2014). Size in micrometres refers to average grain size.

As stated in §1, the main aim of this thesis is to explain how and why certain REs perform better than others when doping barium titanate to increase lifetime. This chapter discusses the finite element modelling of the electronic properties of barium titanate. Finite element modelling can be used to simulate the microstructures that REs cause in BT. This can help interrogate the reasons for the difference in performance of specific REs. It may explain how the different properties combine with different

microstructures to give the overall properties seen experimentally. The results should also suggest possible improvements to these microstructures.

2.2 Impedance Spectroscopy

2.2.1 Impedance Formalisms

Impedance is an A.C. property of materials or devices; analogous to D.C. resistance. Impedance includes an extra term not seen in D.C. resistance, due to the phase difference between current and voltage that can occur in A.C. circuits. Impedance spectroscopy (IS) is a characterization technique which measures the current and voltage of a material over a range of A.C. frequencies. These data give information about the electrical microstructure of the material itself. The different frequencies of an A.C. circuit activate responses from different electrical processes within the sample and can be used to identify electrical heterogeneity in a material (Sinclair, 1995; Kishi, Mizuno and Chazono, 2003). The magnitude of the complex impedance (Z^*) can be calculated as the ratio between the amplitude of the current and voltage measured during impedance spectroscopy (Macdonald, 1987). Z^* is made up of two components, one of which is real and is the resistance of the material, Z' . The other is imaginary or complex; Z'' . The impedance modulus can be used to calculate other formalisms that more clearly represent other electrical properties of the material being measured (Table 2.1).

Table 2.1: Impedance Spectroscopy Formalisms with their respective real and imaginary components listed.

<i>Formalism</i>	<i>Real Component</i>	<i>Imaginary Component</i>
<i>Impedance</i>	Z' - Resistance	Z''
<i>Admittance</i> $(Z^*)^{-1} = Y^*$	Y' - Conductivity	Y''
<i>Electric Modulus</i> $M^* = j\omega C_0 Z^*$	M' - Capacitance	M''
<i>Permittivity</i> $(M^*)^{-1} = \epsilon^*$	ϵ' - Permittivity	ϵ''

IS data can be plotted using one of the formalisms in Table 2.1 in either a Nyquist or Bode plot (Fig 2.2). Often the plateaus or arcs shown can be related to the material's

microstructure. For example, the arcs exhibited in the M^* Nyquist plot of Fig 2.1 can be used to work out the capacitance of the overall system and individual components such as grains and grain boundaries.

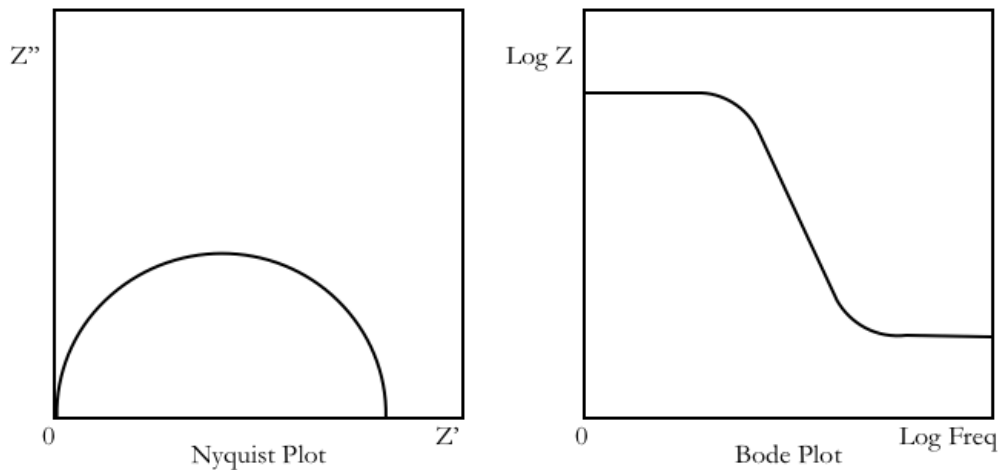


Figure 2.2: Example impedance spectroscopy formalism plots – Left: Nyquist style plot showing real and imaginary parts of impedance. Right: Bode plot showing impedances dependence on frequency (Log Z vs Log Frequency)

Impedance spectra are typically analysed using model circuits (equivalent circuits) to work out the constituent properties of the electrical microstructure. These can be made from any idealised circuit elements but for ceramics are often made from pairs of resistors and capacitors in parallel (RC elements) joined in series (Fig 2.3)(Macdonald, 1987). Typical equivalent circuits can have multiple RC elements, alongside extra terms to ensure a good fit to the measured data. These extra terms are discussed later. Usually, each RC element represents a component of the microstructure that it is modelling (e.g. grain boundaries and bulk) giving the model circuit a grounding in the physical microstructure of the material. Grain boundaries are modelled with higher values for resistance and capacitance than the bulk due to their geometry and higher concentration of defects.

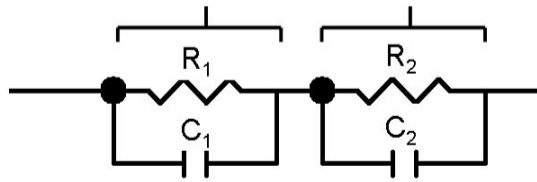


Figure 2.3: RC Circuit used to analyse impedance spectroscopy spectra. The diagram shows two RC circuits joined in series.

Impedance spectra often disagree with the ideal responses modelled by their equivalent circuits. This is often attributed to the presence of material heterogeneity in the sample (West, Sinclair and Hirose, 1997). This is a non-ideal Debye response; a depressed arc in modulus plots (M^*) and a broadened Debye peak in the spectroscopic plots (Z^*). This makes using equivalent circuits to fit data challenging and often an extra constant phase element (CPE) term is used to fit these non-ideal responses. CPEs, unlike RC elements, cannot usually be ascribed to a specific microstructural feature; just to overall material homogeneity. Once an analytical model is chosen and values are ascribed to each component it is compared to the collected experimental data and observed in multiple formalisms to check the fit (Irvine, Sinclair and West, 1990). Care must be taken when choosing and fitting an equivalent circuit as different equivalent circuits can have the same outputs (Abelard and F. Baumard, 1982). Fitting a model to IS data requires experience of the system as well as intuition as to how to best represent the system using electrical components.

It has been shown by Dean et al (2014), using finite element modelling, that a homogeneous grain core gives rise to electric field heterogeneity and this was further explored by Heath et al (2015) who showed that both the core volume fraction and overall geometry of the sample can lead to heterogeneity in the electric field. This implies that the analysis of experimental IS data via equivalent circuits may not result in a direct link to physical microstructure as geometrical features rather than pure microstructural ones can also influence the IS data. This can be described as the electrical microstructure of a sample.

2.2.2 Modelling Impedance Spectra

Using equivalent circuits to understand the impedance spectra of ceramics began in 1969 when RC circuits were used by Bauerle and subsequently Beekmans to model bulk ceramics alongside grain boundaries (Bauerle, 1969; Beekmans and Heyne, 1976). This was expanded to the Brick Layer Model (BLM) where the bulk ceramic is modelled as ‘bricks’ and the grain boundaries as ‘mortar’ when multiple grains are modelled together (Fig 2.4). Subsequently Nafe added a term to account for any current flowing around the grain core (Nafe, 1984).

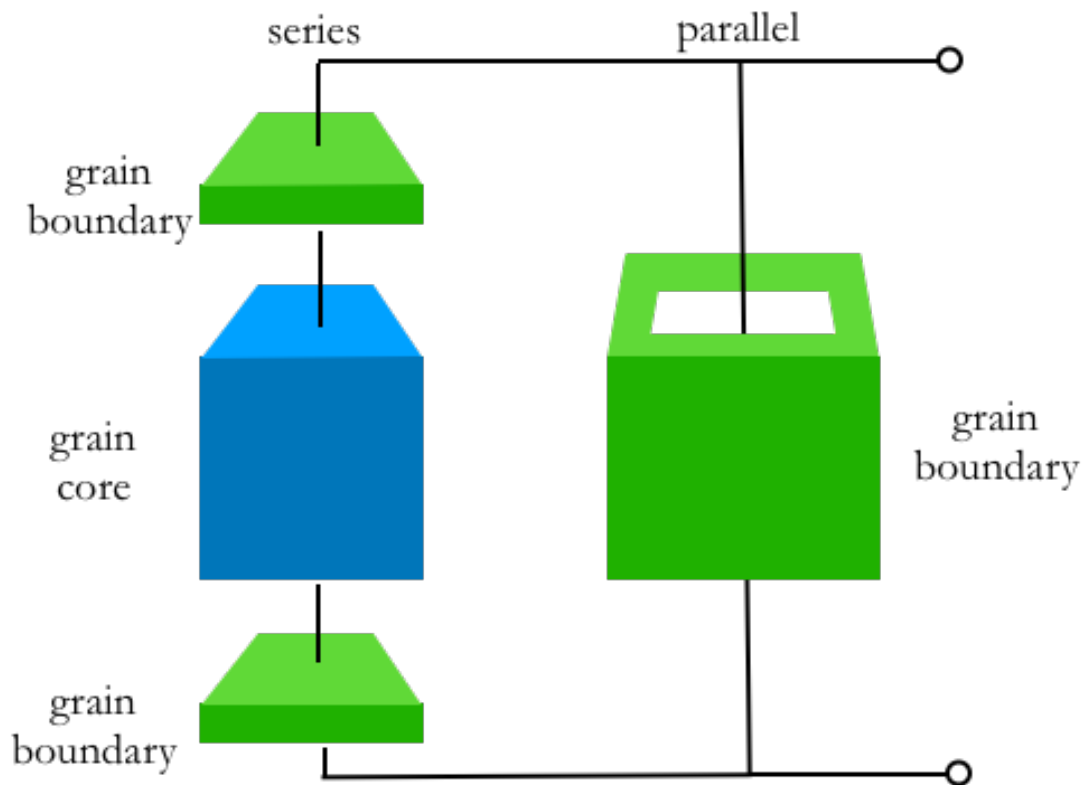


Figure 2.4: Brick Layer Model Schematic adapted from Kidner *et al*(2005). Showing the cubic grain core in blue with the grain boundary components in green modelled in series alongside the parallel grain boundary contribution.

Wen et al (2008) have proposed a simple analytical model for modelling the permittivity of spherical ‘core-shell’ grains using the radii of the cores and shells and their respective permittivities to calculate the grain permittivity. However, the mathematical model presented is not a good analytical model for grains with thick shells. Other attempts at

modelling IS of materials include the finite difference model (FD)(Kidner *et al.*, 2005). This models IS using 6 orthogonally connected ‘cubes’ or RC elements assigned different properties depending on the part of the microstructure the cube represents (Fig 2.5). This technique gives overall agreement with impedance spectra and with other methods, including effective medium theory and FEM. However, the conduction pathways through the model are limited by the orthogonal connections which results in unrealistic electric field distributions as the cores are modelled as cubes (Kidner *et al.*, 2008).

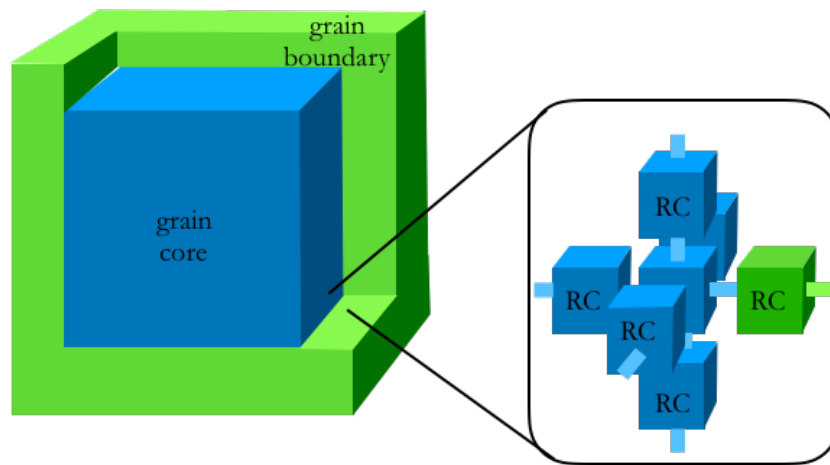


Figure 2.5: Finite Difference Model for Impedance Spectroscopy showing orthogonally connected RC circuits assigned with either the grain core or grain boundary properties.

The overall grain core remains cubic in shape.

Other methods for modelling the impedance of electroceramics include effective medium theory (EMT) based on Maxwell’s equations. It models randomly distributed nested spheres, a grain core and boundary, within an effective medium matrix that is assigned properties like the grain boundaries (Maxwell 1881) . This method also gives good agreement with impedance spectra however it is limited to spheres in its implementation. The effective medium matrix occupies the location of what would be the grain boundaries in a real ceramic. The EMT model also uses (unrealistic) perfectly spherical grain shapes. In the literature EMT and FD methods have been used to model different volume fractions of core and shell microstructures (Kidner *et al.*, 2008). Both methods allow the assignment of individual properties to different regions of the model, which is crucial for investigating the combinatorial effect of both microstructure and

properties. Recreating a realistic microstructure is necessary to be able to separate the contributions made by the material properties from the microstructural features.

2.3 Finite Element Modelling

2.3.1 Introduction

Finite element modelling (FEM) is a mathematical technique that solves partial differential equations. It does this by breaking them into finite sections or elements and subsequently solving these elements as a set of parallel equations. These local solutions can then be used to solve the global system. It has been used to model problems including heat transfer (Daurelle, Occelli and Martin, 1994), structural analysis of bridges (Chan, Guo and Li, 2003) and aircraft (Wen *et al.*, 2018) using equations for heat flow, and stress and strain respectively. It can be used to solve for electronic properties by using it to solve Maxwell's equations (Maxwell 1881). Maxwell's equations, originally published by James Clerk-Maxwell in 1865, are the main equations used to describe the generation of fields, both electric and magnetic, by charges and currents. The equations come in two variants, micro and macroscopic. The macroscopic equations are solved in this work using the FEM code ELCer (Dean, Harding and Sinclair, 2014).

2.3.2 Mesh Generation

FEM works by splitting the problem being solved into finite elements; the generation of finite elements is mesh generation. The models in this work are generated using Voronoi tessellation, which uses a bisection method to generate finite element geometries (Tanemura, Ogawa and Ogita, 1983)(Fig 2.6a). In Voronoi tessellation, an overall 3D shape is seeded with points. The points are then joined by straight lines which are bisected by a plane that is normal to the line. The algorithm terminates the planes when they intersect another plane. This forms finite convex polygons. When complete, the whole 3D shape is meshed. Mirror points can be added to the model to create specific geometries such as squares or cubes (Fig 2.6b). The mirror points can also be used above or below a 2D plane to create a 3D dimensional wire model.

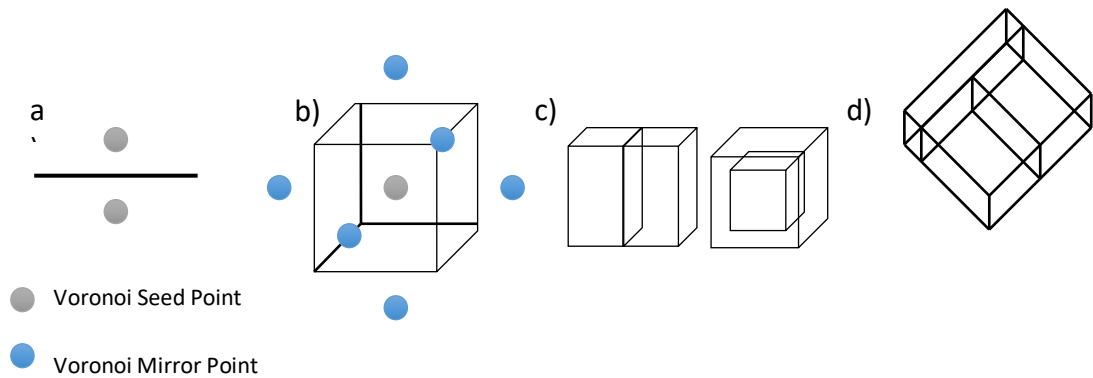


Figure 2.6: a) Voronoi line bisection. b) A 3D structure made using Voronoi line bisection with mirror points. c) Parallel layer and nested cube models built using the **qhull** code (see below). d) A parallel layer wire frame geometry with an extruded electrode layer.

The **qhull** (Barber, Dobkin and Huhdanpaa, 1996) open source software uses an algorithm to identify the surfaces or wire frame of the 3D shape being simulated. This basic geometry can then be duplicated and shrunk or distorted to create the wanted geometry: simple layers, parallel layers, ‘core-shell’ microstructures or grain boundaries (Fig 2.6c). The geometry is then meshed using tetrahedral elements by another open source program – **Gmsh** (Geuzaine and Remacle, 2009), in which the mesh size can be set as a fraction of the total geometry to be meshed. In FEM, a coarser mesh requires less computer time to solve than a much finer mesh due to the total number of elements. Error increases with increasing mesh size so the mesh size needs to be optimised for each geometry simulated. Once the mesh for a simulation has been generated, a reference electrode is added to the top of the model for the FEM calculation using the extrude function in **Gmsh** which extrudes the top layer of into a layer made up of prisms (Fig 2.6d).

2.3.3 ELCer

ELCer (Dean, Harding and Sinclair, 2014) is an in-house code that solves Maxwell’s equations using the finite element method. The generated mesh is uploaded to be solved using **ELCer**. The elements in the mesh are assigned material properties. The

properties required are conductivity and permittivity. The permittivity is considered isotropic for ease of calculation. Induction is neglected as ceramics are not conductive over the frequency range considered. The code constructs the stiffness matrix using the permittivities and conductivities that have been assigned. When simulating a material over a temperature range, the temperature itself is not considered explicitly; instead the properties assigned are modified to account for temperature change. This requires knowledge of the permittivity and conductivity of the material over the temperature range being investigated. This data can be taken from experiment or simulation. After the initial matrices are constructed, each element is solved locally, giving the electric field and current density at each time step. These values are substituted into the global matrix. The current density is set to zero at the free surfaces by a Neumann boundary condition; where the solution to the derivative of the partial differential equation is set. The voltage drop across the simulation is a known value (set using Dirichlet boundary conditions; where the solution to the partial differential equations at the boundary is set). Thus, by integrating the global matrix at a given frequency, the current flowing through the reference electrode can be calculated. The V-I data can then be used to calculate impedance at that frequency (Table 2.1). Finally, the data calculated is saved in the form of a Microsoft Excel file, and a **ZView** (an impedance spectra program) file.

2.4 FEM Workflow

The workflow for the FEM simulations completed in this chapter is detailed in Fig 2.7.

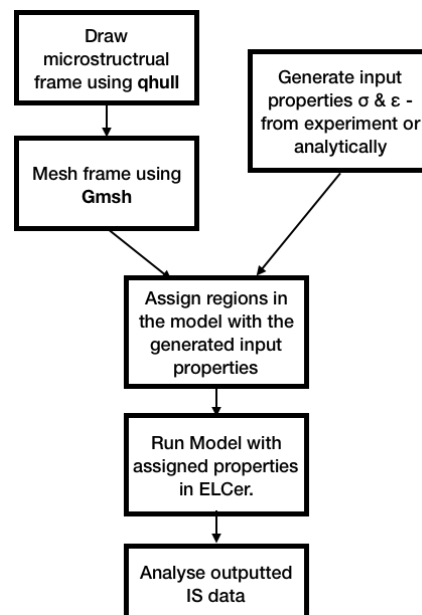


Figure 2.7: FEM simulation workflow for this chapter.

2.5 Bilayer Simulation

2.5.1 Simulation Details

To validate **ELCer** the in house code against analytical equations, the simple layer model (SLM); two capacitors in series (Fig 2.8a, Eq 2.1), and the parallel layer model (PLM); two capacitors in parallel (Fig 2.8b, Eq 2.2) were compared to the analytical solution shown in the respective equations. Two individual $10\mu\text{m}^3$ model cubes, one split horizontally and the other split vertically were generated with a mesh size of 0.09.

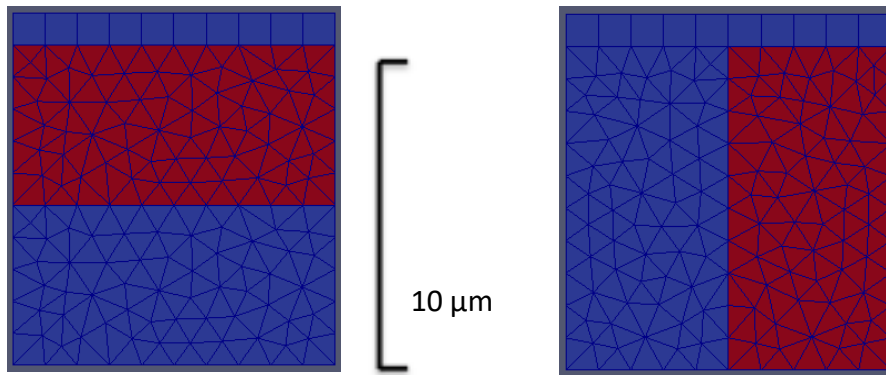


Figure 2.8: A cross section of $10\mu\text{m}$ cubes meshed using **Gmsh** with a mesh size of 0.09 a) Simple Layer Model, b) Parallel Layer Model.

$$\frac{1}{C_{series}} = \frac{1}{C_{layer1}} + \frac{1}{C_{layer2}} \quad (2.1)$$

$$C_{parallel} = C_{layer1} + C_{layer2} \quad (2.2)$$

The properties for the layers (Table 2.1) were generated analytically based on straight lines generated from the approximate gradients of the curves shown by Jeon et al (2014) for ‘core’ and ‘shell’ barium titanate. The generated property profiles do not overlap. In

the simulations one layer (blue) was assigned ‘shell’ permittivities and conductivities and the other ‘core’ (red) permittivities and conductivities. A range of temperatures: 0°C-150°C (273.15K-423.15K) was investigated. The reference electrode was assigned a permittivity value of 0 and a conductivity of $1 \times 10^3 \mu\text{Sm}^{-1}$. Even though this is an unrealistic property it makes the electrode a constant value which allows the potential difference to be calculated simply with reference to this constant. All values assigned are shown in Table 2.1. The models were simulated from 1Hz – 0.1 GHz. M* Nyquist plots were generated. The total capacitance value was also calculated using the appropriate analytical solutions utilising the relationship between capacitance and permittivity (Eq. 2.1, 2.2).

Table 2.1: Properties assigned to the core, shell and electrode for the SLM and PLM investigation, generated by fitting straight lines to the BT core and shell signals from Jeon et al (2014)

<i>Temperature</i> (°C)	<i>Core Properties</i>		<i>Shell Properties</i>		<i>Electrode Properties</i>	
	σ (μSm^{-1})	ϵ (Fm ⁻¹)	σ (μSm^{-1})	ϵ (Fm ⁻¹)	σ (μSm^{-1})	ϵ (Fm ⁻¹)
0	1×10^{-4}	1800	1×10^{-4}	1700	1×10^3	0
10	1×10^{-4}	1850	1×10^{-4}	1650	1×10^3	0
20	1×10^{-4}	1900	1×10^{-4}	1600	1×10^3	0
30	1×10^{-4}	1950	1×10^{-4}	1550	1×10^3	0
40	1×10^{-4}	2000	1×10^{-4}	1500	1×10^3	0
50	1.25×10^{-4}	2050	1.25×10^{-4}	1450	1×10^3	0
60	1.5×10^{-4}	2100	1.5×10^{-4}	1400	1×10^3	0
70	1.75×10^{-4}	2150	1.75×10^{-4}	1350	1×10^3	0
80	2×10^{-4}	2200	2×10^{-4}	1300	1×10^3	0
90	2.25×10^{-4}	2250	2.25×10^{-4}	1250	1×10^3	0
100	2.5×10^{-4}	2300	2.5×10^{-4}	1200	1×10^3	0
110	2.75×10^{-4}	2350	2.75×10^{-4}	1150	1×10^3	0
120	3×10^{-4}	2400	3×10^{-4}	1100	1×10^3	0
130	3.25×10^{-4}	2450	3.25×10^{-4}	1050	1×10^3	0
140	3.5×10^{-4}	2500	3.5×10^{-4}	1000	1×10^3	0
150	3.75×10^{-4}	2550	3.75×10^{-4}	950	1×10^3	0

2.5.2 Results and Discussion

The graphs (Fig 2.9a and 2.9b) show that in the case of the SLM and PLM the values obtained from FEM are a good match with the analytical solutions (Eq. 2.1, 2.2) with SLM having a maximum 2% variance from the analytical values and the PLM having a maximum 8% variance. The variance from analytical could be explained by the large mesh size as this may introduce error.

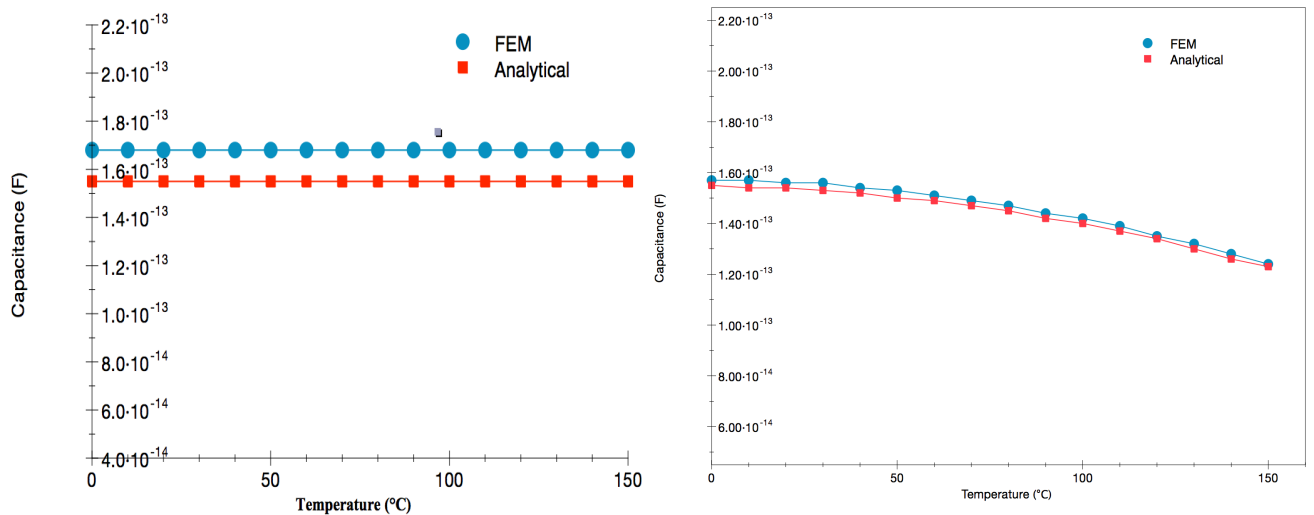


Figure 2.9: Capacitance vs Temperature plots for a) SLM – Variance 2% b) PLM – Variance 8%.

The M^* Nyquist plots of the SLM and PLM are single arcs (Fig 2.10). Though the microstructures have regions with two different assigned material properties no second response arc is seen. The values assigned are close together – separated by less than three orders of magnitude - and therefore the phase difference between the two regions is insufficient for separate arcs on the plot to be seen. This is also possible in experimental IS data when time constants of separate regions are similar. Hence choosing the correct equivalent circuit when analysing IS data is difficult, as merged arcs are difficult to resolve and there can be many solutions to choose from. For microstructures with many different areas with similar properties it may be very difficult to attribute specific bulk properties to any specific phase analytically or through simulation. Overall it is clear that **ELCer** gives good agreement with analytical models and can be used to simulate IS for generated microstructures. Input properties, permittivity and conductivities for simulation must be obtained either from experiment

or simulation. Ideal properties can be investigated to ascertain if there is an observable relation between properties of specific areas and resultant overall bulk properties over temperature.

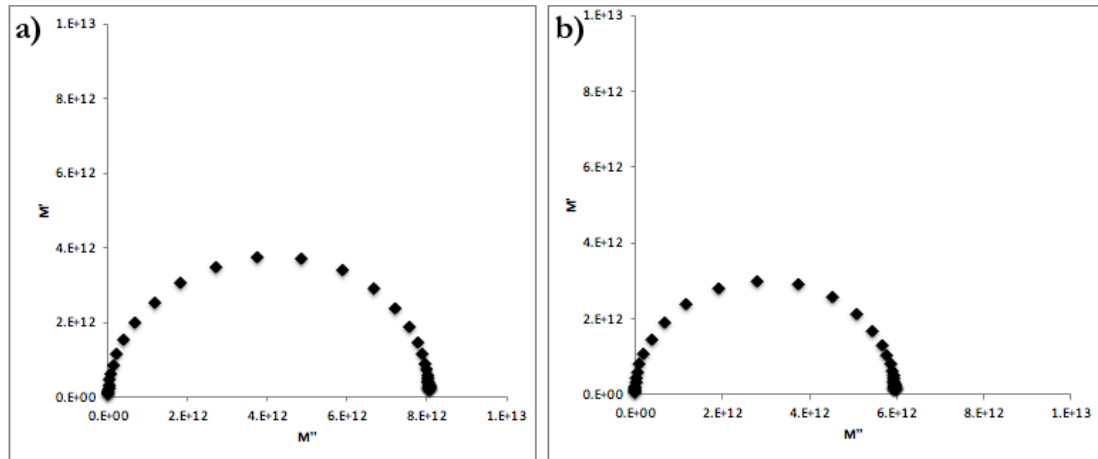


Figure 2.10: M^* Nyquist Plots showing single arcs for a) simple layer and b) parallel layer models at 150°C. The lack of a secondary arc is because the assigned permittivities are separated by less than three orders of magnitude.

2.6 Core-Shell Microstructure Simulation

2.6.1 Simulation Details

The relationship between individual core and shell permittivities and the overall capacitance of a single “core-shell” grain was investigated. Both core volume fraction and input permittivities were varied. A ‘core-shell’ $10\mu\text{m}^3$ nested cube microstructure was generated with core volume fractions, 20%, 50%, 60%, 70%, 80% and 90% using the methods outlined previously §2.3.2 (Fig 2.11). The 50% core volume fraction cube was tested at varying mesh sizes using the input parameters from the SLM/PLM investigation to check for convergence and to pick the most appropriate mesh size. The final mesh size used was 0.05.

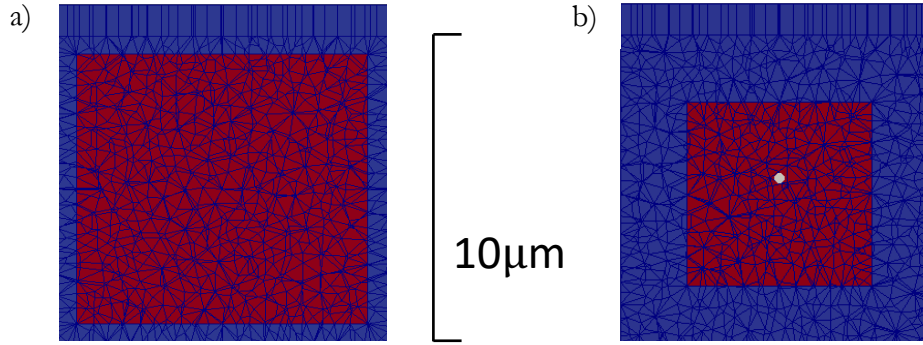


Figure 2.11: Cross sectional images of created geometries with a mesh size 0.05 of a) 70% core volume fraction b) 20% core volume fraction

‘Core’ input permittivity values for this investigation were created using a straight-line gradient generated by drawing an approximate straight line fit for the 0-150°C range at 10°C intervals for the pure BaTiO₃ experimental signal reported by Jeon et al (2014). A flat shell permittivity at $\epsilon_r = 1700$ was chosen for the same temperature range. The zero-gradient shell line was then rotated clockwise about the 0°C coordinate, creating 4 shell permittivity straight lines with gradients ranging from -2.5 to -10 (Fig 2.12). In all simulations, the core permittivity gradient (Fig 2.12) was kept the same and the shell permittivity gradient was varied. A conductivity of $1 \times 10^{-4} \mu\text{Sm}^{-1}$ was selected and this value was kept the same for both the ‘core’ and ‘shell’ components throughout. The reference electrode was assigned a permittivity value of 0 and a conductivity of $1 \times 10^3 \mu\text{Sm}^{-1}$.

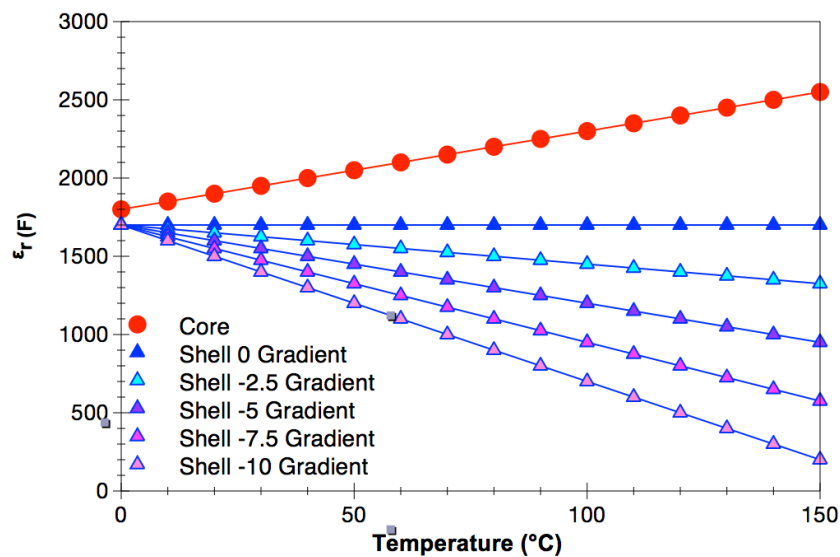


Figure 2.12: Input core and shell permittivities straight lines generated for simulation purposes with the shell inputs varied with increasing negative gradient (0 to -10)

Each core volume fraction was simulated once with each of the five shell permittivity gradients shown, through the 1Hz-0.1GHz range. From each M^* spectrum created, the total capacitance value was obtained from $1/M^*$. Capacitance vs temperature graphs were generated which were converted into TCC (temperature coefficient of capacitance) curves for each gradient and core volume fraction. Room temperature was taken to be 30°C for the TCC calculation as 25°C was not a temperature simulated during these calculations.

2.6.2 Results and Discussion

The TCC graphs generated for different core volume fractions with different shell gradients (Figs 2.12-14) show several trends. As the shell volume fraction decreases, the overall contribution from the shell permittivities decreases non-linearly. The non-linearity increases with increasing shell gradient. This suggests that the combination of core volume fraction and the shell properties is important for optimising these core-shell structures. The plots also suggest that, as the difference in permittivity between the core and shell increases, the TCC is increasingly affected as evidenced by the high-temperature ends of the curves where the difference between permittivities is greatest.

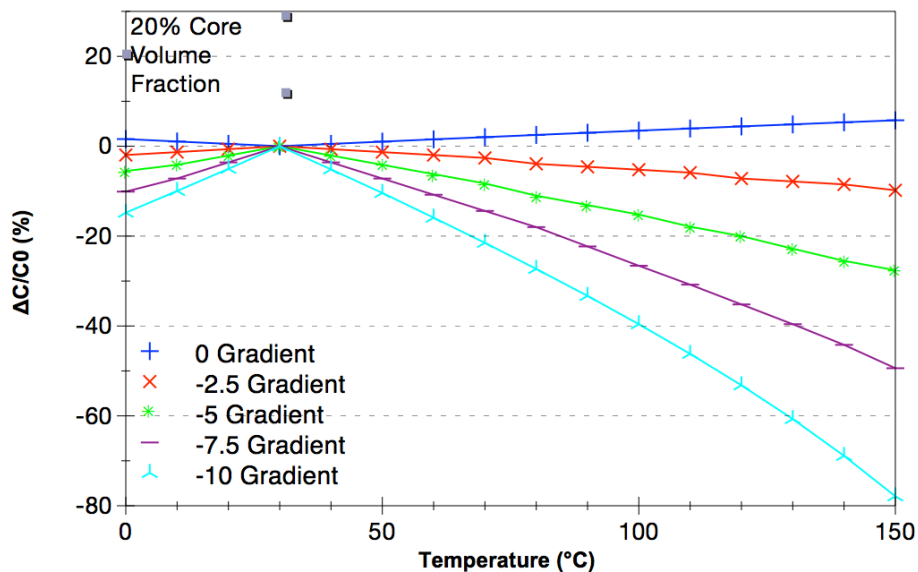


Figure 2.13: TCC ($\Delta C/C^0$ %) curve for a 20% core volume fraction grain, core input permittivity and conductivities were kept the same and shell input permittivities were varied as per Figure 2.12.

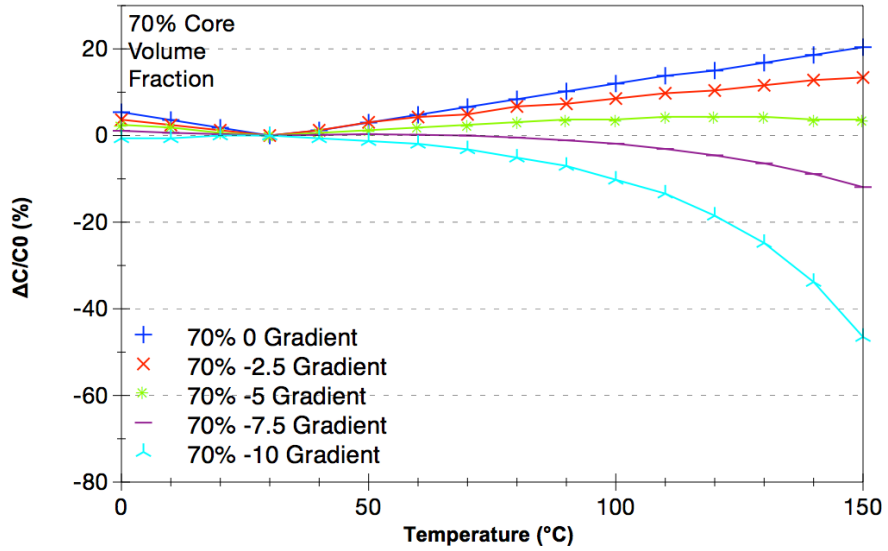


Figure 2.14: TCC ($\Delta C/C\%$) curve for a 70% core volume fraction grain, Figure 2.13: TCC curve for a 20% core volume fraction grain, core input permittivity and conductivities were kept the same and shell input permittivities were varied as per Figure 2.12.

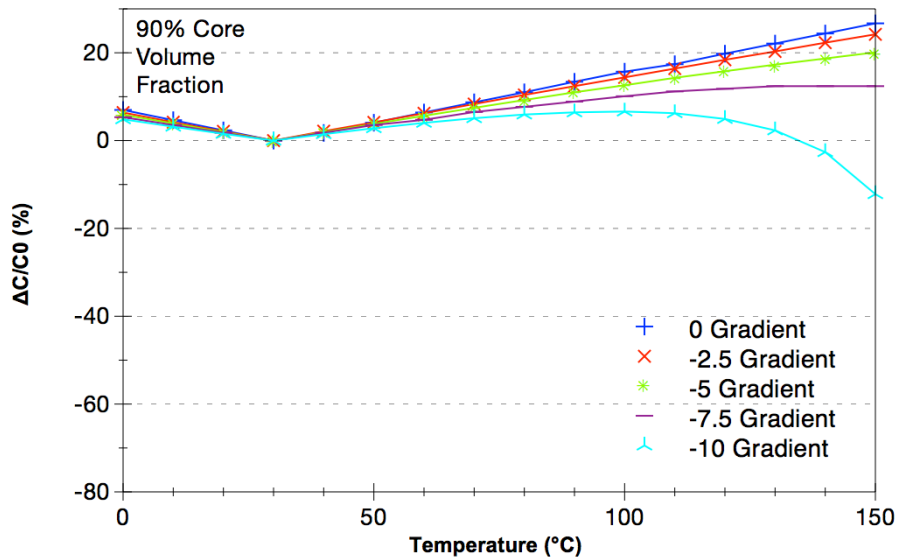


Figure 2.15: TCC ($\Delta C/C\%$) curve for a 90% core volume fraction grain, Figure 2.13: TCC curve for a 20% core volume fraction grain, core input permittivity and conductivities were kept the same and shell input permittivities were varied as per Figure 2.12.

The largest deviation of TCC is observed at 150°C for all core volume fractions and input permittivity gradients. The TCC value for every volume fraction at 150°C at every shell gradient was plotted to better interrogate the relationship between input permittivities and output TCC (Fig 2.16). The plot shows that the relationship between shell gradient, core volume fraction and TCC is not linear, and this is exacerbated in shells with steeper gradients. This non-linear relationship becomes more cubic (see cubic line of best fit) with increasing shell gradient and suggests that the link between microstructural regions, their assigned properties and the bulk properties of the material cannot be predicted by a simple analytical relationship.

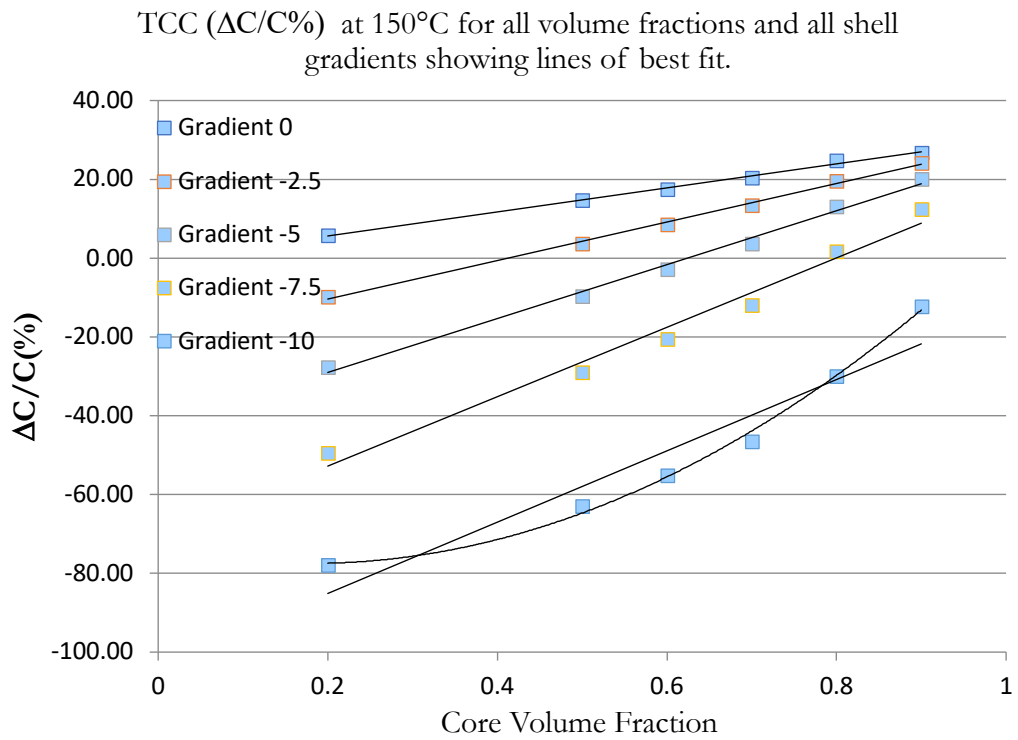


Figure 2.16: TCC (%) at 150°C for Input Shell Permittivity Gradients 0, -2.5, -5, -7.5 and -10 at core volume fractions 20%, 50%, 60%, 70%, 80% and 90% showing lines and curves of best fit.

It has also been shown by Dean et al (2014) and Heath et al (2015) that even simple microstructures with single input properties can give rise to electrical heterogeneity that is not directly relatable to specific microstructural features. This electrical heterogeneity is thought to be from the 3D shapes formed by areas of the microstructure. Experiment

also shows that shells have a rare-earth content gradient (Jeon *et al.*, 2014) due to the diffusion of rare-earths towards the core as the grain grows. This means that, in FEM, shells should be modelled by successive thin shells with different properties per rare-earth content. It is difficult to obtain these properties by experiment due to the small dopant level and the difficulty in obtaining completely homogenous samples to measure. Exploring other smaller scale simulation techniques may help bridge this gap.

2.7 Conclusions

FEM as a technique can provide valuable insight to the relationship between material, microstructural and electrical properties. The technique requires the user to input properties for individual areas of the microstructure. These can come from experiment or simulation. The results of simulating ‘core-shell’ microstructures with simple linear properties show that the relationship between core and shell properties and bulk properties is not linear. Impedance spectroscopy is of limited value for analysis of materials with microstructural regions with very similar properties. Merged M^* Nyquist plots make attributing properties to physical microstructural features difficult. Exploring rare-earth doping of BT using a smaller scale simulation technique may be the best way of continuing to explore this system, and obtain realistic properties to input into future FEM simulations. The linking of two different scale simulation techniques via these properties will allow a feedback loop between different simulation scales as well as comparison with experimental results.

2.8 References

Abelard, P. and F. Baumard, J. (1982) *Study of the dc and ac electrical properties of an yttria-stabilized zirconia single crystal [(ZrO₂)_{0.88}-(Y₂O₃)_{0.12}]*, *Physical Review B*. doi:

10.1103/PhysRevB.26.1005.

Barber, C. B., Dobkin, D. P. and Huhdanpaa, H. (1996) ‘The Quickhull Algorithm for Convex Hulls’, *ACM Trans. Math. Softw.* New York, NY, USA: ACM, 22(4), pp. 469–483. doi: 10.1145/235815.235821.

- Bauerle, J. E. (1969) 'Study of solid electrolyte polarization by a complex admittance method', *Solid State Communications*, 7(15), p. ii. doi: 10.1016/0038-1098(69)90484-0.
- Beekmans, N. M. and Heyne, L. (1976) 'Correlation between impedance, microstructure and composition of calcia-stabilized zirconia', *Electrochimica Acta*, 21(4), pp. 303–310. doi: 10.1016/0013-4686(76)80024-2.
- Chan, T. H. T., Guo, L. and Li, Z. X. (2003) 'Finite element modelling for fatigue stress analysis of large suspension bridges', *Journal of Sound and Vibration*, 261(3), pp. 443–464. doi: 10.1016/S0022-460X(02)01086-6.
- Daurelle, J. V, Occelli, R. and Martin, R. (1994) 'Finite-Element Modeling of Radiation Heat Transfer Coupled with Conduction in an Adaptive Method', *Numerical Heat Transfer, Part B: Fundamentals*. Taylor & Francis, 25(1), pp. 61–73. doi: 10.1080/10407799408955910.
- Dean, J. S., Harding, J. H. and Sinclair, D. C. (2014) 'Simulation of impedance spectra for a full three-dimensional ceramic microstructure using a finite element model', *Journal of the American Ceramic Society*, 97(3), pp. 885–891. doi: 10.1111/jace.12750.
- Geuzaine, C. and Remacle, J.-F. (2009) *Gmsb: A 3-D Finite Element Mesh Generator with Built-in Pre- and Post-Processing Facilities*, *International Journal for Numerical Methods in Engineering*. doi: 10.1002/nme.2579.
- Heath, J. P., Dean, J. S., Harding, J. H. and Sinclair, D. C. (2015) 'Simulation of Impedance Spectra for Core-Shell Grain Structures Using Finite Element Modeling', *Journal of the American Ceramic Society*, 1931(36020), p. n/a-n/a. doi: 10.1111/jace.13533.
- Irvine, J. T. S., Sinclair, D. C. and West, A. R. (1990) 'Electroceramics: characterization by impedance spectroscopy', *Advanced Materials*, 2(3), pp. 132–138. doi: 10.1002/adma.19900020304.
- Jeon, S.-C., Yoon, B.-K., Kim, K.-H. and Kang, S.-J. L. (2014) 'Effects of core/shell volumetric ratio on the dielectric-temperature behavior of BaTiO₃', *Journal of Advanced*

Ceramics, 3(1), pp. 76–82. doi: 10.1007/s40145-014-0096-y.

Kidner, N. J., Homrighaus, Z. J., Ingram, B. J., Mason, T. O. and Garboczi, E. J. (2005) ‘Impedance/dielectric spectroscopy of electroceramics-part 1: Evaluation of composite models for polycrystalline ceramics’, *Journal of Electroceramics*, 14(3), pp. 283–291. doi: 10.1007/s10832-005-0969-0.

Kidner, N. J., Perry, N. H., Mason, T. O. and Garboczi, E. J. (2008) ‘The brick layer model revisited: Introducing the nano-grain composite model’, *Journal of the American Ceramic Society*, 91(6), pp. 1733–1746. doi: 10.1111/j.1551-2916.2008.02445.x.

Kishi, H., Mizuno, Y. and Chazono, H. (2003) ‘Base-Metal Electrode-Multilayer Ceramic Capacitors: Past, Present and Future Perspectives’, *Japanese Journal of Applied Physics*, 42(Part 1, No. 1), pp. 1–15. doi: 10.1143/JJAP.42.1.

Macdonald, J. R. (1987) *Impedance spectroscopy : emphasizing solid materials and systems*. New York : New York .

Maxwell, J. C. and Niven, W. D. (1881) *A Treatise on Electricity and Magnetism V1 (1881)*. Oxford: Clarendon Press.

Nafe, H. (1984) ‘Ionic conductivity of ThO₂- and ZrO₂-based electrolytes between 300 and 2000 K★’, *Solid State Ionics*, 13(3), pp. 255–263. doi: 10.1016/0167-2738(84)90040-7.

Sinclair, D. C. (1995) ‘Characterization of Electro-materials using ac Impedance Spectroscopy’, *Boletín de la Sociedad Española de Cerámica y Vidrio*, 65, pp. 55–66.

Tanemura, M., Ogawa, T. and Ogita, N. (1983) ‘A new algorithm for three-dimensional voronoi tessellation’, *Journal of Computational Physics*, 51(2), pp. 191–207. doi: [https://doi.org/10.1016/0021-9991\(83\)90087-6](https://doi.org/10.1016/0021-9991(83)90087-6).

Waser, R., Baiatu, T. and Härdtl, K. H. (1989) ‘Degradation of dielectric ceramics’, *Materials Science and Engineering: A*. Elsevier, 109, pp. 171–182. doi: 10.1016/0921-5093(89)90583-2.

Wen, H., Wang, X., Gui, Z. and Li, L. (2008) 'Modeling of the core-shell microstructure of temperature-stable BaTiO₃ based dielectrics for multilayer ceramic capacitors', *Journal of Electroceramics*, 21(1–4 SPEC. ISS.), pp. 545–548. doi: 10.1007/s10832-007-9240-1.

Wen, Y., Yue, X., Hunt, J. H. and Shi, J. (2018) 'Feasibility analysis of composite fuselage shape control via finite element analysis', *Journal of Manufacturing Systems*. Elsevier, 46, pp. 272–281. doi: 10.1016/J.JMSY.2018.01.008.

West, A., Sinclair, D. and Hirose, N. (1997) *Characterization of Electrical Materials, Especially Ferroelectrics, by Impedance Spectroscopy*, *Journal of Electroceramics - J ELECTROCERAM*. doi: 10.1023/A:1009950415758.

3 Atomistic Simulation Methods

3.1 Introduction

Atomistic simulations form the bulk of the work done in this thesis. This chapter discusses the basics of atomistic simulation methods including atomistic forcefields, molecular dynamics, static simulations and Monte Carlo simulations. A brief discussion of analysis techniques that can be used on the data gathered from atomistic simulations is also included. Enhanced sampling of atomistic simulations including metadynamics, is discussed in §6.

3.2 Introduction to Forcefields

In this work, atomistic simulation methods refer to those methods whose primary concern is simulating the atoms in a system by treating them as a combination of nuclei and electronic effects. This is achievable due to the Born Oppenheimer approximation (Born and Oppenheimer, 1927) (Eq 3.1).

$$\psi_{total} = \psi_{electronic} \times \psi_{nuclear} \quad (3.1)$$

The approximation states that because the velocities of the electrons around the nuclei are much greater than the velocity of the nuclei itself that you can treat them separately. Thus, the total wavefunction of the system is a product of the nuclei wavefunction and the electronic wavefunction. Quantum mechanical methods are mainly concerned with solving the wavefunction for the electrons.

Atomistic methods predominantly calculate the forces on the nuclei by solving the atomistic forcefield equation which is a classical approximation of the forces exerted on the atoms by its electrons. Atomistic methods can also be called forcefield, classical or potential based methods. These methods neglect calculating the electronic behaviour of a system explicitly and are therefore less computationally expensive than quantum methods. As they are less expensive they can be used to calculate large cell sizes of hundreds of thousands of atoms efficiently.

Quantum methods are generally considered to be more accurate than atomistic methods however, the number of atoms that can be simulated is limited to a few thousand. Another limitation of many quantum mechanical methods is the necessity to simulate the ground state of a system rather than excited states. Simulated excited states is challenging so this can limit the use of quantum mechanical simulations in the field of functional ceramics, as the behaviours we are most interested in occur in excited states. It is also usually necessary to calculate both minimum energy states and excited states to quantify the difference between the two, so other methods such as atomistic simulation need to be used instead.

Atomistic forcefield simulations of ionic solids assume that the nuclei interactions can be modelled using Newtonian mechanics and that the nuclei take the form of charged hard spheres as per the Born model. In atomistic methods, both the static and dynamic properties of a system can be calculated.

Atomistic forcefields (Eq 3.2) are mathematical equations used to describe the potential energy of the simulated chemicals. As per Equation 3.2 the total potential energy of a system is the sum of the energies of the individual components. The forcefield for a whole and varied system can be made up from many components, including but not limited to short range pair potentials, angular terms and long range Coulombic interactions.

$$V_{total} = V_{bonds} + V_{angles} + V_{torsions} + V_{electrostatics} + V_{van\ der\ Waals} \quad (3.2)$$

Forcefields are fitted to recreate the real system as accurately as possible. They can be fitted using data from *ab initio* calculations or from experimental spectra such as XRD and TEM. They are often fitted to a combination of the two to replicate the specific properties of the system that are going to be investigated. Forcefields are fitted for specific scenarios and systems; as creating a universal forcefield that recreates all chemical systems within reasonable accuracy is currently an unrealistic goal. This is due to the variability exhibited across different systems.

3.2.1 Short-range Interactions

3.2.1.1 Two-Body Interactions

Two body or pair potentials describe the interaction between two atoms in the simulation as a function of distance. The two atoms can be either the same or different species. These potentials include a term to describe the strong repulsion or Pauli repulsion atoms feel when their electron clouds are overlapping or too close together, and a term which describes the attraction of the ions to one another due to van der Waals forces (Fig 3.1). Equilibrium is reached when the two bodies are at an ideal radius r from each other and this usually corresponds to the ideal interatomic distance.

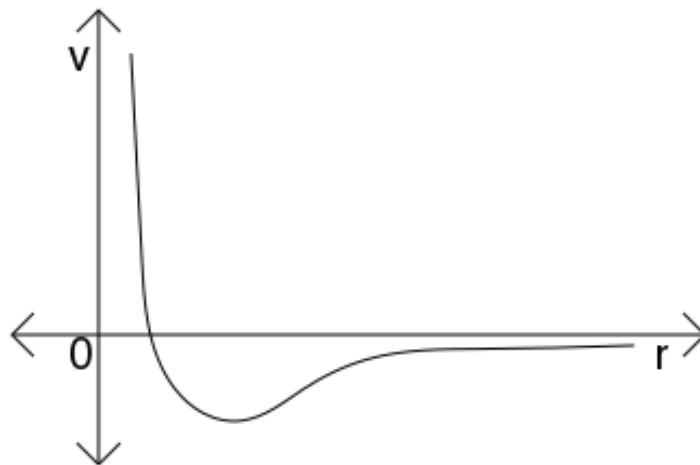


Figure 3.1: Graph showing a typical two-body potential form with potential energy v as a function of distance r .

Buckingham (1938)(Eq 3.3) and Lennard-Jones (Eq 3.4) are examples of typical two body terms used in this work.

$$V_{ij} = \sum_{i \neq j}^n A_{ij} \exp\left(-\frac{r_{ij}}{\rho}\right) - \frac{C_{ij}}{r_{ij}^6} \quad (3.3)$$

$$V_{ij} = \sum_{i \neq j}^n 4\varepsilon_{ij} \left[\left(\frac{\sigma_{ij}}{r} \right)^n - \left(\frac{\sigma_{ij}}{r} \right)^m \right] \quad (3.4)$$

For the Buckingham potential (Eq 3.3) and the Lennard-Jones potential (Eq 3.4) the exponential term and the n-index term are the repulsive terms respectively. The r^6 term (Eq 3.3) and the m-index term (Eq 3.4) act as the attractive van der Waals interactions. In the case of the Buckingham potential A , ρ and C are the terms that must be fitted for a specific interaction within a system. For a Lennard-Jones potential, ε and σ are the terms that must be fitted. ε represents the depth of the potential energy well and σ is typically the sum of the ions radii. In the Lennard-Jones potential, the n and m terms are typically 12 and 6 respectively. These indices determine the strength of the repulsive and attractive terms of the potential. If the potential needs to be less repulsive then a smaller n value can be used. Both the Lennard-Jones and Buckingham potentials produce a relatively computationally inexpensive good approximation of the two body interactions experienced in simple systems including ionic solids.

3.2.1.2 Three-Body Interactions

Three body potentials (Leach, 2001) are used to maintain a specific angle between three atoms in the system (Eq 3.5). They are required in situations where the bonding character of the atoms encourages an ideal angle between the ions. The atoms in the triplet can be the same or different species. It encourages the ideal angle by introducing an energy penalty when the angle θ deviates from the ideal θ_0 during the simulation.

$$V_{ij} = \frac{k_\theta}{2} (\theta - \theta_0)^2 \quad (3.5)$$

In the titanate models used in this work, the O^{2-} - Ti^{4+} - O^{2-} triplet requires a three-body term to encourage the angle between these atoms to remain at 90° as this is the ideal angle for the system.

3.2.2 Long-range Interactions

The long-range interactions or Coulombic interactions of the ions in the simulation are modelled using the Coulomb sum (Leach, 2001). The Coulomb sum calculates the electrostatic forces felt by the ions in the system using the formal charges ascribed in the forcefield (Eq 3.6). In an ionic solid most of the potential energy contributions come from the electrostatic interactions.

$$V_{ij} = \sum_{ij} \frac{q_i q_j}{r_{ij}} \quad (3.6)$$

where q_i and q_j are the charges of a pair of ions in the lattice and r_{ij} is the distance between the pair. The electrostatic interactions calculated using Coulombs law do not include contributions that would come from polarisation or multipoles. The cut-off distance for the short-term interactions does not apply for the electrostatic (long-range) interactions. This is because electrostatic effects contribute to the potential energy over a much larger distance than a few lattice sites. The electrostatic effect decays as a reciprocal function of the distance from each ion, the rate of decay is r^{-1} , however the number of interacting ions increases by r^2 . This makes the total energy contribution from the Coulomb sum conditionally convergent.

3.2.3 Cores and Shells

In the atomistic forcefield discussed so far, the charged rigid Born model ions are not capable of representing any effects caused by the electron density of the atom. They assume the electron density is fixed. In modelling, ionic solids, polarisability has significant effects when defects, surface effects and or grain boundaries are introduced as the non-stoichiometry introduces a dielectric boundary. In these situations, it is often necessary to use the Dick and Overhauser model (Dick and Overhauser, 1958) of a “core-shell” ion as part of the forcefield to approximate polarisability. In this model, polarisable ions are modelled using a spherical, positively charged mass or “core” connected via a spring to a larger massless negatively charged “shell”. The sum of the core and shell charge equals the value of the formal charge on the overall ion.

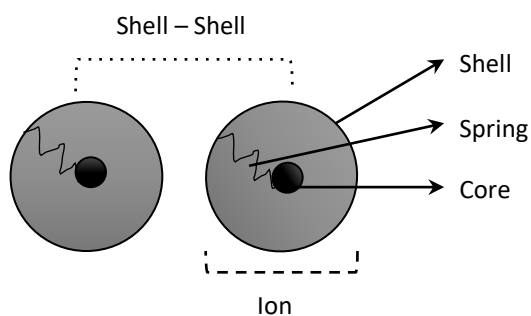


Figure 3.2: Diagram illustrating the components of the Dick and Overhauser (1958) “core-shell” model showing the cores, shells and connecting springs.

During the calculation, for ions using the shell model, the Coulomb interaction between the core and shell is turned off, allowing the ionic point charge of the nuclei and the sphere of the shell to overlap each other. Within a calculation the two-body interaction is considered operational between the shells, if both ions have shells, and between the shell and the nuclei of an atom without a shell. The three-body interactions are considered operational between the cores of the atoms; this allows the desired angle to be maintained more easily. The spring is assigned a constant k , as per Hooke’s law, that allows the shell to freely oscillate harmonically about the core (Dick and Overhauser, 1958). The potential energy V_i stored in the spring (Eq 3.7) is easily derivable from Hooke’s law where δ is the length of the spring, or in this case, the distance between core and shell.

$$V_i = \frac{1}{2} k \delta^2 \quad (3.7)$$

The greater the spring constant, the less the shell can oscillate and thus the less polarizable the ‘electron cloud’. This is illustrated by Equation 3.8 where y is the charge of the shell and k is the fitted spring constant. This model approximates the electron cloud surrounding an ion as a perfect sphere which is useful in many situations it however falls short in situations where distinct non-spherical electron cloud distortions occur e.g. Jahn-Teller distortions (Leach, 2001). In practice, forcefields with cores and shells can, in molecular dynamics, be treated in two different ways. In the first case, the shell is kept massless and the shells are relaxed to the cores each time the core moves. In the second case, the shell is assigned a small mass of its own, and undergoes particle

motion with the spring acting as a tether. The second method is considered to generate less reliable statistics due to the fact that it can make the calculation unstable as the time evolution of the system will not follow the true free energy surface of the system, subsequently limiting the timestep size that can be used. In large systems the cost of relaxing the shells after every move can be prohibitively expensive.

$$\text{Ion Polarisability} = \frac{y^2}{k} \quad (3.8)$$

3.3 Energy Optimisations

3.3.1 Calculating Lattice Energies

Calculating the static lattice energy of a system, is one of the basic techniques for simulating ionic solids. A calculated lattice energy can also be used to calculate the second electron oxygen affinity energy to complete a Born-Haber cycle calculation using Hess' Law (Atkins, 2014) (Fig 3.3). This is necessary, as the second electron oxygen affinity varies from oxide to oxide due to its local chemistry, and the depth of the potential well confining the oxygen electron cloud (Harding and Pandey, 1984) .

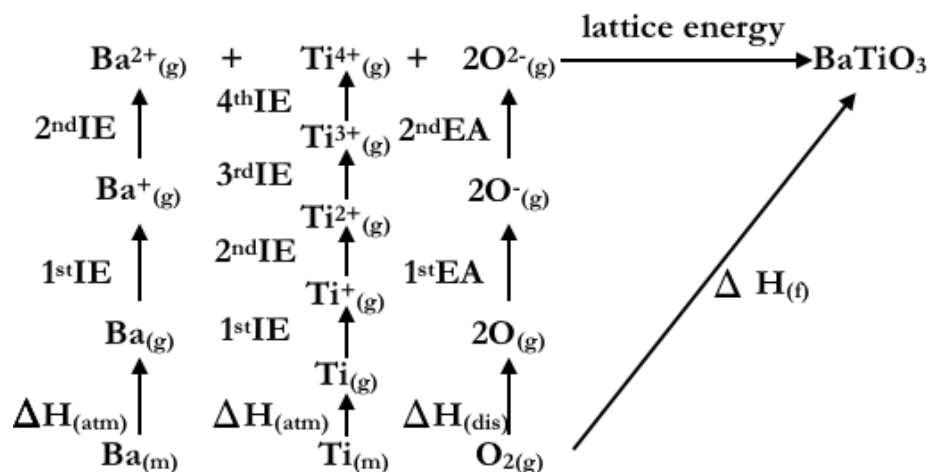


Figure 3.3: Born-Haber cycle calculation diagram for barium titanate applying Hess' law adapted from Freeman *et al* (2011)

The lattice energy can also be used to help calculate both lattice formation energies and defect formation energies. They are also key for determining preferable configurations

in systems with high levels of disorder. At its basic level, calculating the lattice energy or potential energy of the system involves solving the forcefield equation (Eq 3.2) for a specific system. Once calculated other algorithms including rational functional optimisations or defect calculations can be used to find out information on features of the system. All static calculations in this work were calculated using the General Lattice Utility Program (GULP)(Gale, 1992). Static calculations calculate the total energy of the system by solving the forcefield equation typically without considering pressure and temperature effects per the law of thermodynamics, making the calculations simpler and cheaper. In the case of crystals, the repeating periodic nature of the crystal can be taken advantage of by reducing the crystal to a smaller symmetric form to speed up the lattice energy calculation. Static simulations can be altered to consider pressure using a PV term and temperature effects within the quasi harmonic approximation however this makes the calculation much more expensive.

3.3.1.1 Periodic Boundary Conditions

When studying the bulk properties of a solid ionic system it is impossible to calculate the potential energy of the number of atoms in a real, finite sized experimental sample. To overcome this and to allow simulation to be compared to experiment, periodic boundary conditions are utilised (Fig 3.4) (Leach, 2001).

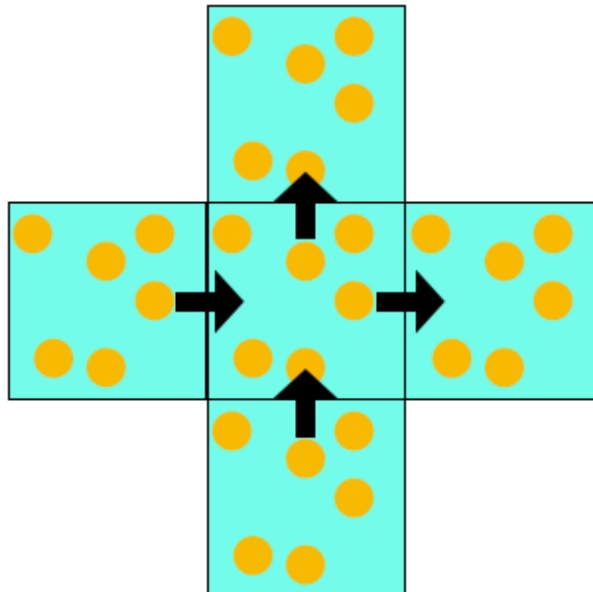


Figure 3.4: Image showing a schematic of cubic periodic boundary conditions.

Periodic boundaries allow a pseudo-infinite bulk to be simulated and simultaneously removes external surfaces from the calculation. This works by assuming the box of

atoms being simulated interfaces at each box face of the simulation with an image of itself. Thus, an atom in a minimisation that sits on the top face of the simulation cell may appear on the bottom face of the simulation cell from one iteration to the next as the boundaries are periodic. These boundary conditions are ideal for periodic, regular ionic lattices as the atomic structure lends itself to being repeated. Care must be taken (when using periodic boundary conditions) with the size of the cell as the it interacts with all images of itself, this can frustrate motion at some of the boundaries and create artefacts in the statistics taken from these simulations. If the cell being simulated is large enough these artefacts can be considered small enough to be negligible. Periodic boundary conditions can be cubic or orthorhombic in nature and maintain a 90-degree angle between images, however more commonly parallelepiped boundaries are used which allows the angles of the box to fluctuate, but maintain the tessellation of the box. The minimum image convention states that due to periodic boundary conditions, the interactions within the cell should be limited to an atom only interacting with the nearest image of every other atom in the system, rather than the infinite images generated by the periodic boundaries (Leach, 2001). This reduces the burden of calculation to a much smaller number of interactions

3.3.1.2 Calculating Short-range Interactions

Calculating the total forcefield and thus the total potential energy of a system, relies on the sum of all the possible interactions (Eq 3.2). As the number of atoms, N , in the system increases, the number of ion interactions that must be calculated increases quadratically. This makes it prohibitively expensive to calculate the interactions between all pairs of atoms simulated other than for very small systems. As the distance between the pair of atoms increases, the contribution to the overall energy of the short-range interaction decreases to near zero (Eq 3.4, 3.5). Therefore, a cut off distance is introduced to the simulation beyond which the short-range interactions are assumed to be zero. This is typically of the order of 12\AA , however it must not be greater than the distance prescribed by minimum image convention used in the simulation. The cut off distance used in research has been increasing over time due to increasing available computer power. Generally, the greater the cut off the greater the accuracy of the simulation. If the cut off is small, often the potentials being used are truncated so abruptly that artefacts are created in the short-range interactions calculated (Fig 3.5)

Tapering functions can be used to make the transition at the cut off less abrupt (Fig 3.5) (Leach, 2001). They can be specified as part of the interatomic potential set. The cut off combined with the minimum image convention can greatly reduce the number of interactions that must be calculated, making the simulation much more efficient.

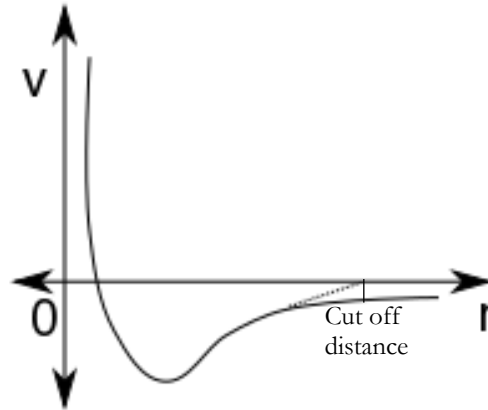


Figure 3.5: Graph showing abrupt truncation of a two-body potential (Solid line) and a tapering function (Dashed line) that can be used to overcome this.

3.3.1.3 Ewald Summation

The cut-off distance for the short-range interactions does not apply for the electrostatic or long-range interactions. This is because electrostatics contribute to the potential energy of the system over a much greater distance than a few lattice sites. The electrostatic effect decays as a function of the distance from each ion. The rate of decay is r^{-1} , however the number of ions being interacted with increases by r^2 . This makes the total energy contribution to the potential energy of the system from the Coulomb sum [6] a conditionally convergent sum. If this conditionally convergent sum is solved directly it converges very slowly if at all.

The Madelung potential (Eq 3.9) defines the potential energy due to electrostatics felt by one ion due to all the other ions in the lattice (Glasser, 2012).

$$V_i = \frac{e}{4\pi\epsilon_0} \sum_{j \neq i} \frac{z_j}{r_{ij}} \quad (3.9)$$

where V_i is, the potential energy felt by ion i , e is the unit of elementary charge, ϵ_0 is the permittivity of free space, r_j is the distance between the i th and the j th ion and z_j is the

number of charges on the j th ion.

To solve this sum for all atoms in a periodic system during a simulation quickly and efficiently the Ewald summation (Ewald, 1921) is used. The Ewald summation is a special case of the Poisson summation formula (Kittel, 1996) which takes advantage of the periodic nature of the electrostatic interactions to solve the Coulomb sum. It does this by splitting the Coulomb sum into a sum of three terms (Eq 3.10). Two of the terms are the sum of the potential energy in real space and in reciprocal space respectively. The third term is the potential energy of the ion itself. For the Ewald summation to correctly converge the unit cell being simulated must be charge neutral.

$$V_{electrostatics} = V_{real} + V_{reciprocal} - V_{self}(3.10)$$

In the Ewald summation, the electrostatic charge of each ion in the lattice is represented by a point charge lattice. Gaussian distributions with their centre located at each lattice site, where the area of the Gaussian equals the charge of the ion, are sequentially subtracted from the point charge lattice and then added back on to allow Equation 3.10 to be solved (Fig 3.6).

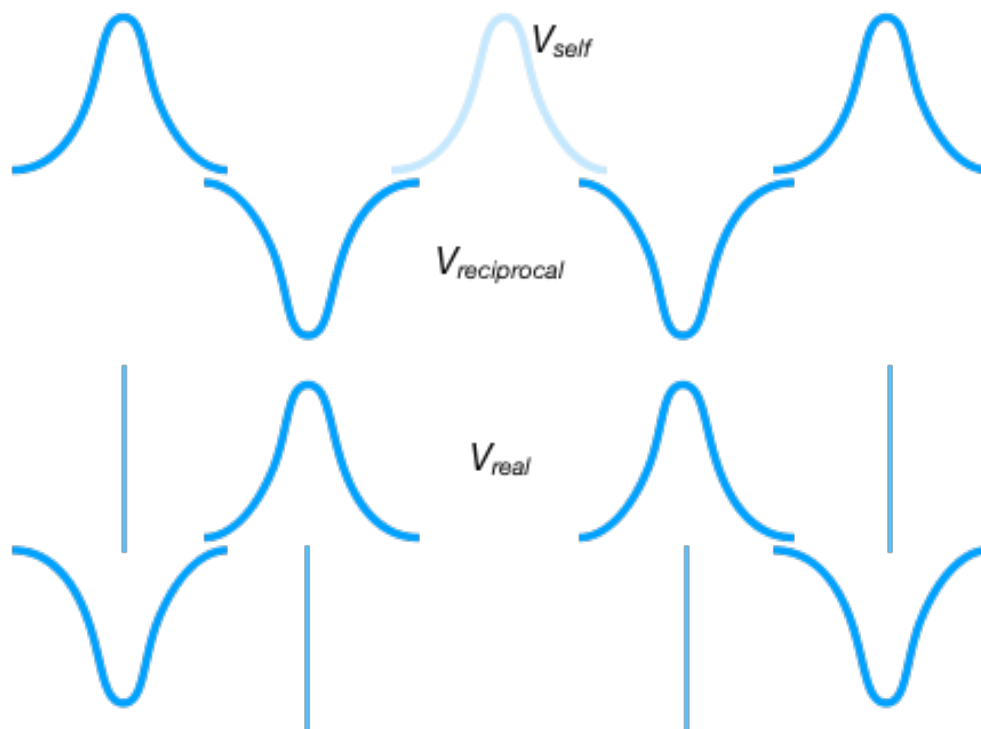


Figure 3.6: Graphical representation of the Ewald summation adapted from (Kittel, 1996).

The charge of the ion at the reference point of the calculation does not contribute to the potential energy at its own location, giving the V_{self} (Eq 3.11) term which consists of the charge distribution for the reference point ion in the form of a single Gaussian. $V_{reciprocal}$ (Eq 3.12) is the sum of the Gaussians in the lattice; a continuous Gaussian distribution. This continuous Gaussian distribution sum is difficult to solve within real space quickly, therefore by using a Fourier transform the sum can rapidly converge and be solved in reciprocal space. V_{real} (Eq 3.13) is a lattice of point charges with the negative $V_{reciprocal}$ Gaussian distribution subtracted from it. This results in the point charges being screened and an equation that is easily solvable in real space.

$$V_{self} = \frac{\alpha}{4\pi^3\epsilon_0} \sum_{j=1}^N q_j^2 \quad (3.11)$$

$$V_{real} = \frac{1}{4\pi\epsilon_0} \sum_{\mathbf{L}=\mathbf{0}}^{\infty} \sum_{n<j}^N \frac{q_n q_j}{|\mathbf{L} + \mathbf{r}_{jn}|} \operatorname{erfc}(\alpha|\mathbf{L} + \mathbf{r}_{jn}|) \quad (3.12)$$

$$V_{reciprocal} = \frac{1}{2V\epsilon_0} \sum_{\mathbf{k}=\mathbf{0}}^{\infty} \frac{\exp(-\frac{k^2}{4\alpha^2})}{k^2} \left| \sum_{j=l}^N q_j \exp(-i\mathbf{k} \cdot \mathbf{r}_j) \right|^2 \quad (3.13)$$

where \mathbf{k} is the reciprocal lattice vector. Given by: $\mathbf{k} = \frac{2\pi}{V^{\frac{1}{3}}} (\ell, m, n)^{\perp}$.

3.3.2 The Minimisation Problem

The minimum energy configuration of a system is of great interest to atomistic simulators, both as a starting configuration for future calculations, for finding structural equilibrium and for calculating an optimised lattice energy for Hess cycles and similar methods (Leach, 2001).

The potential energy surface of a system is a multi-dimensional energy surface where the energy of a system is given as a function of its coordinates (Frenkel, 2002) (Fig 3.7). A minimum for a given system can be mathematically defined as the point at which both the gradients and second derivatives of the potential energy surface are zero. For a system with a given set of coordinates, finding the global minimum energy of a system is inherently problematic. This is because a potential energy surface for a system can be complex and iteratively solving the forcefield for each point of the potential energy surface is combinatorically and computationally too expensive and time

consuming. However, unless the whole of the potential energy surface is searched systematically, any minima found cannot be proven to be the global minimum. As this type of searching is not feasible for systems larger than a few atoms, a minimization algorithm or downhill search method is often used to find minima. The larger the system being simulated, the more degrees of freedom and the longer a minimisation can take.

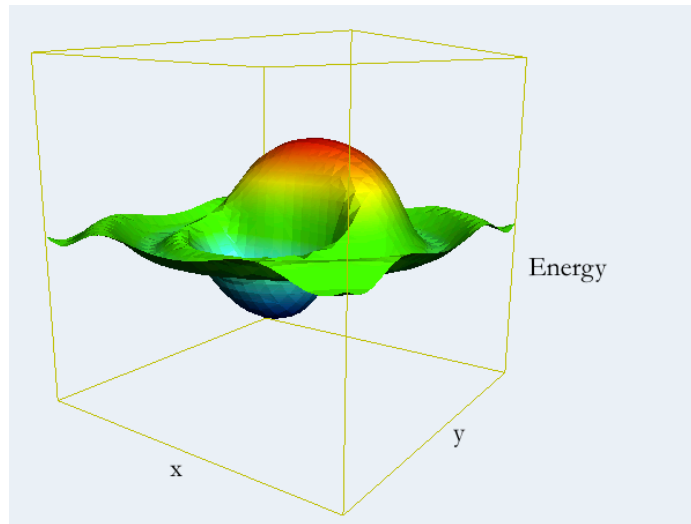


Figure 3.7: Example Potential Energy Surface of a System.

3.3.3 Energy Optimisations

There are many algorithms (Press *et al.*, 1993) that can be used to search for a minimum in atomistic simulations. They vary in method, accuracy and speed and their limitations. This work uses a combination of the methods. An energy optimisation searches for a minimum on a potential energy surface. All optimisations are given an initial configuration of the system. Once the energy of the initial configuration is evaluated the algorithm then searches for configurations with lower and lower total energies, until a minimum is found.

3.3.3.1 Conjugate Gradient Method

The conjugate gradient method using the Fletcher-Reeves algorithm (Fletcher and Reeves, 1964) uses progressive line searches that are conjugate to one another, to locate the minimum of a system (Fig 3.8). Using the initial configuration, the direction with the steepest gradient is determined. The algorithm then searches along this direction of the potential energy surface to find the minimum. Once found, the gradient of the minima is used to calculate the conjugate or non-interfering direction to search in. The line search for the minimum in the new direction is then completed. The second two steps are then repeated until an overall minimum is found. As the conjugate gradient method only evaluates the gradients of the potential energy surface, this is a first order searching method.

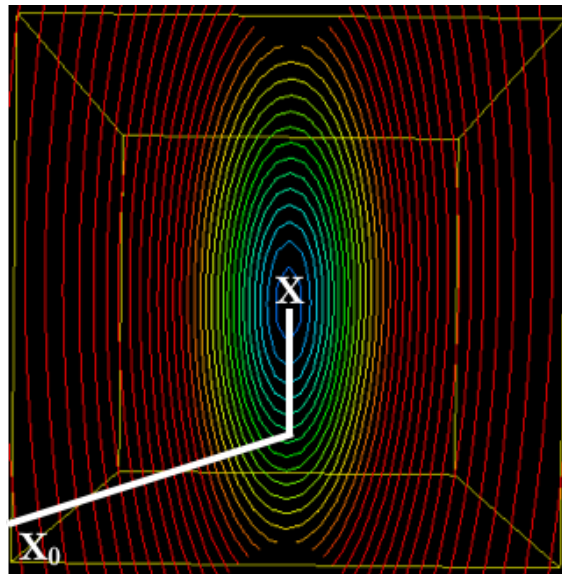


Figure 3.8: Illustration of the steps taken during the operation of the conjugate gradients method on a second order polynomial.

One limitation of the conjugate gradient method is that as the complexity of the system increases a greater and greater number of steps must be calculated to find the minimum. Conjugate gradients is useful for very large non-symmetric systems as it does not require the calculation of a second derivative matrix (Hessian matrix). However it will fail if the hessian matrix is not a positive definite matrix.

3.3.3.2 Newton-Raphson Method

Unlike conjugate gradients the Newton-Raphson method (Leach, 2001) is a second order minimisation method. It uses both the gradient or first derivative of the potential energy surface as well as the second derivative, the hessian matrix, to minimise a system. To do this the potential energy surface of the system is written in the form of a Taylor expansion (Eq 3.14) that is the sum of the energy at position x , the vector of the first derivatives g and the hessian matrix H of the second derivatives.

$$U(x + \delta x) = U(x) + g(x) + H(x) \quad (3.14)$$

The next step from position x , δx is determined using g and the inverted hessian matrix H from the previous step (Eq 3.15). This means the next step δx is intelligently informed which can reduce the number of steps needed to find the minimum. For the algorithm to work successfully, H must have all positive eigenvalues, if negative eigenvalues are present, saddle points rather than minima can be found, making the method unstable.

$$x + \delta x = -\frac{g(U(x))}{H(U(x))} \quad (3.15)$$

The algorithm also requires the calculation and inversion of the hessian matrix, which is computationally slower and more expensive with increasing system size. These features give competing speed ups and slowdowns to the overall algorithm. To overcome this, quasi Newton-Raphson methods have been developed, to reduce the number of occasions on which the hessian matrix needs to be fully evaluated. There are many competing schemes for this, however the one utilised by GULP is the Broyden-Fletcher-Goldfarb-Shanno (BFGS) method (Shanno, 1970). BFGS is one of the most accurate quasi Newton-Raphson methods available. It uses an approximation of the hessian matrix based on the value of the current position x and the first derivatives g of the first step to determine δx the next step (Eq 3.15). When the value of the energy at x falls below or rises above a certain threshold due to an abnormal step choice, or when a certain number of iterations have been completed, the full hessian matrix H is computed and inverted to check for accuracy. H in full is also calculated for the final configuration to check that a minimum has been found.

3.4 Defect Calculations

So far the methods explained in this chapter deal only with calculating energies for charge neutral perfect crystals. Perfect crystal lattices only provide limited information about the materials being simulated. Real materials contain defects, and these defects often result in phenomena or materials properties that are of use. The perfect crystal is only an ideal. For all real crystal systems, the introduction of a defect increases the entropy S of a system where the total free energy of formation G is given by Equation 3.16 (Atkins, 2014) where T is the temperature in Kelvin. The introduction of defects also increases the enthalpy of formation of the overall system H .

$$G = H - TS(3.16)$$

This results in a non-zero minimum G for all temperatures above 0K, resulting in the spontaneous formation of point defects at all temperatures above 0K. The defects that form in a system can range in size from point defects to grain boundaries and dislocations. In this work, we only deal with simulating point defects, and clusters of point defects. As the Ewald Summation is only accurate for a system that is charge neutral (Ewald, 1921), mathematical corrections are needed to overcome this limitation, and allow defects to be simulated.

3.4.1 Types of Defect

Point defects in crystals can be categorised into five different types (Fig 3.9) . These point defects can exist singularly or in defect complexes. Defect complexes are often more energetically favourable as they can restore charge equilibrium to the system. The defects in this work are bulk defects. Defects at the surface of a crystal will have different chemistry due to the interface.

Firstly, a vacancy also known as the Shottky defect in the case of metals, is an ion missing from an occupied lattice site. Secondly, an interstitial is the introduction of an ion into the space in-between the crystal lattice sites. Thirdly, the Frenkel pair defect consists of a vacancy and an interstitial formed by the ion that has just vacated the vacancy site. Fourthly anti-site defects occur where ions are found occupying the wrong lattice site, the electrostatic neutrality of the system is conserved. These first four types of defect are intrinsic defects, because they can form in a pure crystal, without

impurities. Finally, substitution is the replacement of a different species onto a lattice site. The substituted ion can be of the same, more positive or less positive charge than the ion being substituted. This is an extrinsic defect, as its presence alters the stoichiometry of the system.

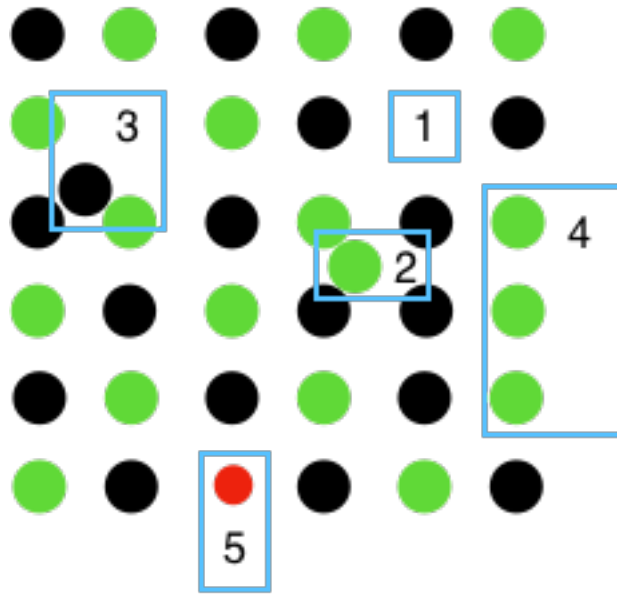


Figure 3.9: Schematic illustrating the five types of point defect: 1. Vacancy, 2. Interstitial, 3. Frenkel Defect, 4. Anti-site Defect, 5. Substitution.

Kroger-Vink (1956) notation is commonly used to define and label point defects. It takes the form of a defect identifier, with an associated subscript and superscript. The defect identifier illustrates the type of defect: atom, vacancy, electron or hole. The subscript illustrates the lattice site the defect is located on. This can be an element symbol or *i* for interstitial. Electrons and holes do not typically have a lattice site associated with them. The superscript can be dots to represent a positive net charge, the apostrophes, negative net charge compared to the non-defective lattice or a cross where there is difference in the net charge of the lattice due to the defect. The example Dy_{Ba}^{\cdot} is a rare-earth ion Dysprosium substituted onto the Barium site of the barium titanate lattice with a positive net charge of one, as Ba is 2+ and Dy is 3+. Vacancies are denoted with V .

3.4.2 Mott-Littleton Simulations

The Mott-Littleton (ML) (1938) approach to defect simulations involves calculating the energy it costs to insert a defect into a perfect crystal. It is also known as the embedded cluster approach. ML is useful when the defects involved are below the dilute limit of a system. This is the case when an element is a low-level dopant in a material, e.g. rare-earth doping of barium titanate. A prerequisite for ML defect calculations is that the system is optimised before introducing defects; this ensures the accuracy of the calculation. Both individual and defect clusters can be simulated using this approach. In this method, the crystal surrounding the defect or cluster of defects is divided into two nested spherical regions (3.10).

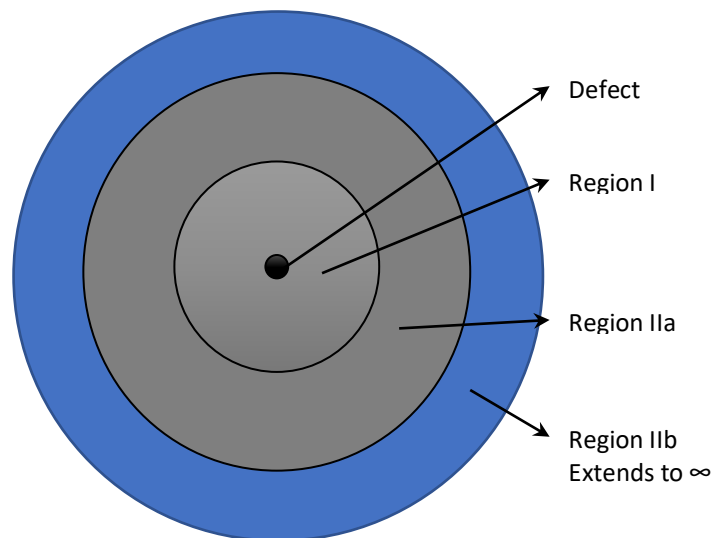


Figure 3.10: Schematic of the Mott-Littleton Defect Calculation.

In the inner defect-containing region (Region I), the interactions between the atoms are calculated explicitly this is because these ions are closest to the defect and will therefore be the most affected by the defect. In the outermost region (Region IIb) the interaction of the ions with the defect is approximated using a continuum method where the only interaction with the defect is coulombic. Therefore, the movement of the ions due to the defect are treated harmonically. This is the Mott-Littleton approximation. The interactions between the Region I and the inner part of the outer region (Region IIa) which has a radius given by the sum of the cut off distance and the radius of region I are also calculated explicitly. However, the positions of the ions in Region IIa are

calculated using the harmonic approximation. The total energy of the defect or defect cluster is given by Equation 3.17. Where x represents the displacements of the inner region and ξ the displacements of the outer region. When the energy of the defect is being minimised, it is not possible to provide an explicit expression for the minimum configuration as the displacements of the atoms outside Region I, rely on the displacements inside Region I. In this scenario, a minimum is reached when all the forces acting on the ions in Region I are zero.

$$E = E_1(x) + E_{12}(x, \xi) + E_2(\xi) \quad (3.17)$$

The larger the radius of Region I the better converged the calculation. The radius of Region IIa must equal to or greater than be the sum of the radius of Region I and the cut off distance of the potentials being used. This ensures that all of atoms in Region IIb only react Coulombically to the presence of the defect as the short-range interactions are cut off. The appropriate radii for Region I and IIa can be fitted for a specific system by calculating it for progressively larger radii and looking for convergence. The converged values will oscillate about a final value due to the different layers of atoms that are included in each region as the radii increase. Once this convergence is reached, the smallest converged radii is chosen as this is the most efficient and cost effective choice. The M-L method is unsuitable for evaluating systems such as solid solutions where there are many more defects present than at the dilute limit.

3.5 Transition State Theory and Saddle Point Searching

As previously discussed, we are often not interested in the static optimised structures of an atomic system, perfect or defective, as they cannot tell us about the dynamic behaviour and properties of the system. Chemical reactions, diffusion, phase transitions and many other physical phenomena occur at energies higher than those used for optimisations. To investigate these phenomena, approaches other than downhill optimisations are required.

Transition state theory is a theory in chemistry developed to understand the reaction rates of chemical processes (Truhlar, Garrett and Klippenstein, 1996). It states that there is a transition state between the reactants and products of a reaction, or as investigated in this work, the start and end points of a diffusion event. It states that the transition state is located at a saddle point on the potential energy surface of a system. The energy difference between the start state and transition state of an event is the E_a or activation energy of the reaction or hopping event. This activation energy can be used to calculate the rate of reaction, or in this case; the diffusion constant of an ion species.

3.5.1 Definition of a Saddle Point

A saddle point is defined mathematically as a point on a surface where the second derivative hessian matrix H has only one negative eigenvector (Banerjee *et al.*, 1985). This means that the point is a minimum in all directions except for one Fig 3.11.

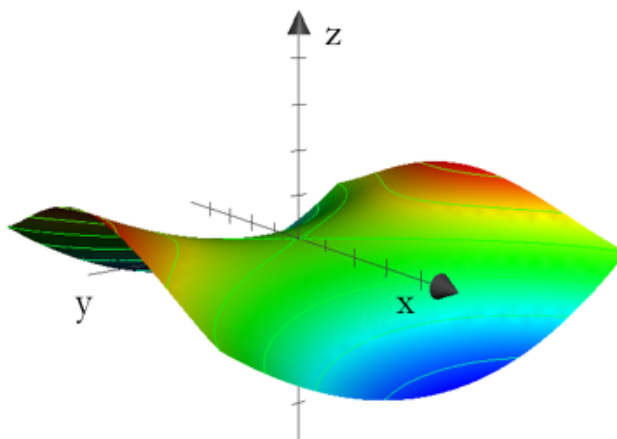


Figure 3.11: Schematic showing a potential energy surface with a saddle point.

This definition means that mathematically, the saddle point of an energy surface can be identified by second order derivative methods. However, all previously discussed search

methods only search downhill. This is a problem when transition points will always be found at a higher energy than genuine minima in a system.

3.5.2 Rational Functional Optimisations

To find a saddle point in static atomistic calculations, uphill rather than downhill searches can be utilised. The rational functional optimisation (Banerjee *et al.*, 1985) is one such uphill search method. A starting position for the transitional ion in the crystal is chosen. This consists of Frenkel pair and an extra lattice site vacancy (Fig 3.13). One is the vacancy that the ion has left, and the other is vacancy the ion is travelling to. The starting location of the interstitial is chosen to ensure it does not lie along any of the symmetry lines of the crystal and so that it is close to the expected transition point.

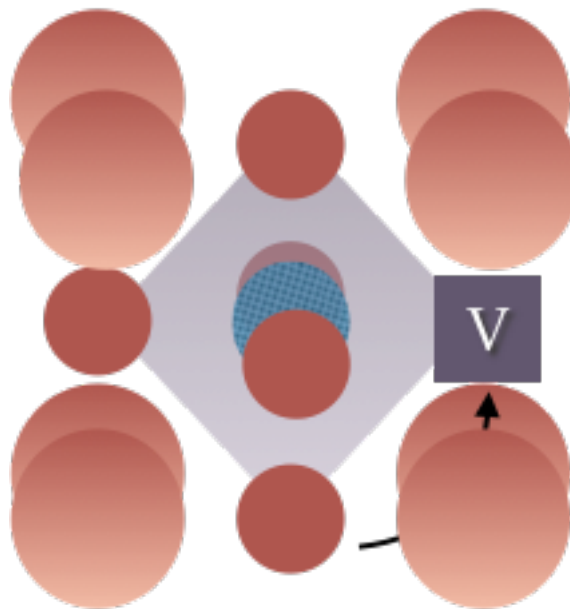


Figure 3.13: Schematic of the starting positions of the defects for a rational functional optimisation calculation of Oxygen diffusion.

The method works by calculating the inverse hessian matrix H at the location of the transitional ion. The algorithm then moves the ion upwards along its local least steep gradient one step and then the hessian matrix is re-evaluated. These steps continue until

the state in which the inverse second derivative hessian matrix only has one negative eigenvector and therefore contains a maximum. Once this is found the Newton-Raphson optimiser is run until the tolerance factor for the norm of the energy gradient (gnorm) is reached. The energy of the ground state from the defect calculation is then subtracted from the energy of the transition state to reveal the overall barrier height. There are a few main limitations of the RFO method. Firstly, choosing the starting position requires quite extensive knowledge of the system being simulated as it must be chosen so that it is both close to the saddle point and not on any crystal symmetry lines. Limitation two is that RFO is very slow, both because the calculation takes a long time, and because moving the transitional ion is limited to a very small step. The small step size is to ensure the calculation does not accidentally miss the transition point. Thirdly, there is no guarantee that the saddle point found corresponds to the transition state being searched for since other transition states may exist nearby. Finally, the RFO only provides information about the location of the saddle point, there is no other information given about the potential energy surface, such as the pathway itself or other barriers.

3.5.3 Nudged Elastic Band

The nudged elastic band (NEB) method (Leach, 2001) is a method of finding the transition state and the minimum pathway of a known reaction or diffusion event. It does this by optimising images of configurations between a start and end state on a pathway. To begin, the start and end state of the reaction or diffusion must be known. Then configurations are generated linking these the start and end configurations, this is often done with linear interpolation. Generally, the greater the number of images, the greater the accuracy of the calculation. Too many images however, can lead to kinks in the pathway. The configurations are linked together using springs to ensure the configurations stay in order. The images are then all optimised (Fig 3.14) using the BFGS optimiser (Shanno, 1970). As the images are linked together by springs, the forces applied to the atoms due to the springs are ignored during optimisation. Only the forces perpendicular to the springs are considered.

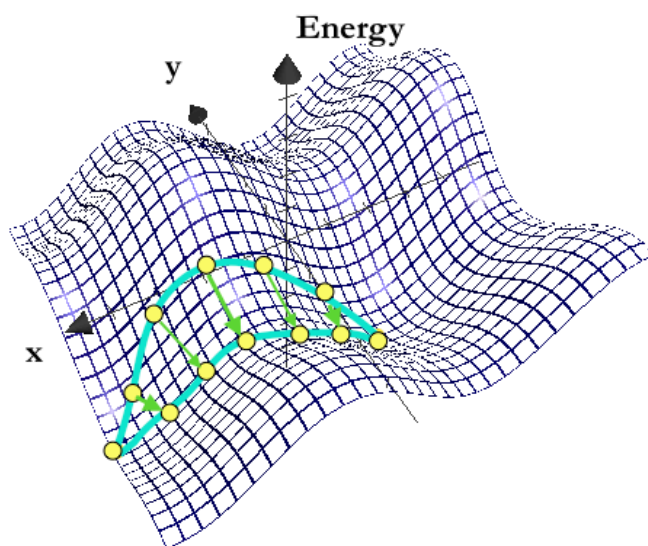


Figure 3.14: Example of an NEB calculation potential energy surface illustrating the initial images selected and the subsequent optimised images.

NEB calculations provide significantly more information about the potential energy surface than RFO calculations. When NEBs are properly minimised the entire lowest pathway can of transition can be revealed. The transition point itself may not be the exact position of one of the images, and subsequent smaller NEB runs can be used to find the location specifically. In operation, some NEB calculations struggle when the forcefield includes atoms utilising the shell model. This is because some algorithms do not have the relaxations of the shells onto the cores explicitly built into the minimisation and it can lead to overestimated and incorrectly minimized pathways. Another limitation of the NEB is that it requires the correct parameterization of the springs being used, if the springs are too stiff, the simulation will fail to find the true minimum. Conversely springs that are too soft may allow the minimum pathway that is found to be inaccurate.

3.6 Monte Carlo Simulation

Monte Carlo (MC) simulation is the general name by which several techniques using random or pseudo-random sampling can be used in atomistic simulation to generate a sample of atomistic configurations per a Boltzmann distribution (Leach, 2001). This is useful if you are not interested in the dynamic properties and trajectories of a system. Monte Carlo simulations can be carried out for non-equilibrium states and systems [39]. The Monte Carlo algorithm invented by Ulam (1949), named after Monte Carlo because of the casinos found in the principality, is an algorithm that can be used to generate a random sample of configurations of a system.

The techniques full name is the Metropolis Monte Carlo method which combines the idea of random sampling from Ulam's original technique with the Metropolis algorithm (Metropolis *et al.*, 1953) for generating a Markov chain of states (Norris, 1997). If the sample generated is truly random, it will replicate the properties of the overall population and replicate a Boltzmann distribution. This allows us to obtain the properties of the entire potential energy surface much more quickly than by sequential or time dependent sampling.

The method used for atomistic simulation typically consists of a starting configuration, a user determined acceptance criteria and a random number generator. The algorithm works as follows:

- The energy of the starting configuration is calculated.
- A new configuration is generated, either by swaps or steps to move the ions around.
- The energy of the new configuration is then evaluated, if the energy is lower than the starting configuration the move is automatically accepted.
- If not the energy is used to calculate the acceptance criteria for the move.
- A random number is generated and if it is larger than the acceptance criteria the new configuration is rejected, if it is smaller or equal to the criteria the move is accepted.
- The steps are then repeated.

The longer an MC calculation is run the more accurately the distribution of the system is replicated. In the case of an atomistic simulation involving temperature and pressure

this distribution is a Boltzmann distribution. It is important to note that per the ergodic hypothesis, the configurations visited over a long MC run will equal the configurations visited in an MD run, providing both runs are long enough. For an in-depth discussion of Monte Carlo methods, the reader is directed to Binder (1988).

3.7 Molecular Dynamics

Molecular Dynamics (MD) is a simulation technique that uses classical mechanics to evolve a system along a time dependent trajectory, using Newton's second equation of motion (Eq 3.18)

$$F_i = m_i a_i \quad (3.18)$$

where F is, the force exerted on a particle i , m is the mass of the particle i and a is the acceleration of particle i . In a similar way to static calculations MD uses the forcefields previously discussed and evolves them time dependently to explore the trajectories of the atoms. Unlike many static calculations, thermodynamic information is included in the calculation explicitly.

3.7.1 Leapfrog Verlet Algorithm

Solving the expressions to move the atoms over time requires rapid efficient integration methods to ensure the calculation is cost effective. One of the most commonly used integration algorithms is the Leapfrog Verlet algorithm. The Verlet method is a finite difference method used to solve the MD equations. It works by calculating velocities and positions at time $t - \Delta t$ to calculate by integration the velocities at $t + \Delta t$. This takes the form of two Taylor expansions of newtons equations of motion (Eq 3.23, 3.24). The expansions can be combined to solve for the current timestep.. In the Leapfrog Verlet variant of the algorithm, to ensure high accuracy and reduce the error in calculating the velocities and positions, the positions are calculated using half timesteps, allowing the size of the timestep to be larger than for traditional Verlet. As the velocities and positions are updated in turn using the previously calculated numbers they are thought to be "leapfrogging" over one another.

$$x_i(t + \Delta t) = x_i(t) + v_i(t)\Delta t + \frac{1}{2} \frac{f_i(t)}{m_i} \Delta t^2 + \frac{1}{6} \frac{\ddot{x}_i(t)}{m_i} \Delta t^3 \quad (3.23)$$

$$x_i(t + \Delta t) = x_i(t) - v_i(t)\Delta t + \frac{1}{2} \frac{f_i(t)}{m_i} \Delta t^2 - \frac{1}{6} \frac{\ddot{x}_i(t)}{m_i} \Delta t^3 \quad (3.24)$$

Where x is the position of the particles, v is their velocity, f is the forces acting on the particles and m is the masses of the particles. The Leapfrog-Verlet is economical with storage, and can be implemented when simulating very large systems. Smaller timesteps can be used to increase the accuracy of the positions and velocities. The algorithm conserves the energy of the system well.

3.7.1 Thermodynamic Ensembles

Thermodynamic ensembles are statistical ensembles that allow a simulated system to exist at equilibrium by imposing certain conditions upon the system (Fig 3.15)(Leach, 2001). They facilitate the calculation of thermodynamic properties of a system which is crucial for evolving positions and velocities in MD calculations. Simulating real systems is infinitely complex and by imposing certain conditions on the simulation, a good approximation of the thermodynamic properties can be obtained. The constraints concern the thermodynamic properties of the simulation box, including but not limited to the volume, temperature, pressure and number of particles.

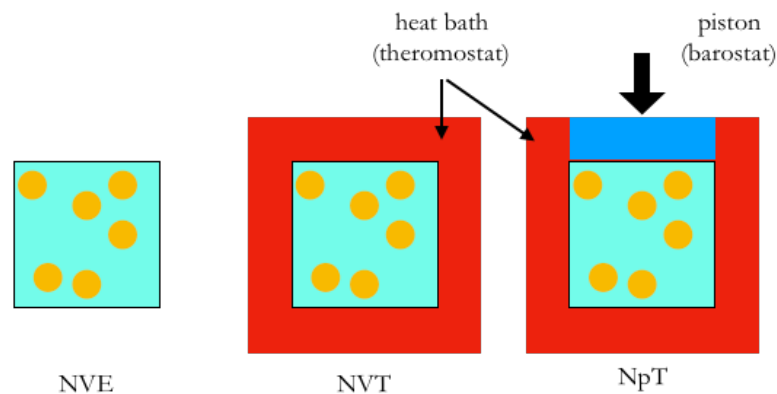


Figure 3.15: Schematic of NVE, NVT and NpT ensembles.

The microcanonical ensemble, or NVE ensemble keeps N the number of particles constant, V , the volume of the simulation box, constant and E , the energy of the system constant. This allows the pressure and temperature of the system to fluctuate during the calculation. No energy or particles may transfer to the surroundings. If a given energy of a system is known, an NVE calculation can be used to find equilibrium states for that energy. The NVE ensemble is achieved by running a standard MD calculation, solving the (conservative) Hamiltonian. To achieve other ensembles extra mathematical terms must be added.

In the canonical (NVT) ensemble, the number of particles, the volume and the temperature is kept constant. This is achieved by allowing energy to leave and enter the system using a mathematical thermostat or heat bath. The exchange of energy continues until the system finds equilibrium. This type of simulation is useful for examining systems at a known temperature. NVT calculations can be used to work out the Helmholtz free energy of a system. The Nose-Hoover thermostat is used in this ensemble (Eq 3.24) (Hoover, 1985). NVT calculations are considered more stable than many other types of ensemble.

In the Isobaric-Isothermal (NpT) ensemble, the number of particles, temperature and pressure is kept the same. This allows the volume and energy to fluctuate to achieve the given temperature and pressure. For this type of calculation, a heat bath or thermostat and a barostat are needed. The barostat exerts an external pressure on the system from all directions, and lets the volume fluctuate. NpT calculations are useful for calculating the Gibbs free energy of a system. This work uses the Nose-Hoover thermostat (Eq 3.24) (Hoover, 1985) and the Berendsen barostat (1984) (Eq 3.25) for these calculations. NpT calculations are usually considered to be the ensemble most like experiment out of the ensembles described here.

3.7.2 Mean Squared Displacement

Mean squared displacement (MSD) is an analysis technique used on the outputted trajectory from molecular dynamics calculation to work out the deviation from a specific position or mean movement of a particle over time (Eq 3.25) (Frenkel, 2002).

$$MSD = \langle (x - x_0)^2 \rangle = \frac{1}{N} \sum_{n=1}^N (x_n(t) - x_n(0))^2 \quad (3.25)$$

where N is the number of particles being considered, x_0 are the positions of the particles in their reference states and $x(t)$ are the particle positions at time t . It can be used to calculate diffusion coefficient D and the activation energy E_A (Eq 3.26) from MD simulations (Eq 3.27).

$$D = D_0 \exp\left(-\frac{E_A}{RT}\right) \quad (3.26)$$

$$\langle (x - x_0)^2 \rangle = 2dDt \quad (3.27)$$

The output from the MSD calculation is traditionally displayed as a graph of log of the cumulative displacement of the particles vs log time (Fig 3.16). The first section of the graph is ignored when calculating diffusion coefficients, this is the ballistic regime where the displacement of the particles is independent of the local forces acting on the particles. To ensure that the statistics for the diffusive events are reliable this initial ballistic part of the MSD is discounted. Once the first hopping event has been seen there is a vast change in gradient of the MSD. The reliability of the diffusion constant calculated from the gradient of the MSD relies upon the statistics of multiple diffusive events. If there are not enough events seen in the calculation the diffusion constant will not be reliable. To encourage diffusive events to occur, the simulation box can be heated, or more charge carriers can be introduced.

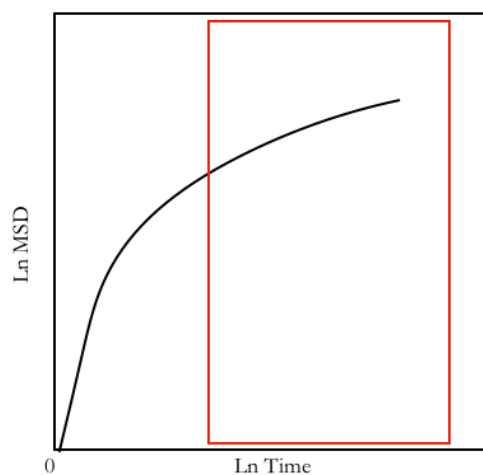


Figure 3.16: Example of outputted MSD graph showing log cumulative displacement vs log time. The gradient of the non-ballistic regime is used to calculate the diffusion coefficient. The red box shows the area of the calculation the MSD would be calculated from.

3.8 Software Used

In this work GULP (Gale, 1992) was used for all static lattice calculations. This included lattice optimisations, ML calculations and RFO calculations. DL_POLY Classic (Smith and Forester, 1996) and DL_POLY 4 (Todorov *et al.*, 2006) were used for all MD simulations. Simulations with 10000+ atoms were carried out using DL_POLY 4 for efficiency. MSD calculations were carried out using DL_POLY's in built MSD code, and the code from Project Aten - dlputils (Young, 2017). Random sampling methods were carried out using custom Python code.

3.9 References

Atkins, P. W. (Peter W. (2014) *Atkins' physical chemistry*. Tenth edit, *Physical chemistry*. Tenth edit. Edited by J. De Paula and J. de Paula. Oxford, United Kingdom: Oxford, United Kingdom : Oxford University Press, 2014.

Banerjee, A., Adams, N., Simons, J. and Shepard, R. (1985) 'Search for stationary points on surfaces', *The Journal of Physical Chemistry*. American Chemical Society, 89(1), pp. 52–

57. doi: 10.1021/j100247a015.

Berendsen, H. J. C., Postma, J. P. M., van Gunsteren, W. F., DiNola, A. and Haak, J. R. (1984) 'Molecular dynamics with coupling to an external bath', *The Journal of Chemical Physics*. American Institute of Physics, 81(8), pp. 3684–3690. doi: 10.1063/1.448118.

Binder, K. (1988) *Monte Carlo simulation in statistical physics : an introduction*. Edited by D. W. Heermann, D. W. (Dieter W. . Heermann, and D.W.Herman. Berlin : Berlin .

Born, M. and Oppenheimer, R. (1927) 'Zur quantentheorie der molekeln', *Annalen der Physik*, 20(84), pp. 457–484. doi: 10.1002/andp.19273892002.

Buckingham, R. A. (1938) 'The Classical Equation of State of Gaseous Helium, Neon and Argon', *Proceedings of the Royal Society of London. Series A, Mathematical and Physical Sciences (1934-1990)*, 168(933), pp. 264–283. doi: 10.1098/rspa.1938.0173.

Dick, B. G. and Overhauser, A. W. (1958) 'Theory of the dielectric constants of alkali halide crystals', *Physical Review*, 122(1950), pp. 90–103. doi: <http://dx.doi.org/10.1103/PhysRev.112.90>.

Ewald, P. P. (1921) 'Die Berechnung optischer und elektrostatischer Gitterpotentiale', *Annalen der Physik*. Leipzig, 369(3), pp. 253–287. doi: 10.1002/andp.19213690304.

Fletcher, R. and Reeves, C. M. (1964) 'Function minimization by conjugate gradients', *The Computer Journal*, 7(2), pp. 149–154.

Freeman, C. L., Dawson, J. a., Chen, H.-R., Harding, J. H., Ben, L.-B. and Sinclair, D. C. (2011) 'A new potential model for barium titanate and its implications for rare-earth doping', *Journal of Materials Chemistry*, 21(13), p. 4861. doi: 10.1039/c0jm04058d.

Frenkel, D. (2002) *Understanding molecular simulation : from algorithms to applications*. 2nd ed. Edited by B. Smit. San Diego : San Diego .

Gale, J. (1992) 'GULP (General Utility Lattice Program)', *Royal Institution, London*.

Glasser, L. (2012) 'Solid-State Energetics and Electrostatics: Madelung Constants and Madelung Energies', *Inorganic Chemistry*. American Chemical Society, 51(4), pp. 2420–2424. doi: 10.1021/ic2023852.

Harding, J. H. and Pandey, R. (1984) 'Calculation of the oxygen potential in the mixed oxide (U, Pu)O_{2-x}', *Journal of Nuclear Materials*, 125(2), pp. 125–137. doi: 10.1016/0022-3115(84)90540-3.

Kittel, C. (1996) *Introduction to solid state physics*. 7th ed. New York : New York .

Kröger, F. A. and Vink, H. . (1956) 'Relations between Concentrations of Imperfections in Crystalline Solids', in Seitz, F. and Turnbull, D. (eds) *Solid State Physics*. New York: Academic Press, pp. 307–435.

Leach, A. R. (2001) *Molecular modelling : principles and applications*. 2nd ed. Harlow: Harlow : Prentice Education, 2001.

Metropolis, N., Rosenbluth, A. W., Rosenbluth, M. N., Teller, A. H. and Teller, E. (1953) 'Equation of State Calculations by Fast Computing Machines', *The Journal of Chemical Physics*, 21(6), pp. 1087–1092. doi: 10.1063/1.1699114.

Metropolis, N. and Ulam, S. (1949) 'The Monte Carlo Method', *Journal of the American Statistical Association*. Taylor & Francis Group, 44(247), pp. 335–341. doi: 10.1080/01621459.1949.10483310.

Mott, N. F. (1938) 'Part IA.-Energy levels in real and ideal crystals. Energy levels in real and ideal crystals', *Trans. Faraday Soc.* The Royal Society of Chemistry, 34(0), pp. 822–827. doi: 10.1039/TF9383400822.

Norris, J. R. (1997) *Markov Chains, Cambridge Series in Statistical and Probabilistic Mathematics*. Cambridge: Cambridge University Press. doi: DOI: 10.1017/CBO9780511810633.

Press, W. H., Teukolsky, S. A., Vetterling, W. T. and Flannery, B. P. (1993) *Numerical Recipes in FORTRAN; The Art of Scientific Computing*. 2nd edn. New York, NY, USA: Cambridge University Press.

Shanno, D. F. (1970) 'Conditioning of quasi-Newton methods for function minimization', *Mathematics of Computation*, 24(111), pp. 647–656. doi: 10.1090/S0025-5718-1970-0274029-X.

Smith, W. and Forester, T. R. (1996) 'DL_POLY_2.0: A general-purpose parallel molecular dynamics simulation package', *Journal of Molecular Graphics*. Elsevier, 14(3), pp. 136–141. doi: 10.1016/S0263-7855(96)00043-4.

Todorov, I. T., Smith, W., Trachenko, K. and Dove, M. T. (2006) 'DL_POLY_3: New dimensions in molecular dynamics simulations via massive parallelism', *Journal of Materials Chemistry*, 16(20), pp. 1911–1918. doi: 10.1039/b517931a.

Truhlar, D. G., Garrett, B. C. and Klippenstein, S. J. (1996) 'Current Status of Transition-State Theory', *The Journal of Physical Chemistry*. American Chemical Society, 100(31), pp. 12771–12800. doi: 10.1021/jp953748q.

4 Simulation of Dynamic Tilt in Perovskites

4.1 Introduction

Perovskites, as discussed in §1, are materials with the general form ABX_3 . These minerals, including barium titanate, can undergo phase transformations resulting in different polymorphs with the same stoichiometry. In many of the phases exhibited by perovskites, the general structure is still that of corner sharing B-site octahedra with the A-sites forming a sub-lattice, sitting on the 12-coordinate site. However, a deviation from unity in the tolerance factor often results in octahedral tilting and distortion to compensate for the A and B site size mismatch (Reaney and Ubic, 1999). This chapter discusses tilting in perovskites, its classifications, the simulation of experimental spectra of tilted perovskites from molecular dynamics, comparison to space-group simulation and experimental results. The aim of this chapter is to successfully simulate experimental spectra from MD, compare this to experimental results, and probe the geometries invisible to typical experiments. This will allow the prediction of TEM patterns for perovskites, providing extra geometrical analysis and feedback for forcefield fitting, and allowing assessment of experimental spectra.

4.2 Tilted Perovskites

4.2.1 Structure-Property Relationships in Perovskites

As mentioned in §1 structure-property relationships are key to understanding and thus manipulating materials for specific purposes. For example, in the case of pure barium titanate at the tetragonal-cubic phase transition near the Curie temperature (~ 120 - 130°C) (Fig 4.1), the permittivity of barium titanate spikes massively, and then drops off rapidly (Van Santen and Jonker, 1947) This is due to the c/a unit cell length ratio in tetragonal barium titanate approaching unity. As the c/a ratio approaches unity the energy required to make the titanium ion go off-centre gets progressively smaller, as the distance to travel to go off-centre decreases. This increases the bulk permittivity. When the c/a ratio reaches unity the barium titanate is cubic, which prevents the titanium ion going off-centre at all, resulting in the large drop in permittivity.

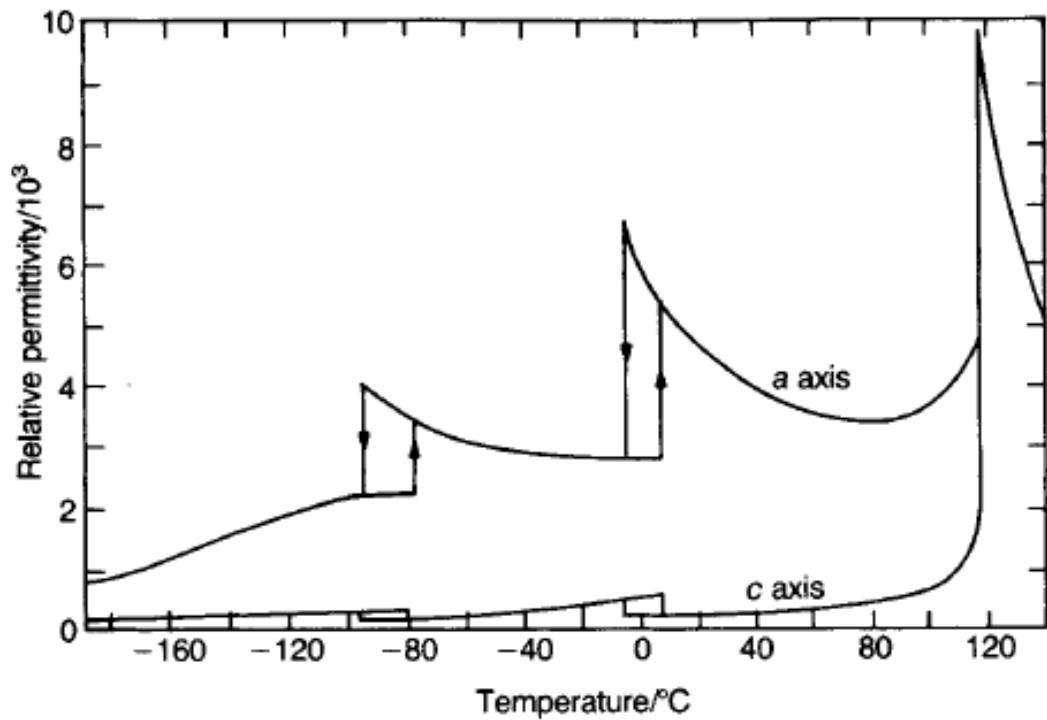


Figure 4.1: Pure barium titanate single crystal Permittivity vs Temperature data
 Reproduced from Merz (1949) <http://dx.doi.org/10.1103/PhysRev.76.1221>.

This example of a structure-property relationship in perovskites exemplifies why studying such relationships is crucial for understanding why certain materials exhibit certain behaviour. In the perovskite material family, another well understood but poorly numerically quantified structural feature is tilting.

4.2.2 Tilt in Perovskites

As mentioned in §4.1 tilt in perovskites occurs when the BX_6 corner-sharing octahedra tilt or rotate to compensate for the size ratios between A, B and X sites. The dependence of tilt on the size ratio was demonstrated by Reaney *et al* (1999), where tilt was linked to the tolerance factor t for perovskites which predicts the stability of a given perovskite as determined by Goldschmidt (1926) (Eq 4.1).

$$t = (R_A + R_O) / [2^{1/2}(R_B + R_O)] \quad (4.1)$$

where R_A , R_{Ba} and R_X are the radii of the A, B and X site ions respectively. The closer the resulting value is to unity, the more likely the perovskite phase is to form. An example of tilt is the prototype perovskite, calcium titanate (Fig 4.2). Orthorhombic calcium titanate shows tilting along all three of its unit cell axes.

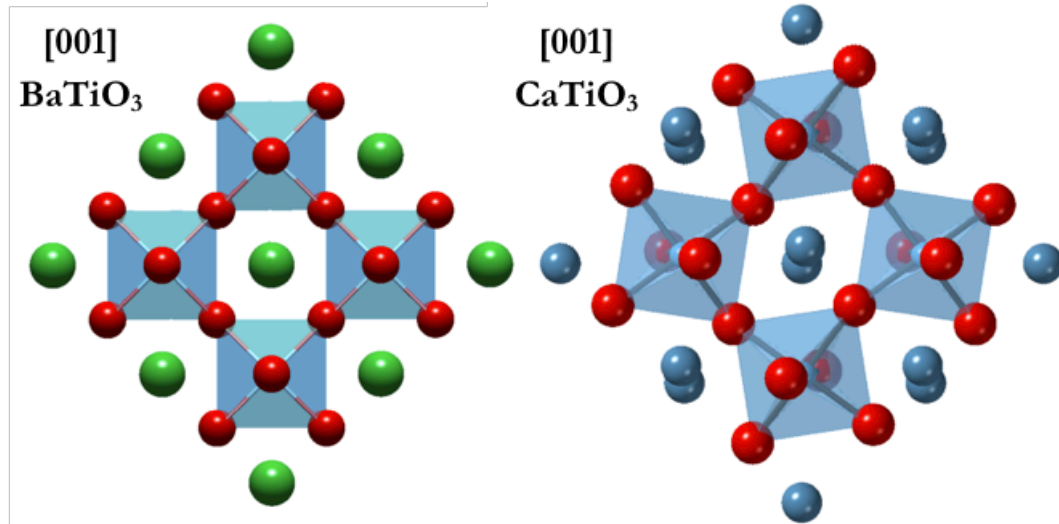


Figure 4.2: Orthorhombic calcium titanate unit cell, next to Cubic barium titanate cell [001] direction. Tilt can clearly be seen in the calcium titanate.

When one octahedron in a perovskite is tilted about one of its axes, the surrounding octahedra in the plane normal to the axis of rotation are constrained in their response to the initial tilt (Glazer, 1972). These constraints can extend for a long distance in a perfect lattice. The octahedra in the other two planes are not constrained and may tilt in a different direction. The sum of these rotations creates a net ‘tilt’ away from the perfect cubic perovskite.

Net tilt can be observed experimentally, through the space groups obtained from X-ray diffraction patterns as well as transmission electron microscopy patterns (Woodward and Reaney, 2005) and results in super-lattice reflections in the latter due to the net off-centring of the ions in the bulk ceramic (Fig 4.3).

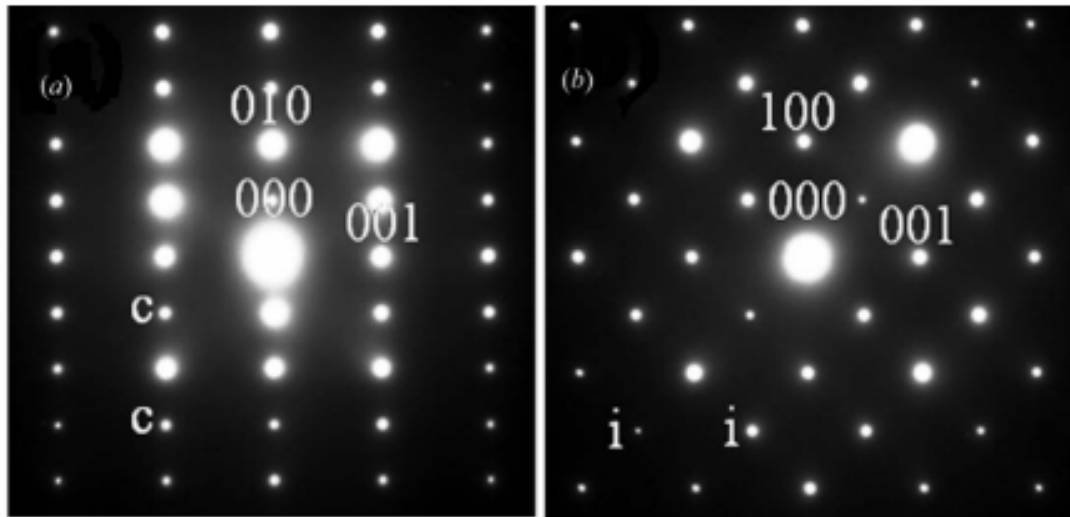


Figure 4.3: Example of TEM super-lattice reflections due to tilt (i and c) in calcium titanate view directions a) [100], b) [010] (Woodward and Reaney, 2005).

4.3 Introduction to TEM and XRD

4.3.1 Bragg Diffraction

The fundamental physics that explains both transition electron microscope (TEM) diffraction patterns and X-ray diffraction (XRD) patterns is the same. Proposed by father and son, William Henry and William Lawrence Bragg (1913), Bragg diffraction or Bragg's Law (Eq 4.2) describes how X-rays and other small wavelength waves are diffracted by crystalline materials. When X-rays are fired at a crystalline material, they scatter off the multiple layers of ions within the crystal and either remain in phase, interacting constructively, or ending up out of phase, interacting destructively with each other (Fig 4.4). Waves with sub-nanometre ($<10\text{\AA}$) wavelengths give the greatest convergence/interference pattern, as the wavelengths are a similar length to the interatomic distances found in crystals.

$$n\lambda = 2d\sin\theta \quad (4.2)$$

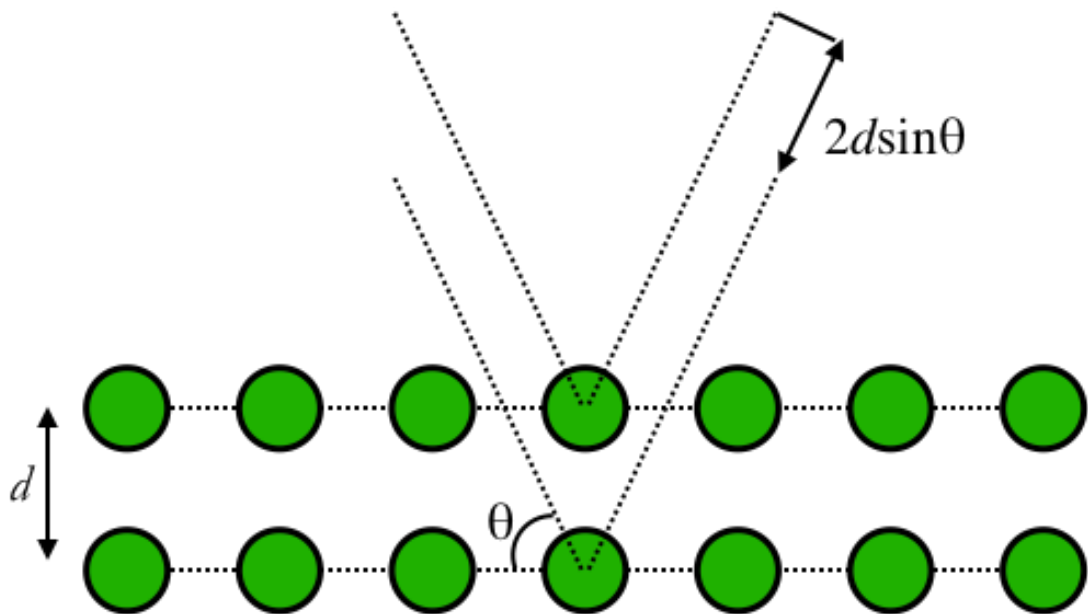


Figure 4.4: Diagram of Bragg Scattering

Bragg's law states that for a crystal with interatomic spacing d and a radiation source with wavelength λ the constructive interference will occur at angle θ . Working backwards from the angle at which constructive interference is observed, interatomic layer spacings can be determined. By scanning over a full range of incidence angles θ , the diffraction pattern for a material can be accessed. Depending on the type of initial radiation; X-rays; neutrons or electrons, this pattern looks different. The diffraction pattern provides information about the presence of other phases, defects, and internal strain.

4.3.2 X-ray Diffraction (XRD)

4.3.2.1 The Diffractometer

One of the earliest instruments used in materials science to perform experimental diffraction was the powder X-ray diffractometer (Fig 4.5). The fundamental components of a modern diffractometer are an X-ray source, a goniometer and an X-ray detector (Fultz, 2008). Electronic control systems are also needed to relate the detected scattered X-rays to the angle between source and sample. There are many different arrangements of the four basic components possible. Polycrystalline samples

are usually diffracted using the Debye-Scherrer method, which uses monochromatic X-rays over the range 0-180° to interrogate the sample.

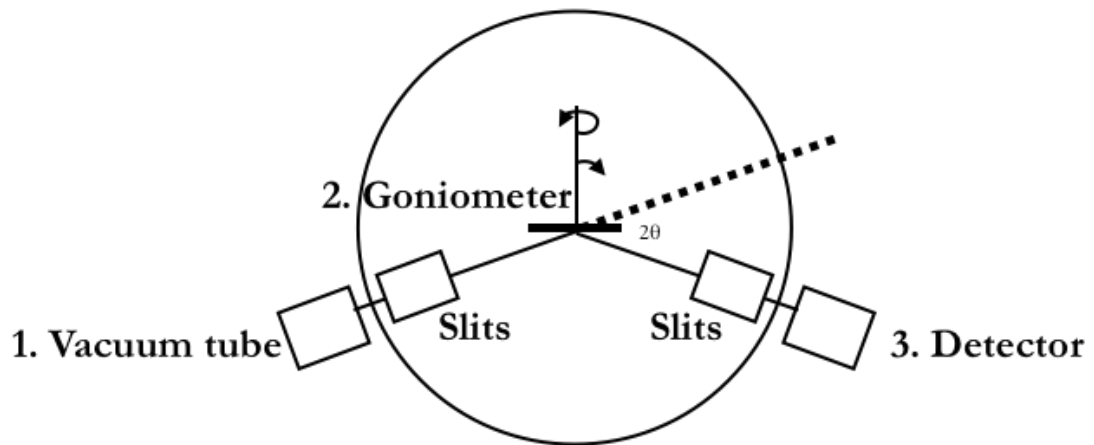


Figure 4.5: Schematic of X-ray Diffractometer adapted from Fultz (2008)

The three main components of the X-ray diffractometer are commonly arranged as shown in Figure 4.5. Their purpose and basic operation is discussed below.

1. The X-ray source is most commonly a vacuum tube diode that uses a copper filament to thermionically produce X-rays. These X-rays are then filtered using slits to produce a single phase coherent X-ray beam focused in the direction of the sample. Filters are used on the vacuum tube source to eliminate the characteristic X-rays of the source filament. Different filaments are often used to produce specific wavelengths.
2. The goniometer facilitates the rotation of the sample in the X-ray beam. Some X-ray diffractometers keep the sample static and rotate the X-ray source and detector. Goniometers provide precise measurable rotation. An entire X-ray scan of a sample, rotates through the full 2θ to 180° range of angles.
3. The detector collects the resultant X-rays scattered by the sample. Each absorbed X-ray causes the detector to emit a pulse of electricity. The sum of the pulses for a given 2θ is the intensity. To ensure coherence and ease of analysis, two sets of slits, singular vertical slits, and horizontal Soller slits (1924) are used in front of the detector. The horizontal slits allow only angles scattered at 2θ to

pass through to the detector, and the Soller slits correct any axial divergence in the rays detected.

The sample being interrogated by XRD can be a single crystal or a powder. When probing a single crystal, only one orientation of the crystal is observed by the X-ray beam, even when the sample is rotated, leading to a limited number of high intensity peaks or diffraction spots being observed. These 2D spot diffraction patterns are like those observed in transmission electron microscopy. In the case of powder diffraction, the same material is arranged in multiple orientations allowing the detector to detect coherence or high intensity at more 2θ values than for a single orientation. The aggregated values from many orientations allow the whole structure of the material to be probed from one polycrystalline, powder sample rather than many individual orientations of a single crystal sample, which would be time consuming and expensive to facilitate.

4.3.2.2 XRD Spectra

X-ray diffraction spectra is most often visualised as a graph showing intensity of the X-rays observed at all angles of 2θ (Fig 4.6). This collates the information from the entire scanning range of the X-ray diffractometer into one graph. There is typically low level background noise in the spectra which can be eliminated by subtracting the spectra of the background noise of the diffractometer without the sample.

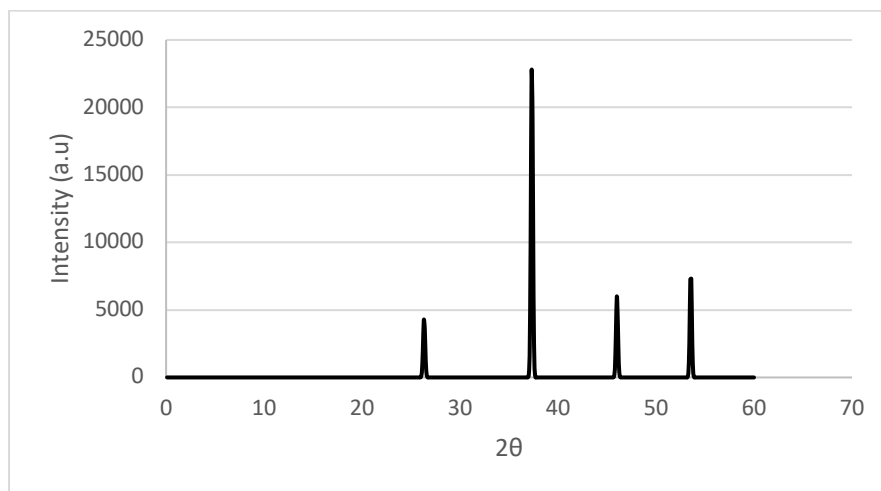


Figure 4.6: X-ray diffraction spectra for cubic barium titanate (Aoyagi *et al.*, 2002).

4.3.2.3 Analysis of X-ray Diffraction Patterns

The resultant spectra from XRD can be analysed in two different ways. Firstly, it can be indexed, this process relates the individual peaks in the spectra to a specific reciprocal lattice position (in Miller indices). From this the d-spacing for each indexed peak and unit cell length can be calculated. In a cubic cell indexing the peaks and working out the d-spacing is straight forward (Eq. 4.3).

$$\frac{1}{d^2} = \left(\frac{1}{a^2}\right) [h^2 + k^2 + l^2] \quad (4.3)$$

where d is the lattice spacing, h , k and l are the Miller indices of the plane and a is the unit cell length. By calculating d for each of the high intensity peaks using Bragg's law (Eq. 4.2) and calculating the $1/d^2$ value for each peak, the Miller indices can be worked out by dividing through by the common factor ($1/a^2$).

For crystal structures other than cubic, or solid solutions combining multiple space groups, indexing the pattern can become more complex. Auto-indexing programs are used to determine the index and intensity of each peak and the respective R-factor or discrepancy index; a measure of how reliable the intensity of the peaks is.

The second method for analysing XRD spectra is through an iterative modelling process. This is often used for unknown substances and complex systems. An XRD pattern from a model is calculated, and then compared to the experimental result. This is then iteratively improved until the model matches the experiment. The data can be fitted using many different methods, Rietveld refinement (1969) is one of the most common. MD calculations have also been used to identify the thermal ellipsoid parameters included in the refinements due to the kinetic vibrations of the atoms (Auffinger, Masquida and Westhof, 2002).

4.3.3 Transmission Electron Microscopy

Electron microscopes, first developed and trialled during the 1930s, can observe very small features of materials, in the range of 50-100 pm (Fultz, 2008). As an electron has a

very small wavelength (1.23nm) this allows much smaller objects to be seen than by a light microscope. The transmission electron microscope (TEM) forms images by firing electrons through a specimen. The sample must be 100nm or thinner, to allow the electrons to pass through and to ensure a uniform width is exposed to the beam.

4.3.3.1 The Microscope

The creation of diffraction patterns in transmission electron microscopy (TEM) is a similar process to that used in XRD. In TEM however, a beam of electrons is used as the source of radiation. An electron microscope consists of 6 components in its most basic form (Fig 4.7).

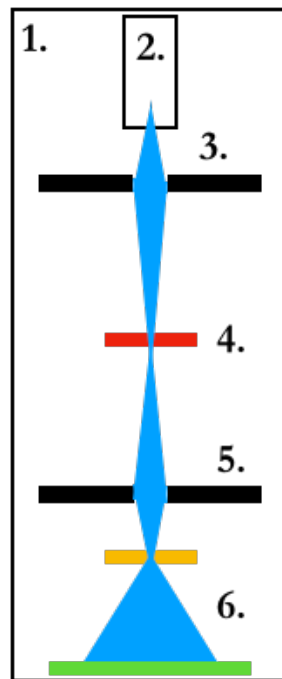


Figure 4.7: Schematic of basic transmission electron microscope adapted from (Fultz, 2008)

1. The vacuum system of an electron microscope removes gas atoms that would deflect the electron beam reducing the effectiveness of the device. The vacuum system is typically pumped down to 10^{-4} Pa or less. Much lower vacuum pressures are needed if the TEM is high-voltage, this is to safeguard against arcs being generated.
2. The electron source, or electron gun, is typically a tungsten or lanthanum hexaboride filament heated to high temperatures to produce electrons. The

filament is heated by a high powered electrical source, and the resultant beam directed towards the positively charged anode has an acceleration of between 60 and 300 keV. The acceleration voltage can be altered to change the magnification of the sample. The gun itself is negatively biased to ensure the electrons leave the filament to create the electron beam. As electron beams can damage the sample being investigated, the higher the voltage and longer the exposure the more likely this is to occur. For a typical ceramic sample, the beam is accelerated to between 100-200keV.

3. The condenser lenses focus the electron beam to produce a more condensed 'point-like' electron beam. These lenses control the 'spot-size' of the beam, or the size of the area of the sample which is hit by the beam. The 'spot size' can vary between 0.0001 and 0.5\AA^{-1} . The first condenser lens corrects for astigmatism, the second controls the spread of the beam hitting the sample. The lenses are typically magnetic lenses, controlling the charged electron beam via a magnetic field. The deflector coils can be oriented around the beam to focus the beam centrally, or at the sides of the beam to deflect the beam side to side.
4. The sample is either held in the sample holder rod suspended on a small grid, or for self-supporting samples is placed directly in the rod. The sample rod is attached to goniometers to facilitate the rotation of the sample during the operation of the microscope.
5. In the diffraction TEM configuration, the objective lenses are found after the sample holder. They focus and magnify the beam that has passed through the sample. They are typically magnetic lenses like those used for the condenser lenses.
6. The fluorescence screen and cameras are found below the specimen; they are usually paired with a final set of projection lenses which take the output from the objective lens and further magnify the resultant image. The beam that has been diffracted by the sample is then projected onto the fluorescence screen, which fluoresces when an electron hits the surface. The diffracted electron beam hitting the fluorescence screen produces a visible TEM spectrum from the

monochromatic electrons. This can be observed directly or indirectly, via cameras, by the operator of the machine.

The sample preparation for TEM can be carried out in many ways. Often a larger sample is manufactured first and then cut down and finally thinned using a fixed ion beam (FIB) to get the sample to 100nm in thickness or less. The sample itself is typically circular and approximately 3mm in diameter. For brittle substances, such as ceramic, achieving such a small sample without fractures is a highly skilled job.

4.3.3.2 TEM Outputs

Depending on the set-up and imaging mode of the TEM, many different outputs may be obtained. These include but are not limited to: long or short exposure selected area diffraction patterns (SADP), backscattered TEM and laue diffraction (Fig 4.8).

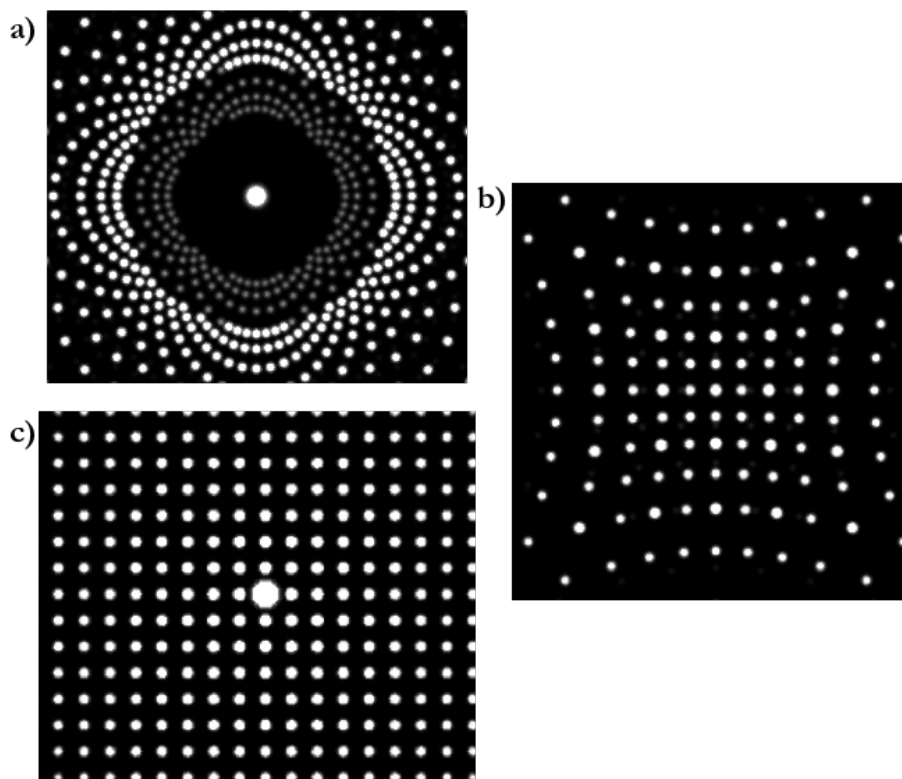


Figure 4.8: Examples of TEM imaging modes, a) laue diffraction, b) backscattered laue diffraction, c) Selected area diffraction pattern. The diffraction patterns show reciprocal space depictions of the system being diffracted.

4.3.3.3 Selected Area Diffraction Patterns

In this work, we are concerned with SADPs as an output from TEM. SADPs consist of spots, that are produced due to the constructive and destructive interference of the electron beam when transmitted through the sample. These spots, or areas of high intensity, like those seen in single crystal XRD spectra, can reveal information about the crystal structure such as the atomic spacing, ionic correlations, and the overall crystal structure. The diffraction patterns observed are the projected reciprocal lattice of the crystal in that orientation (Fultz, 2008). Selected area diffraction patterns can be simulated from atomic positions by calculating the reciprocal lattice of the atomic positions.

4.3.3.4 Effect of Exposure Time on Diffraction Patterns

The time that a sample is exposed to the electron beam when in diffraction mode affects the resultant visible spectra. Short exposure diffraction patterns are SADPs where the time that the sample has been exposed to the beam is between 5-16 seconds. Long exposure diffraction patterns are between 50-100 seconds and further information about the sample can be observed including diffuse scatter which is indicative of weak correlation between ions in the solid. Long exposure times can damage the sample.

4.3.3.5 Analysis of Transmission Electron Microscopy Diffraction Patterns

SADPs can be indexed and used to identify the crystal structure and d-spacing of the crystal being examined. SADPs taken over multiple zone-axis are needed to index the entire crystal structure. The patterns are indexed with relation to the pseudo-cubic cell (Fig 4.9) as this is the convention in literature. This is important when it comes to non-cubic crystals as literature can report a zone axis that does not match the zone axis given in simulation. When simulating TEM patterns the zone axis identified is the zone axis of the simulated crystal, cubic or not. The zone axes seen in experiment and those simulated must match each other and so a conversion from the real crystal axis to the pseudo-cubic axis must take place (Fig 4.9)

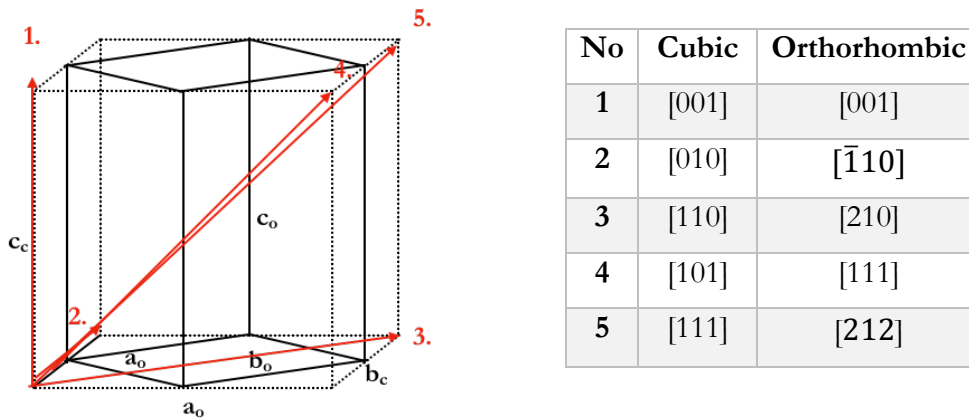


Figure 4.9: Pseudo-cubic and orthorhombic cell relations with the view directions and their corresponding equivalents listed.

Once indexed, the patterns can be compared to known or simulated patterns to identify crystal structures and d-spacing. Other features such as diffuse scatter and Kikuchi lines can be identified and associated with specific features such as uneven surfaces or scratches in the sample.

4.4 Definitions of Tilt in Perovskites

4.4.1 Tilt in Perovskites

As discussed in §4.2 octahedral tilting is an important bulk structural phenomenon found in perovskites with overall Goldschmidt factors of 0.96 and below (Reaney and Ubic, 1999). This net tilt can be observed in TEM diffraction patterns as super-lattice reflections, and in XRD as d-spacings consistent with the space-group associated with the tilt. General tilt classification has been attempted by many scientists most predominantly by Glazer (1972) and Beanland (2011). Their models are reviewed in detail in §4.4.2. One limitation common to these classification systems is the lack of interrogation of the dynamic behaviour of the system. To be able to observe and classify tilt they both require the bulk of the perovskite to exhibit tilting. As tilting occurs due to ion size ratios within a perovskite, it is reasonable to assume that regions within heavily doped, or solid solution perovskites may also exhibit local tilting due to different local chemistry and thus a lower local Goldschmidt factor. These small regions of tilt currently cannot be seen and quantified using conventional experimental spectra,

although they may be viewed using high resolution methods such as HRTEM. XRD and TEM diffraction patterns may also be observing this local tilt behaviour, which could generate artefacts, or lead to misinterpretation of this behaviour.

4.4.2 Existing Definitions of Tilt and Their Limitations

As previously mentioned §4.4.1 there have been many mathematical definitions of tilt reached by different scientists in the last four decades. The most well-established definition is that of Glazer. In the first and subsequent paper (Glazer, 1972, 1975) he identified 23 possible tilt systems in perovskites and classified the type of tilting using a system subsequently called Glazer notation. He also linked the 23 tilt systems to their respective crystallographic space groups. By assuming the prototype perovskite structure to be perfectly cubic, with no tilt and geometrically perfect octahedra, Glazer notation then identifies overall tilt as a sum of tilts, either in-phase, anti-phase or no tilting (Fig 4.10), in each of the cubic unit cell directions a, b and c. Tilt phase is identified by looking at the tilt angle between two octahedra projected along one plane (x, y or z) and relating it to the subsequent layer of octahedra in that direction. If the tilt angle is in the same direction, the tilt is in phase. If there is no angle of tilt there is no tilting, and if the angles of tilt seen are in opposing directions then the tilt is classified as anti-phase tilting.

Although net tilting in perovskites has been observed, classified and mathematically simulated using ideal space groups, the dynamical behaviour of the tilted octahedra has not been thoroughly interrogated.

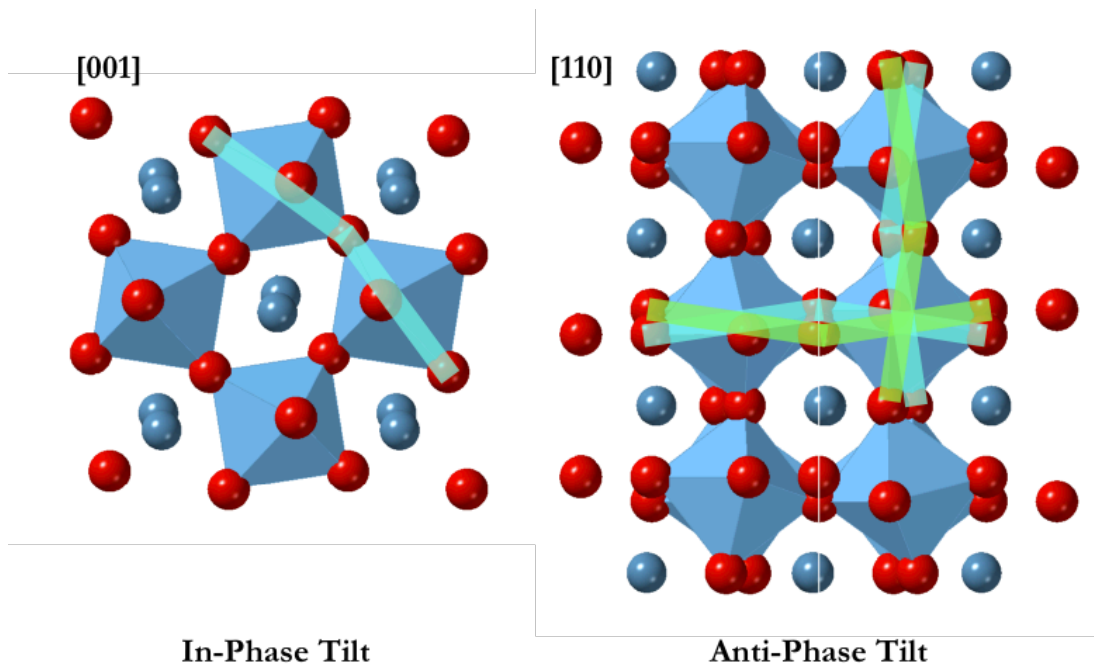


Figure 4.10: In-phase and Anti-phase tilting highlighted in the calcium titanate cell.

Cubic systems with no tilt are represented as $a^0a^0a^0$ in Glazer notation. If the magnitude of tilt is the same in multiple directions the same letter is used. The super script 0 + or – denotes no tilt, in phase tilt and anti-phase tilting respectively. The Glazer notation for the calcium titanate system is thus $a^-b^+a^-$ denoting anti-phase tilting with the same magnitude along two axis and in-phase tilting along the other. This corresponds to the orthorhombic space group No. 62 - pnm which equivalent to pbm as the only difference is the cell orientation. The number of possible tilt systems was revised downwards to 15 by Howard and Stokes (1998) as some of the original 23 systems were proven to be equivalent.

The main limitation of Glazer notation is that the octahedra are assumed to remain perfect. This presumed lack of distortion in the octahedra is unlikely in certain scenarios: low tolerance factor perovskites; solid solutions including tilted perovskites; hybrid organic-inorganic perovskites; and highly defective systems. Another significant limitation is that the tilting is defined by an external reference frame, in this case the perfect pseudo cubic perovskite cell. This makes it easy to link the tilts to specific space groups, however it only works if perfect centrosymmetric octahedra are assumed. This is a problem for many perovskites which derive their electrical properties from off-centre A and B sites. Glazer notation also implies that the tilt motion comprises three distinctive sequential moves. This is not the case in real dynamic systems. Glazer

notation also has no way of classifying tilt during phase changes, only the end states of the transition. Finally, Glazer notation is not quantitative; the only information stated about the tilts themselves is whether some are equivalent and in what direction each subsequent layer of the system tilts.

Richard Beanland (2011) described tilt in a more generalised manner for the purposes of examining tilt around grain boundaries. His method accounts for small octahedral distortions and non-centrosymmetric octahedra to model and explain tilting at phase boundaries. It does this by using a tensor description for octahedra to describe their tilting, and an operator to describe the type of connection between adjacent octahedra (Fig 4.14). This system has advantages over Glazer notation as it facilitates description of phase boundaries and non-regular octahedra. However, like Glazer notation, this model relies on external reference frames for defining the direction and relationship of tilt.

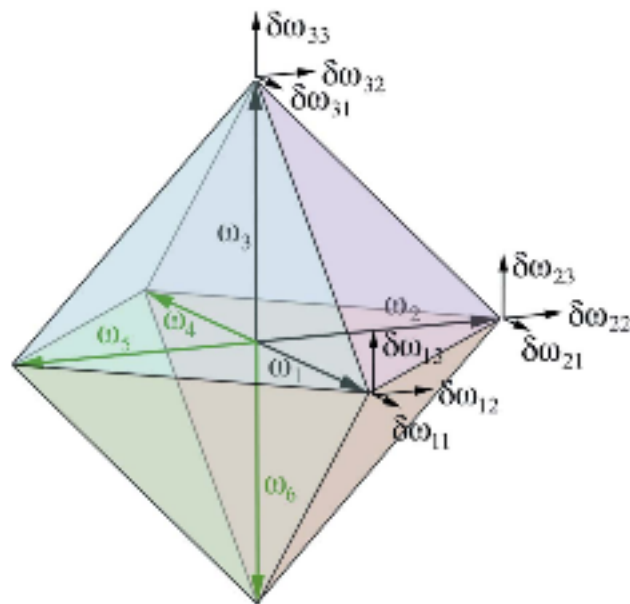


Figure 4.11: Beanland's definition of tilt (2011) [Reproduced with permission of the International Union of Crystallography](#)

Fundamentally although both Beanland and Glazer and others have created definitions for overall net tilt, they lack quantitative values for tilt angles. Neither scheme considers the dynamic motion of tilted perovskites, and how this may link to tilt phase changes. To overcome these limitations another method of tilt analysis has been developed in conjunction with this thesis.

4.5 Geometrical Tilt Analysis

4.5.1 Defining Tilt from Geometry

One of the most fundamental limitations of previous definitions of tilt in perovskites is the tendency to relate tilt to a cubic cell that has been distorted. This is useful when relating tilted systems to specific space groups. However, as previously discussed, this creates issues when the octahedra are not regular. To overcome this an internal reference frame was used in this work. This allows the simulated ceramic to be in any orientation and eliminates the need to impose an external cubic frame of reference on the cell which can cause description of the tilt structure to vary depending which direction is chosen as x , y and z respectively.

Another decision that must be made when defining tilt (in the BX_6 octahedra) is whether the angle of tilt itself is between the $X-X-X$ sites or the $B-X-B$ sites (Fig 4.16). In this work the tilt angle is described using the $X-X-X$ sites. This allows non-centrosymmetric octahedra to be accommodated.

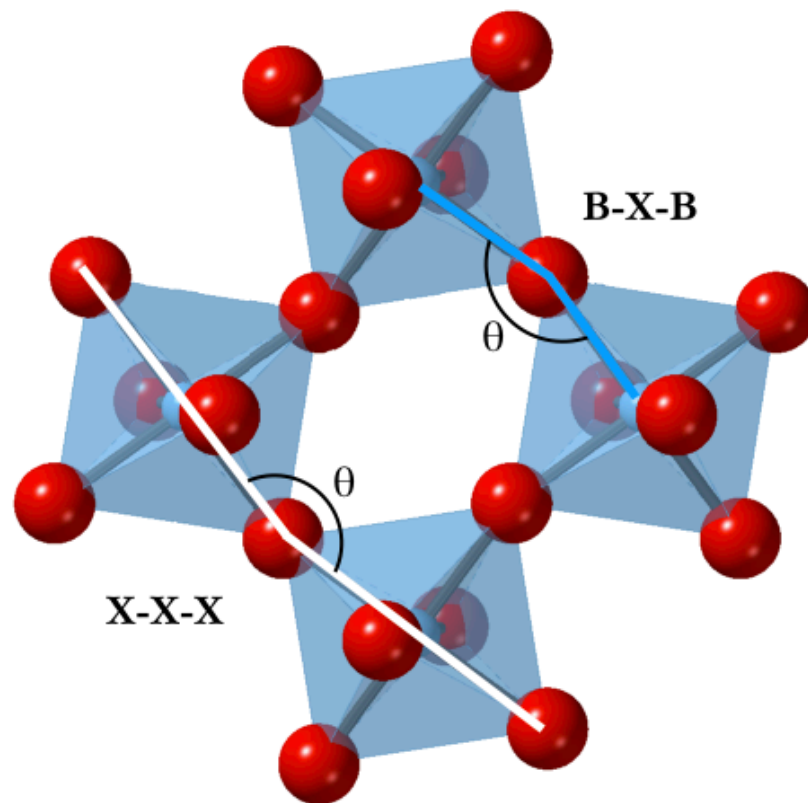


Figure 4.12: Possible definitions of tilt angles; X-X-X and B-X-B.

This work uses X-X-X to facilitate off centre octahedra.

Information about the crystal structure can be calculated using well known geometric formulae. Volumes of the B-site octahedra and A-site irregular dodecahedra (cubo-octahedra) can be calculated by splitting the octahedra and dodecahedra into irregular tetrahedra and using Equation 4.4 on all constituent tetrahedra (Fig 4.13).

$$V = \sqrt{\frac{1}{288} \text{Det} \begin{bmatrix} 0 & 1 & 1 & 1 & 1 \\ 1 & 0 & d_{12}^2 & d_{13}^2 & d_{14}^2 \\ 1 & d_{12}^2 & 0 & d_{23}^2 & d_{24}^2 \\ 1 & d_{13}^2 & d_{23}^2 & 0 & d_{34}^2 \\ 1 & d_{14}^2 & d_{24}^2 & d_{34}^2 & 0 \end{bmatrix}} \quad (4.4)$$

where V is the tetrahedral volume, and d_{12} etc are the lines connecting the vertices in the irregular tetrahedra.

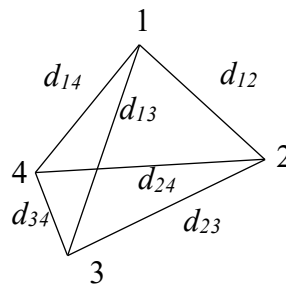


Figure 4.13: Diagram of an irregular octahedra with vertices and edges labelled as per Eq 4.4.

A measure of the distortions of an octahedra can be calculated using the quadratic elongation formulae (Eq. 4.5) and the distortion index (Eq. 4.6) (Momma and Izumi, 2011) where l_0 is the edge length of a regular polyhedron with the same volume l_{av} is the average length of the edges in a given octahedra and l_i is the length of a given edge of a octahedra. The Dipole displacements of A-site and B-site ions away from their central lattice point can be calculated as the difference between the centroid of the surrounding X-site ions and the position of the A or B site ion.

$$\langle \lambda \rangle = \frac{1}{n} \sum_{i=1}^n \left(\frac{l_i}{l_0} \right)^2 = (4.5)$$

$$D = \frac{1}{n} \sum_{i=1}^n \frac{|l_i - l_{av}|}{l_{av}} (4.6)$$

The tilt phase as per Glazer notation can be also calculated geometrically in a generalised way for all simulated perovskites by calculating and comparing torsion angles.

For a given A-site (Fig 4.13a), each side of the bounding B-site -X-site – B-site lattice box is examined in turn. The midpoints between B-sites along two ‘parallel’ edges are calculated. Then these midpoints M_1 and M_2 are connected via a rod (Fig 4.13b). The X-sites X_1 and X_2 are also connected via rods to the midpoint of their respective B-sites (Fig 4.13c).

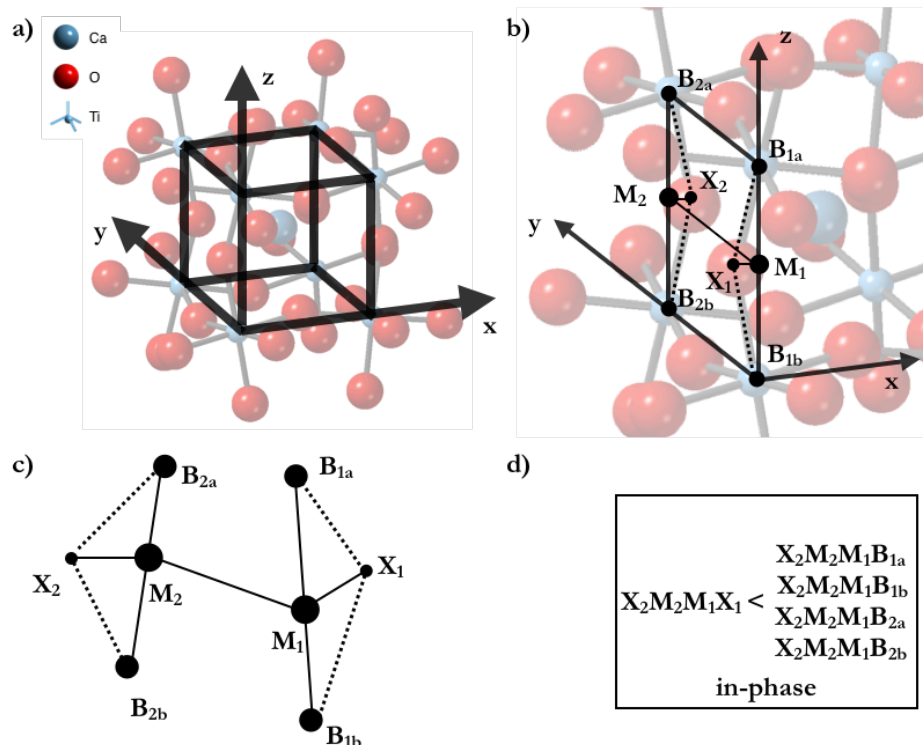


Figure 4.14: Tilt Phase Calculation in PALAMEDES. a) Identification of A-site box. b & c) Identification of B-sites, midpoints and X-sites. d) definition of in-phase tilting, all other results are anti-phase.

This allows the angle of torsion between all connected members to be calculated. In a method, analogous to a method used to identify cis or trans molecules, if the specific angle $X_2M_2M_1X_1$ (Fig 4.13d) is the smallest of all five angles of the angles interrogated as per the legend, then that pair of edges of the box surrounding an A-site is counted as in-phase. All other results are considered anti-phase. The no-phase state is a combination of tilt angle $\sim 180^\circ$ and the edges counted as anti-phase. For each pair of edges examined, in-phase edges are scored as 1 and anti-phase edges are scored as -1. The average of these in each of the cell directions over the entire simulation gives a value between -1 and 1.

This allows the magnitudes of tilt angles in the cell directions and the calculated phase tilt to give a generalised, more realistic, alternative to Glazer. The larger the number of edge pairs in each direction that score the same value, the longer the phase persistence length of the tilt. This persistence length is valuable for assessing micro tilted regions and tilt phase transitions. The code written to perform all of the geometrical analysis detailed here on DL_POLY_4 (Todorov *et al.*, 2006) output files was written in house by Dr Christopher M. Handley and is detailed in Appendix 1.

4.6 Time Dependent Simulation of Tilt - TEM, and XRD Spectra

4.6.1 Introduction

Simulation of tilted perovskites has been done successfully. These simulations have been linked back to Glazer's tilt definitions and space groups and have been very useful for identifying tilted structures. The simulation of tilted perovskites over time has yet to be attempted. The reason for this was explained by Woodward and Reaney (2005) as the limitations of computer time, power and expense. In the 13 years since, developments in hardware and software have made the time dependent simulation of perovskites possible. In this work the aim was to simulate experimental spectra of tilted perovskites from molecular dynamics simulation. This feedback loop from dynamical simulation will help facilitate validations of forcefields and identifications of defects in experimental samples.

4.6.2 Molecular Dynamics Details

The molecular dynamic simulations were all run using the NpT ensemble as it is best for comparison to experiments carried out under standard conditions. Simulations were run between 100 and 10000 timesteps. Timesteps were 0.5fs in length. The forcefields used for each calculation are detailed in each results section as well as simulation size and length.

4.6.3 Effective Sampling of Molecular Dynamics

As MD simulations have such small timesteps (femtoseconds), they typically are not run for more than nanoseconds. Experimental techniques however, collect data over much longer periods of time (seconds – minutes), but do so less frequently than MD. For example, a TEM sample exposed to an electron beam with energy 200keV would see a single electron every 1×10^{-11} seconds assuming a constant flow of electrons, this is 4 orders of magnitude longer than femtoseconds (1×10^{-15}). Therefore, the TEM is seeing the sample much less often than an MD calculation. Using all of the data from an MD run to simulate experimental spectra may over-sample configurations due to the timestep difference between experimental and simulation.

MD calculations can be run and only print the trajectory every n^{th} timestep. This would be a better approximation of the sampling of a TEM than a trajectory printed every timestep. However, without prior knowledge of the system, an arbitrary selection of n could enforce over-sampling of specific configurations due to the periodic nature of atomic oscillations in solid materials. Monte Carlo sampling is an effective strategy to sample the MD trajectory. The fitting of the sampling scheme is discussed below.

Simulated TEM and XRD spectra are generated with CrystalMaker Suite (2018)

4.7 Proof of Concept – Barium Titanate and Calcium Titanate

4.7.1 Simulation Details

To simulate experimental spectra for calcium titanate, a box size of $\sim 100 \times 100 \text{ \AA}$ was used. This was a $20 \times 20 \times 20$ cell box of 160000 atoms at 50K. The size is a good approximation of a small aperture SADP sample in a TEM. The same forcefield as that

in §5 was used, apart from the Ca-O interaction as detailed in Table 7.1 and an altered Ti-O interaction to encourage the system to remain orthorhombic during dynamic simulation. The simulation was equilibrated for 5000 timesteps and run for 10000 timesteps printing the trajectory every timestep. The same size box and simulation was undertaken for pure barium titanate using the forcefield in §5.

Table 7.1: Ca-O Interaction from Dawson (2012) and adapted Ti-O interaction for this work.

Buckingham Potential $A \exp(-\rho/r) - C/r^6$				
Interacting ions		A (eV)	ρ (Å)	C (eV Å⁶)
Ca	O	1375.0	0.3325	15.21

Lennard-Jones 7-6 Potential $E_0 \left[\left(\frac{R_0}{r} \right)^7 - 2 \left(\frac{R_0}{r} \right)^6 \right]$				
Interacting Ions		E₀(eV)	R₀(Å)	
Ti	O	0.01194	4.719	

4.7.2 Sampling of Raw Data

The 10000 timestep history file was sampled both sequentially and randomly using Monte Carlo sampling as per Table 7.2. As can be seen in the table the averages and standard deviations fail to change much past 1000 timesteps for random sampling. However, this is a very low temperature calculation at 50K and to ensure applicability to higher temperatures 20% was decided upon as being a more suitable number of frames to sample. For more in-depth analysis of dynamics, sequential sampling is more appropriate as it includes all of the dynamical information, unfortunately this over samples in comparison with experimental techniques.

4.7.3 PALAMEDES Output

Table 7.2: PALAMEDES angles output for random and sequential sampling of CT simulated at 50K showing the average octahedral volume for the system, the standard deviation, minimum and maximum octahedral volumes seen in the sample. The angle X+ refers to the angle of tilt calculated in the positive x direction for each octahedra.

<i>Random Sampling</i>	<i>Average Oct Vol (\AA^3)</i>	<i>STD Oct Vol</i>	<i>Min Oct Vol</i>	<i>Max Oct Vol</i>	<i>Average Angle x+</i>	<i>Min Angle x+</i>	<i>Max Angle x+</i>	<i>STD Angle x+</i>
100	9.9193	0.0637	9.369	10.1881	159.0785	154.0014	164.6074	0.9763
200	9.9192	0.0638	9.3366	10.1967	159.0812	154.0014	164.8479	0.9766
500	9.9191	0.0638	9.3715	10.2134	159.0829	154.0173	164.83	0.9775
1000	9.919	0.06395	9.3672	10.2171	159.08475	154.11965	164.7193	0.9774
2000	9.919025	0.0639	9.3572	10.217775	159.08385	154.0014	165.0326	0.97685
5000	9.91898	0.06396	9.34775	10.21396	159.0847	153.9837	165.0326	0.97708
<i>Sequential Sampling</i>	<i>Average Oct Vol (\AA^3)</i>	<i>STD Oct Vol</i>	<i>Min Oct Vol</i>	<i>Max Oct Vol</i>	<i>Average Angle x+</i>	<i>Min Angle x+</i>	<i>Max Angle x+</i>	<i>STD Angle x+</i>
100	9.9175	0.0655	9.3215	10.2093	159.1255	154.4814	164.0318	0.9822
200	9.9166	0.0666	9.3215	10.2093	159.137	154.4814	164.0318	0.9888
500	9.9184	0.0648	9.3715	10.2093	159.0977	154.4814	164.0216	0.9867
1000	9.9189	0.06405	9.34815	10.20535	159.0874	154.5566	164.06135	0.9852
2000	9.91885	0.064025	9.369425	10.20685	159.0886	154.54465	164.21025	0.9842

The outputs show that sampling randomly is more effective than sampling sequentially. 2000 of 10000 frames is an appropriate amount of random sampling for this system. The sequential sampling is inappropriate as the same average volume as for random sampling still hasn't been equalised at 2000 steps sampling. This is inefficient.

Table 7.3: PALAMEDES Phase output for CT and BT at various temperatures.

	<i>Temperature</i> (K)	<i>x</i>	<i>y</i>	<i>z</i>
<i>CT</i>	50	-1	-1	1
<i>CT</i>	150	-1	-1	1
<i>CT</i>	350	-1	-1	1
<i>BT</i>	350	0	0	0

The code correctly identifies the phase tilt for CT as two anti-phase tilts and one in phase tilt, this corresponds to the $a^+b^+a^-$ and for BT $a^0a^0a^0$. The angles are quantified and the volumes of the octahedra do not change much over the 50-350K temperature range for CT.

Table 7.4: PALAMEDES average angles and standard deviation output for randomly sampled CT and BT simulations at various temperatures in the positive x, y and z direction from each octahedra.

<i>Temperature</i> (K)	<i>octahedral</i> <i>volume</i>		<i>x</i> ⁺ (°)		<i>y</i> ⁺ (°)		<i>z</i> ⁺ (°)	
	AVE	STD. DEV	AVE	STD. DEV	AVE	STD. DEV	AVE	STD. DEV
50	9.93	0.06	159.03	0.80	159.03	0.80	158.65	0.86
150	9.93	0.13	159.56	1.56	159.28	1.44	158.92	1.52
350	9.93	0.12	160.17	2.74	160.17	2.74	159.82	2.73
<i>BT-350</i>	10.65	0.02	179.8	0.04	179.7	0.06	179.8	0.04

It is clear from Table 7.3 that the CT force field behaves as expected with increasing angle of tilt and standard deviation with increasing temperature. Though the octahedral volume does not change, its standard deviation does gets larger. The BT simulation at 350K gives a very defined cubic structure, with no tilting and tilt angles very close to 180°.

4.7.4 Comparison to Experimental Spectra

4.7.4.1 X-ray Diffraction

The predicted CT spectra compares very well with experiment (Figure 7.14) although they do not match perfectly. This is due to the fit of the forcefield and its ability to replicate the density of states for the system investigated as well as the difference in temperature between room temperature experiment and 50K simulation. The forcefield fit could be improved with improved forcefield fitting. The thermal contributions even at 50K in the simulated spectra can be seen in the form of some broadened peaks. This gives a good indication of thermal effects on CT in XRD and reduces the need to calculate thermal ellipsoids when predicting XRD from simulations.

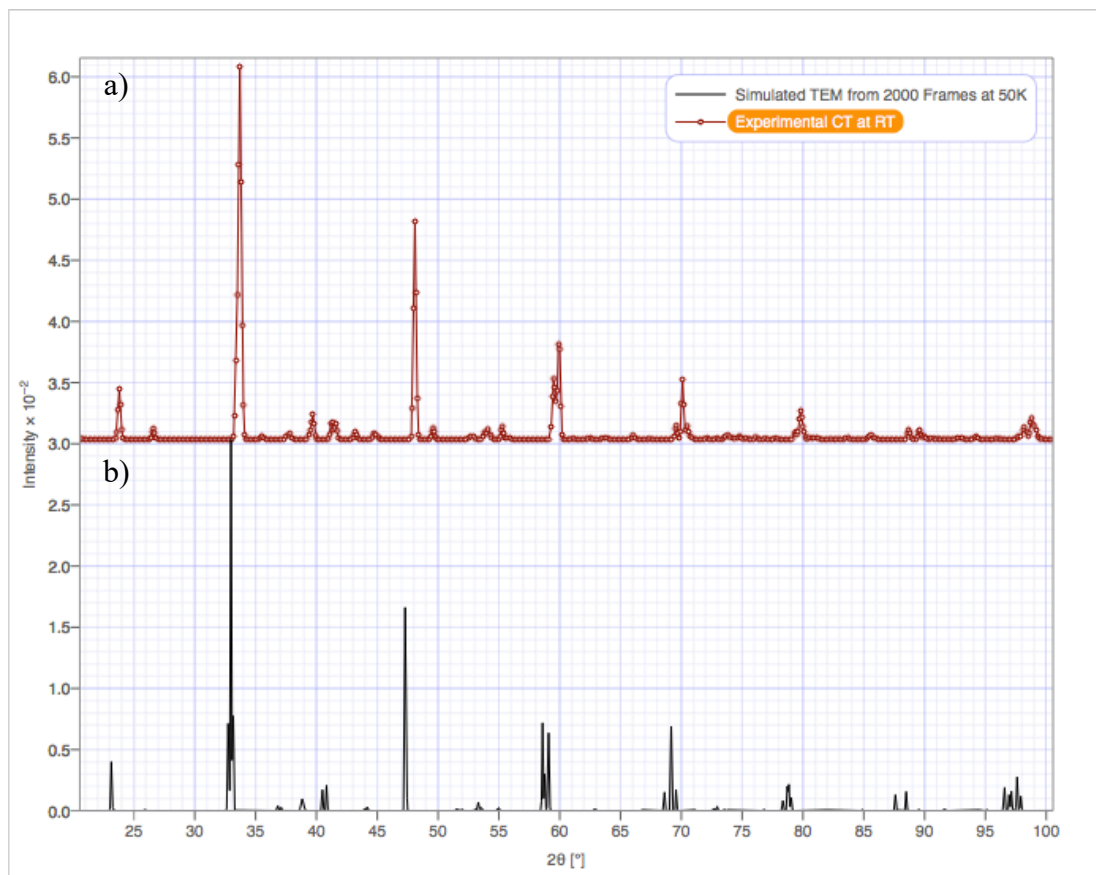


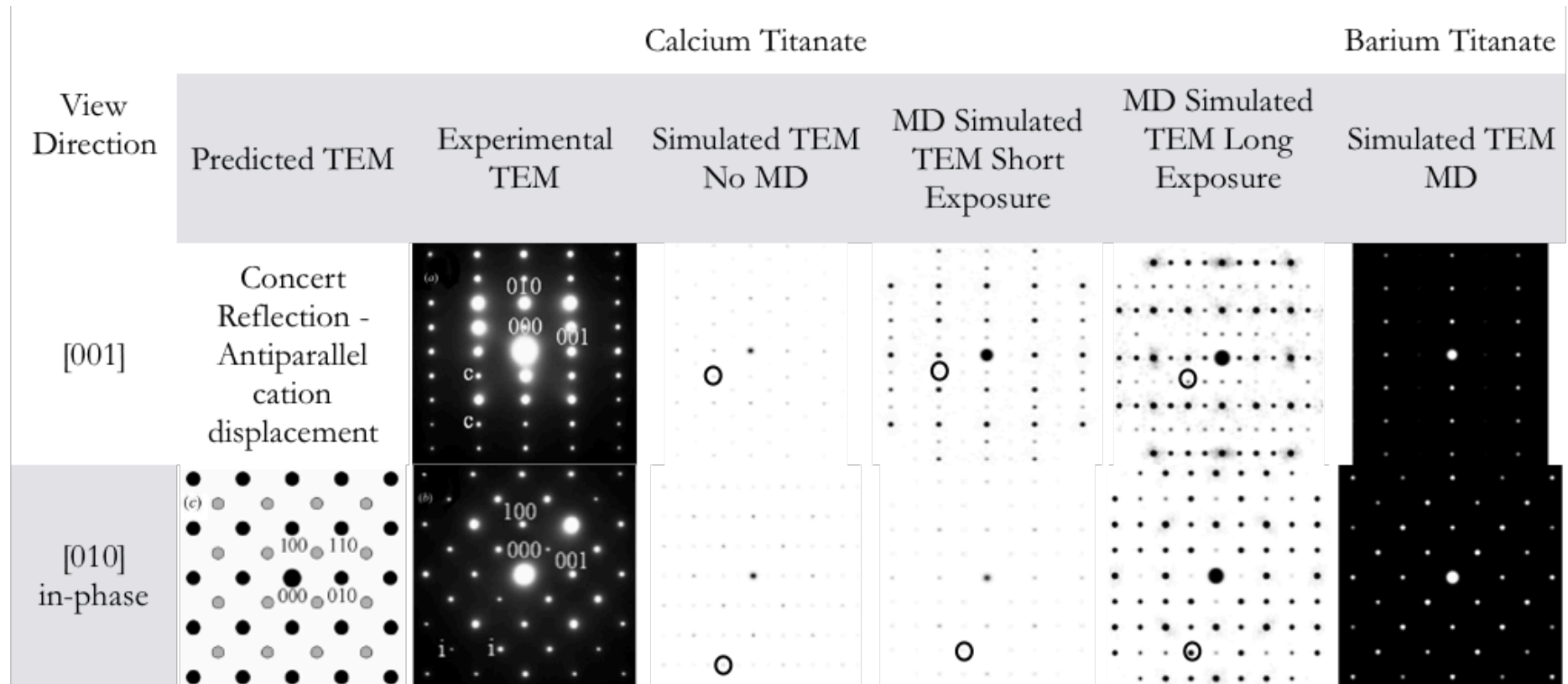
Figure 7.15: XRD spectra for a) simulated CT from an the average structure of 2000 randomly sampled frames and b) experimental orthorhombic CT (Yashima and Ali, 2009).

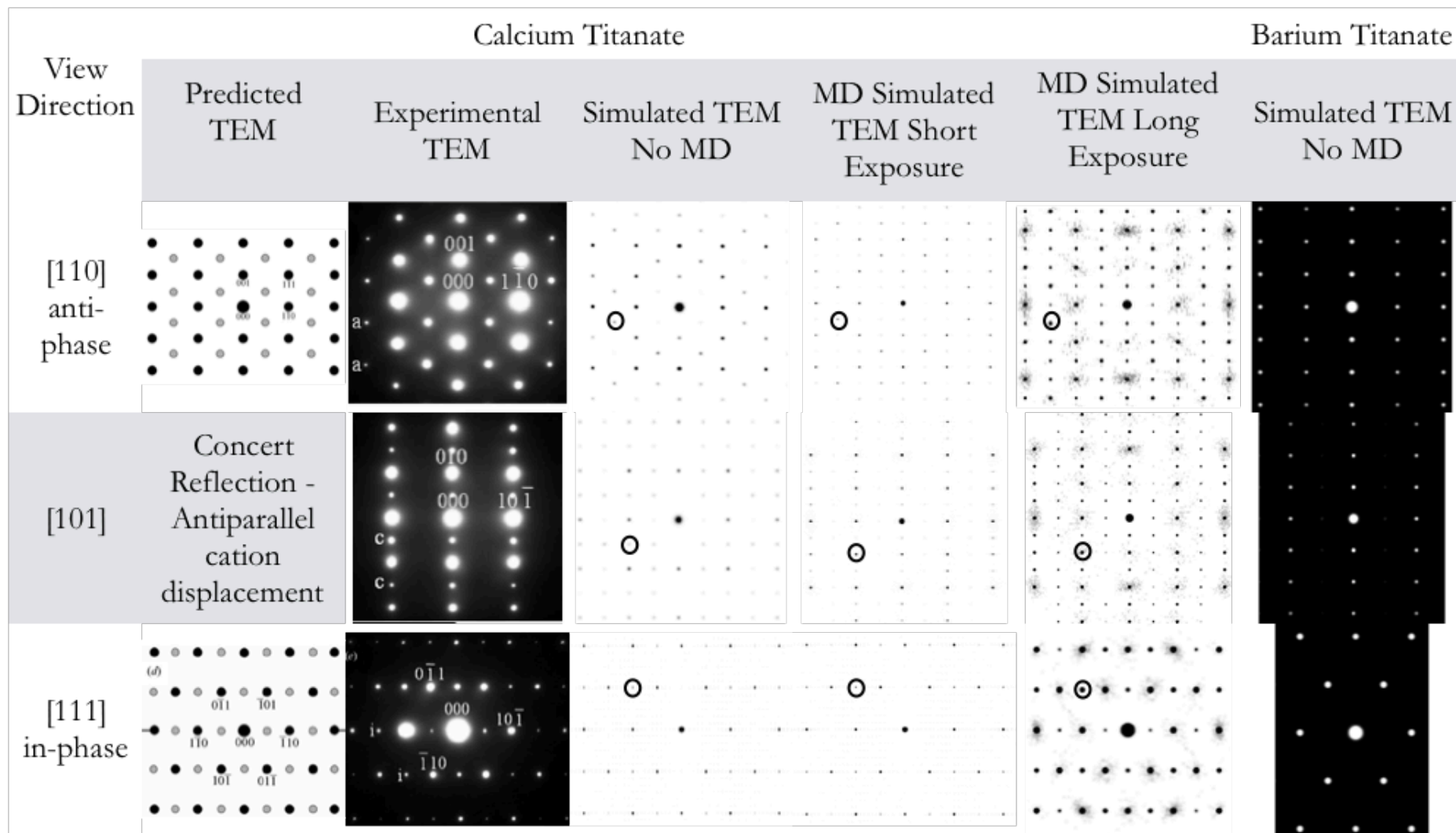
4.7.4.2 TEM

The predicted CT TEM compare well with experiment (Figure 7.16), by increasing the intensity of the plot, diffuse scatter can be seen around the main spots in the pattern suggesting cation-correlation. This allows us to predict a long exposure TEM. The perfect unit cell simulation does not get this scatter. This technique combines with the outputs from PALAMEDES can be used to inform about tilt on the local level and link the quantitative numbers and angles of tilt to the observed structure.

Figure 7.16: TEM spectra for analytical and experimental CT from Woodward and Reaney (2005)

and simulated CT at 50K from an ideal cell, from a structure averaged from 2000 MD frames at low intensity – to represent short exposure TEM SADP and high intensity to represent high exposure TEM SADP. BT was simulated from 2000 frames randomly sampled from MD. Super reflections are ringed in black. BT exhibited no such super-reflections.





4.8 Results – Methyl-Ammonium Lead Iodide

4.8.1 Simulation Details

To simulate experimental spectra for methyl-ammonium-lead-iodide (MALI), a box size of $\sim 45 \times 45 \text{ \AA}$ was used at 330K. The forcefield used was by Handley and Freeman (2017). The simulation was equilibrated for 1000 timesteps and run for 4000 timesteps printing the trajectory every timestep. The PALAMEDES output and the simulated TEM were outputted from this calculation.

4.8.2 PALAMEDES Output

The PALAMEDES output for MALI at 330K shows non-180° angles of tilt in the positive and negative directions in all three axes (Table 7.4). The average angle in for each axis in both directions are not equal suggesting a higher level of disorder in the model than for CT which had almost equal average angles in both directions. The phase output (Table 7.5) suggests that in at least two directions MALI is cubic, however the variation in average tilt angles disagrees with this. In the z direction a phase tilt value of 0.5 was given suggesting some coordinated motion of the in-phase type in this axis.

Table 7.4: PALAMEDES angles output for MALI at 330K showing average octahedral volume, and standard deviation and the average angle standard deviation in all three directions x, y and z, in both the positive and negative directions.

Temperature (K)	octahedral volume		x+(°)		x-(°)		y+(°)		y-(°)		z+(°)		z-(°)	
	AVE	STD. DEV	AVE	STD. DEV	AVE	STD. DEV	AVE	STD. DEV	AVE	STD. DEV	AVE	STD. DEV	AVE	STD. DEV
330	46.31	1.95	154	5.59	158	3.76	151	4.38	157	5.81	152	2.98	149	2.61

Table 7.5: PALAMEDES Phase output for MALI showing no net phase tils in the x and y directions and 0.5 phase tilt in the z direction.

Temperature (K)	x	y	z
330	0	0	0.5

4.8.3 Comparison to Simulated Experimental Spectra

4.8.3.1 TEM

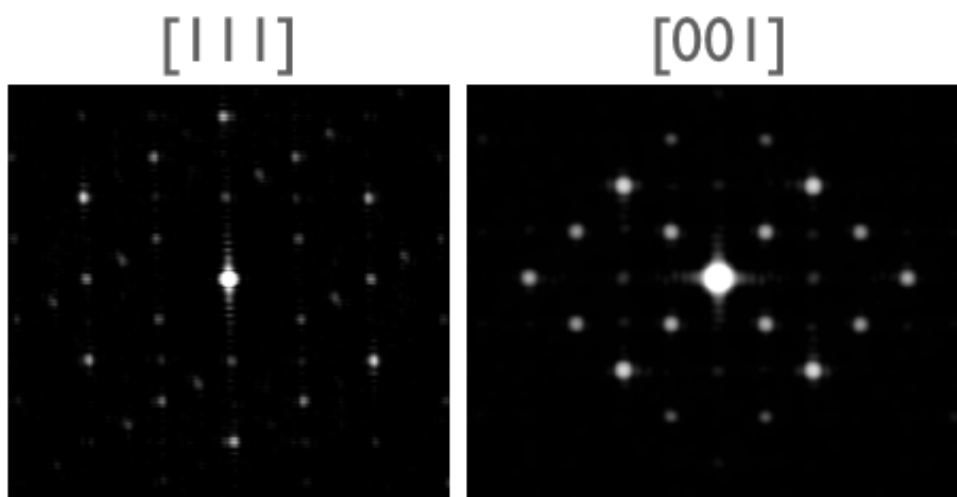


Figure 7.17: Predicted TEM of MALI from randomly sampled MD at 330K

A TEM SADP has been predicted for MALI and shows some indications of net tilting in the z direction in the [111] zone axis (Fig 7.17) which is supported by the PALAMEDES Phase output (Table 7.5). The numbers from PALAMEDES show that the angles of tilt in MALI are different in multiple directions suggesting that distortion of the octahedra and dodecahedra play an important role in the structure of the material. This is to be expected due to the organic A-site having the ability to rotate freely especially at higher temperatures. In the [001] direction there seems to be no indication of super-reflections supporting the phase tilt analysis. Subsequent analysis is needed to tell whether the rotation of the organic A-site is what influences this tilt behaviour.

4.9 Conclusions

We can successfully simulate time averaged XRD spectra and TEM diffraction patterns of perovskites. The TEM diffraction patterns for CT include the correct super reflections. These patterns include temperature averaging effects eliminating the need for calculation of thermal ellipsoids in XRD simulation. This averaged structure

includes thermal information which allows the TEM pattern to be simulated for both short and long exposure, unlike idealised patterns.

The PALAMEDES code is capable of determining the angles of tilting including averages, minimums and maximums, and correlating this to tilt phase. This gives us a form of notation analogous to glazer notation. For the prototype systems CT and BT this matches glazer notation. We can predict TEM patterns for MALI, which up until now have not been shown experimentally.

Sampling of MD data is key for recreating spectra that is similar to those from experiment as sequential sampling can oversample the trajectory. 20% random sampling of total frames for a large system was deemed to be appropriate.

The created spectra could be used as a metric by which to test existing and future forcefields. Indexing currently has to be done by hand for simulated TEM and XRD patterns, as Crystal Maker indexes all mathematically possible reflections, not just the strong reflections which are the ones comparable to experimental signal.

4.10 References

Aoyagi, S., Kuroiwa, Y., Sawada, A., Yamashita, I. and Atake, T. (2002) 'Composite Structure of BaTiO₃ Nanoparticle Investigated by SR X-Ray Diffraction', 71(5), pp. 1218–1221. doi: 10.1143/JPSJ.71.1218.

Auffinger, P., Masquida, B. and Westhof, E. (2002) 'Structural and Dynamical Characterization of Nucleic Acid Water and Ion Binding Sites', in Schlick, T. and Gan, H. H. (eds) *Computational Methods for Macromolecules: Challenges and Applications*. Berlin, Heidelberg: Springer Berlin Heidelberg, pp. 61–70.

Beanland, R. (2011) 'Structure of planar defects in tilted perovskites', *Acta Crystallographica Section A*, 67(3), pp. 191–199. doi: 10.1107/S0108767311002042.

Bragg, W. (1913) 'The Diffraction of Short Electromagnetic Waves by a Crystal', in *Proceedings of the Cambridge Philosophical Society*, pp. 43–57.

CrystalMaker Software Ltd (2018) 'CrystalMaker'. Oxford, United Kingdom.

- Dawson, J. A. (2012) 'Atomistic Simulation of Electroceramics', (December).
- Fultz, B. (Brent) (2008) *Transmission electron microscopy and diffractometry of materials*. 3rd ed. Edited by J. M. Howe. Berlin: Berlin : Springer, c2008.
- Glazer, A. M. (1972) 'The classification of tilted octahedra in perovskites', *Acta Crystallographica Section B*, 28(11), pp. 3384–3392. doi: 10.1107/S0567740872007976.
- Glazer, A. M. (1975) 'Simple ways of determining perovskite structures', *Acta Crystallographica Section A*. International Union of Crystallography (IUCr), 31(6), pp. 756–762. doi: 10.1107/S0567739475001635.
- Goldschmidt, V. (1926) 'Die Gesetze der Krystallochemie', *Naturwissenschaften*. Berlin/Heidelberg, 14(21), pp. 477–485. doi: 10.1007/BF01507527.
- Handley, C. M. and Freeman, C. L. (2017) 'A new potential for methylammonium lead iodide', *Physical Chemistry Chemical Physics*, 19(3), pp. 2313–2321. doi: 10.1039/C6CP05829A.
- Howard, C. J. and Stokes, H. (1998) 'Group-theoretical analysis of octahedral tilting in perovskites', *Acta Crystallogr. Sect. B-Struct. Sci.*, 54, pp. 782–789.
- Merz, W. J. (1949) 'The Electric and Optical Behavior of BaTiO_3 Single-Domain Crystals', *Physical Review*. American Physical Society, 76(8), pp. 1221–1225. doi: 10.1103/PhysRev.76.1221.
- Momma, K. and Izumi, F. (2011) 'VESTA 3 for three-dimensional visualization of crystal, volumetric and morphology data', *J. Appl. Crystallogr.*, 44, pp. 1272–1276. doi: 10.1107/S0021889811038970.
- Reaney, I. M. and Uvic, R. (1999) 'Dielectric and structural characteristics of perovskites and related materials as a function of tolerance factor', *Ferroelectrics*. Taylor & Francis, 228(1), pp. 23–38. doi: 10.1080/00150199908226123.

Rietveld, H. M. (1969) 'A profile refinement method for nuclear and magnetic structures', *Journal of Applied Crystallography*, 2(2), pp. 65–71. doi: 10.1107/S0021889869006558.

Van Santen, J. H. and Jonker, G. H. (1947) 'Effect of Temperature on the Permittivity of Barium Titanate', *Nature*. Nature Publishing Group, 159, p. 333.

Soller, W. (1924) 'A New Precision X-ray Spectrometer', *Phys. Rev. American Physical Society*, 24(2), pp. 158–167. doi: 10.1103/PhysRev.24.158.

Todorov, I. T., Smith, W., Trachenko, K. and Dove, M. T. (2006) 'DL_POLY_3: New dimensions in molecular dynamics simulations via massive parallelism', *Journal of Materials Chemistry*, 16(20), pp. 1911–1918. doi: 10.1039/b517931a.

Woodward, D. I. and Reaney, I. M. (2005) 'Electron diffraction of tilted perovskites', *Acta Crystallographica Section B: Structural Science*. International Union of Crystallography, 61(4), pp. 387–399. doi: 10.1107/S0108768105015521.

Yashima, M. and Ali, R. (2009) 'Structural phase transition and octahedral tilting in the calcium titanate perovskite CaTiO_3 ', *Solid State Ionics*. Elsevier B.V., 180(2–3), pp. 120–126. doi: 10.1016/j.ssi.2008.11.019.

5 Rare Earth Doping of Barium Titanate

5.1 Introduction

As discussed in §1, BaTiO₃ has a high relative permittivity at room temperature making it ideal for achieving large volumetric efficiencies in capacitor applications (Haertling, 1999). In dielectric applications, the movement of oxygen ions and therefore oxygen vacancies in the bulk ceramic is believed to be crucial in determining the mechanisms by which the capacitors fail (Waser, Baiatu and Härdtl, 1989). The movement and build up at interfaces of charged species can lead to short circuits and electrical break down. Preventing oxygen vacancy creation and movement is therefore key to extending the lifetime of BaTiO₃ in capacitor applications. Ceramic BaTiO₃ both contains intrinsic oxygen vacancies due to cation vacancies (Yoo, Song and Lee, 2002) and reduces readily at its interfaces with electrodes leading to the production of a small concentration of oxygen vacancies that can migrate into the solid (Jida and Miki, 1996). In capacitors with dielectric ceramic layers a few microns thick, it is crucial that movement of these vacancies is controlled as the distance they must migrate to reach an electrode and begin to build up is very small.

Oxygen diffusion in BaTiO₃ has been extensively studied experimentally both in undoped single crystals (Kessel, De Souza and Martin, 2015) and polycrystals (Müller and Härdtl, 1989) giving activation energies ranging from 0.5 to 1.28 eV (Maier, Schwitzgebel and Hagemann, 1985; Müller and Härdtl, 1989; Kessel, De Souza and Martin, 2015). Simulation studies using both density functional theory (Erhart and Albe, 2007) and atomistic techniques using both static and dynamic (Islam, 2002; Uberuaga and Vernon, 2013; Zulueta *et al.*, 2016) methods have been used to look at the migration pathway, the activation energies and the diffusion constants of oxygen vacancy migration in many perovskites.

For MLCC applications, BaTiO₃ is frequently doped with trivalent rare earth (RE) ions to improve its electrical properties (Sakabe *et al.*, 2002) as discussed in §1. The incorporation of these RE ions affects the microstructure of the ceramic, producing core-shell grain structures that can be used to improve the temperature dependence of capacitance for MLCCs (Kishi *et al.*, 1997) as well as their electrical stability. It has been shown experimentally that doping with mid-size (0.9-0.94 Å (Shannon, 1976)) trivalent

RE ions leads to improved lifetimes of MLCCs with Dy³⁺ giving large improvements (Itoh *et al.*, 2002; Sakabe *et al.*, 2002; Kishi, Mizuno and Chazono, 2003; Hahn, Sohn and Han, 2009). These RE dopants have also been experimentally linked to decreased oxygen migration in BaTiO₃. It is still unclear why Dy³⁺ is the best ion for large stability improvements.

Simulations of RE doping of BaTiO₃ using atomistic techniques (Freeman *et al.*, 2011) have reported that large RE ions substitute primarily on the A-site in BaTiO₃ and small RE ions predominantly on the B-site, while mid-sized RE ions are observed to dope on both sites in self compensation. The influence of both divalent and trivalent dopant ions on oxygen migration has also been studied in SrTiO₃ revealing that the influence of dopants on oxygen vacancies extends into the surrounding lattice further than the two lattice sites (Schie, Waser and De Souza, 2014). All the trivalent ions investigated can strongly trap oxygen vacancies in SrTiO₃ when doped solely on the B-site.

The effect of RE ions has also been simulated in materials for fuel cell applications, including ceria (Wang, Chroneos and Schwingenschlogl, 2013) where the ionic radius of the RE was shown to be key in determining the activation energy of oxygen vacancies. Quantum mechanical methods have been utilised to look at the interaction of REs and the movement of oxygen vacancies in BaTiO₃ but this has been limited to looking at only the closest lattice sites to individual dopants. Trapping of oxygen vacancies in BaTiO₃ was shown to be more effective with B-site only dopants due to the -1 charge on the RE attracting the positive charge of the vacancy (Honda *et al.*, 2011). Here we use static lattice simulation techniques to present a study of midsize RE ions in the BaTiO₃ lattice to understand how ions such as dysprosium, gadolinium and yttrium trap oxygen vacancies and investigate how effective they are over increasing distances. Static lattice calculations can only give information about the thermodynamics of the simulation scenarios. For kinetic information about the system, other simulation techniques such as molecular dynamics must be used.

5.2 Forcefield Details

The potential set used for barium titanate in all calculations was that of Freeman *et al.* (2011) (Table 5.1- 5.3). RE potentials for Gd and Y from Lewis and Catlow (Lewis and Catlow, 1985) (Table 5.4). These forcefields were shown to be compatible in the paper

of Freeman *et al* (2011) The Dy potential was fitted as part of this work as no Dy³⁺ - O²⁻ interaction was found in the literature. It was fitted to match the trends seen in the Lewis and Catlow set of potentials, as well as structural information from literature. It gives a good match to these criteria.

Table 5.1: Barium titanate forcefield Freeman *et al* (2011) Two-body potentials

Buckingham Potentials $A \exp(-\rho/r) - C/r^6$

Interacting ions		A (eV)	ρ (Å)	C (eV Å ⁶)
Ba	O	1150.0	038037	55.0
O	O	22764	0.149	43.0
Lennard-Jones 7-6 Potential $(E_0 \left[\left(\frac{R_0}{r}\right)^7 - 2 \left(\frac{R_0}{r}\right)^6 \right])$				
Interacting Ions		E ₀ (eV)	R ₀ (Å)	
Ti	O	0.01234	4.719	

Table 5.2: Barium titanate forcefield Freeman *et al* (2011) Three-body potentials

Three Body Potential $\frac{1}{2}k_2(\theta_0 - \theta)^2$

Species			k_2 (eV)	θ_0 (°)	Cutoffs(Å)		
O	Ti	O	1.82	90	2.5	2.5	3.5

Table 5.3: Barium titanate forcefield Freeman *et al* (2011) Cores and Shells

Cores and Shells

Species	Core Charge (e)	Shell Charge (e)	Spring Constant (eV Å ⁻²)
Ba	+3.45	-1.45	56.23
Ti	+4.00	-	-
O	+0.472	-2.472	15.41

Table 5.4: Rare Earth Potentials (Lewis and Catlow, 1985) Two-body potentials

Buckingham Potentials $A \exp(-\rho/r) - C/r^6$

Interacting ions		A (eV)	ρ (Å)	C (eV Å ⁶)
Y	O	1345.1	0.3491	0.0
Gd	O	1366.8	0.3551	0.0

5.2.1 Fitting the Dy - O Potential

The Dy - O interaction Buckingham potential was fitted in-house to the published Dy₂O₃ structure (Antic *et al.*, 1993). The forcefield was fitted iteratively to match the lattice parameters found in the literature and to ensure consistency with RE³⁺ potentials published by Lewis and Catlow (Lewis and Catlow, 1985)(Table 5.5). The A and ρ values fit within the trends of the RE³⁺ values published. There was no reliable materials properties information to compare to.

Table 5.5: Dysprosium potential fitted for this work.

Buckingham Potential $A \exp(-\rho/r) - C/r^6$				
Interacting ions		A (eV)	ρ (Å)	C (eV Å ⁶)
Dy	O	1346.05	0.3527	0.0

5.3 Rare Earth Doping Schemes

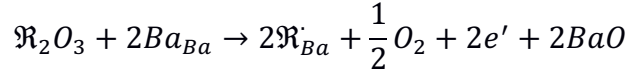
5.3.1 Introduction

When doping an ionic solid, maintaining charge neutrality is key for both solving the Ewald summation and for representing a real crystal system. As such, simply substituting an ion with another of different charge is not possible. Doping schemes are the methods by which charge neutrality can be maintained whilst making substitutions within the lattice. These can take the form of a combination of any of the defect type discussed in §3 The possible and likely defect configurations for REs in barium titanate have already been theorised (Buscaglia *et al.*, 2001; Freeman *et al.*, 2011).

5.3.2 Doping Schemes

In this work, four possible defect compensation schemes for trivalent rare earths in barium titanate as published by Buscaglia *et al.*(2001) plus the fifth from Freeman *et al.* (2011) were simulated for Y, Gd and Dy dopants. Experimental values for oxygen dissociation and liberation of electrons from titanium ion were used (Haynes *et al.*, 2016).

Scheme 1. Electronic compensation:



$$E_s = \frac{1}{2} \left[2E_{sub,Ba}^{\mathfrak{R}^{3+}} + 2E_{sub}^{Ti^{3+}} + 2E^{e^-} - \frac{1}{2}D_{O_2} + 2E_A^{O^{2-}} + 2E_L^{BaO} - 2E_L^{\mathfrak{R}_2O_3} \right]$$

Scheme 2. Substitution of RE^{3+} at Ba^{2+} with Ti^{4+} vacancy compensation:



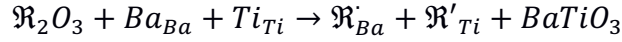
$$E_s = \frac{1}{4} \left[4E_{sub,Ba}^{\mathfrak{R}^{3+}} + E_{vac}^{Ti^{4+}} + E_L^{BaTiO_3} + 3E_L^{BaO} - 2E_L^{\mathfrak{R}_2O_3} \right]$$

Scheme 3. Substitution of RE^{3+} at Ti^{4+} with O^{2-} vacancy compensation:



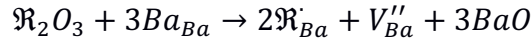
$$E_s = \frac{1}{2} \left[2E_{sub,Ti}^{\mathfrak{R}^{3+}} + E_{vac}^{O^{2-}} + E_L^{TiO_2} - E_L^{\mathfrak{R}_2O_3} \right]$$

Scheme 4. Substitution of RE^{3+} at Ba^{2+} and RE^{3+} at Ti^{4+} leading to self-compensation:



$$E_s = \frac{1}{2} \left[E_{sub,Ba}^{\mathfrak{R}^{3+}} + E_{sub,Ti}^{\mathfrak{R}^{3+}} + 2E_L^{BaTiO_3} - E_L^{\mathfrak{R}_2O_3} \right]$$

Scheme 5. Substitution of RE^{3+} at Ba^{2+} with Ba^{2+} vacancy compensation:



$$E_s = \frac{1}{2} \left[2E_{sub,Ba}^{\mathfrak{R}^{3+}} + E_{vac}^{Ba^{2+}} + 3E_L^{BaO} - E_L^{\mathfrak{R}_2O_3} \right]$$

5.4 Defect Energies in Barium Titanate

5.4.1 Calculation Details

All static simulations were carried out using the GULP code (General Utility Lattice Program) Version 4.2 (Gale, 1992). The cut off distance used in all cases was 12Å. The Ba and O ions were treated using the Dick and Overhauser (1958) shell model to include electronic polarisation effects. Static lattice defect simulations were carried out

using the Mott-Littleton method (1938). The region diameters used in all Mott-Littleton calculations were 21Å for region I and 33Å for the inner part of region II. These were the converged region diameters for the largest of all the defect complexes, or Mott-Littleton clusters.

The formation energies (E_f) of the dissociated defect energies for each compensation scheme were calculated from the values of individual defects simulated. All defects in each scheme were also simulated within a M-L to calculate the final solution energy (E_s) or associated energy of each compensation scheme. The preferred arrangements of the defects were taken from Dawson (2012). The binding energy (E_b) is calculated as the energy gained by having the defects in the scheme located adjacent (associated) to each other.

5.4.2 Hess Cycles

The Hess Cycle for Dy_2O_3 and Y_2O_3 were calculated to compare the lattice energies calculated by Freeman *et al* (2011). All lattice energies were comparable with those in the published literature. These values are necessary for calculating defect energies.

5.4.2.1 Dy_2O_3

The Hess Cycle for Dy_2O_3 using the new Dy - O Potential was calculated as follows:

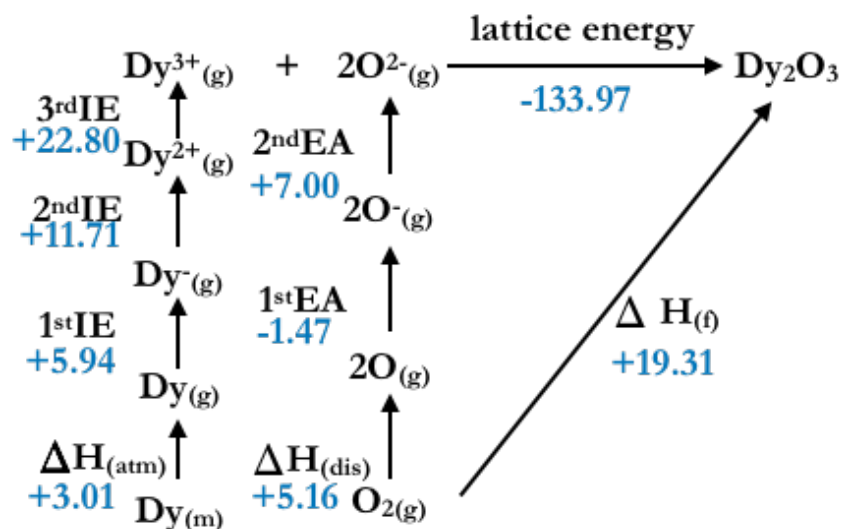


Figure 5.1: Figure showing the calculated Born-Haber cycle for Dy_2O_3 . All energy values shown are in eV.

5.4.2.2 Y_2O_3

The Hess Cycle for Y_2O_3 using the Y - O Potential (Lewis and Catlow, 1985):

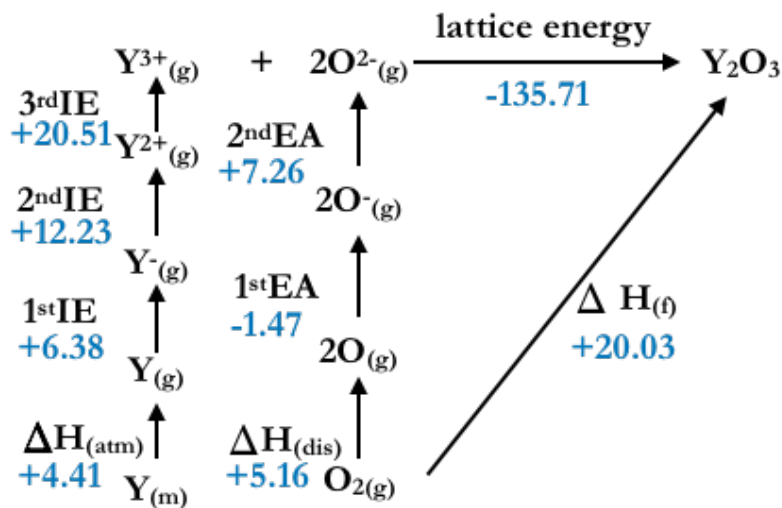


Figure 5.2: Figure showing the calculated Born -cycle for Y_2O_3 . All energy values shown are in eV.

Table 5.6: Table of calculated crystal lattice energies and second oxygen affinities for Y, Gd and Dy, Gd taken from Freeman *et al*(2011).

Rare Earth	Ionic radius (\AA)	Lattice Energy (eV)	2 nd Oxygen Affinity (eV)
Y	0.9	-135.713	7.26
Dy	0.913	-133.967	7.00
Gd	0.938	-133.068	7.23

5.4.3 Defect Energies

Table 5.7: Energy of formation for individual defects doping rare earths into BaTiO₃ (dilute limit) calculated here for Y and Dy, Gd taken from Freeman *et al*(2011).

Defect	Energy of formation (E_f) (eV)		
	Ba	Ti	O
Vacancy	19.50	98.96	24.65
Ti³⁺	-	43.24	-
Y	-25.75	51.96	-
Dy	-25.17	53.09	-
Gd	-24.83	53.72	-

Table 5.8: Energy of solution (Dissociated defect energy) for rare earth compensation in BaTiO₃ (dilute limit).

Rare earth	Ionic radius (Å)	Energy of solution (E_s) (eV)				
		RE _{Ba} + e ⁻	RE _{Ba} + V _{Ti}	RE _{Ti} + V _O	RE _{Ba} + RE _{Ti}	RE _{Ba} + V _{Ba}
Y	0.9	10.59	2.40	4.50	0.95	2.99
Dy	0.913	10.43	2.11	4.76	0.93	2.67
Gd	0.938	10.209	2.00	4.94	0.97	2.58

Table 5.9. Binding energy for isolated rare earth defects in BaTiO₃ (negative sign denotes binding)

Rare earth	Ionic radius (Å)	Binding Energy (E_b) (eV)				
		RE _{Ba} + e ⁻	RE _{Ba} + V _{Ti}	RE _{Ti} + V _O	RE _{Ba} + RE _{Ti}	RE _{Ba} + V _{Ba}
Y	0.9	-6.11	-0.18	-3.47	-0.07	-0.25
Dy	0.913	-2.29	-0.19	-3.58	-0.06	-0.83
Gd	0.938	-3.62	-0.14	-3.63	-0.06	-0.25

Table 5.10: Final solution energy (Associated defect energy) for rare earth compensation mechanisms into BaTiO₃

Rare earths	Ionic radius (Å)	Final Solution Energy (E_{fs}) (eV)				
		RE _{Ba} + e ⁻	RE _{Ba} + V _{Ti}	RE _{Ti} + V _O	RE _{Ba} + RE _{Ti}	RE _{Ba} + V _{Ba}
Y	0.9	4.48	2.21	1.03	0.88	2.73
Dy	0.913	7.91	1.92	1.18	0.87	1.85
Gd	0.938	6.59	1.86	1.32	0.9	2.3

The binding, solution and formation energies follow the trends set out in Freeman *et al* (2011) due to the same potential set being used. The fitted Dy - O potential closely follows the trends seen in Freeman *et al* (2011) which agree with experiments (Makovec, Samardžija and Drogenik, 2005; Mizuno *et al.*, 2007) which show that mid-size rare earths can dope both on the A and B-site with some preference to dope in a self-compensatory manner and also a preference to dope on the B-site with associated oxygen vacancies.

For Gd, Y and Dy the two energetically most favourable defect configurations are the substitution of RE³⁺ at the Ti⁴⁺ site with O²⁻ vacancy compensation and substitution of RE³⁺ at both the Ti⁴⁺ site and the Ba²⁺ site leading to self-compensation. The \mathfrak{R}'_{Ti} substitutions bind to the $V_{O}^{\bullet\bullet}$ vacancy to create a tightly bound $V_{O}^{\bullet\bullet}$ defect held between two \mathfrak{R}'_{Ti} substitutions. This linear arrangement of charges (Fig 5.3) and high binding energies (Table 5.9) makes it unlikely that \mathfrak{R}'_{Ti} defects will be able to trap extra, intrinsic $V_{O}^{\bullet\bullet}$ (Fig 5.3).

The associated \mathfrak{R}'_{Ba} - \mathfrak{R}'_{Ti} self-compensating pair has a positive \mathfrak{R}'_{Ba} situated diagonally from the \mathfrak{R}'_{Ti} (Fig 5.3). The negatively charged RE doped B-site can attract a positively charged migrating $V_{O}^{\bullet\bullet}$. As the binding energies of the RE doped AB pairs for the ionic radii investigated are quite small (Table 5.9) both lone and associated \mathfrak{R}'_{Ba} and \mathfrak{R}'_{Ti} are expected to be present in the bulk material in the self-compensation case. The lone \mathfrak{R}'_{Ti} defects should be the most effective at trapping the migrating $V_{O}^{\bullet\bullet}$ due to the high

colombic attraction between the oppositely charged species. Conversely a lone $\mathfrak{R}_{Ba}^{\cdot}$ defect will repel a migrating $V_{O}^{\cdot\cdot}$ due to the like charges and therefore was not studied in this thesis. The other three possible doping schemes $4\mathfrak{R}_{Ba}^{\cdot}$ and $V_{Ti}^{\cdot\cdot\cdot}$, $2\mathfrak{R}_{Ba}^{\cdot}$ and $V_{Ba}^{\cdot\cdot}$ and electronic compensation are increasingly less likely to occur in the lattice due to their large solution energies. All three are also less likely to trap oxygen vacancies due to their preferred geometrical arrangement in the lattice and the charge distributions present (Fig 5.3). $4\mathfrak{R}_{Ba}^{\cdot}$ and $V_{Ti}^{\cdot\cdot\cdot}$ may be the exception to this rule due to the titanium vacancy which is likely to attract $V_{O}^{\cdot\cdot}$. However, the geometrical arrangement of $4\mathfrak{R}_{Ba}^{\cdot}$ in a ring above a $V_{Ti}^{\cdot\cdot\cdot}$ would repel $V_{O}^{\cdot\cdot}$ from one side of the defect complex whilst attracting them from the other side.

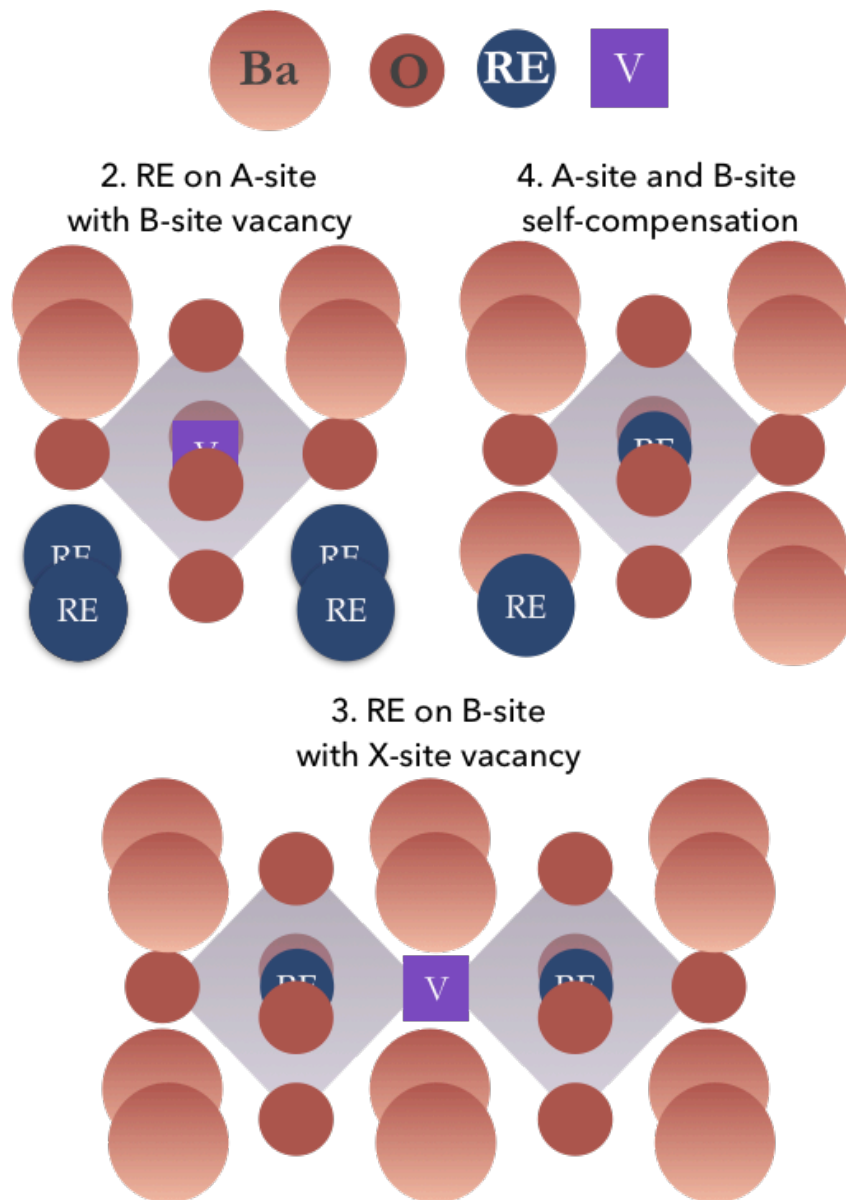


Figure 5.3: Associated defect complex spatial arrangements for compensation schemes 2, 3 and 4.

5.5 Defect Populations in Barium Titanate

5.5.1 Calculation Details

The likelihood that each RE ion investigated will exhibit a given compensation mechanism at equilibrium over a range of temperatures was calculated using statistical mechanics (5.1).

$$P_i(i) = \exp(-E_i(i)/k_B T) / \sum_j \exp(-E_i(j)/k_B T) \quad (5.1)$$

$P_i(i)$ is the probability of a specific defect compensation scheme, i , occurring given that the rare earths are included in the lattice $E_i(i)$ is the energy calculated for the formation of the defect compensation scheme, $E_i(j)$ is the total energy of all the defect schemes, being either E_s for associated defects or E_d for disassociated defects; k_B is the Boltzmann constant and T is the temperature in Kelvin. Both the associated and dissociated defect compensation scheme energies were included in the calculation so show the likelihood of associated schemes as well as dissociated schemes.

5.5.2 Defect Populations

Equation (5.1) was used to calculate the probability of each dopant exhibiting the different compensation schemes both associated and dissociated across the device operation and sintering temperature range (Figure 5.4, a-c).

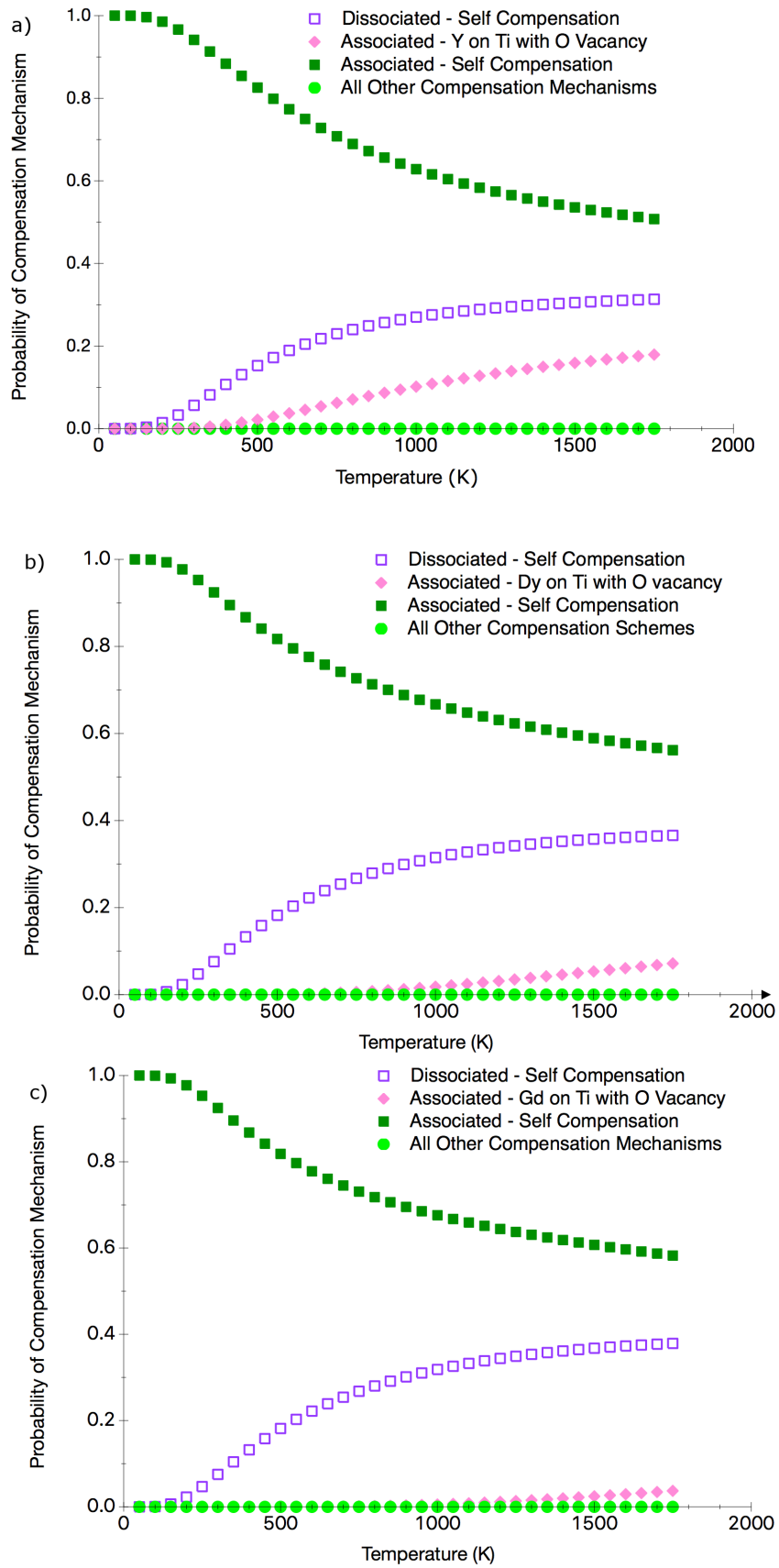


Figure 5.4: Probabilities of type of defect concentration in BaTiO₃ at equilibrium versus temperature in the range 0-1750K for a) Y, b) Dy and c) Gd.

5.5.3 Discussion

Y, Dy and Gd will primarily dope in a self-compensatory manner in the temperature regime achieved during sintering (up to $\sim 1750\text{K}$). This compares well with experiment (Makovec, Samardžija and Drogenik, 2005; Mizuno *et al.*, 2007). For the values of the ionic radii investigated (0.9-0.938 Å), all dopants exhibit associated and dissociated $\mathfrak{R}_{Ba}^{\cdot}$ and \mathfrak{R}'_{Ti} defects as well as \mathfrak{R}'_{Ti} defects compensated by V_{O}^{\cdot} at high temperatures. As the ionic radii increase from Y through to Gd, the affinity for doping on the titanium site decreases. The probability of seeing both associated and dissociated pairs for all rare earths investigated is high due to the very low binding energy of this scheme. The defects corresponding to each compensation scheme can exist separately within the bulk ceramic if charge neutrality is maintained. They can also associate with each other to minimize their overall energy.

5.6 Oxygen Self-diffusion in Barium Titanate

5.6.1 Calculation Details

Saddle points for an oxygen ion moving between vacant lattice sites were calculated using the rational functional optimization method (RFO) in GULP (see §3). NEB was not used as when NEB in DL_POLY Classic was utilised barrier heights of $\sim 8\text{eV}$ were calculated. This massive discrepancy is likely to be due to the fact that the DL-POLY algorithm does not allow the shells in each replica to relax resulting in inflated energy barriers. Unlike lowest pathway searches such as nudged elastic band methods, in the RFO calculation only a single saddle point may be found at a time with no pathway information obtained. RFO uses an uphill search method to identify the point at which only one eigenvalue of the hessian matrix is negative and thus a saddle point. In the oxygen ion self-diffusion case; one O^{2-} ion and one vacancy were used. The ion starting location was chosen close to the half way point between ion sites, avoiding the crystal symmetry (Fig 5.5). Due to the large barrier heights seen in the NEB the RFO calculation was carried out using varying spring constants to see the effect the shell model has on the barrier height. The calculation was carried out using oxygen shell spring values, k , ranging from 15.41 to 24.21 eV Å⁻². A calculation with no shells was also carried out.

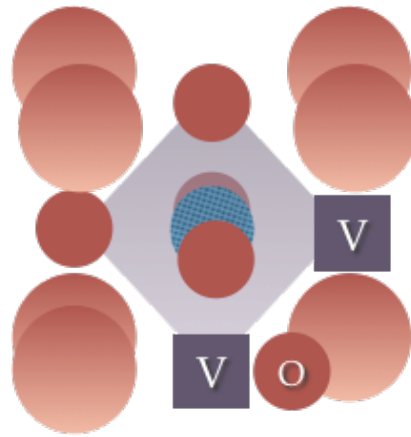


Figure 5.5: Starting configuration for Oxygen Diffusion Scenario in RFO.

5.6.2 Results and Discussion

The barrier to migration for an oxygen vacancy in a pure BT lattice was calculated to be 0.84 eV for the spring value $15.41 \text{ eV } \text{\AA}^{-2}$ (Table 5.11). This compares well with the recent literature value (Kessel, De Souza and Martin, 2015) $0.70 \pm 0.04 \text{ eV}$ for single crystal BT where the difference in value can be attributed to the fact that the energy calculated is an internal energy and that measured in experiment is an enthalpy (Harding, 1990). However, simulation without or with limited polarisation included via the shell model drastically affected the migration barrier calculated increasing it from 0.84 at the fitted spring value to 3.44 when no springs were used. This shows why models that account for polarisation are especially important for ionic solids with very polarisable ions such as oxygen in them.

Table 5.11: Oxygen migration barriers for varied shell springs k

Spring (k)	Barrier (eV)
15.41	0.84
16.21	0.93895684
16.61	0.90015323
17.01	0.87392079
24.21	1.33364228
∞	3.44

Self-diffusion RFO calculations were also tried for Barium and Titanium diffusion to try and compare the values to available experimental values for self-diffusion, however the calculations did not resolve. The Oxygen simulation case took a week to complete as a serial job. The cation diffusion calculations ran for 40 days and did not resolve. This is likely to be due to the limitations of the RFO method (see §3). The start point must be very carefully chosen, and for cation self-diffusion this is nearly always on a symmetry line, which prevents the calculation from successfully being carried out or too far away from the saddle point to resolve.

5.7 Oxygen Vacancies around Rare Earth Dopants

5.7.1 Calculation Details

The effect of A and B site self-compensatory rare earth pairs on the migration of oxygen vacancies in the lattice was further investigated as they were the most energetically favourable for all the REs investigated and lone B-site dopants are theoretically most likely to trap oxygen vacancies. The energy of a single oxygen vacancy at the 60 nearest neighbouring oxygen lattice sites surrounding RE dopants was simulated using GULP (Gale, 1992) and Mott-Littleton calculations (1938). Two scenarios were investigated: an oxygen vacancy around a RE-doped self-compensatory associated pair and an oxygen vacancy around a lone RE doped on a B-site. These scenarios were used to map the potential energy surface for oxygen vacancies near RE dopants. An oxygen vacancy around a lone RE doped on a A-site was not investigated due to the repulsion that would be felt between a 2- charged oxygen vacancy and the 1+charged rare earth dopant.

5.7.2 Results and Discussion

The associated $\mathfrak{R}_{Ba}^i\text{-}\mathfrak{R}'_{Ti}$ pair may offer the greatest chance of trapping intrinsic $V_O^{\bullet\bullet}$ due to the ability of the exposed negative \mathfrak{R}'_{Ti} to attract a positive $V_O^{\bullet\bullet}$. However, a lone \mathfrak{R}'_{Ti} may be better at trapping $V_O^{\bullet\bullet}$ as it can attract the vacancies from all directions. Here both the associated $\mathfrak{R}_{Ba}^i\text{-}\mathfrak{R}'_{Ti}$ pair and dissociated substitutional rare earth defects (lone \mathfrak{R}'_{Ti} defects) were further investigated as the binding energies are so low. The energy of

an oxygen vacancy in the 60 nearest neighbour oxygen sites to the dopants was mapped in 3D space (Figure 5.6, a-d). As can clearly be seen, the oxygen vacancy landscape surrounding the lone \mathfrak{R}'_{Ti} is symmetrical (Figure 5.6, a, c). This is to be expected due to the octahedral point group symmetry of the lone dopant. Each concentric shell of the oxygen lattice sites exhibits energies that decrease in magnitude away from the dopant i.e. the position of the oxygen vacancy is less favourable the further it is from the rare-earth defect. This is to be expected due to the octahedral point group symmetry of the lone dopant. The first shell of oxygen lattice sites has an energy of -3.44 to -3.56 eV from Y to Gd showing that a lone \mathfrak{R}'_{Ti} tightly binds an oxygen vacancy.

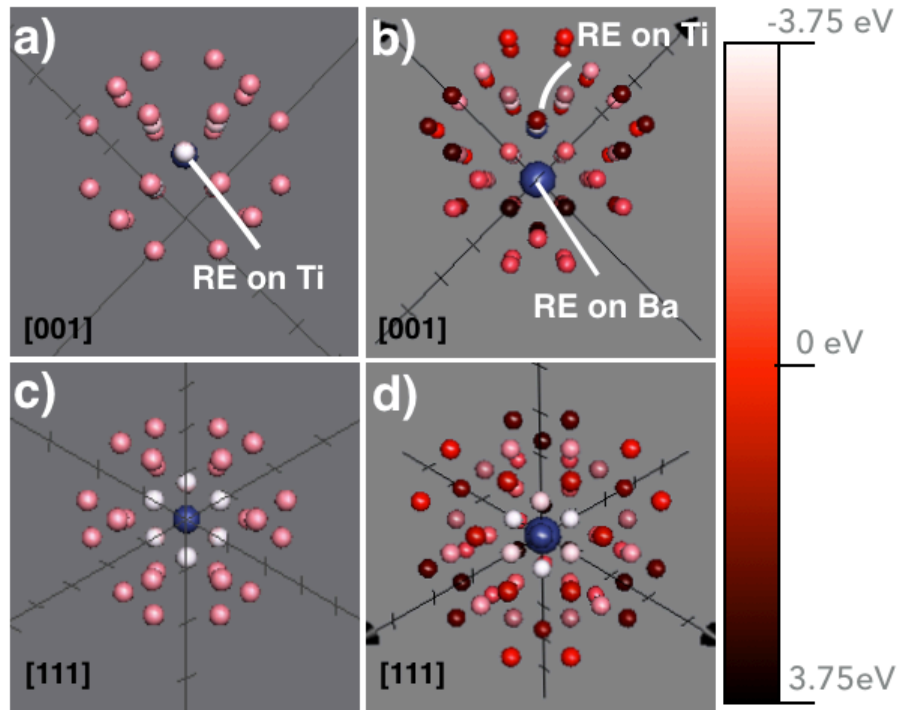


Figure 5.6: A plot of the binding energies of an oxygen vacancy in nearest neighbour lattice sites compared to defects at infinite separation, view direction (UVW) is shown. The colors of the lattice sites correspond to the energy of the position per the right-hand scale bar. a, c) A lone Dy (Blue) doped on the B-site; b, d) a Dy pair (Blue) doped on both an A and B site. The values for Gd and Y were calculated and were very similar. The trends remained the same.

In the case of the $\mathfrak{R}'_{Ba}-\mathfrak{R}'_{Ti}$ pair (Figure 5.6 b, d), the V_O landscape is asymmetric. The most favourable positions are in the perpendicular plane bisecting the $\mathfrak{R}'_{Ba}-\mathfrak{R}'_{Ti}$ pair with energies for Y-Gd from -3.54 to -3.60 eV. This low energy is unexpected because

the positive charge created by the \mathfrak{R}_{Ba} might be expected to repel the positive $V_{\ddot{O}}$. The next most favourable sites for $V_{\ddot{O}}$ are the three remaining sites in the \mathfrak{R}'_{Ti} coordination shell. The binding energies for these sites range from -3.13 to -3.23 eV with RE of increasing radii. The 18 most favourable sites are either in-between the dopants or on the \mathfrak{R}'_{Ti} side of the cluster. After these there are favourable sites on the \mathfrak{R}_{Ba} side of the cluster, suggesting that there may be migration paths that can trap $V_{\ddot{O}}$ approaching from any direction. In all cases, only a small energy difference is observed between the trapping ability of different RE ions. The maps (Figures 5.7 a-d) show that RE dopants, whether lone \mathfrak{R}'_{Ti} or \mathfrak{R}_{Ba} - \mathfrak{R}'_{Ti} pairs, can interact with vacancies in the lattice up to four sites away. This explains why RE dopants are effective in low amounts. Assuming perfect mixing and an even distribution, ~ 3 at% of RE dopants could influence all the lattice sites in a barium titanate ceramic. The values for Gd and Y were calculated and were very similar. The trends remained the same.

5.8 Oxygen Diffusion around Rare Earth Dopants

5.8.1 Calculation Details

Based on the mapped oxygen vacancy potential energy surfaces, a migration path for an oxygen vacancy moving away from the defects was investigated. The path was picked using the lowest energy chain of oxygen vacancy sites away from the dopants. This was then investigated using saddle point searches to find the energy barriers to oxygen vacancy migration along this chain to assess the ability of RE dopants to trap intrinsic oxygen vacancies. Saddle points for an oxygen ion moving between vacant lattice sites were calculated using the rational functional optimization method. The difference in energy between a vacancy at a specific site and the saddle point is calculated. This is the $V_{\ddot{O}}$ migration barrier.

5.8.2 Results and Discussion

Lattice site and saddle point energies for a single trajectory moving away from the dopants were plotted for both the lone B-site dopant case and the AB doped associated pair case. The trends shown for dopant pathways involving only the B-site are similar to

those shown for transition metal ions doped in SrTiO₃ (Schie, Waser and De Souza, 2014). However, the magnitude of the trapping energies is much smaller $\sim 0.5\text{eV}$. Similarly, these results also show that dopant ions influence the lattice many sites away. In both scenarios, the oxide vacancies at lattice sites 1 and 2 (Fig 5.7a, b) in the coordination shells of the REs are energetically favoured compared to dopants at infinite separation, due to the coulombic attraction between the defects.

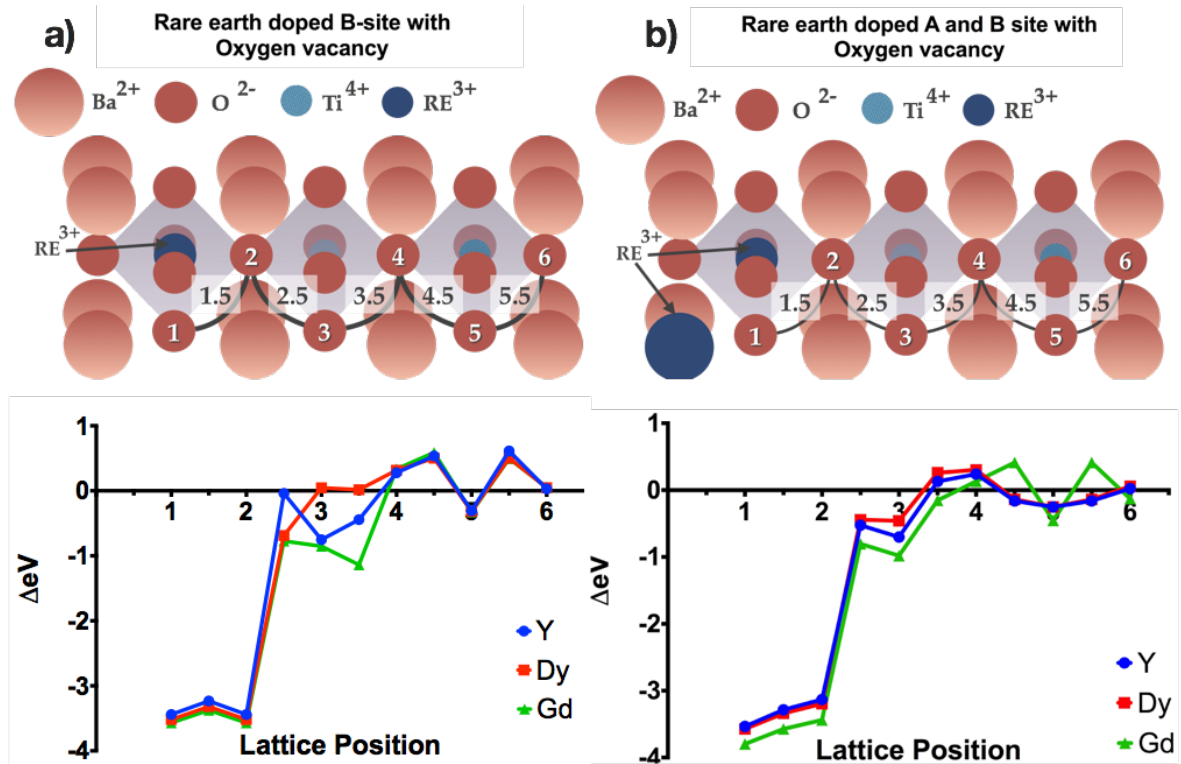


Figure 5.7: Schematics of the simulations carried out and graph showing the change in energy compared to defects at infinite separation. Vacancy lattice sites investigated are integers 1-6 and saddle points investigated are decimals 1.5-5.5. a) A lone RE-doped B-site in an unassociated AB pair and b) an A and B doped associated RE pair.

In the lone \mathcal{R}'_{Ti} case, sites 1 and 2 are equally favourable with a trapping energy of -3.44 eV (Y) to -3.56 eV (Gd) and a small barrier to migration of between 0.19 and 0.21 eV between the sites. There is a much greater barrier to moving the vacancy further away, from site 2 to 3 ranging from 2.79 to 3.40 eV. This is expected, due to the large coulombic attraction between the negative \mathcal{R}'_{Ti} and the positive V_O making it difficult for the vacancy to escape from the dopant. Conversely going from site 3 to 2 towards the RE the barrier to migration is small or non-existent. The largest migration barrier is 0.71 eV in the case of Dy, highlighting how attractive the dopants can be to oxygen

vacancies. In the RE associated pair case (Figure 5.5b) the $V_{\text{O}}^{\ddot{}}$ will bind to both the $\mathfrak{R}_{\text{Ba}}^{\dot{}}$ and $\mathfrak{R}'_{\text{Ti}}$ when it is located on position 1. There is a large trapping energy of -3.53 to -3.59 eV. This binding is stronger than that for position 1 for the isolated $\mathfrak{R}'_{\text{Ti}}$ defect. The lower energy at $V_{\text{O}}^{\ddot{}}$ position 1 for the RE pair scenario (Fig 5.5b) is unexpected as it was assumed that the positively charged $\mathfrak{R}_{\text{Ba}}^{\dot{}}$ defect would repel the positively charged $V_{\text{O}}^{\ddot{}}$ and therefore would bind less strongly than the lone $\mathfrak{R}'_{\text{Ti}}$ case. Some of the saddle points found are not at a higher energy than the two nearest lattice sites. This is possible as RFO calculations do not necessarily find the highest saddle point along the simulation pathway, they just find a saddle point. This makes it difficult to find the ‘correct’ saddle point. These results were included for completeness. These calculations take 40+ days on a single core (and cannot be parallelised yet). The method for possible parallelisation is discussed in the GULP manual (Gale, 1992).

Overall it is clear (Fig 5.7a, b) that all REs investigated have similar energetics when trapping oxygen vacancies in both doping scenarios despite the different ionic radii. It is likely, therefore that the ability of REs to diffuse through the lattice and become well dispersed (as well as their preferred compensation scheme) will be key to explaining why some REs give greater stability improvements in barium titanate MLCCs.

To explain why a $V_{\text{O}}^{\ddot{}}$ binding to a $\mathfrak{R}_{\text{Ba}}^{\dot{}}$ - $\mathfrak{R}'_{\text{Ti}}$ pair is energetically more favourable than binding to a single dissociated $\mathfrak{R}'_{\text{Ti}}$, the structure of the surrounding lattice was studied. Interatomic distances were calculated and analysed. When the oxygen vacancy is located in between the $\mathfrak{R}_{\text{Ba}}^{\dot{}}$ - $\mathfrak{R}'_{\text{Ti}}$ pair, the remaining oxygens in the perpendicular bisecting plane relax diagonally inwards towards each other due to the reduction in coulombic repulsion because of the presence of the vacancy. They move away from the B-site by $\sim 0.1 \text{ \AA}$ and towards the A-site by $\sim 0.4 \text{ \AA}$ (Fig 5.8a). The reduced charge screening between the doped RE pair due to the $V_{\text{O}}^{\ddot{}}$ and the inward relaxation of the remaining oxygens results in the two RE substitutional ions moving diagonally away from each other (Fig 5.8b). These combined movements also push the two oxygens in the plane of the $\mathfrak{R}_{\text{Ba}}^{\dot{}}$ away from the $\mathfrak{R}_{\text{Ba}}^{\dot{}}$ dopant, increasing the interatomic distance by $\sim 0.1 \text{ \AA}$ each (Fig 5.6c). This is the $\mathfrak{R}_{\text{Ba}}^{\dot{}}$ attempting to reduce its coordination due to the smaller ion size of the dopant (0.9 \AA compared to 1.4 \AA for Ba).

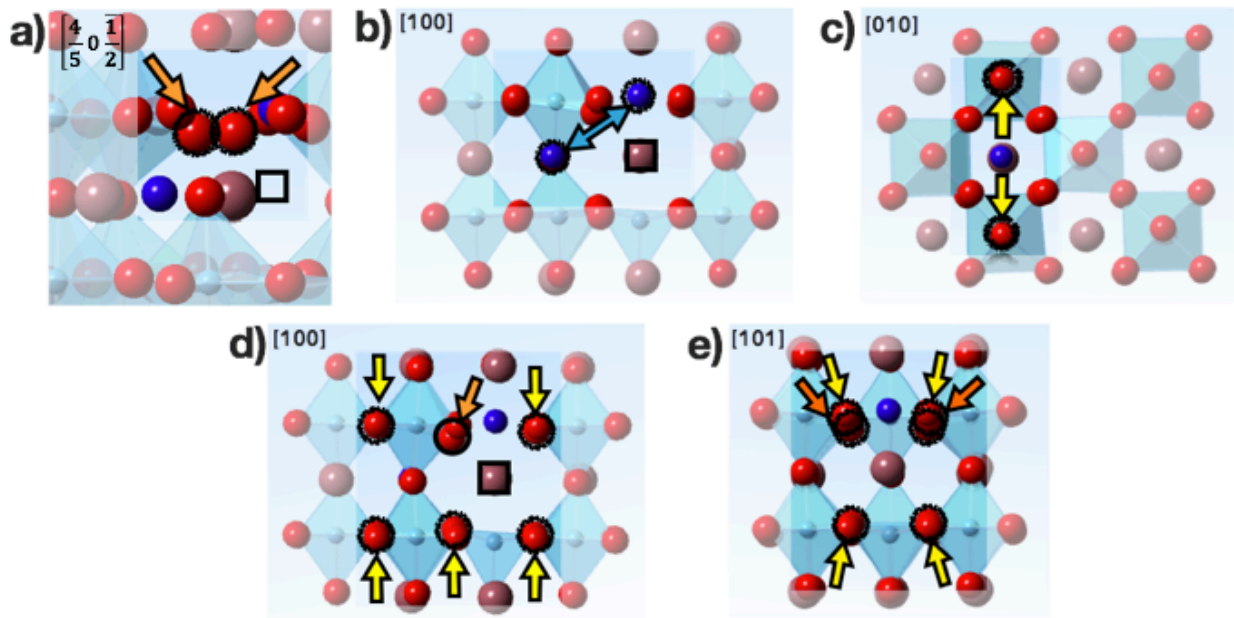


Figure 5.8: Images showing BaTiO_3 lattice surrounding an RE doped AB pair (blue coloured) with an oxygen vacancy shown as a black square. Oxygen vacancies in the plane bisecting the two rare earths (orange), other oxygen movements (yellow). Crystallographic view directions $[UVW]$ are indicated. a) shows the movement of the remaining nearest oxygens diagonally inwards in orange. b) highlights in blue the movement of the \mathfrak{R}_{Ba} and the \mathfrak{R}'_{Ti} diagonally away from each other. c) shows the movements in yellow of the oxygens in the plane of the \mathfrak{R}_{Ba} where the Ba – O distance increases. d) and e) shows in yellow the movement of the other oxygens surrounding the dopants in relation to the oxygens between the dopants in orange.

Other relaxations include the oxygens in the dopant coordination shells located above and below the V_{O} . These relax out of plane towards the vacancy both vertically (Fig 5.6d) and horizontally (Fig 5.6e). The oxygens in the perpendicular plane bisecting the dopants move the furthest. The relaxations involving all ion types extend into the surrounding lattice and stabilise the defect complex by allowing the \mathfrak{R}_{Ba} to partially reduce its coordination from twelve on the standard Ba site to eleven. The presence of the V_{O} does not, therefore, cause large repulsions between the RE pair due to the presence of these large relaxations. This can account for the ability of the associated

$\mathcal{R}_{Ba} - \mathcal{R}'_{Ti}$ pair to trap intrinsic oxide vacancies more strongly at close quarters than lone \mathcal{R}'_{Ti} dopants.

5.9 Conclusions

It is evident that, despite the differences in their ionic radii, mid-size RE ions (0.9-0.95 Å) can all trap oxygen vacancies with similar energetics when doped in the self-compensatory manner. RE dopants affect oxygen vacancies up to four lattice sites away, illustrating why they are effective in small amounts. At close quarters, AB associated pairs are the most energetically favourable mechanism for trapping oxygen vacancies due to the large lattice relaxations that occur around the defect cluster. The differences in performance between REs observed experimentally are likely to be partly due to the preference of the RE to dope in a self-compensatory manner and therefore gain the ability trap oxygen vacancies. If the formation of self-compensated defects alone mattered, ionic radius arguments would suggest that Gd should give the greatest stability improvements. However, experiment shows that the greatest improvement is given by Dy. Therefore, the ability of the different rare earths to diffuse through the lattice and achieve wide distribution during processing is also likely to be significant for performance gains in MLCCs. Further investigation of RE diffusion in barium titanate will be addressed in §7 of this thesis. As the migration barriers calculated in this chapter are quite high even for the oxygen vacancy migration ($\sim 0.8\text{eV}$), traditional methods for calculating kinetic diffusion information such as mean squared displacement in molecular dynamics will not be sufficient. Advanced sampling methods will be needed; the theory and methodology behind these techniques are discussed in §6.

5.10 References

Antic, B., Oennerud, P., Rodic, D. and Tellgren, R. (1993) ‘The structure characteristics of the diluted magnetic semiconductor $\text{Y}_{2-x}\text{Dy}_x\text{O}_3$ ’, *Powder Diffraction*, 8, pp. 216–220.

Buscaglia, M. T., Buscaglia, V., Viviani, M. and Nanni, P. (2001) ‘Atomistic Simulation of Dopant Incorporation in Barium Titanate’, *Journal of the American Ceramic Society*, 84(2), pp. 376–84. doi: 10.1111/j.1151-2916.2001.tb00665.x

Dawson, J. A. (2012) *Atomistic Simulation of Electroceramics*. University of Sheffield.

- Dick, B. G. and Overhauser, A. W. (1958) ‘Theory of the dielectric constants of alkali halide crystals’, *Physical Review*, 122(1950), pp. 90–103. doi: <http://dx.doi.org/10.1103/PhysRev.112.90>.
- Erhart, P. and Albe, K. (2007) ‘Thermodynamics of mono- and di-vacancies in barium titanate’, *J. Appl. Phys.*, 102(8). doi: 10.1063/1.2801011.
- Freeman, C. L., Dawson, J. a., Chen, H.-R., Harding, J. H., Ben, L.-B. and Sinclair, D. C. (2011) ‘A new potential model for barium titanate and its implications for rare-earth doping’, *Journal of Materials Chemistry*, 21(13), p. 4861. doi: 10.1039/c0jm04058d.
- Gale, J. (1992) ‘GULP (General Utility Lattice Program)’, *Royal Institution, London*.
- Haertling, G. H. (1999) ‘Ferroelectric ceramics: History and technology’, *Journal of the American Ceramic Society*, 82(4), pp. 797–818. doi: 10.1111/j.1151-2916.1999.tb01840.x.
- Hahn, D., Sohn, S. B. and Han, Y. (2009) ‘Effects of Rare-Earth Oxides on Time-Dependent Dielectric Properties of Mn-Doped BaTiO₃’, *Jpn. J. Appl. Phys.*, 48(3). doi: 10.1143/JJAP.48.031404.
- Harding, J. H. (1990) ‘Computer simulation of defects in ionic solids’, *Reports on Progress in Physics*, pp. 1403–1466. doi: 10.1088/0034-4885/53/11/002.
- Haynes, W. M., Lide, D. R., Bruno, T. J. and Haynes, W. M. (William M. . (2016) *CRC handbook of chemistry and physics : a ready-reference book of chemical and physical data*. 97th editi, *Handbook of chemistry and physics*. 97th editi. Boca Raton: Boca Raton : CRC Press, 2016.
- Honda, A., Higai, S., Motoyoshi, Y., Wada, N. and Takagi, H. (2011) ‘Theoretical study on interactions between oxygen vacancy and doped rare-earth elements in barium titanate’, *Japanese Journal of Applied Physics*, 50(9 PART 3), pp. 1–5. doi: 10.1143/JJAP.50.09NE01.
- Islam, M. S. (2002) ‘Computer modelling of defects and transport in perovskite oxides’,

Solid State Ionics, 154–155, pp. 75–85. doi: 10.1016/S0167-2738(02)00466-6.

Itoh, J.-I., Park, D.-C., Ohashi, N., Sakaguchi, I., Yashima, I., Haneda, H. and Tanaka, J. (2002) ‘Oxygen Diffusion and Defect Chemistry in Rare-Earth-Doped BaTiO₃’, *Nihon Seramikusu Kyokai Gakujutsu Ronbunshi*. Tokyo, 110(1281), p. 495. doi: 10.2109/jcersj.110.495.

Jida, S. and Miki, T. (1996) ‘Electron paramagnetic resonance of Nb-doped BaTiO₃ ceramics with positive temperature coefficient of resistivity’, *J. Appl. Phys.*, 80(9), pp. 5234–5239. doi: 10.1063/1.363509.

Kessel, M., De Souza, R. a. and Martin, M. (2015) ‘Oxygen diffusion in single crystal barium titanate’, *Phys. Chem. Chem. Phys.* Royal Society of Chemistry, 17(19), pp. 12587–12597. doi: 10.1039/C5CP01187F.

Kishi, H., Mizuno, Y. and Chazono, H. (2003) ‘Base-Metal Electrode-Multilayer Ceramic Capacitors: Past, Present and Future Perspectives’, *Japanese Journal of Applied Physics*, 42(Part 1, No. 1), pp. 1–15. doi: 10.1143/JJAP.42.1.

Kishi, H., Okino, Y., Honda, M., Iguchi, Y., Imaeda, M., Takahashi, Y., Ohsato, H. and Okuda, T. (1997) ‘The effect of MgO and rare-earth oxide on formation behavior of core-shell structure in BaTiO₃’, *Jpn. J. Appl. Phys. Part 1 - Regul. Pap. Short Notes Rev. Pap.*, 36(9B), pp. 5954–5957.

Lewis, G. V and Catlow, C. R. a (1985) ‘Potential models for ionic oxides’, *Journal of Physics C: Solid State Physics*, 18(6), pp. 1149–1161. doi: 10.1088/0022-3719/18/6/010.

Maier, J., Schwitzgebel, G. and Hagemann, H.-J. (1985) ‘Electrochemical investigations of conductivity and chemical diffusion in pure and doped cubic SrTiO₃ and BaTiO₃’, *Journal of Solid State Chemistry*, 58(1), pp. 1–13. doi: 10.1016/0022-4596(85)90264-6.

Makovec, D., Samardžija, Z. and Drogenik, M. (2005) ‘Solid Solubility of Holmium, Yttrium, and Dysprosium in BaTiO₃’, *Journal of the American Ceramic Society*, 87(7), pp. 1324–1329. doi: 10.1111/j.1151-2916.2004.tb07729.x.

Mizuno, Y., Kishi, H., Ohnuma, K., Ishikawa, T. and Ohsato, H. (2007) 'Effect of site occupancies of rare earth ions on electrical properties in Ni-MLCC based on BaTiO₃', *Journal of the European Ceramic Society*, 27(13), pp. 4017–4020. doi: <https://doi.org/10.1016/j.jeurceramsoc.2007.02.089>.

Mott, N. F. and Littleton, M. J. (1938) 'Conduction in polar crystals. I. Electrolytic conduction in solid salts', *Transactions of the Faraday Society*, 34, pp. 485–499. doi: [10.1039/TF9383400485](https://doi.org/10.1039/TF9383400485).

Müller, A. and Härdtl, K. (1989) 'Ambipolar diffusion phenomena in BaTiO₃ and SrTiO₃', *Materials Science and Processing*. Berlin/Heidelberg, 49(1), pp. 75–82. doi: [10.1007/BF00615468](https://doi.org/10.1007/BF00615468).

Sakabe, Y., Hamaji, Y., Sano, H. and Wada, N. (2002) 'Effects of rare-earth oxides on the reliability of X7R dielectrics', *Jpn. J. Appl. Phys. Part 1 - Regul. Pap. Short Notes Rev. Pap.*, 41(9), pp. 5668–5673. doi: [10.1143/JJAP.41.5668](https://doi.org/10.1143/JJAP.41.5668).

Schie, M., Waser, R. and De Souza, R. a. (2014) 'A simulation study of oxygen-vacancy behavior in strontium titanate: Beyond nearest-neighbor interactions', *Journal of Physical Chemistry C*, 118(28), pp. 15185–15192. doi: [10.1021/jp504436t](https://doi.org/10.1021/jp504436t).

Shannon, R. D. (1976) 'Revised effective ionic radii and systematic studies of interatomic distances in halides and chalcogenides', *Acta Crystallographica Section A*. 5 Abbey Square, Chester, Cheshire CH1 2HU, England, 32(5), pp. 751–767. doi: [10.1107/S0567739476001551](https://doi.org/10.1107/S0567739476001551).

Uberuaga, B. P. and Vernon, L. J. (2013) 'Interstitial and vacancy mediated transport mechanisms in perovskites: A comparison of chemistry and potentials', *Solid State Ionics*. Elsevier B.V., 253, pp. 18–26. doi: [10.1016/j.ssi.2013.08.022](https://doi.org/10.1016/j.ssi.2013.08.022).

Wang, H., Chronos, A. and Schwingenschlogl, U. (2013) 'Impact of doping on the ionic conductivity of ceria: A comprehensive model', *Journal of Chemical Physics*, 138(22). doi: [10.1063/1.4809986](https://doi.org/10.1063/1.4809986).

Waser, R., Baiatu, T. and Härdtl, K. H. (1989) 'Degradation of dielectric ceramics', *Materials Science and Engineering: A*. Elsevier, 109, pp. 171–182. doi: 10.1016/0921-5093(89)90583-2.

Yoo, H.-I., Song, C.-R. and Lee, D.-K. (2002) 'BaTiO₃-[delta]: Defect Structure, Electrical Conductivity, Chemical Diffusivity, Thermoelectric Power, and Oxygen Nonstoichiometry', *Journal of Electroceramics*. Dordrecht, 8(1), pp. 5–36. doi: 10.1023/A:1015570717935.

Zulueta, Y. A., Dawson, J. A., Leyet, Y., Guerrero, F., Anglada-Rivera, J. and Nguyen, M. T. (2016) 'Influence of titanium and oxygen vacancies on the transport and conducting properties of barium titanate', *physica status solidi (b)*, 253(2), pp. 345–350. doi: 10.1002/pssb.201552366.

6 Enhanced Sampling Techniques in Molecular Dynamics

6.1 Introduction

Enhanced sampling techniques are key for looking at phenomena not normally accessed by traditional atomistic simulation techniques. This chapter introduces the theory behind enhanced sampling techniques and discusses the theory of metadynamics and umbrella sampling in depth with a brief discussion of steered molecular dynamics (MD). The development and practical application of these techniques in close packed crystals is further discussed in §7.

6.2 Why do we need enhanced sampling techniques?

MD as discussed in §3 is a powerful technique to simulate time dependent dynamic events using classical mechanics. MD is still, however, far from being able to efficiently simulate a full mole or more of a substance, or events that take more than microseconds to occur. There is a large difference between the length and timescales involved in physical processes such as diffusion, phase transitions and chemical reactions and the length and timescales accessible by standard MD simulations.

Currently MD can efficiently simulate hundreds of thousands of atoms for a short time, or a smaller number of atoms for a longer time. These simulations can fail to sample areas of the free energy surface during the simulation when the potential energy surface is rough, has high barriers that are greater than the thermal fluctuations in the system or multiple local minima (Gervasio, 2008). (Fig 6.1). Although a MD simulation may be perfectly equilibrated the likelihood of overcoming any large barriers during a normal simulation run time is extremely low unless extremely favourable conditions are found. Raising the temperature to see more events is also another approach that can be taken, however some forcefields become unstable at high temperatures and can produce unreliable results.

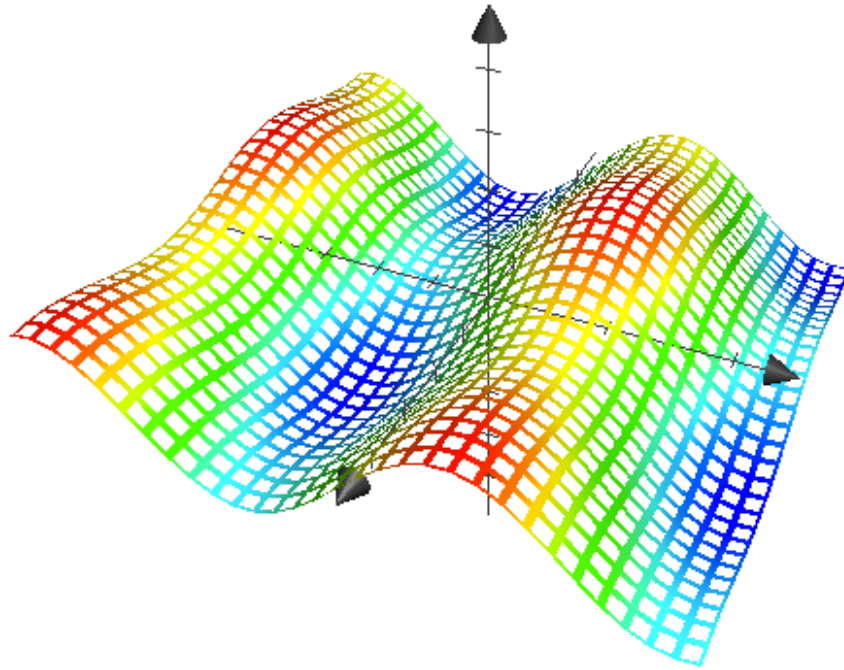


Figure 6.1: Example of a Complex Free Energy Surface.

In a ceramic such as barium titanate, a diffusive event with one charge carrier (an oxygen vacancy) may only be seen once in a 10ns simulation at low temperature. This is a problem when statistical mechanics methods require multiple samples of the same event to give reliable averages of the energies and trajectories involved. The reason for this low successful jump frequency is the high barrier to migration and the lack of charge carriers.

Multiple charge carriers within one simulation can be used to get more reliable statistics but, it is impossible to separate the energies of one hopping event from multiple events. This is because the charge carriers may be interacting with each other and the contributions to the energy or changes in the trajectories due to this interaction cannot be isolated.

An alternative option for simulating diffusive events is the Nudged Elastic Band (NEB) calculation as detailed in §3. However, as mentioned previously NEB methods require knowledge of the start and end states of a pathway as well as some knowledge of the pathway itself to ensure convergence. This is not possible for all scenarios. Other

methods such as saddle point searches §3 can also be used to look for transition states. This technique provides no information about the pathway itself and no guarantee that the smallest local saddle point is found.

To examine rare events in a system, enhanced sampling techniques can be used to overcome the limitations of standard MD. They do this by improving the sampling of MD simulations. Most of these techniques involve adding a bias to the simulation that in some way increases the probability that the event you are looking for occurs. The bias is then removed in post processing to reveal the unbiased pathways and energies involved. The accuracy to which you can remove the bias, and the reliability of the sampling achieved using an enhanced sampling method are the main limitations of any given technique.

There are many enhanced sampling methods that can be implemented to improve the statistics collected from MD each with its own advantages and disadvantages. In this work metadynamics, steered MD and umbrella sampling have been used to sample diffusion pathways in perovskite ceramics.

6.3 Metadynamics

6.3.1 Introduction

Metadynamics as proposed by Laio and Parrinello (2002) is an enhanced sampling technique likened to ‘filling in the free energy surface with computational sand’ (Fig 6.3). It works by progressively biasing an MD run during the simulation to force it to explore new areas of the free energy surface. It has been used with success in many biological and chemical applications including protein folding and docking (Bian *et al.*, 2015; Rather *et al.*, 2017) nucleation and crystallisation events (Quigley and Rodger, 2008a), and surface interactions between crystal surfaces and solute (Freeman, Harding and Duffy, 2008). The filling of the free energy surface FES by ‘computational sand’ is achieved by adding predefined bias, in the form of Gaussian functions (Eq 6.1) along mathematically defined degrees of freedom known as collective variables (Laio and Parrinello, 2002).

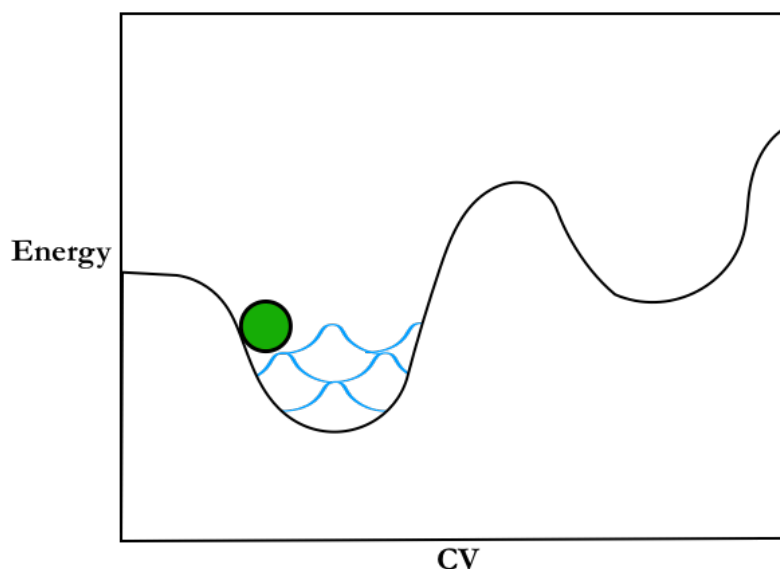


Figure 6.3: FES being filled up by Gaussian ‘sand’.

The collective variables chosen, limit the simulation to exploring the area of interest. The Gaussians are added at regular intervals throughout the simulation, gradually filling up the wells in the free energy surface, overcoming barriers and forcing the simulation to sample other configurations. This history dependent cumulative bias gives the simulation the ‘sampling memory’ it needs to ensure that the free energy surface is sampled more evenly.

$$S(x), t = W e^{-\frac{(S(x)-S(t'))^2}{2\delta s^2}} \quad (6.1)$$

Where $S(x), t$ is the Gaussian functions added as bias with height W , and width δs are used as the ‘metaphorical sand’ in metadynamics. The locations of added Gaussians, as a function of the collective variables used are recorded during the simulation. These locations $S_i(R(t'))$ are taken to be the central position at time t of the Gaussian added. The width of the Gaussian, δs , its height, W , and its deposition stride, τ_G , need to be fitted for each individual simulation scenario to ensure both convergence and efficiency. The rate of deposition of the Gaussians, ω , is given in Eq. 6.2. The cumulative bias V_G potential at time t is defined as a sum of the Gaussians added to the simulation given by Eq 6.3. The final total bias V_G is related to the free energy surface F by Eq 6.4.

$$\omega = \frac{W}{\tau_G} (6.2)$$

$$V_G(S(x), t) = W \sum_{\substack{t'=\tau_G, 2\tau_G, \dots \\ t' < t}} e^{\left(-\frac{(S(x)-S(t'))^2}{2\delta s^2}\right)} (6.3)$$

$$V_G(\vec{S}) = -F(\vec{s}) (6.4)$$

As the integral of a Gaussian is known to be the error function, the free energy surface explored in the simulation can be recovered in post processing easily by integrating the collective bias potential to reveal the underlying energy surface (Fig 6.4)

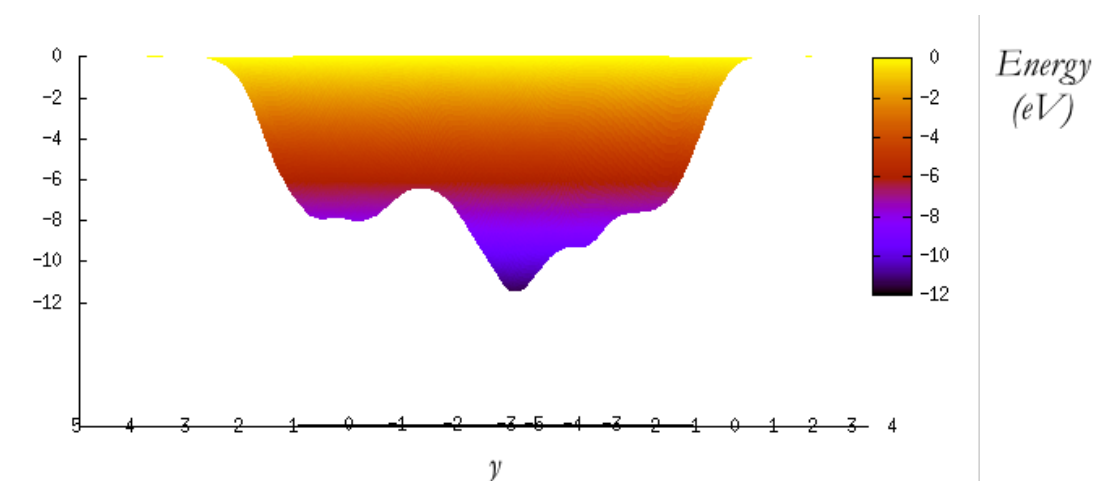


Figure 6.4: Example free energy surface revealed by integration as a function of two directional CVs and energy.

6.1.1 Collective Variables

Collective variables (CVs) are 3D mathematical functions that are used in metadynamics to restrict the degrees of freedom that the simulation can explore. These can be defined as anything, from the position of an atom or the centre of a group of atoms to the distance or angle between atoms. The choice of CVs is very important and needs to be appropriate for the system being explored. Having too many CVs can artificially restrict the area of the free energy surface being investigated whilst simultaneously increasing

the simulation expense. Too few CVs will explore too much of the free energy surface and might not reveal the specific physical process you are looking for.

The CVs for a specific simulation, as discussed by Quigley and Rodger (2008b), must be chosen so that the start and end state of the process you are investigating are clearly defined e.g. the products and reactants for a reaction simulation or the start and finish positions for a diffusive event. If CVs are poorly defined, these states may overlap, and it will not be possible to clearly observe the barrier height, the pathway or whether the reaction or rare event has occurred. The predominant CVs used in this work are CVs defining the absolute position (in terms of the x , y and z coordinates) of an ion that will diffuse.

These CVs are sufficient to describe diffusion in a ceramic lattice as they allow the diffusing atom to fully explore the lowest energy path of diffusion without predetermining the path or the end state. The width of the Gaussian used for each scenario is based upon the standard deviation of the CV in its start and end location. In this work this is the standard deviation of the vibrational amplitude of the diffusing atom in both its start and end lattice sites at equilibration. These CVs would be considered unsuitable in biological simulations, or simulations containing large amounts of solvent, as the atoms themselves can move around inside the simulation box freely thus the absolute position of the atoms can shift significantly throughout a simulation leading to the ‘sand’ being left behind. In the case of solid-state ceramics, the absolute position of an atom is an appropriate choice of CV, as in most cases, the atoms are closely packed and cannot move around very much limiting the range of motion and not allowing the Gaussians added to be left behind.

6.1.2 Advantages of Metadynamics

A significant advantage of metadynamics is that, unlike a rational functional optimisation both the energy and location of the barrier can be explored in one simulation, along with the shape of the diffusion pathway and any other saddle points. Metadynamics, unlike the nudged elastic band, does not require *a priori* knowledge of the system being investigated. However, some knowledge is useful when it comes to fitting the Gaussians. The required knowledge (such as the standard deviations of CVs) can be obtained from the equilibration MD run. When using metadynamics, the rate of sampling of rare events is increased, and multiple pathways can be found in a single

calculation. The 3D shape of a pathway can also be ascertained, unlike NEB and umbrella sampling where users tend to focus on a 2D pathway.

6.1.3 Convergence and Error in Metadynamics

Convergence in metadynamics is achieved by ensuring that the MD motion in the simulation is adiabatically separated from the addition of the bias potential. This often requires narrow and short Gaussians and a long deposition stride rate τ_G . If the MD motion is separated, the free energy surface recovered can be misleadingly narrow, and the barrier height is not statistically reliable (Fig 6.5).

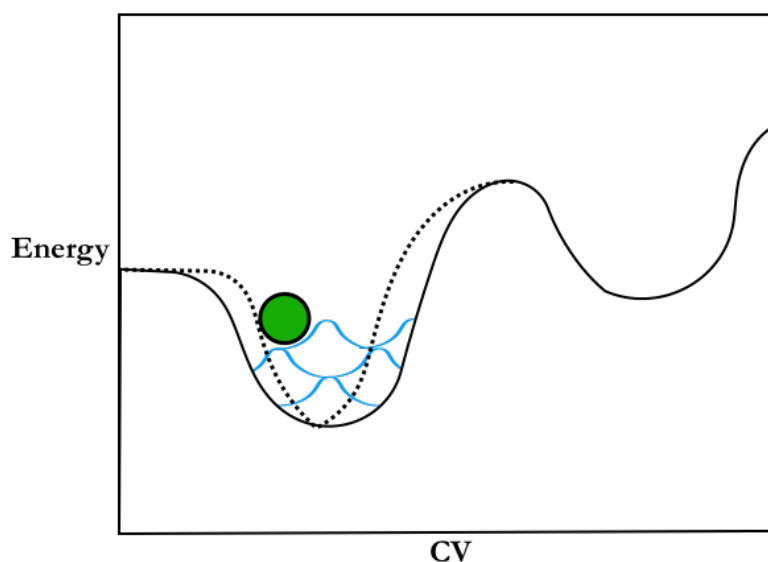


Figure 6.5 Misleadingly narrow MTD profile with real profile to compare.

The reason for the misleading recovered profile is that if the rate of deposition τ_G is too rapid, the MD motion is not conserved, and the system has not had enough time to relax back to an equilibrated state before the addition of a further Gaussian (Fig 6.5). As the position of the CV is used as the centroid of each Gaussian, this will make the recovered energy surface too narrow and can artificially alter the shape and size of the pathway. Conversely a very wide flat Gaussian with a long addition stride can also have misleading consequences as the Gaussian is so shallow that there is not enough driving force to make the system relax down to an equilibrated state in the time given (Fig 6.6a). Unnecessarily long choices of τ_G will also extend simulation time significantly and make calculations less efficient.

One limitation of metadynamics is that it can be prone to ‘over filling’ (Fig 6.6b). This happens when the height of the Gaussian being added artificially overfills the well it is in, meaning that the barrier is overcome at a much higher energy than that of the actual saddle point. One solution to this problem is well-tempered metadynamics. Well-tempered metadynamics is an adaptive bias version of metadynamics developed by Barducci, Bussi and Parrinello (2008). It works by scaling the height of the Gaussian being added by the length of time the simulation spends in the free energy well. This allows the well to be filled rapidly at first and then flattens the Gaussians as the top of the well is approached allowing the top of the well to be fully flattened out before the next well is found and avoiding the overestimation of barrier heights. This overcomes the ‘over filling’ problem in traditional metadynamics. The bias factor used to adapt the Gaussian must be fitted to ensure quick filling of the well followed by slow filling to the top of the well. However, this can add very small Gaussians in a normal metadynamics simulation which is an inefficient use of simulation time.

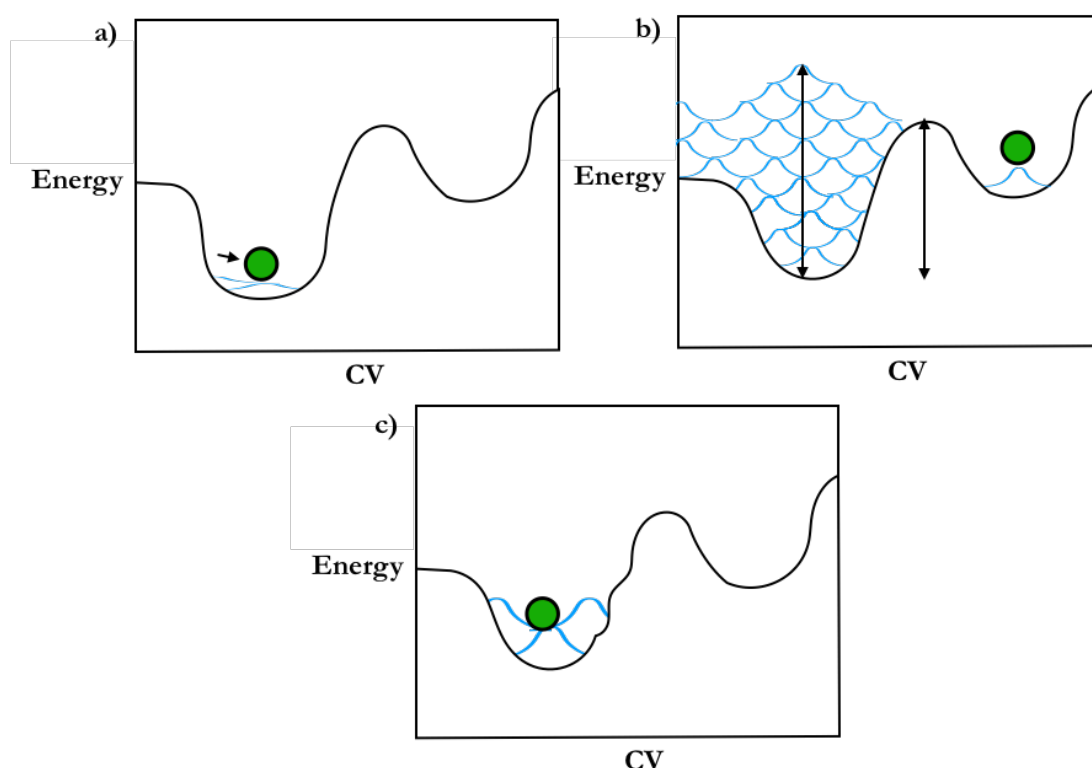


Figure 6.6: Problems with Gaussians, a) too short and wide gaussians, b) Gaussians overfilling, overestimating the barrier height, c) Too large Gaussians masking features of the potential energy well.

Sometimes metadynamics simulations can miss features of the potential energy well that they are filling up. This happens when the Gaussian used is too large and occurs because the bias is too big to see small features in the potential energy well (Fig 6.6c). When using force fields with shell models, it is also important to use a Gaussian that is not too tall and narrow. This can force the cores and shells too far apart, overcoming the core-shell cut-off distance. If this occurs the simulation will fail to relax the cores back onto the shells and cease to run. This can limit the size of Gaussians used in certain simulations and may extend the simulation time significantly as smaller Gaussians must be used.

Most of these issues can be overcome by properly fitting the Gaussians to be used in each system with given CVs. Laio *et al* (2005) showed that the error in metadynamics could be minimised with careful choice of simulation parameters. An explicit equation for the error ϵ in a metadynamics calculation was derived (Eq 6.5). As a function of Gaussian width W , diffusion constant D , the temperature $1/\beta$, the system size S , the Gaussian width δs , and the deposition stride τ_G and C is a dimensionless constant.

$$\bar{\epsilon} = C(d) \sqrt{\frac{S\delta s W}{D\tau_G \beta}} \quad (6.5)$$

This equation relies on some *a priori* knowledge of the system such as the diffusion coefficient D which can come from experiment or simulation. The constant although it may not be immediately known can be estimated after initial simulations are run to optimise the error and efficiency of further simulations. (Barducci, Bonomi and Parrinello, 2011) highlight the use of Equation 6.6 to discover the appropriate ratio between stride, height and deposition rate. Convergence can also be checked once the appropriate height and width of the Gaussians have been chosen, by gradually increasing the deposition rate until no difference in pathway shape and barrier height is observed.

Gervasio *et al* (2008) also showed that the ratio between the width of the Gaussians being used and the size of the region of the free energy space that is being investigated is the main limiting factor when it comes to error. The use of this equation (6.5) assists

in determining the maximum Gaussian width possible for a given system or region of free energy space being investigated. The error in metadynamics simulations, especially the barrier height, can be minimised by taking the average of several calculations of the same metadynamics event.

6.4 Umbrella Sampling

6.4.1 Introduction

Umbrella sampling, introduced by Torrie and Valleau (1977), adds an umbrella shaped bias potential to the overall potential energy Hamiltonian. The potential added is typically a harmonic potential, restraining the simulation harmonically to a region of interest in phase space (Eq. 6.7).

$$V(\vec{s}, t) = \frac{1}{2} \kappa(t) (\vec{s} - \vec{s}_0(t))^2 \quad (6.7)$$

where κ is the spring constant, \vec{s} is the location of the centre of the spring at time t . The information about the region explored is collected as a histogram of the probability of visiting configurations within the region, $P(x)$, during each run (Eq 6.8). The outputted histogram is of the biased probabilities of visiting each configuration given the restraining potential. For a simulation with harmonic potential $U'(x)$ the unbiased probability histogram $P(x)$ can be estimated from the collected histogram $A(x)$ using k_B the Boltzmann constant, T the temperature of the calculation in kelvin. F is an undetermined constant but is not important for an individual calculation. F is a constant and depends on the features of $U'(x)$ and therefore solving for F is the main problem to overcome when combining the outputs from multiple umbrella sampling runs. This is discussed in section §6.4.4.

$$A(x) = -k_B T \ln P'(x) - U'(x) + F \quad (6.8)$$

The simulation with the added umbrella potential is then repeated over many different overlapping areas of interest by moving the bias potential along the reaction (or diffusion pathway). The outputs of these simulations can then be recombined using

various techniques, including umbrella integration and the weighted histogram analysis method, to reveal the underlying free energy surface.

Umbrella sampling has advantages over traditional MD in that the added potential ensures sampling about a given region of interest. The addition of the ‘umbrella’ can allow the system to cross a high-energy barrier and visit more of the free energy surface (Fig 6.8). This encourages sampling of rare events. Much like metadynamics, careful selection of CVs is necessary to ensure that the region of interest on the free energy surface is properly explored.

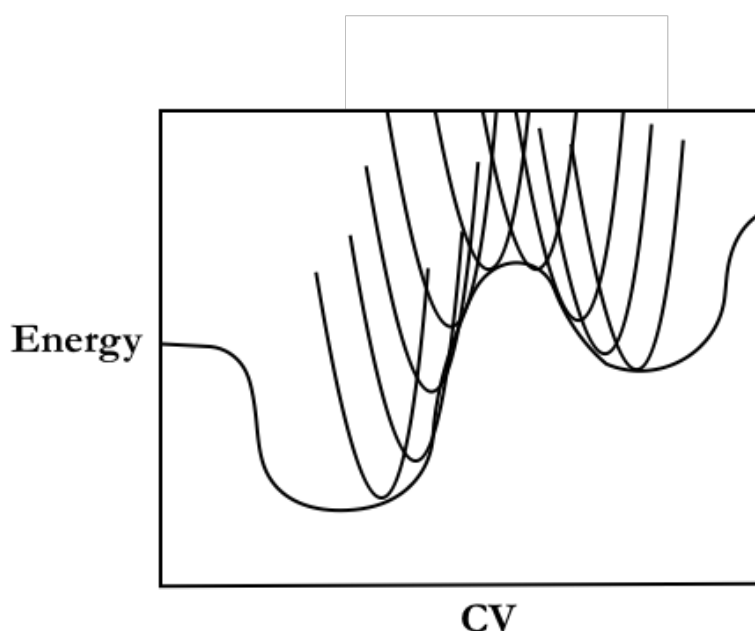


Figure 6.8: Schematic of multiple umbrella sampling runs bridging an energy barrier.

The histograms outputted from all the umbrella sampling runs for one scenario need to be combined and the bias removed to reveal the underlying free energy surface. One method for doing this is discussed in §6.4.4. Firstly, the CVs used and the fitting of the harmonic restraint potential will be discussed.

6.4.2 Collective Variables for Umbrella Sampling

In umbrella sampling, the CVs chosen for metadynamics can be used to ensure that the same specific region of interest in the simulation is investigated. In this work the same CVs were used in both the umbrella and metadynamics calculations. These were the absolute position of the ion being moved. A harmonic restraint was added to the CVs

to investigate the areas of interest for the umbrella sampling runs. The lowest energy pathway calculated from the metadynamics calculations were used to pick the regions of interest in which to perform the umbrella sampling. In this work, these were the bottom of the starting free energy well and the saddle point, needed to calculate a more accurate barrier height.

In practical applications, umbrella sampling can also be carried out as part of one continuous steered MD calculation which allows one calculation to be carried out instead of many. In this version of umbrella sampling the collective variables are steered with a specific force to reach certain values. The steering can be paused multiple times along the pathways to obtain the umbrella sampling for that location.

6.4.3 Fitting Harmonic Potentials

The harmonic potential (Eq. 6.7) used to restrain the umbrella sampling calculations needs to be fitted to ensure that the region of interest is fully examined. For a potential energy surface to be recovered, the umbrellas used to sample the system need to overlap. This is to ensure that the recovered histograms also overlap and can be used to produce an overall free energy surface without gaps. This becomes a challenge with especially steep or rough potential energy surfaces, as in regions with large gradient changes the umbrella sampling run is more likely to sample unequally in the direction of the greatest gradient (Fig 6.9). This is a problem around saddle points and requires the harmonic potential to be stiffer. To sample the same size area of a simulation the harmonic potential must be stiffer and so more simulations are required. This increases the overall cost and length of the simulation run.

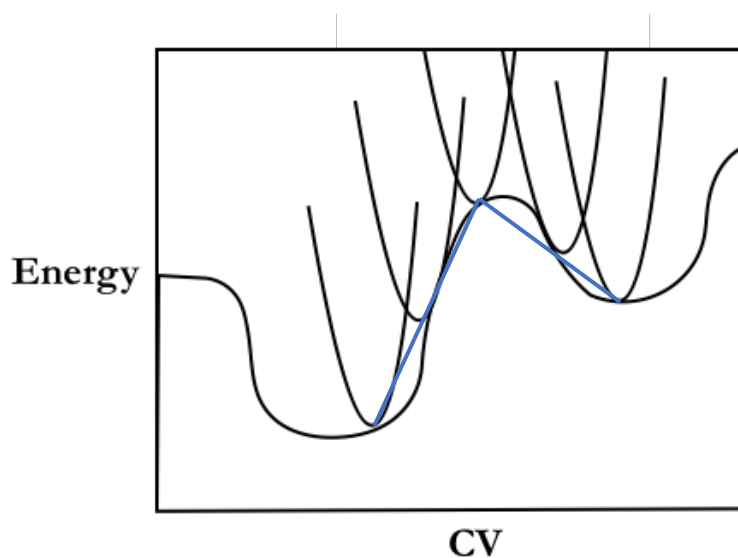


Figure 6.9: Umbrellas on a rough free energy surface not overlapping well. Would produce the free energy surface shown in blue

If examining the histograms of adjacent umbrellas shows that they do not share any visited configurations, then they do not overlap. The spring constant must then be progressively adjusted until the umbrellas do overlap over the area of the free energy surface of interest. If possible, this overlap is achieved at a known maximum such as a saddle point on the free energy surface. This allows the most appropriate spring constant to be chosen for the whole system. If nothing is known about the system before starting, an initial guess at the spring constant can also be used to investigate the entire region of the free energy surface being investigated before refining the spring constant and number of umbrellas used.

6.4.4 Analysing Umbrella Sampling

The free energy surface can be recovered from multiple umbrella sampling runs using various techniques including the weighted histogram analysis method (WHAM) and umbrella integration. In this work 2D WHAM is utilised to produce the free energy surface from the umbrella runs. WHAM was developed as an extension of the multiple histogram method invented by Ferrenberg and Swendsen (1989). It is an algorithm that reweights the histograms obtained from a group of umbrella sampling runs and combines them into a single histogram for the region of the system that has been

investigated. The method requires that the histograms overlap along the reaction pathway.

Each umbrella run produces a histogram; a probability distribution of the likelihood of each configuration visited during that run (Eq 6.9). As the undetermined constant F depends on the location of the centre of the harmonic potential $U'(x)$, it is not immediately obvious how to weight the individual histograms facilitating their combination. The WHAM algorithm combines the individual histograms by solving for the optimum values of F (Kumar *et al.*, 1992) It can be generalised for multiple temperature umbrella sampling and for multiple CV umbrella sampling (Grossfield, 2018). The WHAM equations (Eq. 6.9, 6.10) are used to solve for all F values - F_i and all probability distributions $P_i(x)$ iteratively until self-consistency is achieved.

$$P(x) = \frac{\sum_{i=1}^{N_{sims}} n_i(x)}{\sum_{i=1}^{N_{sims}} N_i \exp\left(\frac{F_i - U_{bias,i}(x)}{k_B T}\right)} \quad (6.9)$$

$$F_i = -k_B T \ln\left\{\sum_{x_{bins}} P(x) \exp\left(\frac{F_i - U_{bias,i}(x)}{k_B T}\right)\right\} \quad (6.10)$$

Where $P(x)$ is the best guess of the unbiased probability distribution, N_{sims} is the number of simulations $U_{bias,i}$ and F_i are biasing potential and free energy shift from simulation i , $n_i(x)$ is the number of counts in histogram bin x , F_i is an unknown.

6.4.5 Limitations of Umbrella Sampling

One of the main limitations of umbrella sampling is that, although the individual calculations are quick, the number of calculations needed to investigate a complete diffusion pathway can be large. This can be computationally expensive. Like Gaussian fitting for metadynamics, fitting the harmonic potential for umbrella sampling is also time-consuming and may require extensive prior knowledge of the system. The selection of CVs face the same limitations as those for metadynamics. Both umbrella sampling and WHAM assume in the derivations of the equations that either the NVT or NPT ensemble is used in the simulation. For WHAM one main limitation of the

technique is the correct selection of the bin size for the histogram. It needs to be small enough to ensure smooth histograms, but large enough to make sure the calculation is efficient.

6.5 Steered MD

Steered MD is a non-equilibrium technique used to force a system from an initial configuration to a final configuration using CVs. This ensures that the simulation produces configurations along a pathway that are often used for other calculations (e.g. umbrella sampling). The steering is done via an inputted force which moves a CV-centred harmonic potential from one value to another linearly over time. The force used, the time taken to move, and the spring potential can be fitted for a specific system. Jarzynski's equality (1997) is used to determine the harmonic restraint on the system Eq 6.11 and Eq 6.12 where W is work done, ΔF is the change in free energy between two states in the system, k_B is the Boltzmann constant and T is the temperature of the system.

$$\langle e^{\frac{-W}{k_B T}} \rangle = e^{\frac{\Delta F}{k_B T}} (6.11)$$

$$\langle W \rangle \geq \Delta F (6.12)$$

The work done to move the restraint is outputted. Averages from steered MD runs can be used to calculate barrier heights from the work done. Steered MD has been used to investigate biological systems, protein folding and unfolding (Booth and Shalashilin, 2016), ion transportation (Wells, Abramkina and Aksimentiev, 2007), protein-protein interaction (Cuendet and Michielin, 2008), and drug discovery (Patel *et al.*, 2014).

One of the main disadvantages of steered MD is that, to get reliable statistics, it can take a long time to run the calculation. However, by combining steered MD with umbrella sampling, a full umbrella sampling calculation of the system can be carried out within one single calculation. This reduces the burden on the scientist setting up and initiating all the calculations needed manually.

6.6 Software Used

In this work metadynamics was implemented using PLUMED 1.3 libraries (Bonomi *et al.*, 2009) patched to DL_POLYClassic (Smith and Forester, 1996). PLUMED is a free-standing library that can be implemented in numerous MD codes. PLUMED has many pre-built CVs available including absolute position, direction and torsion. PLUMED works by adding the bias to the DL_POLY calculation and then passing the information back to the MD code on the fly. All metadynamics calculations in this work were carried out within the NVT ensemble.

PLUMED comes with **sum_hills**, a post processing code that can be used to integrate the Gaussians to reveal the underlying free energy surface. This reduces the number of CVs down to two by integrating out the extra CVs, thus allowing the free energy surface to be visualised in 3D. For simulations where three CVs were used, the dimension reduction was done for each CV in turn. and the lowest barrier height obtained was chosen as the barrier height for that scenario.

A separate Python code was used to search for minima in the region of the diffusion pathway, by searching for the lowest energy along each line of the 3D data produced by the output of **sum_hills**.

For umbrella sampling and steered MD, the same PLUMED 1.3 patched to DL_POLY Classic was also utilised. A combination of steered MD with umbrella sampling, and pure umbrella sampling was used. The WHAM code developed by the Grossfield group (Grossfield, 2018) was used to reweight and analyse output from the umbrella sampling runs.

6.7 References

Barducci, A., Bonomi, M. and Parrinello, M. (2011) ‘Metadynamics’, *Wiley Interdisciplinary Reviews: Computational Molecular Science*, 1(5), pp. 826–843. doi: 10.1002/wcms.31.

Barducci, A., Bussi, G. and Parrinello, M. (2008) ‘Well-Tempered Metadynamics: A Smoothly Converging and Tunable Free-Energy Method’, *Physical Review Letters*, 100(2), p. 020603. doi: 10.1103/PhysRevLett.100.020603.

Bian, Y., Zhang, J., Wang, J. and Wang, W. (2015) ‘On the accuracy of metadynamics

and its variations in a protein folding process', *Molecular Simulation*. Taylor & Francis, 41(9), pp. 752–763. doi: 10.1080/08927022.2014.931680.

Bonomi, M., Branduardi, D., Bussi, G., Camilloni, C., Provasi, D., Raiteri, P., Donadio, D., Marinelli, F., Pietrucci, F., Broglia, R. A. and Parrinello, M. (2009) 'PLUMED: A portable plugin for free-energy calculations with molecular dynamics', *Computer Physics Communications*, 180(10), pp. 1961–1972. doi: <https://doi.org/10.1016/j.cpc.2009.05.011>.

Booth, J. J. and Shalashilin, D. V. (2016) 'Fully Atomistic Simulations of Protein Unfolding in Low Speed Atomic Force Microscope and Force Clamp Experiments with the Help of Boxed Molecular Dynamics', *The Journal of Physical Chemistry B*, 120(4), pp. 700–708. doi: 10.1021/acs.jpcc.5b11519.

Cuendet, M. A. and Michielin, O. (2008) 'Protein-Protein Interaction Investigated by Steered Molecular Dynamics: The TCR-pMHC Complex', *Biophysical Journal*. Cell Press, 95(8), pp. 3575–3590. doi: 10.1529/BIOPHYSJ.108.131383.

Ferrenberg, A. M. and Swendsen, R. H. (1989) 'Optimized Monte Carlo data analysis', *Physical Review Letters*, 63(12), pp. 1195–1198. doi: 10.1103/PhysRevLett.63.1195.

Freeman, C. L., Harding, J. H. and Duffy, D. M. (2008) 'Simulations of calcite crystallization on self-assembled monolayers', *Langmuir*, 24(17), pp. 9607–9615. doi: 10.1021/la800389g.

Gervasio, A. L. and F. L. (2008) 'Metadynamics: a method to simulate rare events and reconstruct the free energy in biophysics, chemistry and material science', *Reports on Progress in Physics*, 71(12), p. 126601.

Grossfield, A. (2018) 'WHAM: an implementation of the weighted histogram analysis method'.

Jarzynski, C. (1997) 'Nonequilibrium Equality for Free Energy Differences', *Phys. Rev. Lett.* American Physical Society, 78(14), pp. 2690–2693. doi:

10.1103/PhysRevLett.78.2690.

Kumar, S., Rosenberg, J. M., Bouzida, D., Swendsen, R. H. and Kollman, P. A. (1992) 'THE weighted histogram analysis method for free-energy calculations on biomolecules. I. The method', *Journal of Computational Chemistry*, 13(8), pp. 1011–1021. doi: 10.1002/jcc.540130812.

Laio, A. and Parrinello, M. (2002) 'Escaping free-energy minima', *Proceedings of the National Academy of Sciences*, 99(20), p. 12562 LP-12566.

Laio, A., Rodriguez-Forteza, A., Gervasio, F. L., Ceccarelli, M. and Parrinello, M. (2005) 'Assessing the accuracy of metadynamics', *Journal of Physical Chemistry B*, 109(14), pp. 6714–6721. doi: 10.1021/jp045424k.

Patel, J. S., Berteotti, A., Ronsisvalle, S., Rocchia, W. and Cavalli, A. (2014) 'Steered molecular dynamics simulations for studying protein-ligand interaction in cyclin-dependent kinase 5', *Journal of Chemical Information and Modeling*, 54(2), pp. 470–480. doi: 10.1021/ci4003574.

Quigley, D. and Rodger, P. M. (2008a) 'Metadynamics simulations of ice nucleation and growth', *The Journal of Chemical Physics*, 128(15), p. 154518. doi: 10.1063/1.2888999.

Quigley, D. and Rodger, P. M. (2008b) 'Metadynamics simulations of ice nucleation and growth', *Journal of Chemical Physics*, 128(15). doi: 10.1063/1.2888999.

Rather, M. A., Basha, S. H., Bhat, I. A., Sharma, N., Nandanpawar, P., Badhe, M., P, G. B., Chaudhari, A., Sundaray, J. K. and Sharma, R. (2017) 'Characterization, molecular docking, dynamics simulation and metadynamics of kisspeptin receptor with kisspeptin', *International Journal of Biological Macromolecules*, 101, pp. 241–253. doi: 10.1016/j.ijbiomac.2017.03.102.

Smith, W. and Forester, T. R. (1996) 'DL_POLY_2.0: A general-purpose parallel molecular dynamics simulation package', *Journal of Molecular Graphics*. Elsevier, 14(3), pp. 136–141. doi: 10.1016/S0263-7855(96)00043-4.

Torrie, G. M. and Valleau, J. P. (1977) 'Nonphysical sampling distributions in Monte Carlo free-energy estimation: Umbrella sampling', *Journal of Computational Physics*, 23(2), pp. 187–199. doi: 10.1016/0021-9991(77)90121-8.

Wells, D. B., Abramkina, V. and Aksimentiev, A. (2007) 'Exploring transmembrane transport through α -hemolysin with grid-steered molecular dynamics', *Journal of Chemical Physics*, 127(12). doi: 10.1063/1.2770738.

7 Diffusion in Barium Titanate

7.1 Introduction

Diffusion in barium titanate plays an important role during the operational lifetime of a device as well as its processing, especially sintering. All ceramics tend to have a small number of intrinsic oxygen vacancies, from the Schottky mechanism due to cation vacancies (Song and Yoo, 2000). However, the concentration is considerably enhanced by reduction during processing (Yang *et al.*, 2004). The diffusion of these vacancies during the lifetime of the device, as previously discussed §5, is believed to play an important role in the degradation of MLCCs. The ability of a rare-earth (RE) to trap oxygen vacancies has already been investigated and it was shown §5 that all mid-size REs can trap oxygen vacancies to the same degree, therefore the difference in observed performance is likely to come from the ability of the dopants to diffuse into the lattice during sintering as well as the preference for certain dopants to form self-compensatory defect complexes.

Experimentally, diffusion in perovskites has been looked at using radioactive ion tracer methods in single crystals to evaluate oxygen diffusion (Kessel, De Souza and Martin, 2015) and cation diffusion (Müller and Härdtl, 1989). It is difficult to directly measure diffusion for when the ion diffusivity is very low however; it is evident from Jeon *et al.* (Jeon *et al.*, 2014) that RE dopants when forming core-shell microstructures have a concentration gradient across the core, and thus some REs can migrate further than others. This migration during sintering can also be enhanced or compromised by grain growth mechanisms and thus cannot be used as a direct measure of the ability of specific RE dopants to migrate. Some experimental measurements of self-diffusion in barium titanate have been carried out, giving an idea of the diffusivity of Ba and Ti in the lattice (Garcia-Verdusch and Lindner, 1952).

7.2 Molecular Dynamics and MSD

Initially the mean squared displacement for oxygen diffusion in barium titanate was calculated over the temperature range 1000-3000K (Fig 7.1). This scenario uses one oxygen vacancy as the charge carrier and was completed using an 8 x 8 x 8 cell using an

NpT ensemble, in DL_POLY Classic using a charge neutralising background. The MSD was calculated using DL_POLY Classics internal MSD calculator.

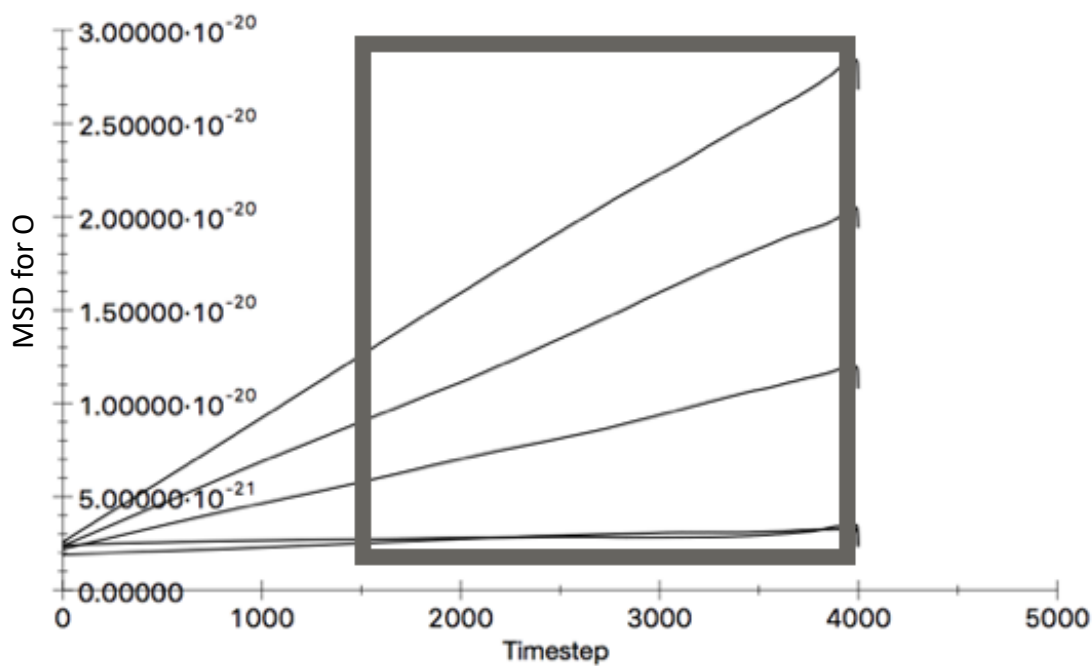


Figure 7.1: MSD for a single oxygen vacancy in barium titanate over temperature range 1000-3000K

It is clear from the MSDs calculated that the migration rate of defects, is too low to use a simple molecular dynamics simulation for diffusion information. In 10ns at the lowest temperatures investigated, no hop was observed. This does not supply enough statistics to be confident of the result. Having more charge carriers is not possible as it will not allow for the exclusion of data due to interaction of the defects. In this case from the single charge carrier simulations, the diffusion constant was calculated to be $\sim 1.2\text{eV}$. We have therefore used metadynamics techniques to obtain the free energy migration pathway and the migration barrier, as this method should give a more reliable activation energy. Steered MD and umbrella sampling were also carried out on the oxygen diffusion scenario for comparison.

7.3 Metadynamics Details

A general introduction to the technique can be found in the review of Laio and Gervasio (2008) and is discussed in §6. Our metadynamics simulations were performed using the DL_POLY Classic (Smith and Forester, 1996) molecular dynamics code in association with the PLUMED-1.3 plug-in (Bonomi *et al.*, 2009). A cell consisting of 8 x 8 x 8 unit cells (2560 ions) was used. The barium titanate forcefield detailed in §5 was used. Each simulation scenario was force minimised and energy optimised and then equilibrated for 5000 timesteps with the NpT ensemble with a Nose-Hoover thermostat (Fig 7.2) The thermostat relaxation time was set to 0.1ps and the barostat to 0.05ps. Production simulations were run for up to 6 ns using the NVT ensemble at a temperature of 298 K. The thermostat relaxation time was set to 0.1ps. A charge neutralising background was used when charge neutrality was not maintained. The corners of the cell were pinned by fixing the positions of four atoms to prevent unphysical translations of the unit cell - this is discussed in §7.3.2.

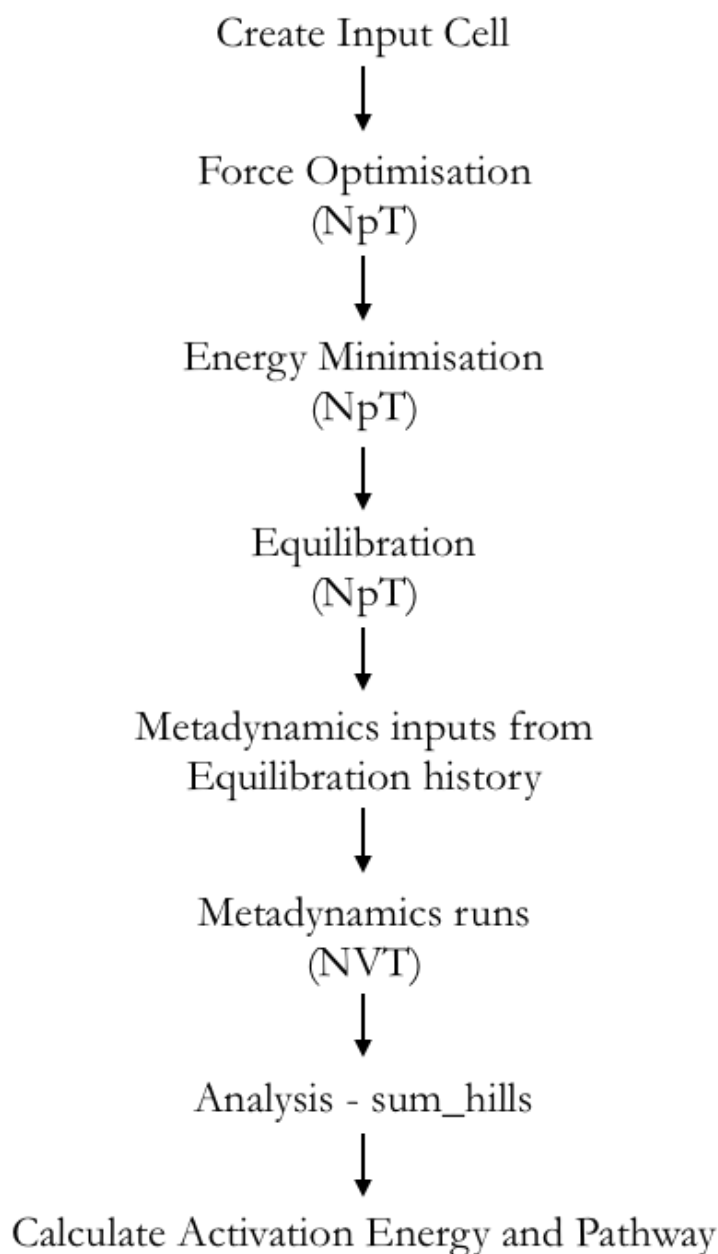


Figure 7.2: Metadynamics Simulation Protocol

7.3.1 Gaussian Fitting

The collective variables (CVs) chosen were the absolute positions in x , y and z of the ion being moved. This choice, although considered inappropriate for some simulation scenarios proved best for simulating the pathways of diffusion in a crystal, without much prior knowledge of the system, and without biasing the pathway the ion took. In the X-X, A-A and B-B hops two positional CVs were used, either the x and y , y and z , or z and x directions (Table 7.1). This is because the pathway of the ion from its' site

to the vacancy was most likely to remain in plane within the simulation, due to the electrostatics of the surrounding ions, and the symmetry of the crystal (Fig 7.3).

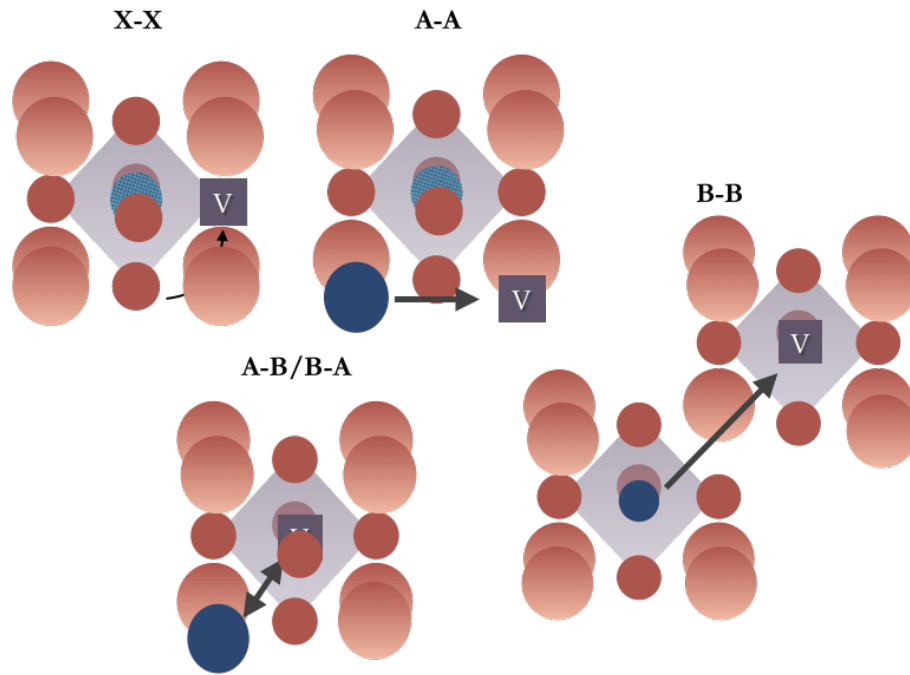


Figure 7.3: X-X, A-A, B-B, A-B and B-A Diffusion Scenarios

In the A-B and B-A hops, the only viable hopping scenario is along the $[111]$ direction in the lattice, which required the three directional CVs, x , y and z (Figure 7.3, Table 7.1). In scenarios where the diffusing ion had cores and shells (Ba, and O) the CV chosen was the position of the shell and not the core. This is to ensure that the gaussians are added smoothly, prevents the core and shell being separated causing the simulation to stop running, and allows the shells to be relaxed back onto the core during the molecular dynamics. Adding the gaussians to the core can also inflate the recovered barrier height (Fig 7.4).

Table 7.1: Number of CVs and directions used for the diffusion scenarios in this work

<i>Hopping Scenario</i>	<i>Number of CVs</i>	<i>Direction of CVs</i>
<i>X-X</i>	2	x, y
<i>A-A</i>	2	x, y
<i>B-B</i>	2	y, z
<i>A-B</i>	3	x, y, z
<i>B-A</i>	3	x, y, z

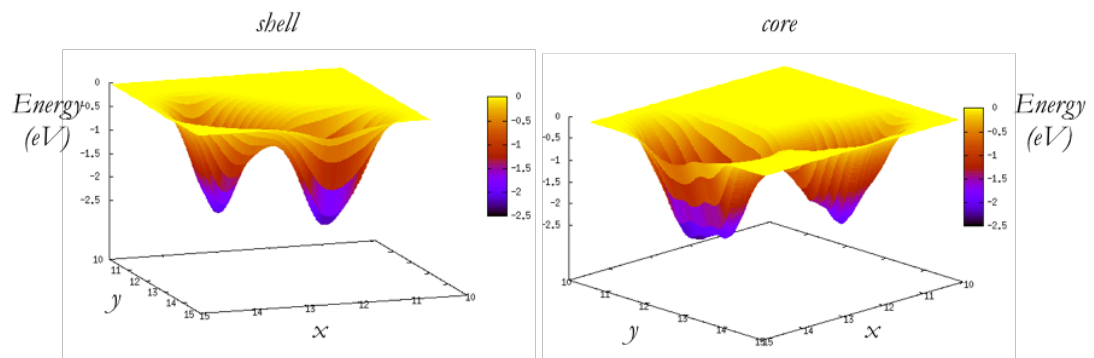


Figure 7.4: Cores vs Shells metadynamics, Left: Free energy surface recovered when adding Gaussians to the shell position as a CV, Right: Free energy surface recovered when adding the Gaussians to the core position. Difference between barrier heights is 0.3eV.

The CVs chosen were monitored using PLUMED_1.3 during the equilibration. The width of all Gaussians was fitted as between one half and one third of the Shannon and Prewitt (1976) ionic radii of the atoms involved. Usually a value of half of the standard deviation of the unbiased positions of the CV is chosen, as recommended by Quigley and Rodger (2008). However, the standard deviations were so small due to the high stiffness of a solid-state ceramic that this definition of width would destroy any simulation efficiency because of the number of Gaussians required to fill the energy landscape. The height of the Gaussian was chosen to be 0.05 eV for the oxygen hops and 0.1eV for the A and B site hops. A combination of the two was used for the RE

hops. This done was to ensure efficient calculations, despite the vast difference in barrier heights between the O ion diffusion ($< 1\text{eV}$) and the cation diffusion ($>4\text{eV}$). The addition rate or stride for the gaussians was increased until convergence of the free energy surface occurred. The smallest stride once convergence was reached was chosen. This was every 100 timesteps or every 50fs. The stride was kept the same for all simulations, once convergence was demonstrated, this was to make it easier to compare and run simulations.

Table 7.2: Fitted Gaussian Parameters for Diffusion Metadynamics

<i>Hopping Scenario</i>	<i>Gaussian Width</i> (\AA)	<i>Gaussian Height</i> (eV)	<i>Stride</i> (fs)
<i>X-X</i>	0.3	0.05	50
<i>A-A</i>	0.4	0.1	50
<i>B-B</i>	0.3	0.1	50
<i>A-B</i>	0.3	0.05	50
<i>B-A</i>	0.3	0.05	50

7.3.2 Cell Corner Pinning

When the Gaussians were being fitted for the B-B hop, it became clear that the second energy well (or lattice site) was not being found. The first half of the pathway appeared easily (Figure 7.5), however the vacancy lattice site was never found. This was also the case for the X-X hop at very long strides ($>150\text{fs}$)

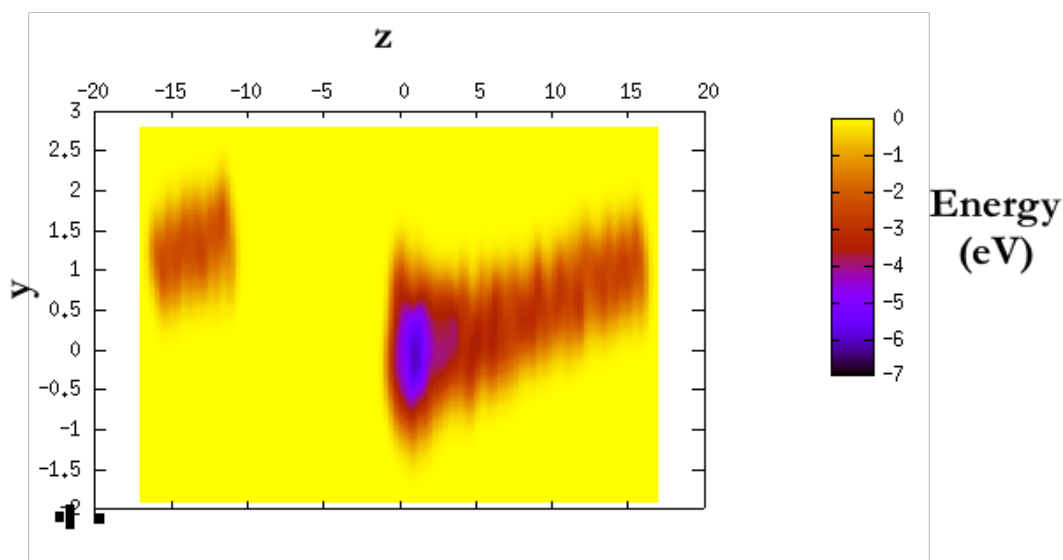


Figure 7.5: B-B Unpinned Trajectory. Lattice Site at (0,0,0), the vacancy is at (0,4,4)-unseen, and migration never finds this vacancy.

When the atom trajectory was viewed using CrystalMaker (2018) it became clear that the energy added to the simulation was so great, and the barrier so high, that the entire simulation box kept moving in a translational manner leading to the second lattice site being completely missed by the diffusing ion. This is an issue with absolute position CVs. As perovskites are relatively close-packed it was determined that if the cell was large enough, and the atoms at the corners of the cell were fixed or frozen post equilibration, the lattice would not have the chance to move in such a translational manner whilst still allowing the diffusion event to occur. It was determined using the X-X hop, calculated with both pinned and non-pinned corners, that the difference in the barrier height was only 0.03 eV and the pathway was the same (Figure 7.6). To allow comparison of calculations, pinned corners were used in all calculations.

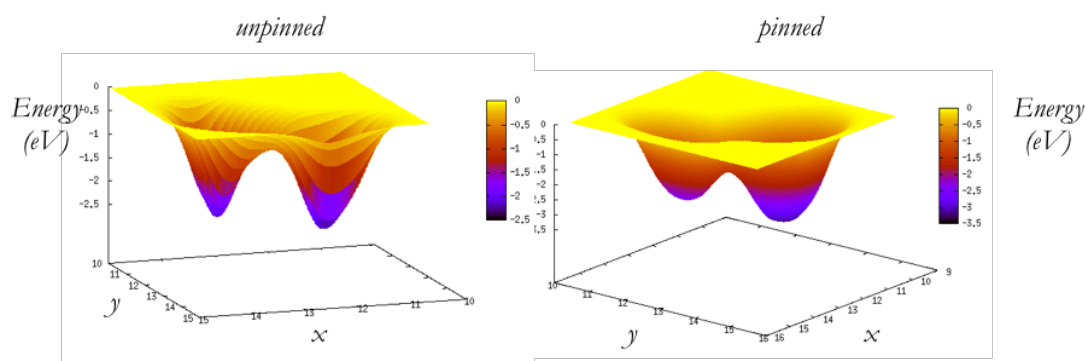


Figure 7.6: Left: Pinned and Right: Unpinned Oxygen Diffusion Pathways.

7.3.3 Metadynamics Runs

For the X-X hop, 5 metadynamics runs were run using starting configurations from equilibration. The barrier height was then averaged giving an average value of 0.90eV and a standard deviation of 0.004. As the standard deviation was so low, it was deemed that because of the close packed nature of the system, the CVs used are highly correlated. This is in agreement with Barducci, Bonomi and Parrinello (2011) who state that the more correlated the CVs the less improvement in error you get from multiple runs.

Therefore, multiple runs were deemed not necessary in other cases, allowing more scenarios to be carried out within the time available. This treatment is appropriate for close-packed ceramic systems where pathways are quite rigidly confined due to the stiffness of the crystal structure and subsequent reduction of the number of accessible pathways across a barrier, and the lack of solvent that is present in most biological simulations.

7.3.4 Analysis of Metadynamics Results

All metadynamics results were analysed using the `sum_hills` utility provided by PLUMED_1.3 (Bonomi *et al.*, 2009). This integrates the Gaussian ‘hills’ added to the calculation to reveal the free energy surface as a function of the collective variables and the energy. A grid size of 200x200x200 was used to complete the calculation. The resultant pathways were then analysed for barrier height using an in-house python script. The script calculates the overall lowest pathway, and the difference between bottom of the free energy well and the saddle point. The barrier height was taken as the lowest barrier height observed during the calculation as this remained the lowest possible regardless of how many times the hop was made. For hops where three CVs were used (A-B and B-A), `sum_hills` was used three times to integrate out each CV in turn. The barrier height was taken to be the smallest barrier calculated from the three.

7.4 Steered MD

Steered MD was carried out on the oxygen diffusion scenario using one absolute position of the core and its direction as a collective variable. The other two ion positions directions were monitored. The steering was carried out moving one oxygen

ion into a single adjacent vacancy (Fig 7.3). The calculations were carried out within the NVT ensemble on the same unit cell with pinned corners as for the metadynamics.

7.4.1 Fitting

In steered MD, both the spring constant and the velocity or speed of the steering must be fitted. The spring constant was trialled at 25, 50, 100 and 200 eV/Å² at a step size of 0.1Å. The calculation crashed at the lower spring constants 25 and 50 suggesting that this was too stiff a spring combined with too large a timestep. For spring constants of 100 eV/Å² and 200 eV/Å² the results and location of the barrier was similar, thus a value of 100 eV/Å² was chosen.

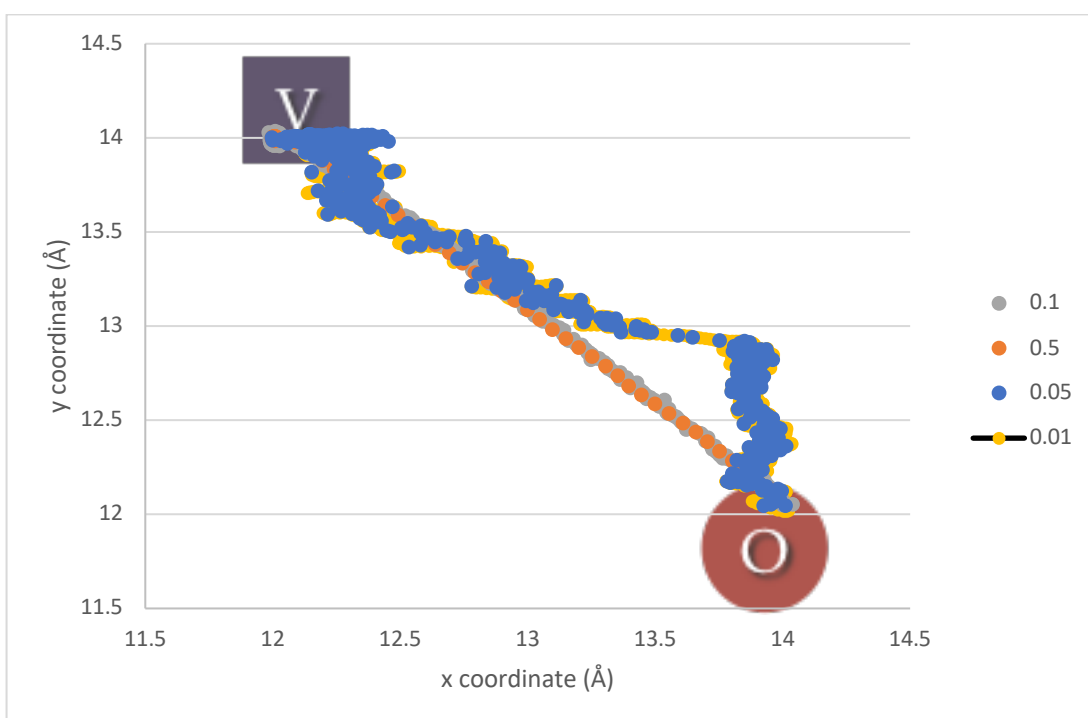


Figure 7.7: Steered MD step size fitting showing an X-X hop with the initial lattice site locate at (14, 12, 14) and the vacancy at (12, 14, 14). Step sizes, 0.1, 0.5, 0.05 and 0.01.

The pathway was examined for convergence (Fig 7.7) and the step size was chosen as 0.05Å.

7.4.2 Analysis Techniques

Steered MD was analysed using the output COLVAR file from the PLUMED run. The work done and CVs were plotted against each other to observe the convergence of the pathway. The location of the barrier was determined to be the point at which the most work was done.

7.5 Umbrella Sampling Calculation Details

Umbrella sampling was carried out as part of a steered MD run. The steered MD moved the oxygen ion for 500fs. Then an umbrella sampling calculation was carried out for 500fs. These two scenarios were repeated until the second lattice site was found. The steered MD had a spring constant of $100\text{eV}\text{\AA}^{-2}$ and a step size of 0.05\AA . The V e run was carried out moving one oxygen ion into a single adjacent vacancy (Fig 7.3). The calculations were carried out within the NVT ensemble on the same unit cell with pinned corners as for the metadynamics.

Like steered MD the springs were fitted to a value of 100. When carrying out analysis using WHAM the histograms overlapped and therefore this was considered to be an appropriate choice of spring constant.

7.6 Self-Diffusion in Cubic Barium Titanate

7.2.1 Self-Diffusion Scenarios

As RE diffusion in BT cannot be explored using experimental techniques self-diffusion in BT was investigated first, to compare to the limited available experimental values (Garcia-Verdusch and Lindner, 1952; Kessel, De Souza and Martin, 2015), and validate the techniques used. The hopping scenarios investigated were oxygen diffusion, barium diffusion and titanium diffusion (Fig 7.3). The most likely pathway for diffusion in the lattice was simulated based on the surrounding electrostatics pathway length. As the RFO for oxygen diffusion was successfully carried out in §5 the calculated value and barrier location obtained there is also included in the discussion and evaluation of methods for simulating diffusion barriers. As we are interested in oxygen diffusion during the operation of electroceramic devices, all calculations were carried out at 298K.

7.6.1 Oxygen Diffusion

Oxygen diffusion in BaTiO₃ has been extensively studied experimentally both in undoped single crystals and polycrystals giving activation energies ranging from 0.5 to 1.28 eV as discussed in §5. In §5 we reported a configurational energy barrier to oxygen migration from a rational functional optimisation calculation as 0.84eV. This fits well with experimental values (Table 7.4).

As the oxygen diffusion scenario (Fig 7.3) is the shortest hop of all studied in this thesis; metadynamics, Steered MD and Umbrella sampling were all carried out and compared. The final metadynamics saddle point is shown (Fig 7.9) with the RFO saddle point, the Steered MD and the Umbrella sampling profile projected onto the same graph. The values from all four types of calculation are in Table 7.3.

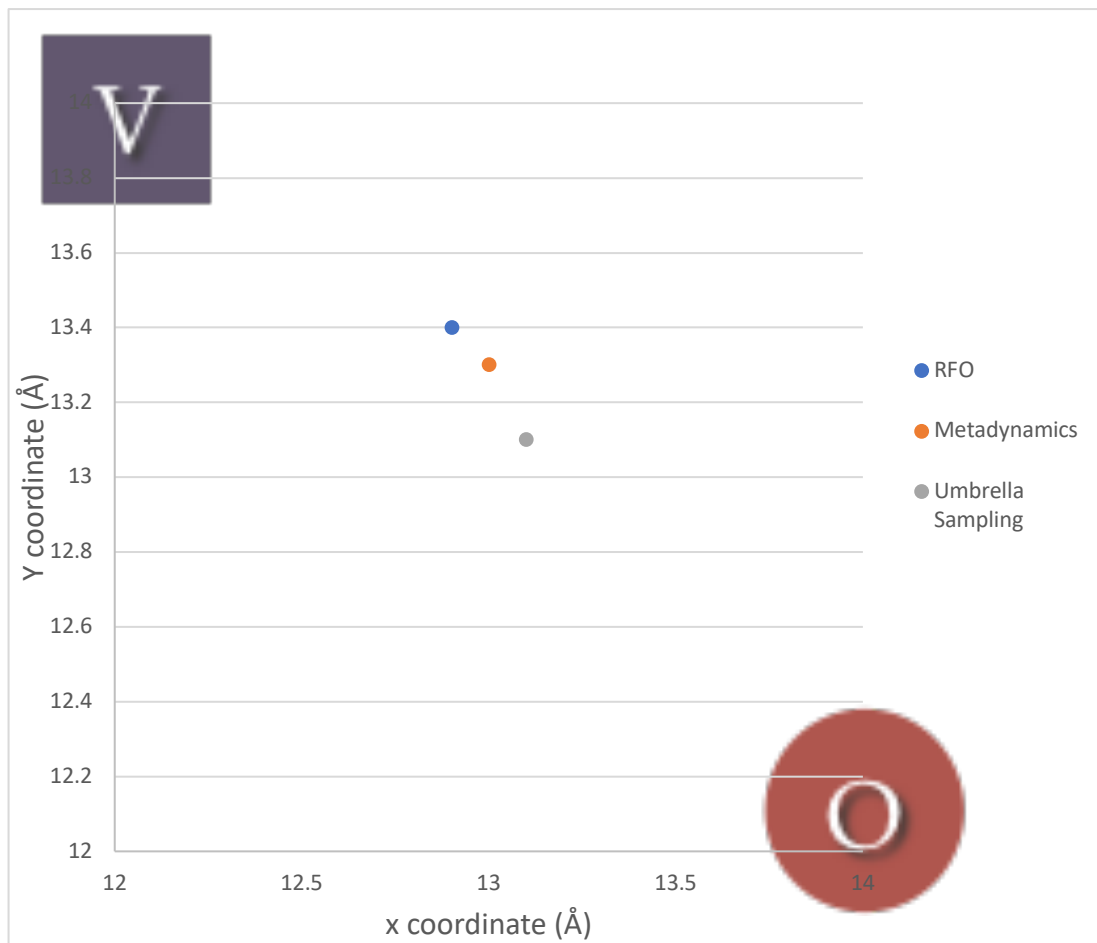


Figure 7.8: Locations of oxygen diffusion saddle points for, metadynamics, RFO and Umbrella sampling with the initial lattice site locate at (14, 12, 14) and the vacancy at (12, 14, 14)..

Table 7.3: Oxygen diffusion activation energies and barrier locations.

<i>Calculation</i>	<i>Activation Energy (eV)</i>	<i>Barrier Location (Å)</i>
<i>RFO</i>	0.84	12.9, 13.4
<i>MSD</i>	1.2	N/A
<i>Metadynamics</i>	0.9	13, 13.3
<i>Umbrella Sampling</i>	0.85	13.1, 13.1
<i>Steered MD</i>	N/A	13.1, 13.1

The saddle point was found in a similar location for all simulation types carried out (Fig 7.8). The energies recovered are also very similar. This indicates that all methods used are possible for discerning the barrier height (configurational energy – RFO, free-energy otherwise) and thus an activation energy for diffusion in barium titanate. These results compare well with literature – 0.74eV (Kessel, De Souza and Martin, 2015). It can clearly be observed (Fig 7.6) that the metadynamics calculation obtains the full pathway of migration as well as the barrier height in one calculation. RFO calculations obtain the least detail about the migration and are extremely sensitive to starting position but the barrier height is very accurate. The length of time it takes to perform an RFO is also prohibitively expensive for the obtained information. Direct use of steered MD produces the least reliable barrier height, due to the sampling problems inherent in the Jarzynski equality §6 and the knowledge of the pathway required for setting up the calculation. However, Steered MD is very useful for setting up the ‘windows’ needed for umbrella sampling. This allows a full run of umbrella sampling to be carried out using only one long calculation, minimising user input. Umbrella sampling is easy to run however; large numbers of calculations are necessary to map the pathway when not combined with steered MD. Metadynamics overall seems to be the best choice of techniques to use when the user has the least information about the system as only CVs to determine a pathway or a configurational relationship is needed. As long as the calculation is run for long enough you gain the most information with the least number of simulations.

7.6.2 Barium Diffusion

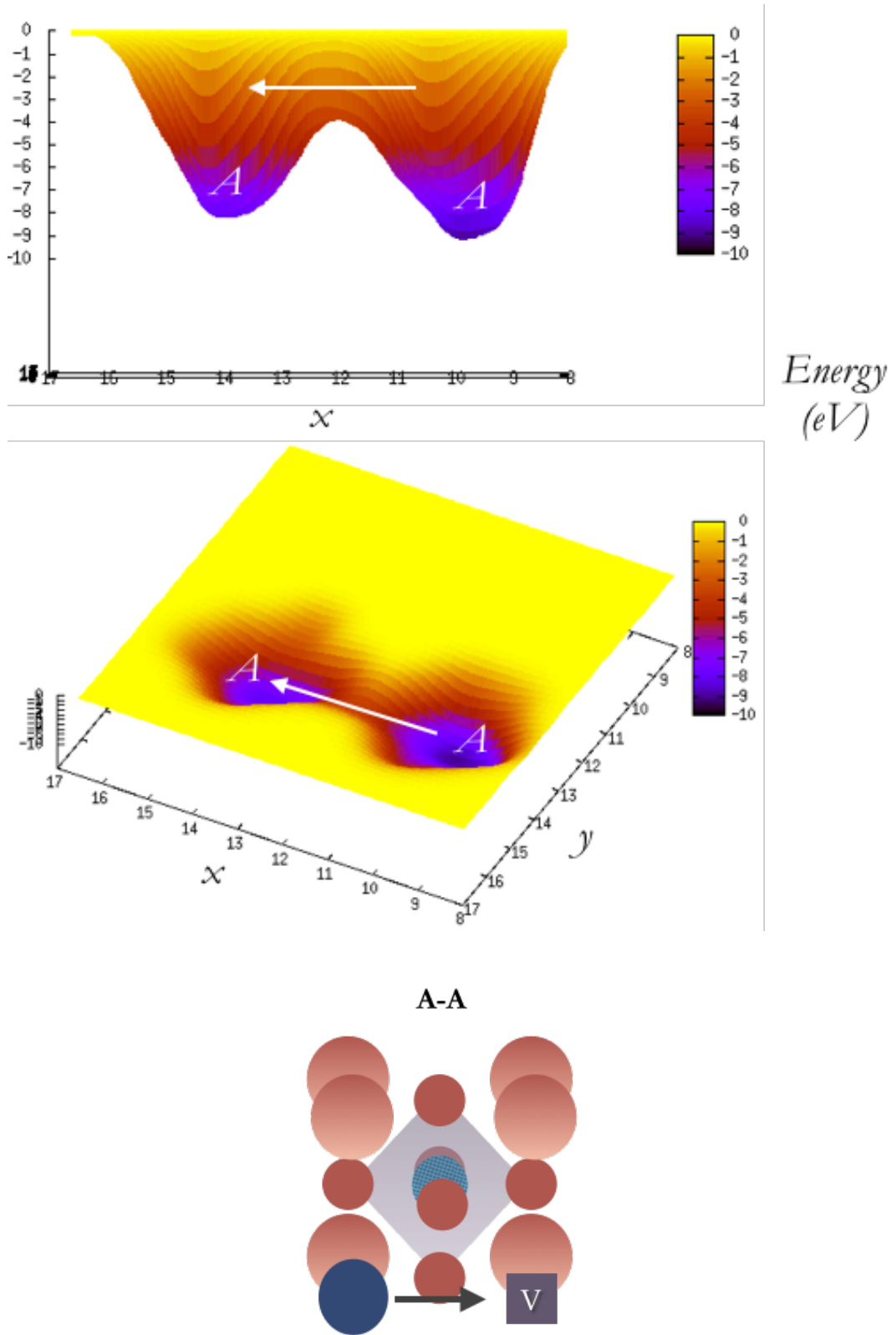


Figure 7.7: A-A self-diffusion pathway for Ba. Lattice sites indicated by A and direction of migration indicated with the arrow. Hopping scenario shown at the bottom.

7.6.3 Titanium Diffusion

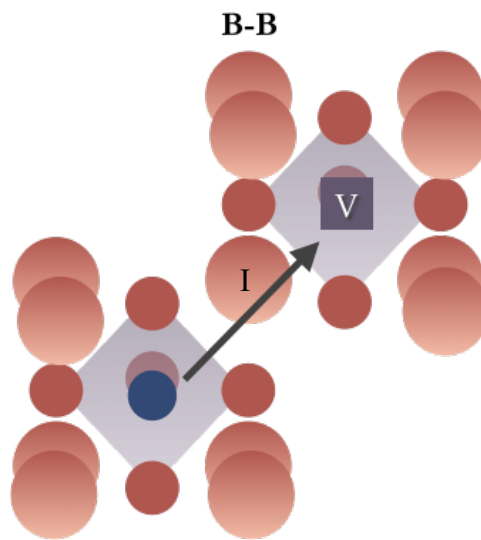
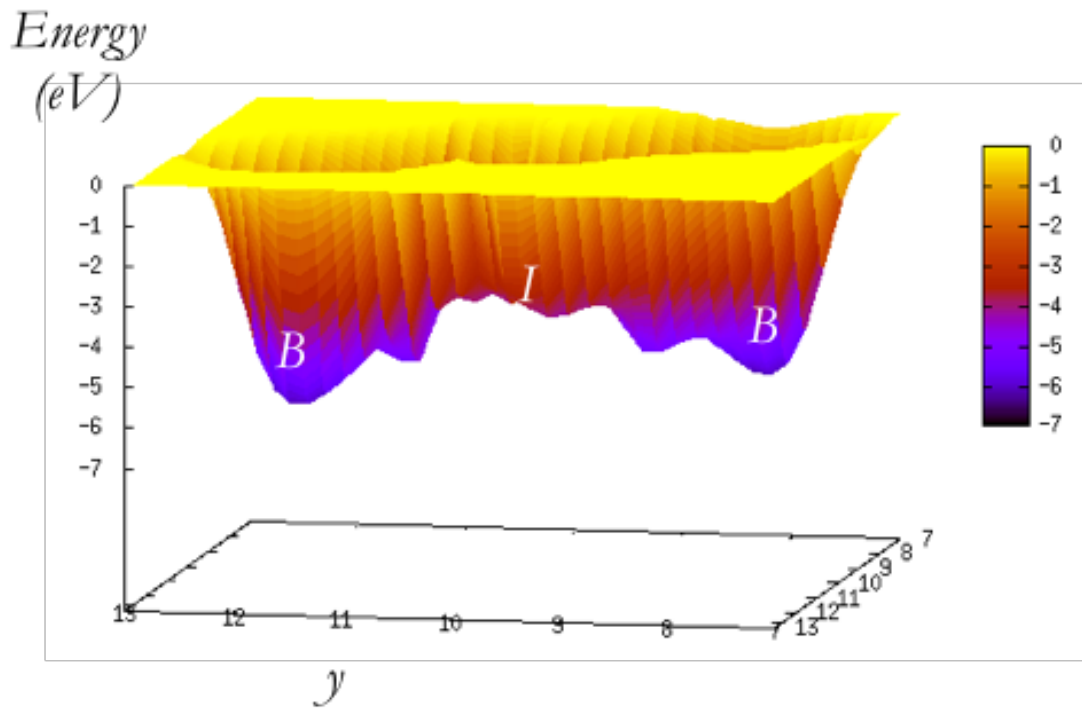


Figure 7.8 B-B Pathway for Ti self-diffusion. Lattice sites indicated by B, interstitial site indicated by I. Hopping scenario shown at the bottom.

7.6.4 Discussion

The literature on cation diffusion in BaTiO_3 is sparse. It is often assumed that the diffusion rate for titanium diffusion is much less than that for barium diffusion due to

the charge effect of the much smaller 4+ ion. However, work by Lee and co-workers (2008) shows that the diffusion rates of the two cations must be similar as in their experiments diffusion of both barium and titanium was observed, however no de-mixing was seen. Some experimental values for the diffusion activation energy in BaTiO₃ and SrTiO₃ exist (Table 7.4). For A-site vacancy diffusion there is the work of Garcia-Verdudch and Lindner(1952) (3.9 eV – Ba in BaTiO₃); Koerfer *et al* (2008). (5.6±1.2 eV – Sr in BaTiO₃); Mayer and Waser (Meyer *et al.*, 2003) (3.5 eV – Sr in SrTiO₃). For B-site vacancy diffusion there is the work of Preis and Sitte (Preis and Sitte, 2006)(3.9±0.7eV –Ti in BaTiO₃); Koerfer *et al* (2008). (5.1±0.6 eV - Zr in BaTiO₃). These are very widely scattered but do not support the notion that vacancy diffusion rates on the A and B site lattices are very different. It should, however, be remembered that these are *activation* energies and could contain an energy contribution to create a mobile vacancy (release a vacancy from being bound to an impurity for example) as well as the migration energy of the mobile vacancy.

Table 7.4: Simulations to obtain migration energies for SrTiO₃ and BaTiO₃. Methods used are TAD (Temperature Accelerated Dynamics), AKMC (Adaptive kinetic Monte Carlo), NEB (Nudged Elastic Band), DFT (Density Functional Theory), RFO (Rational Functional Optimisation). *Defect does not migrate but converts into a Sr anti-site complex.

Ref	Methods	SrTiO ₃		BaTiO ₃	
		V _{Sr} (eV)	V _{Ti} (eV)	V _{Ba} (eV)	V _{Ti} (eV)
(Uberuaga and Vernon, 2013)	TAD; AKMC; (NEB) forcefield from (Meyer et al., 2003)	5.03	Immobile*	6.68	Immobile*
	TAD; AKMC; (NEB) forcefield from (Busker et al., 1999)	3.95	Immobile*	—	Immobile*
(Erhart and Albe, 2007)	NEB, DFT	—	—	5.82 (V _{Ba} ^x) 5.96 (V _{Ba}) 6.0 (V _{Ba})	9.84 (V _{Ti} ^x)
(Walsh <i>et al.</i> , 2011)	NEB, DFT	3.68 (V _{Sr} ^{''}) 2.92 (V _{Sr} ^{''} -V _O ^{••})	—	—	—
(Thomas, Marks and Begg, 2007)	RFO, own forcefield	3.9	11.0	—	—

Several attempts have been made to calculate the diffusion migration energies. These are summarised in Table 7.4. All authors use static lattice methods to calculate the migration although they may use high temperature molecular dynamics to identify the transition (TAD). Most authors use the nudged elastic band (which assumes that both the start and end points of the transition are known). Thomas, Marks and Begg (2007) uses a mode-following method (RFO) which requires only the initial state. All results are internal energies at zero temperature. The result is clearly sensitive to the models used for the interatomic interactions (see the column for strontium vacancies in SrTiO₃). The results (for both simulation and experiment) are too scattered to permit a meaningful comparison except to note that (where results exist), the simulations predict a large difference in diffusion rate between A-site and B-site vacancy diffusion whereas the experiments do not. The migration energies for intrinsic diffusion on the A and B sublattices are very similar – consistent with experiment although the migration energies are higher than the only two experimental results (Garcia-Verdusch and Lindner (1952) for A-site diffusion; (Preis and Sitte, 2006) for B-site diffusion but note the wide error bars). In this work the metadynamics barrier heights obtained for Ba and Ti are similar to each other (Table 7.5) which agrees with the work of Yoo, Song and Lee, (2002) however our Ti self-diffusion pathway also goes interstitial which agrees with simulation results where Sr went immobile (Uberuaga and Vernon, 2013). The X-X barrier height obtained by metadynamics (0.9eV) agrees with experiment (0.74eV) considering the expected differences due to one result being a free energy and the other an entropy. These results suggest that metadynamics is a suitable technique for investigating the trends in activation energies for RE dopants in barium titanate. As these are single metadynamics calculations, the traditional calculation of error from an average does not apply. Instead the error is taken as minus one gaussian height used, as this is likely the height a barrier may be overfilled by in a single hop.

Table 7.5: Self-diffusion activation energies calculated from metadynamics.

	<i>Barrier Height(eV)</i>	<i>Stright Hop Length (\AA)</i>	<i>Error (eV)</i>
<i>Ba</i>	4.9	4.0	-0.1
<i>Ti</i>	5.0	5.7	-0.1
<i>O</i>	0.9	2.83	-0.05

7.7 Rare Earth Diffusion in Barium Titanate

7.7.1 A-A Hop

Table 7.6: Calculated Barrier Height, Error and Hop Length for all A-A Hops.

	<i>Barrier Height</i> (eV)	<i>Hop Length</i> \AA	<i>Error</i> (eV)
<i>Ba</i>	4.9	4.0	-0.1
<i>Y</i>	5.5	4.0	-0.1
<i>Dy</i>	5.3	4.0	-0.1
<i>Gd</i>	5.0	4.0	-0.1

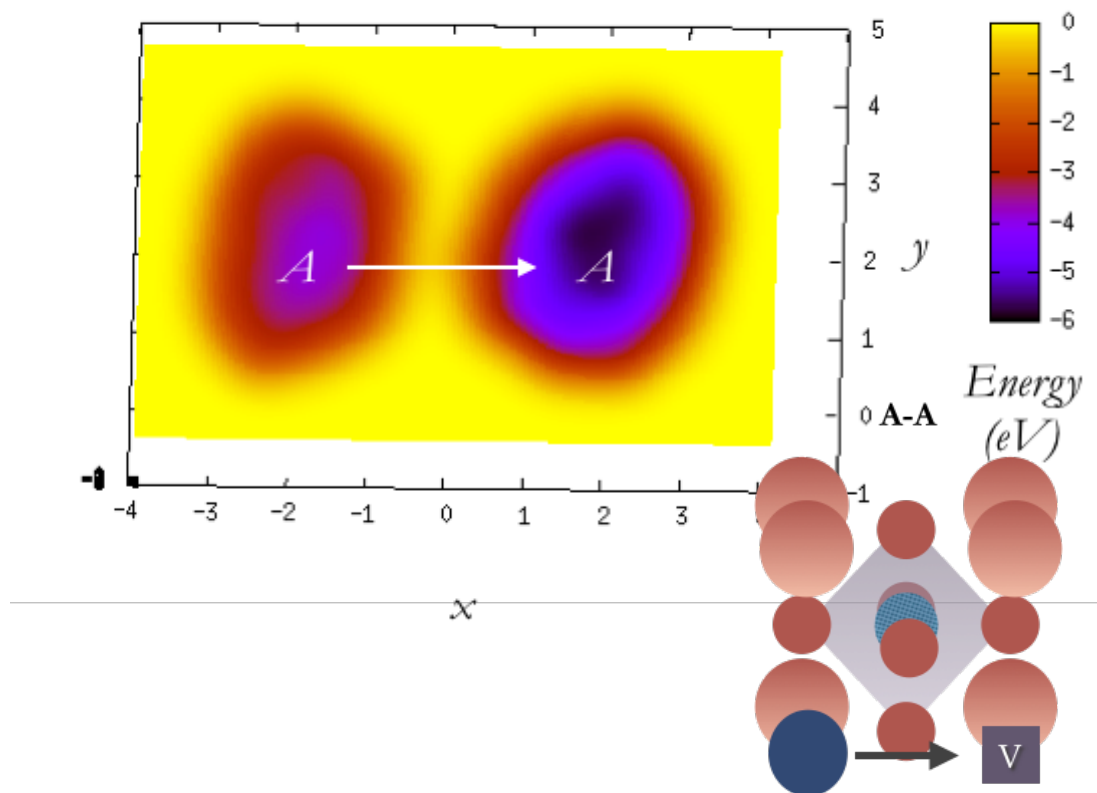


Figure 7.9: A-A Pathway for Dy, A sites are indicated by A and direction of travel is shown with a white arrow. Hopping scenario is detailed at the bottom.

The A-A hop for the REs (Fig 7.8) is the same in length and direction as the Ba self-diffusion case (Fig 7.9). The barrier heights are higher than those for self-diffusion, which is understandable due to the increased charge of the REs and the lack of shells on the REs. The A-A hop is the least likely scenario to occur during RE diffusion as it is the largest barrier height for all REs investigated.

7.7.2 A-B and B-A Hop

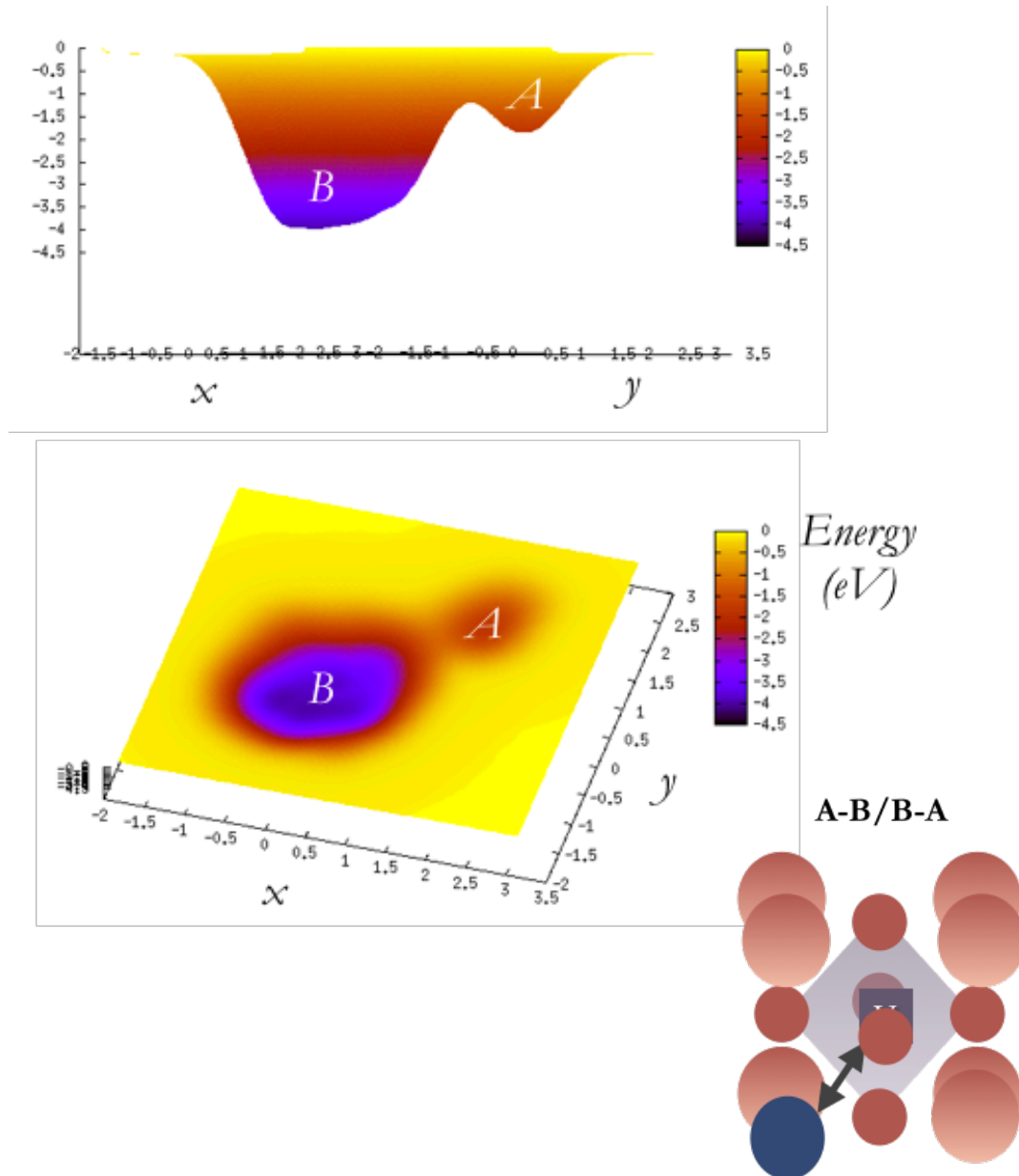


Figure 7.10: A-B/B-A Pathway for Y, A-site noted by A and B site noted by B. Hopping scenario is detailed at the bottom.

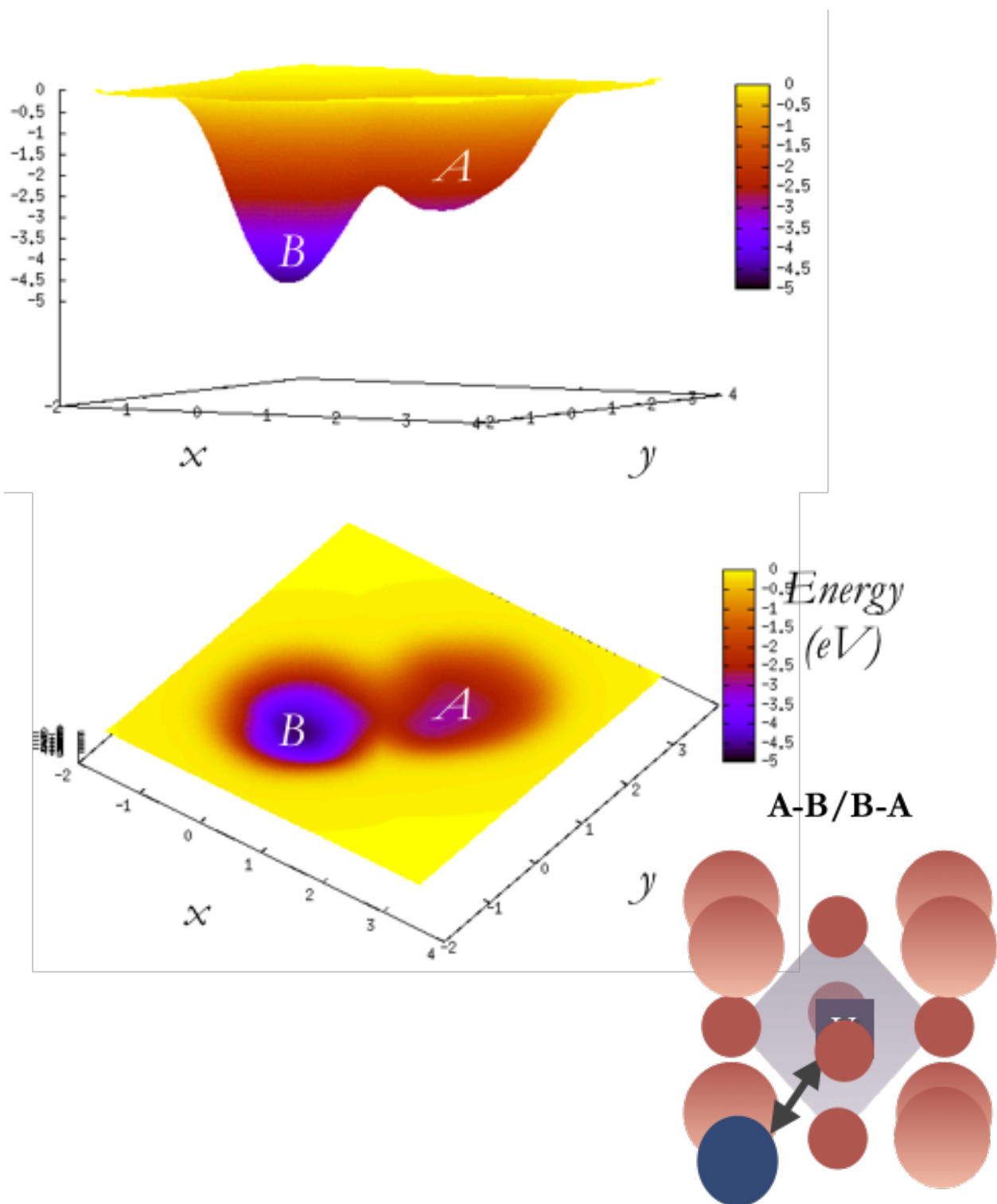


Figure 7.11: A-B/B-A Pathway for Dy. A-site noted by A and B site noted by B.
Hopping scenario is detailed at the bottom.

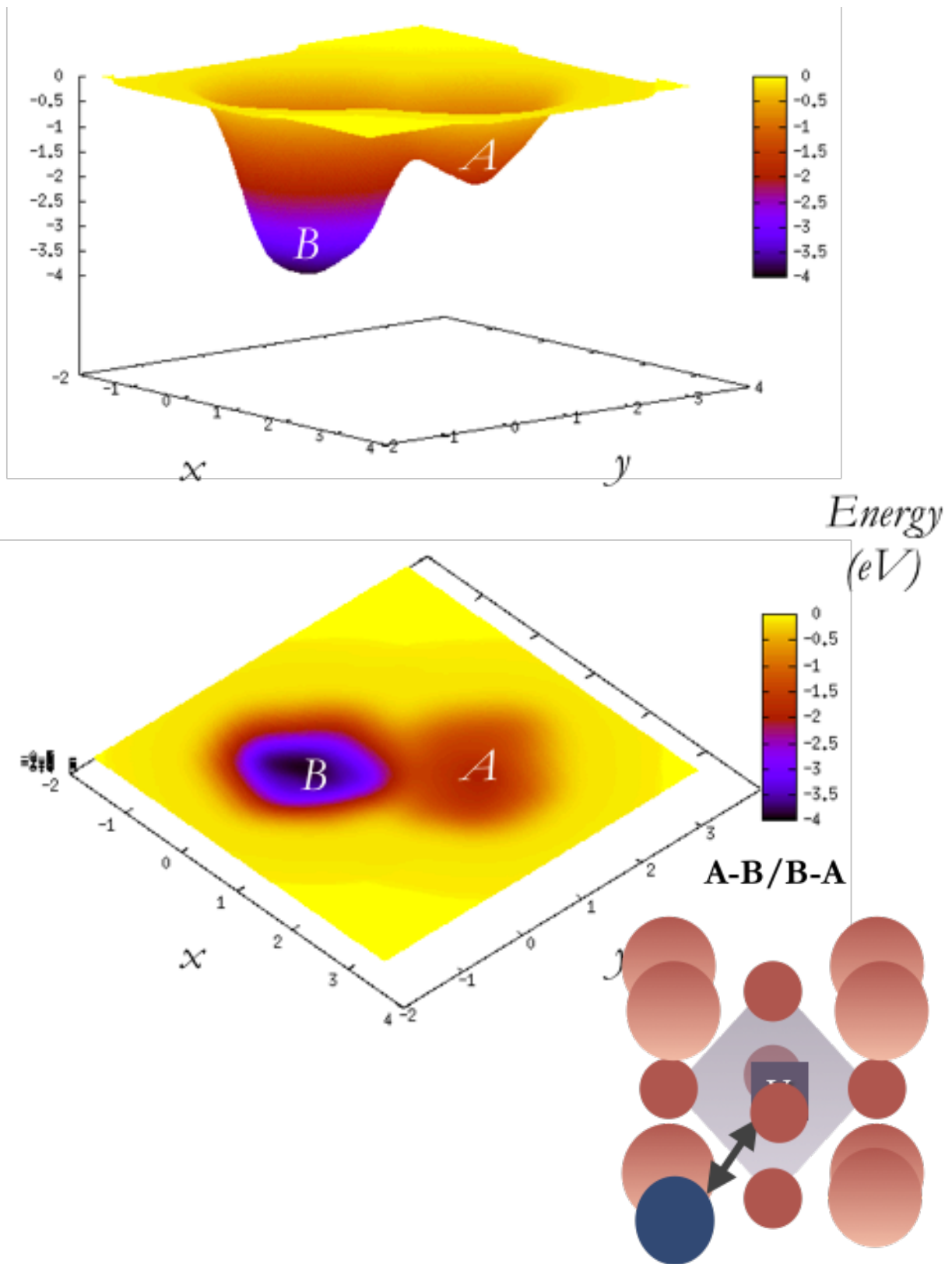


Figure 7.12: A-B/B-A Pathway for Gd. A-site noted by A and B site noted by B. Hopping scenario is detailed at the bottom.

Table 7.7: Projection of collective position variables onto the three orthogonal planes for AB/BA hopping scenarios. The lowest value is the migration energy quoted in

Table 7.8

	<i>A => B (3.46 Å)</i>			<i>B => A (3.46 Å)</i>		
	XY	YZ	XZ	XY	YZ	XZ
<i>Y</i>	0.6	0.6	0.6	2.75	2.75	2.55
<i>Dy</i>	0.5	0.5	0.5	2.25	2.4	2.3
<i>Gd</i>	1.0	0.9	1.0	3.0	3.0	3.0

Table 7.8: Calculated Barrier Height, and Error for A-B/B-A Hop

	<i>A-B Hop</i>		<i>B-A Hop</i>	
	Barrier Height(eV)	Error (eV)	Barrier Height(eV)	Error (eV)
<i>Y</i>	0.6	-0.05	2.55	-0.05
<i>Dy</i>	0.5	-0.05	2.25	-0.05
<i>Gd</i>	0.9	-0.05	3.0	-0.05

As can be seen (Fig 7.10-12) The A-B and B-A hop are the shortest hops possible for the REs. They are also the lowest two in energy for all scenarios. This suggests that mid-size REs diffuse into the BT lattice during sintering by way of a A/B B/A hopping chain. The relaxation of the lattice around the REs, similar to that seen in §5, shortens the hop length for Dy in particular. Y is too small for the A-site which means that it will sit preferentially in such a way to give itself pseudo 9-fold configuration. This off-centre location can be seen in Fig 7.10. This makes Y's A-site well much smaller than for Dy or Gd. For Dy its size gives it more room to rattle when on the A-site (Fig 7.11) which may increase the number of jump attempts. Being the largest Gd sits more comfortably and centrally on the A-site than the other ions, making it harder to leave as it will be held more in place by the surrounding lattice. In this sense Dy really is the 'Goldilocks' ion, as it neither wants to sit on the A or B – site, making it easier to move between the two.

7.7.3 B-B Hop

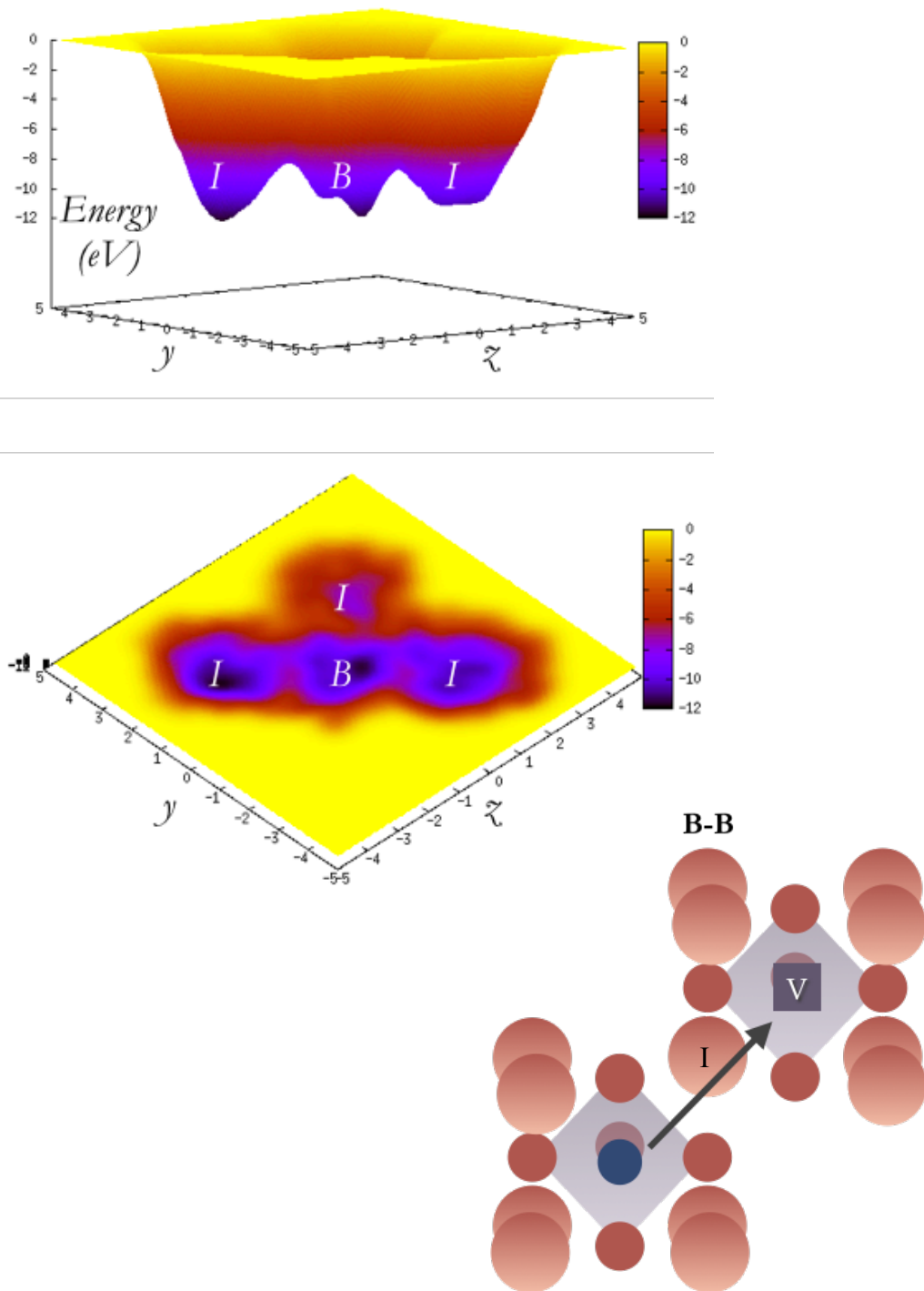


Figure 7.13 B-B Pathway for Y, B-sites denoted by B, Interstitial-sites denoted by I. Hopping scenario is detailed at the bottom.

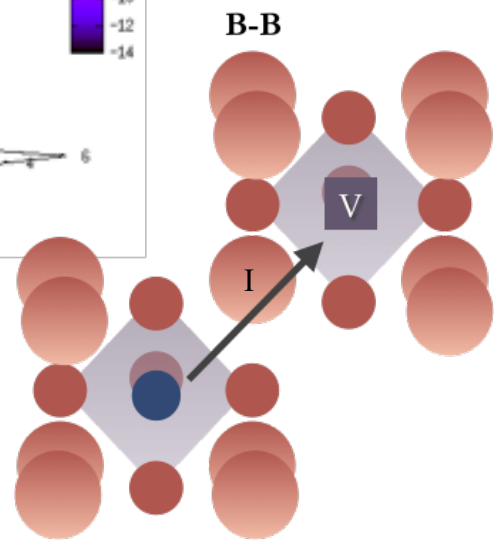
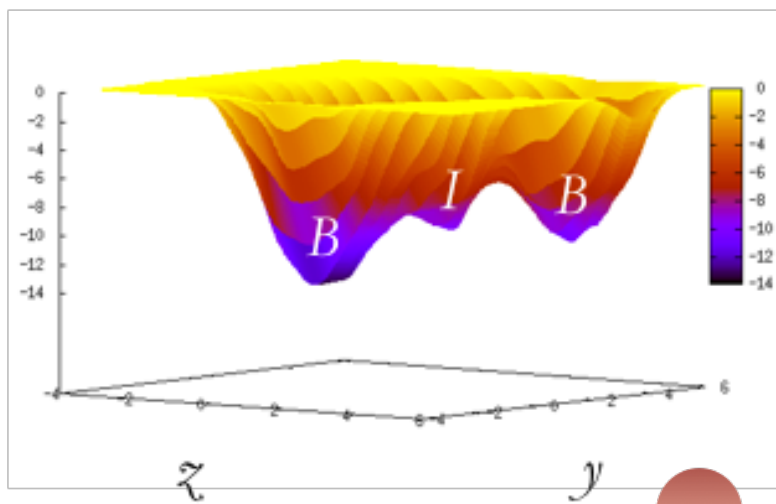
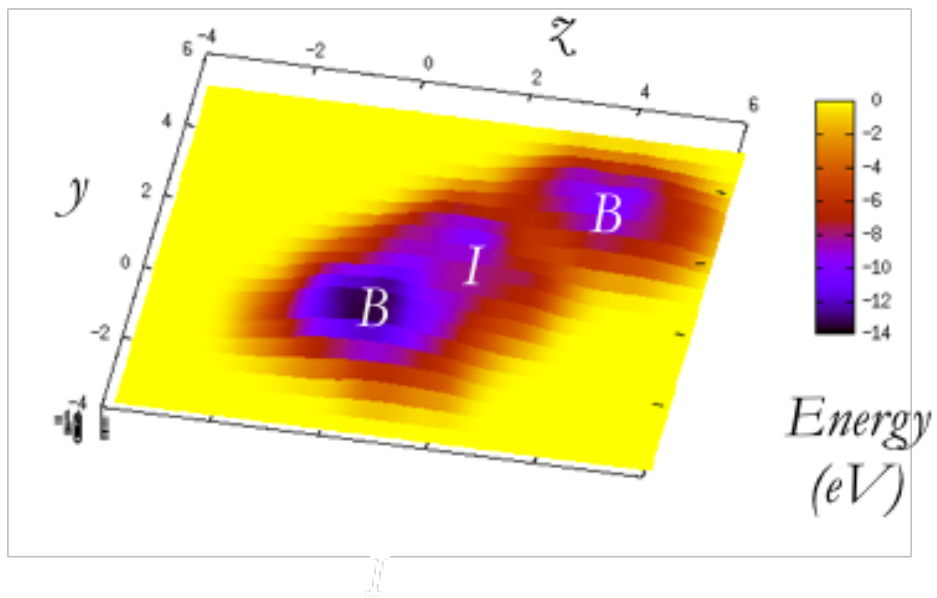


Figure 7.14: B-B Pathway for Dy. B-sites denoted by B, Interstitial-sites denoted by I. Hopping scenario is detailed at the bottom.

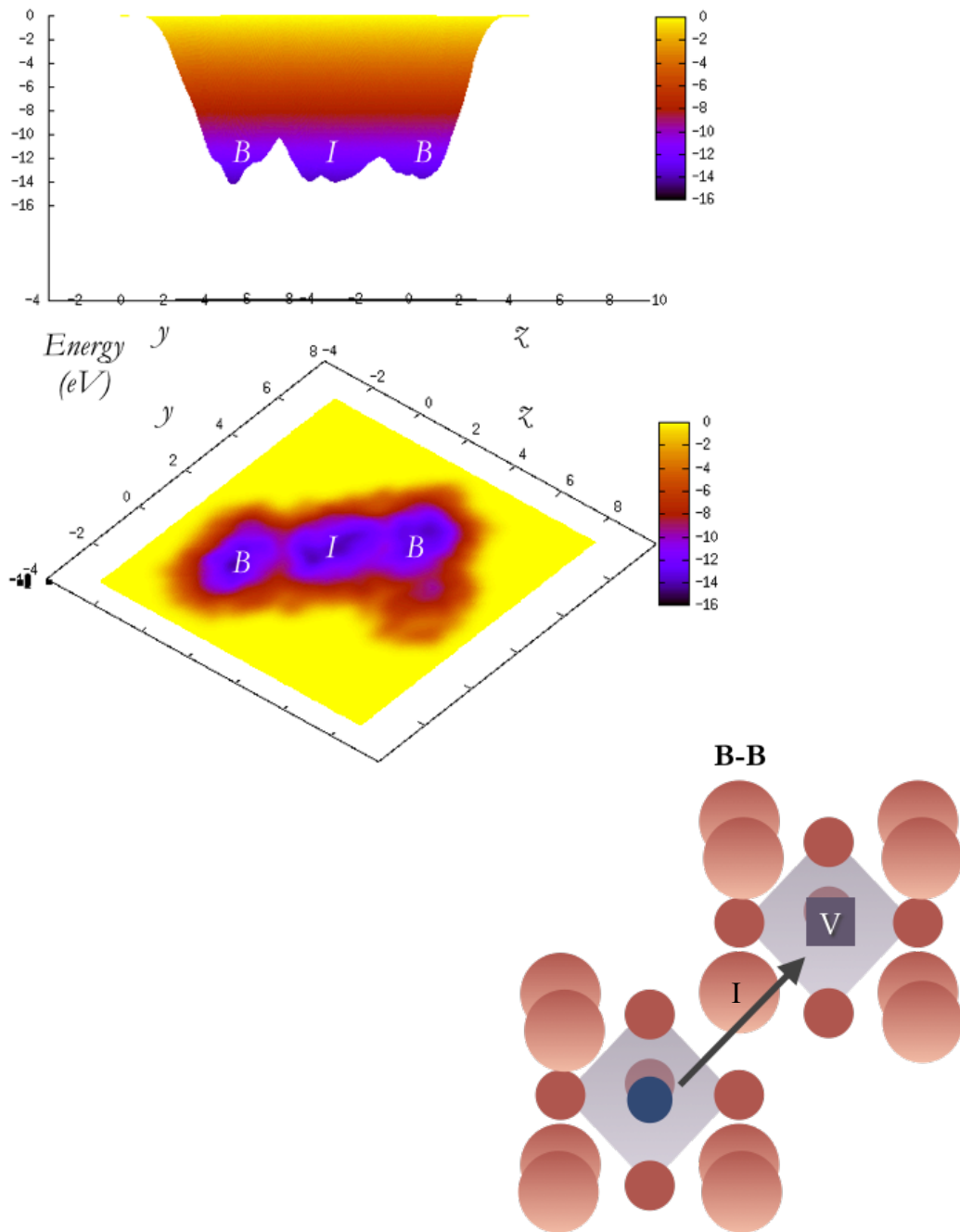


Figure 7.15: B-B Pathway for Gd. B-sites denoted by B, Interstitial-sites denoted by I.
Hopping scenario is detailed at the bottom.

Table 7.9: Calculated Barrier Height, Error and Hop Length for B-B Hop

	<i>Barrier Height(eV)</i>	<i>Hop Length Å</i>	<i>Error (eV)</i>
<i>Ti</i>	5.0	5.7	-0.1
<i>Y</i>	4.0	5.7	-0.1
<i>Dy</i>	3.9	5.7	-0.1
<i>Gd</i>	3.75	5.7	-0.1

The B-B site hop for RE diffusion is the same length as the Ti self-diffusion case (Table 7.9). Like the Ti case there is in an interstitial site similar to those found in the strontium titanate and BT calculations done by Uberuaga and Vernon (2013) found in all three RE examples. The barrier height is the greatest when initially leaving the BO_6 in all scenarios. In the Y case the RE never made it to the second lattice site (Fig 7.13), however it visited 3 out of 4 possible interstitial sites, suggesting the likelihood of the ion making the hop in the B-B case is only 1 in 4. This also suggests that the vacant B-site does not constrain the direction the ion might migrate in initially. The RE barriers are smaller than that for Ti self-diffusion which is to be expected due to having a smaller charge than the titanium ion.

7.7.4 Discussion

7.7.4.1 Activation Energies

The overall metadynamics results for self-diffusion and rare earth diffusion are shown in Table 7.10. For all the REs, the simulations show that the lowest energy migration path involves alternating between the A and B sublattices as the two shortest and lowest energy hops in all cases are the A/B and B/A migration. In this proposed A/B, B/A pathway, the rate-determining step is the $\text{B}_{\text{site}} - \text{A}_{\text{site}}$ barrier crossing. Here the migration energy increases in the order $\text{Dy} < \text{Y} < \text{Gd}$, implying that Dy diffusion will be the fastest and Gd diffusion the slowest.

Table 7.10 Migration energies (eV) for cation diffusion pathways (intrinsic and RE ions) in BaTiO₃ with calculated error. Values are free energies at 298 K. Vacancy mechanism assumed throughout.

<i>Cation (migration pathway)</i>	<i>Path length</i>	<i>Ba</i>	<i>Ti</i>	<i>Gd</i>	<i>Dy</i>	<i>Y</i>
Barrier (eV)	4.0	4.9		5.5	5.3	5.0
(A _{site} -A _{site})		(-0.1)		(-0.1)	(-0.1)	(-0.1)
Barrier (eV)	5.7		5.0	4.0	3.9	3.75
(B _{site} -B _{site})			(-0.1)	(-0.1)	(-0.1)	(-0.1)
Barrier (eV)	3.5			1.0	0.5	0.6
(A _{site} -B _{site})				(-0.05)	(-0.05)	(-0.05)
Barrier (eV)	3.5			3.0	2.3	2.75
(B _{site} -A _{site})				(-0.05)	(-0.05)	(-0.05)

Although all these RE ions can fit into both A and B sites, they are too small to fit comfortably into the A site and too large for the B site. Thus, as the RE ion size decreases from Gd³⁺ to Y³⁺ it is more prone to rattling around in the large A site well, reducing its effective coordination from 12 to 9. The 6-fold coordinate B site is a tight fit for all the RE ions and the effective coordination number is unchanged. A simple explanation for the lowered migration energy for the A_{site}—B_{site} hop lies in this failure of the Dy ion to fit well into either site – this tends to lower the barrier between them.

7.7.4.2 Diffusion Coefficients

We can estimate the different sintering times required for each rare earth to reach an acceptable level of dispersion through the ceramic using a simple diffusion model. For our model, we assume that the rare earth cations are a thin-instantaneous source on surface of the grains and use a solution to Fick's second law (Eq 7.1). Where This model assumes a simple solid-state diffusion model of RE ions from a layer of RE₂O₃ on the surface of a BaTiO₃ crystal as per Fick's Law. The sintering procedure is obviously more complex than this (Paunović, Živković and Mitić, 2010; Jeon, Lee and Kang, 2012) but this is sufficient for our purpose.

$$c(x, t) = \frac{A_0}{\sqrt{\pi Dt}} \exp\left(\frac{-x^2}{4Dt}\right) \quad (7.1)$$

Where c is the concentration at a time t , and distance from the surface x , D is the diffusion constant, and A_0 is the initial concentration. The solution to this equation provides a concentration profile at a time, t (assumed as 1 hour), and various distances, x , from the surface. Therefore, we can estimate the concentration of RE at a certain depth into a grain. The initial concentration, A_0 , is assumed to be 1 molm^{-3} as we are interested in the concentration profiles and this is only a multiplier of this distribution. The diffusion constant can then be calculated (Eq 7.2, Table 7.11).

$$D = f\beta a^2 \nu \exp(-\Delta G_m / k_B T) \quad (7.2)$$

Where D is the diffusion coefficient, β is the structure factor, f is the correlation factor, k_B is the Boltzmann constant, T is the temperature in Kelvin, ΔG_m is the activation energy, ν is the jump frequency, a is the jump distance. We assume that the product of structure factor, β , and correlation factor, f , gives 0.75 as this is in-between the value 0.72 for a bcc lattice (the cations in the perovskite lattice) and 0.78 which is the structure factor for fcc (the Ti – O lattice forms). The ideal jump distance, a , is given in Table for each of the different perfect hops. The activation energy (ΔG_m) is taken as the barrier for the B-A hop as this is significantly larger than the A-B hop and therefore will be the slowest compulsory move in the RE diffusion and thus the rate controlling step. We assume the jump frequency, ν , to be $1.0 \times 10^{12} \text{ s}^{-1}$ as this comparable to the Debye frequency and therefore likely to be of the right order for the vibrational mode responsible for the diffusion process. We used a temperature of 1400 K which is comparable to the sintering temperatures used in industrial processing. The calculated distributions are shown in Figure 7.13.

Table 7.11: Calculated Diffusion Constant

	D_y	Y	Gd
$A/B\ Hop$	5.34E-09	1.29E-10	1.62E-11
D			

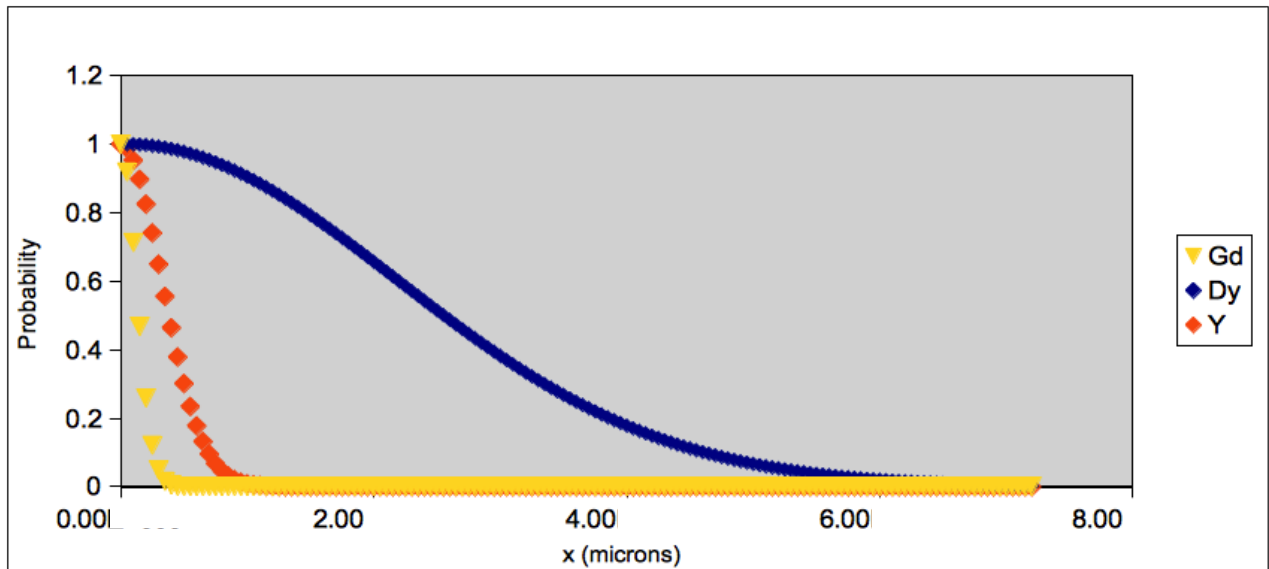


Figure 7.13: Rare-earth concentrations as a function of distance calculated at $T=1400K$, using Diffusion coefficients as calculated in Table 7.11.

All distributions are normalised. We can immediately see a substantial difference between these distributions. The Dy adopts an almost homogeneous distribution across the first micron while the Y population drops much more rapidly over the first micron and the Gd population decays extremely rapidly and is near 0 at 0.25 microns. The change in the activation energy leads to significant differences in the diffusion constant that produce these very different profiles. These suggest that Dy will be able to pass through the perovskite lattice creating an even distribution across the shell making a much more even microstructure. In §5 it was discussed that all investigated rare earths can trap oxygen vacancies to the same degree and it was theorised that the ability of each rare earth to distribute into the lattice is key to understanding the gains in

lifetime performance. The fact that Dy can migrate the furthest into the lattice creating the widest shell means that it should be the most effective at trapping oxygen vacancies during operational temperatures. The very poor diffusion shown by Gd will leave it largely trapped at the surfaces. This means that despite its thermodynamic behaviour that would produce a very good distribution of the Gd cations on the A and B sites §5, it will fail to achieve the desired shell structure and not trap Oxygen vacancies well. We can see that Y would produce the desired shell structure but would potentially require greater Y concentrations, higher temperatures, longer sintering times or other sintering aids to make it comparable to Dy. Y whilst able to dope in a self-compensatory manner also would have a large concentration of B-site doping with oxygen vacancies §5. This would also inhibit yttrium's ability to trap vacancies.

7.8 Conclusions

We have used simulation to demonstrate why Dy is the most effective RE ion to use for improving the electrical characteristics of BaTiO₃-based capacitors. Its ability to trap oxide vacancies is a combination of defect chemistry (thermodynamics) and diffusion behaviour (kinetics). The size of the ion means that the dominant way by which the Dy ion is incorporated into BaTiO₃ is by self-compensation §5. Both the isolated RE_{Ti} defect and the RE_{Ba} - RE_{Ti} pair are effective traps for oxide vacancies but this trapping ability is not significantly different across the REs studied. This is not sufficient to explain why Dy is better than other rare earths like Gd. To explain this requires a consideration of the kinetics of diffusion of rare earth ions in BaTiO₃ and here ion size also plays a role. The size of Dy is such that it fits into both the A-site and the B-site and this enables it to diffuse much faster than other rare earths and so produce a more uniform distribution of the defects that can trap the leakage current associated oxide vacancies. Other RE ions could also do this but would require much higher sintering temperatures or longer sintering times to work effectively. Finally, this study shows the strength of using a range of simulation techniques in combination with experimental data to solve a puzzle of considerable industrial interest. This work shows the power of bias-potential methods like metadynamics to investigate slow processes like cation diffusion in many oxides which are difficult to address by simple dynamical simulations or indeed by experiment. This work has shown that there are many approaches for finding barriers in solid state materials.

7.9 References

Barducci, A., Bonomi, M. and Parrinello, M. (2011) 'Metadynamics', *Wiley Interdisciplinary Reviews: Computational Molecular Science*, 1(5), pp. 826–843. doi: 10.1002/wcms.31.

Bonomi, M., Branduardi, D., Bussi, G., Camilloni, C., Provasi, D., Raiteri, P., Donadio, D., Marinelli, F., Pietrucci, F., Broglia, R. A. and Parrinello, M. (2009) 'PLUMED: A portable plugin for free-energy calculations with molecular dynamics', *Computer Physics Communications*, 180(10), pp. 1961–1972. doi: <https://doi.org/10.1016/j.cpc.2009.05.011>.

Busker, G., Chroneos, A., Grimes, R. W. and Chen, I.-W. (1999) 'Solution Mechanisms for Dopant Oxides in Yttria', *Journal of the American Ceramic Society*, 82(6), pp. 1553–1559. doi: 10.1111/j.1151-2916.1999.tb01954.x.

CrystalMaker Software Ltd (2018) 'CrystalMaker'. Oxford, United Kingdom.

Erhart, P. and Albe, K. (2007) 'Thermodynamics of mono- and di-vacancies in barium titanate', *J. Appl. Phys.*, 102(8). doi: 10.1063/1.2801011.

Garcia-Verdusch, A. and Lindner, R. (1952) 'Selbstdiffusion in Bariummetaltitanat', *Arkiv för Kemi*, 5, p. 313.

Gervasio, A. L. and F. L. (2008) 'Metadynamics: a method to simulate rare events and reconstruct the free energy in biophysics, chemistry and material science', *Reports on Progress in Physics*, 71(12), p. 126601.

Jeon, S.-C., Lee, C.-S. and Kang, S.-J. L. (2012) 'The Mechanism of Core/Shell Structure Formation During Sintering of BaTiO₃-Based Ceramics', *Journal of the American Ceramic Society*, 95(Core/Shell in BaTiO₃), pp. 2435–2438. doi: 10.1111/j.1551-2916.2012.05111.x.

- Jeon, S.-C., Yoon, B.-K., Kim, K.-H. and Kang, S.-J. L. (2014) 'Effects of core/shell volumetric ratio on the dielectric-temperature behavior of BaTiO₃', *Journal of Advanced Ceramics*, 3(1), pp. 76–82. doi: 10.1007/s40145-014-0096-y.
- Kessel, M., De Souza, R. a. and Martin, M. (2015) 'Oxygen diffusion in single crystal barium titanate', *Phys. Chem. Chem. Phys.* Royal Society of Chemistry, 17(19), pp. 12587–12597. doi: 10.1039/C5CP01187F.
- Koerfer, S., De Souza, R. A., Yoo, H. I. and Martin, M. (2008) 'Diffusion of Sr and Zr in BaTiO₃ single crystals', *Solid State Sciences*, 10(6), pp. 725–734. doi: 10.1016/j.solidstatesciences.2007.06.017.
- Meyer, R., Waser, R., Helmbold, J. and Borchardt, G. (2003) 'Observation of Vacancy Defect Migration in the Cation Sublattice of Complex Oxides by Tracer Experiments', *Physical Review Letters*, 90(10), p. 105901. doi: 10.1103/PhysRevLett.90.105901.
- Müller, A. and Härdtl, K. (1989) 'Ambipolar diffusion phenomena in BaTiO₃ and SrTiO₃', *Materials Science and Processing*. Berlin/Heidelberg, 49(1), pp. 75–82. doi: 10.1007/BF00615468.
- Paunović, V., Živković, L. and Mitić, V. (2010) 'Influence of rare-earth additives (La, Sm and Dy) on the microstructure and dielectric properties of doped BaTiO₃ ceramics', *Science of Sintering*, 42(1), pp. 69–79. doi: 10.2298/SOS1001069P.
- Preis, W. and Sitte, W. (2006) 'Electronic conductivity and chemical diffusion in n-conducting barium titanate ceramics at high temperatures', *Solid State Ionics*, 177(35–36), pp. 3093–3098. doi: 10.1016/j.ssi.2006.07.053.
- Quigley, D. and Rodger, P. M. (2008) 'Metadynamics simulations of ice nucleation and growth', *The Journal of Chemical Physics*, 128(15), p. 154518. doi: 10.1063/1.2888999.
- Shannon, R. D. (1976) 'Revised effective ionic radii and systematic studies of interatomic distances in halides and chalcogenides', *Acta Crystallographica Section A*. 5 Abbey Square, Chester, Cheshire CH1 2HU, England, 32(5), pp. 751–767. doi:

10.1107/S0567739476001551.

Smith, W. and Forester, T. R. (1996) 'DL_POLY_2.0: A general-purpose parallel molecular dynamics simulation package', *Journal of Molecular Graphics*. Elsevier, 14(3), pp. 136–141. doi: 10.1016/S0263-7855(96)00043-4.

Song, C.-R. and Yoo, H.-I. (2000) 'Chemical Diffusivity of BaTiO₃- δ : IV, Acceptor-Doped Case', *Journal of the American Ceramic Society*, 83(4), pp. 773–779. doi: 10.1111/j.1151-2916.2000.tb01273.x.

Thomas, B. S., Marks, N. A. and Begg, B. D. (2007) 'Defects and threshold displacement energies in SrTiO₃perovskite using atomistic computer simulations', *Nuclear Instruments and Methods in Physics Research, Section B: Beam Interactions with Materials and Atoms*, 254(2), pp. 211–218. doi: 10.1016/j.nimb.2006.11.069.

Uberuaga, B. P. and Vernon, L. J. (2013) 'Interstitial and vacancy mediated transport mechanisms in perovskites: A comparison of chemistry and potentials', *Solid State Ionics*. Elsevier B.V., 253, pp. 18–26. doi: 10.1016/j.ssi.2013.08.022.

Walsh, A., Catlow, C. R. A., Smith, A. G. H., Sokol, A. A. and Woodley, S. M. (2011) 'Strontium migration assisted by oxygen vacancies in SrTiO₃ from classical and quantum mechanical simulations', *Physical Review B - Condensed Matter and Materials Physics*, 83(22). doi: 10.1103/PhysRevB.83.220301.

Yang, G. Y., Dickey, E. C., Randall, C. A., Barber, D. E., Pinceloup, P., Henderson, M. A., Hill, R. A., Beeson, J. J. and Skamser, D. J. (2004) 'Oxygen nonstoichiometry and dielectric evolution of BaTiO₃. Part I—improvement of insulation resistance with reoxidation', *Journal of Applied Physics*. American Institute of Physics, 96(12), pp. 7492–7499. doi: 10.1063/1.1809267.

Yoo, H.-I., Lee, C.-E., De Souza, R. A. and Martin, M. (2008) 'Equal mobility of constituent cations in BaTiO₃', *Applied Physics Letters*, 92(25), p. 252103. doi: 10.1063/1.2951606.

Yoo, H.-I., Song, C.-R. and Lee, D.-K. (2002) 'BaTiO₃-[delta]: Defect Structure, Electrical Conductivity, Chemical Diffusivity, Thermoelectric Power, and Oxygen Nonstoichiometry', *Journal of Electroceramics*. Dordrecht, 8(1), pp. 5–36. doi: 10.1023/A:1015570717935.

8 Conclusions and Future Work

In this thesis a number of simulation techniques at various time and length scales were utilised to investigate the effects of rare-earth doping in barium titanate. Rare-earth doping can affect the microstructure of such ceramics, forming core-shell structures, improving the temperature stability of the bulk and increasing the lifetime, or number of cycles to failure, of a capacitor made from these materials. The lifetime improvements seen in rare-earth doped are often attributed to the ability of rare-earth elements to trap oxygen vacancies in the lattice and prevent their migration which can lead to electrical breakdown.

In §2 it was shown that finite element modelling can be used to simulate the impedance spectra of complex user generated microstructures. This provided insight into the relationship between local and bulk, microstructural and electrical properties. User generated input properties for individual areas of the microstructure were used to see if a simple analytical relationship between input local properties and the output bulk impedance spectra existed. The relationship between core and shell properties and the bulk properties was established as not linear. No simple analytical relationship was observed. To further explore the effect that rare-earth doping of barium titanate has on its bulk properties it is necessary to obtain realistic properties to input into future FEM simulations. These could be obtained by atomistic simulation, quantum mechanics or experiment. Atomistic methods were used in subsequent sections to investigate rare-earth doping due to its efficiency and the system size that can be simulated. Atomistic simulation can also reveal information about the thermodynamics and kinetics of rare-earth doping in barium titanate.

In §4 X-ray diffraction spectra and transmission electron microscopy selected area diffraction patterns of orthorhombic calcium titanate, cubic barium titanate and methylammonium lead iodide perovskites were simulated from molecular dynamics calculations. The diffraction patterns display the correct super reflections for calcium titanate and no super reflections for cubic barium titanate. The d-spacings for calcium and barium titanate compare well with experiment. The patterns include temperature averaging effects as they were calculated from dynamic simulations. This eliminates the

need for calculation of thermal ellipsoids for the X-ray diffraction spectra, reducing the need for pattern refinement.

The in-house PALAMEDES analysis code is capable of determining the angles of tilt, their averages, minimums and maximums, and calculating tilt phase for each octahedra in the simulated system. The code uses an internal reference frame, allowing for distortions and non-centrosymmetric systems to be analysed. The calculated tilt phase and angles for barium titanate and calcium titanate agree with the analytical Glazer notation for both systems. This shows that PALAMEDES is capable of correctly calculating tilt angles and phase whilst allowing for distortions. In the future it will be utilised on non-perfect systems, including solid solutions and defects.

It is also discussed in §4 that random sampling of the molecular dynamics data is key for generating experimentally comparable XRD and TEM spectra as simulation timesteps are three orders of magnitude smaller than how often the sample is 'seen' experimentally. Approximately 20% random sampling of total frames for a large system on a long time run generated XRD spectra and TEM patterns comparable to experiment and converged tilt averages and standard deviations. We can predict TEM patterns for bulk methyl-ammonium lead iodide which has not yet been possible experimentally. The TEM gives d-spacings which are in agreement with available XRD. The tilt angle analysis gives quantitative values for tilt angles and shows that although the overall structure is viewed as cubic, the tilting in each directions are not equal and opposite, suggesting a higher level of disorder in the system than seen in the XRD or predicted TEM.

In the short term the PALAMEDES code proof of concept with the simulated experimental spectra will be published. Further analysis of TEM and XRD patterns for other perovskites and solid solutions will be possible. Directly simulating the experimental spectra of materials should become standard practise when evaluating new forcefields. It would be interesting to use both experimental and simulated spectra as part of an automated fitting process. Conversely using simulated spectra to explore the arrangements in which and the threshold at which the influence of dopants, can be seen by experimentalists. The geometrical analysis could be extended to cover systems other than perovskites, to better probe the dynamic behaviour of the materials.

In the static atomistic simulation chapter §5, the five possible defect compensation schemes for Gd, Y and Dy in barium titanate were simulated. The probability that each rare-earth would exhibit a given compensation scheme was calculated and these probabilities agreed with experiment. The lowest energy schemes for the mid-size rare-earths were self-compensatory doping, and doping on the B-site with oxygen vacancies generated to compensate.

Mid-size rare-earth ions Gd, Y and Dy (0.9-0.95 Å) were all shown to trap oxygen vacancies with similar energetics (\sim -3.7eV) when doped in the self-compensatory manner both in AB defect pairs and as lone B-site dopants.

Both AB pairs and lone B-site dopants can trap oxygen vacancies from all directions showing that both schemes have a spherical area of influence on the lattice. All rare-earth dopants investigated affect oxygen vacancies up to four lattice sites away, illustrating why they are effective in the small amounts seen experimentally. At close quarters, AB associated self-compensatory pairs are the most energetically favourable mechanism for trapping oxygen vacancies due to the lattice relaxations that occur in the cluster.

Dy experimentally gives the best lifetime improvements, but these results suggest that all mid-size rare earths when doping in a self-compensatory manner should give the same lifetime improvements. According to the calculated probabilities this means that Gd should give the best lifetime improvements as it wants to dope in a self-compensatory manner the most which suggests that the difference in performance comes from the distribution of the rare-earth elements in the lattice, and therefore the rare-earth ion mobility. Repeating these simulations for the whole lanthanide group including Holmium would be useful. Exploring the energetics of mixed rare-earth pairs in the lattice may help offer cheaper alternatives to pure Dy as possible dopants.

The ability of the different rare-earths to diffuse through the lattice and achieve wide distribution during processing was investigated in §7. The ability of the rare-earth ions to migrate is likely to be significant for lifetime performance gains in MLCCs. Firstly self-diffusion of oxygen, barium and titanium were investigated. The self-diffusion of oxygen was simulated using metadynamics, steered MD, umbrella sampling, mean squared displacement and rational functional optimisation. All techniques used produced an activation energy of between 0.8 and 1.2 eV which compares well both

with available simulation values and experimental values. Metadynamics was considered to be the efficient method for simulating diffusion as it requires the least user input and fitting and outputs the most information about shape and direction of the diffusion pathway, along with a relatively accurate barrier height. The calculated barriers from metadynamics for barium and titanium diffusion agreed well with other simulation values, and also agreed with experimental work.

In the case of the rare-earth ions all possible diffusion pathways, A-A, B-B, A-B and B-A, were simulated for Dy, Y and Gd using metadynamics. The A-B and B-A diffusion pathways were the shortest and gave the smallest barriers, suggesting that during sintering rare-earths migrate from the A-site to the B-site and vice versa to get into the bulk ceramic. The B-A hop was determined to be the rate limiting step for rare-earth diffusion in barium titanate. Based on the activation energies for this hop, Dy is the most mobile rare-earth investigated. The size of the Dy ion means that the dominant way by which it is incorporated into BaTiO₃ is by self-compensation §5. Dy is a size such that it fits into both the A-site and the B-site but not well enough to want to stay in either site and this enables it to diffuse much faster than other rare-earths investigated. This higher rate of diffusion would produce a more uniform distribution of the defect clusters that can trap the leakage current associated oxide vacancies explaining Dysprosium's performance gains over other rare-earth elements. Other rare-earth ions could also do this but would require much higher sintering temperatures or longer sintering times to work effectively. Another option may be mixing some different rare-earths together to encourage migration.

This thesis shows the strength of using a range of simulation techniques in combination with experimental data to solve a puzzle of considerable industrial interest. It has also been shown that in solid state ceramics, multiple advanced sampling methods are suitable for finding migration barriers. The appropriate fitting for these techniques has been detailed as well as the limitations of any results obtained.

Metadynamics could be used to investigate other doping scenarios in barium titanate including other rare-earths and transition metals. Activation energies from metadynamics could be used in a kinetic Monte Carlo simulation to confirm the diffusion rates and concentrations. Building a large kMC with diffusion rates that alter themselves as the simulation progresses would be an exciting next step in this work.

Metadynamics could also be used to simulate hopping at sintering temperatures, and eventually building a simulation model which includes liquid states, may help answer whether the presence of liquid during sintering aids the formation of cores and shells and to what degree.

Appendix 1

The PALAMEDES Code

Written in house by Dr Christopher M. Handley with input from this work, the PALAMEDES code was designed to work alongside the work done for this thesis on the simulation of experimental spectra of tilted perovskites. The trajectory of the atoms is output from a MD calculation during the simulation run. This consists of the atomic coordinates at each timestep in the calculation. Using these the PALAMEDES code can calculate the angles, dipoles, volumes and phase tilts for a given system.

Outputs from PALAMEDES

There are several outputs that the PALAMEDES code creates during its analysis of a MD trajectory.

1. HISTORY-TEM

This file provides the average structure of the system over the whole simulation in the form of a single frame DL_POLY history file.

2. Angles Volumes Data

This file provides the average, minimum and maximum volumes and angles and standard deviations for every individual octahedra in the simulation over its time as well as averages taken over all octahedra. It is provided in the text file format.

3. A-site dipoles

This text file provides the average minimum and maximum magnitude of the calculated A-site dipole displacements for all A-sites.

4. B-site dipoles

This text file provides the average minimum and maximum magnitude of the calculated B-site dipole displacements for all B-sites.

5. Tilt Phase

This text file provides the calculated tilt phase and persistence length across all A-sites.